Singlet fission and excimer formation in binary organic pi-systems

Dissertation

der Mathematisch-Naturwissenschaftlichen Fakultät

der Eberhard Karls Universität Tübingen

zur Erlangung des Grades eines

Doktors der Naturwissenschaften

(Dr. rer. nat.)

vorgelegt von

Julian Hausch

aus Laichingen

Tübingen

2023

Gedruckt mit Genehmigung der Mathematisch-Naturwissenschaftlichen Fakultät der Eberhard Karls Universität Tübingen.

Tag der mündlichen Qualifikation:	26.01.2024
Dekan:	Prof. Dr. Thilo Stehle
1. Breichterstatter:	Prof. Dr. Dr. h.c. Frank Schreiber
2. Berichterstatterin:	JProf. Dr. Jannika Lauth

Contents

1. Abstract

Organic semiconductors already illuminate many displays of modern electronic devices. Additionally, they are promising candidates for the evolution of future optoelectronics, such as next-generation solar cells. A factor hindering the wide-spread use of organic solar cells is their comparatively low efficiency. One approach to increase their efficiency is the use of singlet fission, by which excitations are multiplied. After the absorption of a high-energy photon, this would allow to harvest two electron-hole pairs instead of one. Increasing the understanding of singlet fission can contribute to the development of commercially available organic solar cells, which implement singlet fission for efficiency enhancement. Therefore, singlet fission has been widely investigated in the past decades.

An ongoing difficulty in the research of singlet fission is the challenge to distinguish between singlet fission and excimer formation. Since both processes require electronic interaction between multiple molecules and contain similar photophysical steps, there are debates on the assignment of experimental fingerprints to one or the other. Even the role of excimer formation within the singlet fission process is discussed.

In this work, anthradithiophene (ADT), an organic semiconductor, which intrinsically exhibits singlet fission and excimer formation at the same time, is combined with a wide range of other organic semiconductors in thin binary films. In these samples, the intermolecular interactions of the ADT molecules are changed by structural variations and by the addition of photoelectronic decay channels. These changes influence singlet fission and excimer formation differently, allowing to disentangle both effects. The key findings of this work are summarized in the following.

- Combining ADT with a high band gap material leads to concentration-dependent changes in the polarizability of the environment. Since different states react differently to changes in polarizability, these changes are used to distinguish between fingerprints of excimers and fingerprints of states characteristic for singlet fission.

- Adding small amounts of a low band gap material to ADT creates an energetic funnel of excitations from ADT to the admixed compound. By choosing a highly efficient singlet fission material as second compound, this sample design enables

to increase the singlet fission efficiency and to decrease the losses due to excimer formation compared to neat ADT.

- Mesostructural changes are introduced to the ADT crystallites by preparing binary films containing ADT and a low band gap material, which phase-separate. This leads to a drastic decrease in excimer luminescence, making it possible to detect luminescence assignable to the intermediate state of singlet fission, the ^{1}(TT) state. Additionally, the investigation of this system uncovered a correlation between the intensity of the luminescence of the ^{1}(TT) state and the excited-state delocalization.
- Lastly, temperature-dependent measurements showed that excimer formation and singlet fission in ADT are sensitive to the sample temperature. Additionally, these measurements, in combination with further methods, are used to investigate the trap sites in thin films of a limited intermixing system containing ADT.

2. Deutsche Zusammenfassung

Organische Halbleiter werden inzwischen häufig als Leuchtelemente in Bildschirmen moderner Elektrogeräte verwendet. Zusätzlich sind sie vielversprechende Materialien für die Weiterentwicklung optoelektronischer Bauteile, beispielweise Solarzellen der nächsten Generation. Ein Grund, weshalb organische Solarzellen derzeit noch keine großflächige Verwendung finden, ist ihre geringe Effizienz. Eine Möglichkeit zur Effizienzsteigerung wäre die Verwendung der Singulettaufspaltung, durch welche Anregungen verdoppelt werden können. Dies würde die Erzeugung von zwei Elektronen-Loch-Paaren durch die Absorption nur eines hochenergetischen Photons ermöglichen. Ein detailliertes Verständnis der Singulettaufspaltung könnte den Wegbereiter für ihre Verwendung in zukünftigen organischen Solarzellen darstellen. Mit dieser Motivation wurde in den letzten Jahrzehnten die Singulettaufspaltung intensiv erforscht.

Die Unterscheidung zwischen Singulettaufspaltung und Exzimerbildung stellt eine Herausforderung für die Erforschung der Singulettaufspaltung dar. Da beide Prozesse elektronische Wechselwirkung zwischen mehreren Molekülen benötigen und über vergleichbare photophysikalische Pfade verlaufen, gibt es Debatten bei der Zuordnung experimenteller Feststellungen zum einen oder anderen Prozess. Zusätzlich ist es noch nicht abschließend geklärt, welche Rolle die Exzimerbildung für die Singulettaufspaltung spielt.

In dieser Arbeit wird Anthradithiophen (ADT) mit diversen anderen organischen Halbleitern in binären Dünnfilmen kombiniert. ADT wurde gewählt, da es als Reinmaterial bereits Singulettaufspaltung und Exzimerbildung gleichzeitig aufweist. Mit binären Dünnfilmen können die intermolekularen Wechselwirkungen beeinflusst werden. Dies geschieht durch Veränderungen der Molekülanordnung oder durch das künstliche Hinzufügen von elektronischen Zerfallskanälen. Durch dieses Vorgehen können Singulettaufspaltung und Exzimerbildung unterschiedlich beeinflusst werden, was zur Unterscheidung der Prozesse beiträgt. In dieser Arbeit konnten dazu die folgenden Erkenntnisse gewonnen werden.

- Statistische Mischungen aus ADT und einem Material mit größerer Bandlücke führen zu konzentrationsabhängigen Polarisierbarkeitsänderungen. Anhand der Re-

aktion unbekannter elektronischer Zustände auf Änderungen der Polarisierbarkeit können diese Zustände identifiziert werden und somit Exzimeren oder Zuständen des Singulettaufspaltungsprozesses zugeordnet werden.

- Das Beimischen kleiner Mengen eines Materials mit kleinerer Bandlücke als ADT erzeugt eine energetisch dirigierte Bewegung der Anregungen von ADT zum beigemischten Material. Da das beigemischte Material eine sehr hohe Singulettaufspaltungseffizienz besitzt, können durch diese Probenkonstruktion die Singulettaufspaltungseffizienz erhöht und die Verluste durch Exzimerbildung verringert werden.

- Die Kombination von ADT mit einem Material, welches sich gegen ADT phasenseparіert und eine kleinere Bandlücke als ADT hat, führt zu mesostrukturellen Änderungen der ADT-Kristallite. Dies führt zu einer drastischen Verringerung der Leuchtkraft der Exzimere, wodurch die Detektion des schwach strahlenden ^{1}(TT)-Zwischenzustands des Singulettaufspaltungsprozesses, ermöglicht wird. Hierbei wird darüber hinaus eine Korrelation zwischen der Strahlungsintensität des ^{1}(TT)-Zustands und der Delokalisierung des angeregten Zustands festgestellt.

- Mit dem zuletzt untersuchten, partial mischenden, binären System, bestehend aus ADT und einem zweiten Material mit größerer Bandlücke, werden temperaturabhängige Messungen durchgeführt. Damit konnte sowohl für die Singulettaufspaltung als auch für die Exzimerbildung eine Abhängigkeit von der Probentemperatur nachgewiesen werden. Die Kombination der temperaturabhängigen Messungen mit den Resultaten weiterer durchgeführter Experimente ermöglicht darüber hinaus eine Untersuchung von Fallenzuständen.

3. Introduction

Semiconducting materials find a wide range of applications in the modern world as they are used in artificial lights, computers, photovoltaic cells and many more applications [1, 2]. Until now, most of these applications are based on inorganic semiconductors with silicon as the most prominent and most wide-spread example. However, over the past decades, the usage of organic semiconductors (OSCs), which are carbon-based, has increased rapidly [3]. Most displays of smartphones are already based on OSCs, where slimmer displays with less power consumption and higher image quality can be manufactured, thus in many ways superior to their inorganic counterparts [4]. The flexibility of the organic material makes it even possible to build devices with foldable displays [5].

While organic optoelectronic-based displays already find application in mass-produced devices, organic photovoltaics (OPV) are currently evolving into this direction [6]. Compared to silicon-based photovoltaics, OPV have a smaller energy consumption in production, effectively leading to an ecologically more friendly device [7]. Additionally, OPV are lighter and more flexible than inorganic photovoltaics [8] and they can also be made of transparent materials, which makes new areas accessible for power generation [9–13]. Although significant improvements have been made in the past decades in power conversion efficiency, the inorganic counterparts still outperform OPV in this regard [14, 15]. One possibility to further improve the power conversion efficiency of OPV is the implementation of singlet fission, an excitation-multiplying process, which makes it possible to harvest two electron-hole pairs from just one photon in solar cells [16–19].

In this work, the process of singlet fission is investigated. Singlet fission can not only boost the efficiency of photovoltaics and photodetectors in the above-described way, but the intermediate state of singlet fission, which is spin entangled, can potentially also be used for quantum computing [20, 21]. Additionally to that, singlet fission is intriguing for fundamental research as well, since it is a process that starts with one excitation with electron and hole strongly bound to the same molecule and ends up with two independent and spatially separated excitations. This requires the presence of multiple molecules in close spatial proximity and provides new insights into the details of intermolecular interaction [22].

Complementary to singlet fission, excimer formation, a process in which one excita-

tion delocalizes over two molecules, thereby increasing the electron-hole distance [23], is investigated in this work. The delocalization over two molecules during excimer formation makes this process strongly dependent on the intermolecular interplay and hence the molecular arrangement [24–27]. Understanding the physical details behind excimer formation, which is an excited-state relaxation, can not only help in its applications in lasers [28] and organic light emitting diodes [29], but also helps completing the understanding of singlet fission, since the role of excimer formation in the singlet fission process is debated [30–32]. This debate ranges from the assignment of experimental fingerprints to the excimer [31] or to an intermediate state of singlet fission [30] to the question whether excimer formation facilitates [33–35] or hinders [31, 36–41] singlet fission.

Both multimolecular processes, singlet fission and excimer formation, are known to depend on the intermolecular interaction, which can be steered by the geometrical arrangement and by the freedom of motion of the involved molecules [26, 27, 42–45]. However, it is still not possible to predict how these processes are affected by e.g. certain changes in the molecular arrangement [46–48]. For an application of either of these effects in OSC-based devices, a full understanding of the connection between structural changes and changes of the photophysical processes would be a milestone. This understanding would open a pathway to adapt the photophysics of a given material to the desired properties for application by controlled changes in molecular arrangement.

In this work, an OSC material, namely anthradithiophene (ADT), is investigated, which exhibits excimer formation and singlet fission at the same time in the solid state. Binary thin films are used to influence the structure and photophysics of ADT in multiple ways. This enables to change the balance between excimer formation and singlet fission, which allows both processes to be disentangled for studies of the material, and also shows ways of tuning the photophysics of ADT to suit requirements.

This dissertation is organized as follows. In Chapter 4, theoretical concepts and already gained knowledge in this field are summarized, which form the basis for this dissertation. Therein, possible excitation and relaxation pathways of the characteristic π-system of an OSC as well as intermolecular interactions in solid state OSCs are introduced. Consecutively, the employed experimental techniques are briefly described in Chapter 5. The most important techniques are X-ray scattering methods for the structural characterization and time-resolved spectroscopic methods for insights in the time evolution of excited states after photoexcitation. An overview of all used OSCs and their characteristic properties is given in Chapter 6. Chapters 7-10 state the results of this work. Each results chapter starts with a brief introduction, followed by a structural and optical characterization of the produced samples, before analyzing the photophysics

based on time-resolved measurements. The results of each chapter are summarized in a conclusion. Chapter 7 focuses on the polarization-dependent spectral shift of excimer emission in binary mixtures, which enables to distinguish between spectroscopic fingerprints of excimer formation and singlet fission. In Chapter 8, an increase in singlet fission yield is achieved by preparing statistical mixtures of ADT and small amounts of a smaller band gap material. The singlet fission yield is increased, because this material combination allows for efficient energetic funneling, which is followed by singlet fission. Combining ADT and a small band gap material, which phase-separate, made it possible to detect the intermediate state of singlet fission in Chapter 9. Additionally, a correlation between excited-state coherence and detectability of the intermediate state was found. Finally, Chapter 10, focuses on the impact of changes in sample temperature on the photophysics of ADT. There, it was found that changes in sample temperature can impact the balance between singlet fission and excimer formation in ADT. Chapter 11 is the last chapter of this work and summarizes all results before giving an outlook on possible future work.

4. Fundamentals

The following chapter briefly displays the theoretical background on which this work is based on. A short general introduction of OSCs is followed by a description of their homomolecular and heteromolecular solid state. After that, excited states and transitions of OSCs are discussed, which will be the main part of this chapter. For a broader and more detailed insight into the theoretical background the reader is referred to the references given in the respective sections.

4.1. Small-molecule organic semiconductors

The main constituents of small-molecule OSCs are carbon and hydrogen, but also fluorine, chlorine, nitrogen, sulfur or oxygen can be found in common materials [50, 51]. The backbone of OSCs is built of rings of carbon atoms that are bound to each other by their sp^2 orbitals. Compared to the sp^2 orbitals, the p_z orbitals, with their highest electron density perpendicular to the ring of carbon atoms, only interact weakly between neighboring carbon molecules (Figure 4.1a,b) [52, 53]. Due to the orientation of the p_z orbitals, the interaction with other carbon atoms leads to a strong delocalization of the hybridized orbitals, which are called π orbitals (Figure 4.1c) and the weak interaction results in a relatively small energetic difference between the bonding and anti-bonding orbitals [53]. In the ground state of an OSC molecule, all binding orbitals are filled with

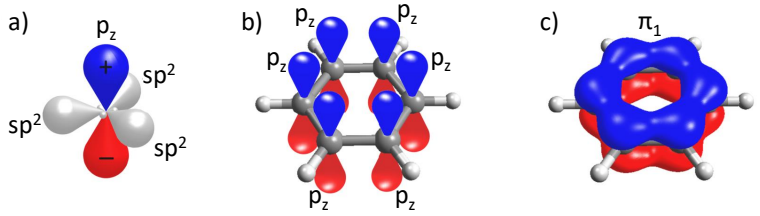

Figure 4.1.: (a) sp^2 and p_z orbitals of a carbon atom. (b) Orientation of uncoupled p_z orbitals in benzene. Note that this is not an existing orbital of benzene due to non-negligible coupling effects. (c) Coupling leads to a hybridization of the p_z orbitals, forming π orbitals, the lowest energy one of which (π_1) is shown. Figure modified from Ref. [49].

electrons, while all anti-bonding orbitals are empty. In this configuration, the orbital of highest energy, that is filled with electrons is called the highest occupied molecular orbital (HOMO), while the orbital of lowest energy that is not filled with electrons in the ground state is called the lowest unoccupied molecular orbital (LUMO) [53]. The energetic difference between HOMO and LUMO is a first indication for the electronic excitation energy of an OSC and has typical values in the range between 1 and 4 eV. Since the π orbitals are the most weakly bound orbitals, these steer the interaction of one molecule with the surrounding molecules. Here, the electron density, which is distributed relatively far away from the molecular backbone, plays a critical role, since it enables strong intermolecular coupling, allowing efficient transfer of charges and energy, giving the material its semiconducting properties [54].

4.2. Organic semiconductors in the solid state

The focus of this work is on the properties of binary thin films of OSCs prepared by vacuum-deposition (see Section 5.1). The used preparation method leads to polycrystalline films [55], in which the density of grain boundaries and defects is too high to be neglected. Single crystals provide an alternative in which impurities and grain boundaries do not play a significant role. In solid OSCs, the intermolecular interaction is high and strongly influences the properties, as will be explained in Section 4.3. To quantify this effect, experiments can be performed with the material dilutely dissolved in solution, where intermolecular interaction can be neglected.

4.2.1. Neat thin films of organic semiconductors

The following section only describes the structure of vacuum-deposited neat thin films, since this work is focused on the influence of structural changes on the photophysical properties of a vacuum-deposited material. It should be noted that, although only marginally addressed in this work, morphological investigations are also of great scientific interest, *inter alia* due to their importance for surface and interface engineering [56].

In vacuum-deposition an independent initial nucleation of multiple grains occurs, which, due to symmetry arguments, are randomly oriented within the surface plane for weakly interacting substrates [55]. For this reason, thin films are expected to be macroscopically isotropic within the surface plane and either anisotropic in the out-of-plane direction, or isotropic in all directions. If the described anisotropy is present, the corresponding sample is called uniaxially anisotropic, while the case of a random orientation of the grains with respect to all directions is called powder-like [57]. There is also a third

common case, called amorphous, in which no repeating structure of the molecules can be found. This case is not relevant for this work and hence will not be further explained.

Further details about structure and its determination in thin films can be found in Section 5.2.1.

4.2.2. Heteromolecular thin films of organic semiconductors

All heteromolecular films in this work were produced by vacuum co-deposition of two molecular species, hence only this case is discussed in the following. In this setup, three different scenarios for the resulting structure can be distinguished, which are namely phase-separation, co-crystal formation and statistical intermixing [58]. Multiple of these scenarios can be present for one heteromolecular system.

Assuming spherical molecules of type A and B and only intermolecular interaction between directly neighboring molecules, the free energy of mixing

$$F_{\text{mix}} = k_{\text{B}}T(x_A \ln x_A + x_B \ln x_B) + (W_{AA} + W_{BB} - 2\,W_{AB}) \tag{4.1}$$

is a good guidance for the preferred structure of an unknown heteromolecular system [58]. Here, k_{B} is the Boltzmann constant, T the temperature, x_A (x_B) is the concentration of type A (B) molecules, W_{AA} (W_{BB}) is the interaction energy between two molecules of type A (B) and W_{AB} is the interaction energy between one molecule of type A and one of type B. At high temperatures the entropic term $x_A \ln x_A + x_B \ln x_B$ dominates the free energy and statistical intermixing is preferred. At lower temperatures the intermolecular interaction $\chi\, k_{\text{B}}T = W_{AA} + W_{BB} - 2\,W_{AB}$ is the dominant term and different scenarios evolve, depending on the interaction energies. If the interaction energy between neighbors of the same kind is larger than between neighbors of different kind, it is preferred that neighboring molecules are of the same kind, resulting in phase-separation. This scenario is described in more detail in Appendix C. At the other extreme, when it is energetically preferred that neighboring molecules are of different type, co-crystal formation with alternating molecular species is expected. In the intermediate regime, where no large energetic difference in intermolecular interaction is present, the entropic term also dominates at lower temperatures and statistical intermixing is observed. All three scenarios are sketched in Figure 4.2.

The molecules used for vacuum co-deposition in this work are not spherical, which means that the similarity in geometric shape of the two molecules has to be taken into account additionally. For this purpose, the geometric similarity ϵ is a good guidance,

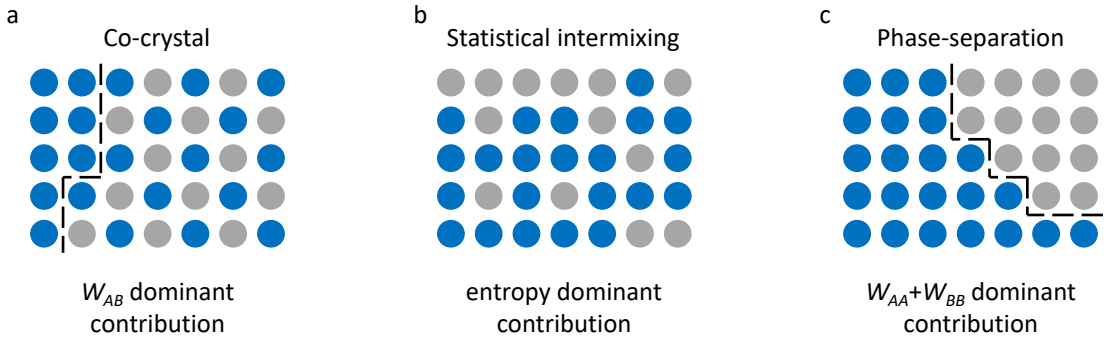

Figure 4.2.: The possible equilibrium structures of two different spherical molecular compounds are sketched with blue and grey circles. Depending on the temperature and the intermolecular interaction energies, co-crystal formation (a), statistical intermixing (b) or phase-separation (c) is preferred. Inspired by Ref. [58].

which is defined as

$$\epsilon = 1 - \frac{\Delta}{\tau} \tag{4.2}$$

with the minimum non-overlapping volume Δ and the maximum overlapping volume τ of the two molecules under consideration [59, 60]. In principle, two molecules with a high geometric similarity are expected to exhibit statistical intermixing due to low lattice stress upon the replacement of a molecule with one of the other species. However, as pointed out earlier in this section, geometric similarity alone does not control the mixing behavior, but also other factors such as intermolecular interaction [58] or molecular rigidity play an important role [59].

4.3. Excited states and transitions

Organic molecules can absorb and store energy. One common way for organic materials to do so is by absorption of photons that lead to an excitation of the molecule, which eventually releases this energy again and thereby loses its excitation [53]. Two types of excitations will be discussed in the following chapter, which are namely vibrational and electronic excitations. Additionally, the connection between vibrational and electronic excitation will be explained and transitions between the ground state and the excited state as well as transitions between two excited states will be discussed.

4.3.1. Intermolecular and intramolecular vibrations

The atomic nuclei of a molecule can oscillate with respect to each other in a molecule, which means that a molecule is in principle made up of many coupled, multi-dimensional quantum-mechanical oscillators. For molecules without cylindrical symmetry, there are $3N - 6$ different modes of intramolecular motion, with N being the total number of atoms in the molecule. These modes of motion are called intramolecular vibrations or intramolecular vibrational modes and can be treated like quantum-mechanical oscillations with their assigned particle called phonon. The most important vibrational modes of the molecules studied in this work are dominated by stretching modes between two covalently bonded carbon atoms (C-C stretching mode) and mostly have a phonon energy of around 0.17 eV [61].

In solid state, there are also intermolecular vibrations in addition to the intramolecular vibrations. Intermolecular vibrations are driven by the motion of two molecules with respect to each other that are bound to each other by van der Waals forces. Since the intermolecular forces are weaker than the intramolecular forces, also the resonance frequencies and consequently the phonon energies are comparatively lower for intermolecular vibrations [62]. In fact, most phonon energies assigned to intermolecular motions have energies below the thermal energy at room temperature, which means that thermal activation of intermolecular vibrations has to be taken into account in measurements at room temperature.

4.3.2. Electronically excited states of isolated molecules

In Section 4.1 it was explained that electrons in π orbitals have the highest energy in the ground state of an OSC and thus control the lowest possible electronic excitations. Hence the HOMO and LUMO and additionally the orbitals energetically below the HOMO (HOMO$-n$, which is $n \in \mathbb{N}$ orbitals below the HOMO in energy) and above the LUMO (LUMO$+n$, which is $n \in \mathbb{N}$ orbitals above the LUMO in energy) play an important role in the construction of excited states [53]. Recall that the construction of the molecular π orbitals in Section 4.1 was done for a single π electron, i.e. while neglecting electron-electron interaction. Treating the interaction between π electrons as perturbation results in excited states not simply being described as a single configuration, i.e. electrons occupying and not occupying certain molecular orbitals, but as a linear combination of multiple such configurations [53]. In Figure 4.3 this is exemplary illustrated for the energetically lowest excited singlet state S_1. This linear combination is called configuration interaction and the assigned states are eigenstates of an isolated molecule and are called adiabatic states. The individual configurations, which contribute to the

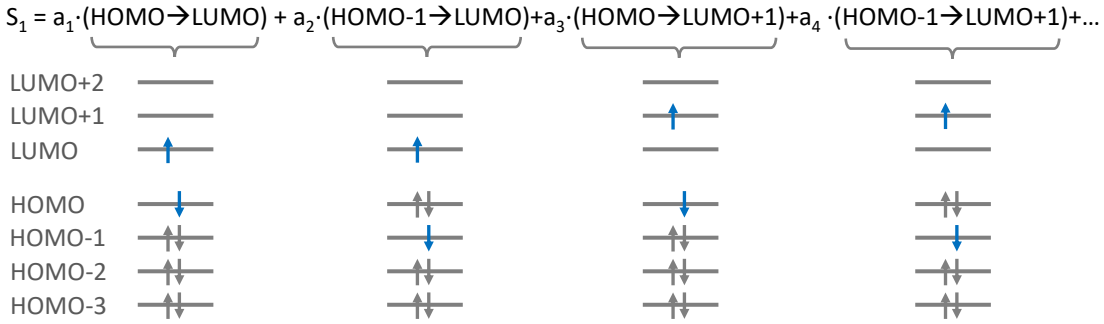

Figure 4.3.: Due to electron interaction, the adiabatic state S_1 is a linear combination of multiple configurations. Representative configurations are sketched by depicting the distribution of electrons over the most relevant molecular orbitals. Inspired by Ref. [53].

adiabatic states, are no eigenstates and are called diabatic states.

So far, the excited state has been described by the electron configuration, which is the spatial distribution of the electrons bound to the molecule. However, further properties are part of the state of the molecule, which are namely motion of the atomic cores in the molecule and the spin of the electron. If the energy levels of the electronic states are well separated and no heavy ions are in the structure of the molecule, the motion of the light electrons, the relatively heavier atomic nuclei and the change in spin all occur on different timescales (here they are listed from short to long timescales) and hence their wavefunctions can be separated, which is called the Born-Oppenheimer approximation [63, 64]. Considering an electronic excitation due to the absorption of a photon under this approximation, we start with the Hamiltonian

$$\hat{H} = \hat{H}_0 + \hat{H}_{\mathrm{ph}} \tag{4.3}$$

with the Hamiltonian of the isolated molecule $\hat{H}_0$ and the perturbation caused by photonic radiation $\hat{H}_{\mathrm{ph}}$ and use Fermi's golden rule to calculate the transition rate

$$k_{if} = \frac{2\pi}{\hbar} |\left\langle \psi_f \right| \hat{H}_{\mathrm{ph}} \left| \psi_i \right\rangle|^2 \rho, \tag{4.4}$$

where $|\psi_i\rangle$ and $\left|\psi_f\right\rangle$ are the initial and final state and are both eigenstates of the isolated molecule and ρ is the density of final states. Now the Born-Oppenheimer approximation is applied and, due to the short timescale of photon absorption, results in the photon only changing the electronic wavefunction $|\psi_{\mathrm{el}}\rangle$, but not the wavefunction of the atomic cores

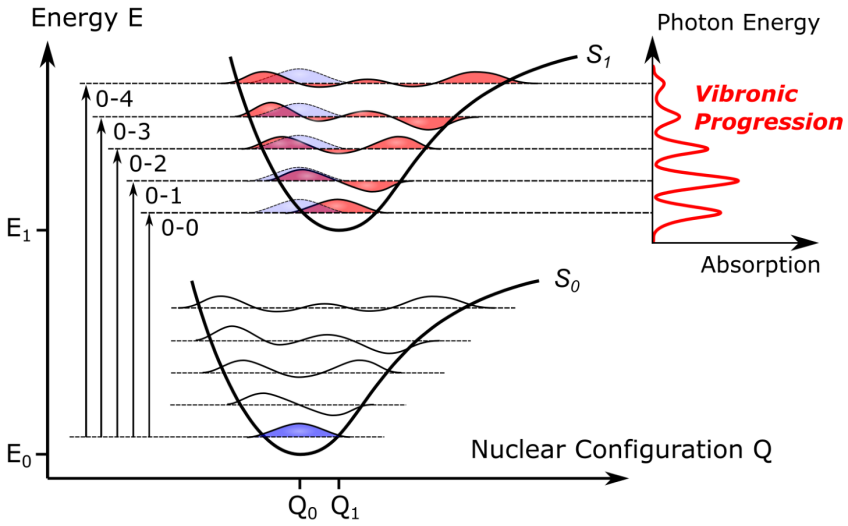

Figure 4.4.: Sketch of the origin of vibronic progression. Due to different nuclear arrangements being energetically most favorable for the S_0 (configuration Q_0) and the S_1 state (configuration Q_1), the molecular arrangement of the vibrational ground state of the S_0 state overlaps with multiple vibrational states of the S_1 state (overlap of blue and red areas). As a result, the transition between the two electronic states splits into multiple absorption peaks with an energetic spacing depending on the vibrational quanta involved (upper right corner). Figure from Ref. [49].

$|\psi_{\text{vib}}\rangle$ or the spin wavefunction $|\psi_{\text{spin}}\rangle$ [53]. This simplifies Equation 4.4 to

$$k_{if} = \frac{2\pi}{\hbar} \left| \langle \psi_{\text{el},f} | \hat{H}_{\text{ph}} | \psi_{\text{el},i} \rangle \right|^2 \cdot \left| \langle \psi^f_{\text{vib},f} | \psi^i_{\text{vib},i} \rangle \right|^2 \cdot \left| \langle \psi_{\text{spin},f} | \psi_{\text{spin},i} \rangle \right|^2 \rho. \tag{4.5}$$

The first factor is the excitation of electrons caused by the photon. The second factor represents a vibrational excitation coupled to the electronic excitation, which can occur since the electron distributions of the initial state and the final state differ and the energetically most favorable arrangement of the atomic cores depends on the distribution of electrons. This means that the vibrational wavefunctions assigned to the initial electronic state ($\psi^i_{\text{vib},n}$) are different to those assigned to the final electronic state ($\psi^f_{\text{vib},m}$), explaining the use of the superscripted indices for the wavefunctions of the atomic cores, which tell the electronic state [65]. Consequently, two atomic wavefunctions assigned to two different electronic states in general do not have identical eigenfunctions. The last factor is spin conservation and $\left| \langle \psi_{\text{spin},f} | \psi_{\text{spin},i} \rangle \right|^2 = \delta_{fi}$ with the Kronecker delta δ_{fi} holds true for all photonic transitions investigated in this thesis. The spin states will be discussed in further detail later in this section.

For a better understanding of the role of the atomic wavefunction in electronic transi-

tions, a more intuitive picture of the coupling between electronic and vibrational excitations, which is called vibronic coupling, will be introduced in the following. The picture is based on a coordinate Q, which represents the geometric distortion of the atoms in the molecule. Since the arrangement of atomic cores with minimum energy depends on the electronic state of the molecule, the minimum energy is at different values of Q for different electronic states. Distortions of the molecule along Q away from this minimum leads to an increase in energy. From a quantum-mechanical point of view, the potential around this minimum in Q can be seen as an oscillator assigned to the respective electronic state with eigenfunctions and eigenenergies. Now, an electronic excitation initially only changes the electronic state, but not the nuclear arrangement (Born-Oppenheimer approximation), i.e. the given nuclear arrangement of the initial state is transferred to the final electronic state, in which it can be described as a linear combination of multiple atomic wavefunctions assigned to the final electronic state [53]. This means that an electronic excitation can be accompanied by vibrational excitations, which is called vibronic excitation and can be seen in absorption and emission spectra (Figure 4.4). In such spectra, the absorbed or emitted photon energy is then not only the energy difference between the two electronic states involved, but the possible addition of vibrational quanta leads to multiple peaks assigned to one electronic transition that are energetically separated by the energy of the respective vibrational quanta involved.

Since electrons are fermions, the total wavefunction of two electrons, which is the spatial wavefunction multiplied with the spin wavefunction, has to be antisymmetric under exchange of two electrons. For the ground state of a molecule, this means that all orbitals energetically below the LUMO are occupied with two electrons each and each pair of electrons in the same orbital has an antisymmetric spin wavefunction to make the total wavefunction antisymmetric. Since the only antisymmetric spin wavefunction of two electrons is the singlet with a spin of zero, the molecule in ground state is also in the singlet state and this state is called S_0. In an excited state one electron is promoted from an orbital below the LUMO to an orbital above the HOMO, resulting in two orbitals occupied by only one electron each. In this configuration the spatial wavefunction can be symmetric or antisymmetric, hence the spin wavefunction can be in the antisymmetric singlet configuration with spin zero or in one of the three symmetric triplet configurations with spin $\hbar$. Due to the exchange energy, the triplet state of a given orbital configuration is generally lower in energy than the singlet state [53].

After introducing the states with the lowest energies for a single molecule, the transitions between these will be discussed. Since the energies of phonons and excitons are well above the thermal energy in case of the molecules relevant in this work, the molecule is expected to be in electronic and vibrational ground state if no external energy

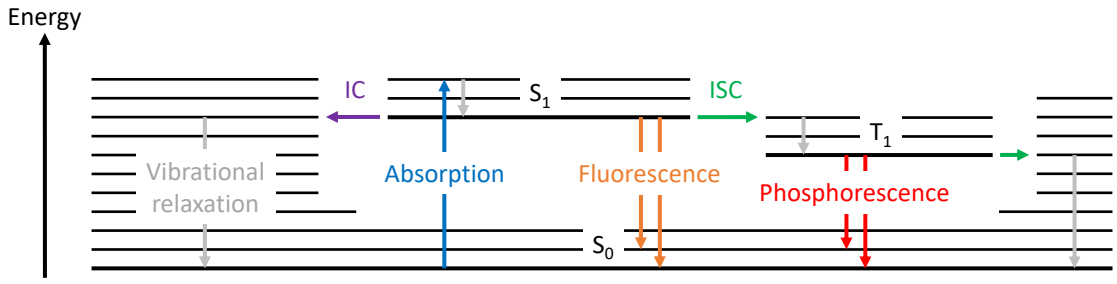

Figure 4.5.: Jablonski diagram including the single molecule states and transitions relevant for this work. Absorption, fluorescence and phosphorescence are transitions, which cause luminescence, while vibrational relaxation, internal conversion (IC) and intersystem crossing (ISC) are mostly considered luminescence quenching channels. Inspired by Ref. [66].

is transferred to the molecule. In this work molecules are excited into the lowest possible electronic singlet state by absorption of photons with matching energy. Photonic excitation into the triplet state can be neglected due to spin conservation during excitation [53, 67]. After excitation, the vibrational excitations decay first, and the molecule will end up in the lowest possible S_1 state [68]. This process is called vibrational relaxation (grey arrows in Figure 4.5). From there, three decay mechanisms are possible, one of which is internal conversion (IC), an isoenergetic transition to a vibrational excitation of a lower-energy electronic state of the same spin manifold (purple arrow in Figure 4.5), which is then usually followed by vibrational relaxation [69]. Alternatively, the excited singlet state can decay radiatively to a lower energy state of the same spin manifold, which is called fluorescent decay (orange arrows in Figure 4.5) [67, 69]. The third possibility is ISC, which is an isoenergetic transition to a vibrational excitation of a state with different spin manifold and hence requires a change in the spin wavefunction (green arrows in Figure 4.5) [53, 68, 69]. This change is mainly driven by spin-orbit coupling and is more efficient if the molecule under investigation has heavy atoms built-in. The state with a different spin wavefunction, which is a triplet state, also requires a change in the spin wavefunction to decay back to the singlet ground state. This can happen either by ISC to a singlet state [68] or alternatively by a radiative process called phosphorescence (red arrows in Figure 4.5) [67]. The difference between fluorescence and phosphorescence is that phosphorescence requires a change in the spin wavefunction while fluorescence does not, which makes the latter the more efficient mechanism [67]. Both mechanisms are summarized under the term luminescence.

4.3.3. Electronically excited states of molecules in aggregates

So far, only excited states of isolated molecules have been discussed. In the following, the admolecule will be placed in an environment of molecules of the same kind, which results in two main changes, namely a polarizable environment now being available and molecules being in close proximity, leading to electronic intermolecular interaction.

These effects will be introduced in the following with the example of a neat OSC forming a herringbone structure, i.e. having two translationally inequivalent molecules per unit cell. Before considering the whole aggregate, the photophysics of one isolated unit cell containing two molecules has to be understood. In the ground state, the interaction between the molecules leads to a small change in energy of the ground state. The more interesting case is the presence of one S_1 excitation, which delocalizes over both molecules due to intermolecular interaction [70]. Two new states evolve, one is an addition of the two localized excitations, the other one a subtraction. This leads to an energetic splitting of the two newly formed states, which, however, is not the main source of the splitting if the molecules are sufficiently close. Instead, the admixture of the charge transfer (CT) state, an excited state in which a molecular anion and a molecular cation neighbor each other, causes most of the splitting [71]. Because of symmetry arguments, the CT state strongly couples to the symmetric linear combination, while it barely couples to the antisymmetric state, leading to a strong energetic splitting of the two S_1 states [71], which is called Davydov splitting [72].

Now the unit cell is put into an aggregate, which means that there is a repeating lattice of unit cells. This creates a polarizable environment for the molecule and since the dipole moment of a molecule changes upon excitation or relaxation [53], the environment energetically relaxes after both these processes. As a result, the photon energy absorbed during absorption is larger than the energy of the excited state and the photon energy emitted during relaxation is smaller than the energy of the excited state. The difference between absorbed and emitted photon energy is called Stokes shift [67]. Additionally to creating an environment, the presence of neighboring unit cells means that an excitation is not only delocalized within one unit cell, but can also be delocalized over multiple unit cells. This delocalization is called excited-state delocalization, which is the number of molecules an exciton is distributed over, and has to be distinguished from exciton delocalization, which describes the average distance between electron and hole within an exciton. The excited-state delocalization can mathematically be described as a linear combination of localized excitons and leads to an energetic splitting between the resulting states that is usually too small to be resolved spectroscopically and hence called exciton band [53, 73]. The reason for the small energetic difference between the states

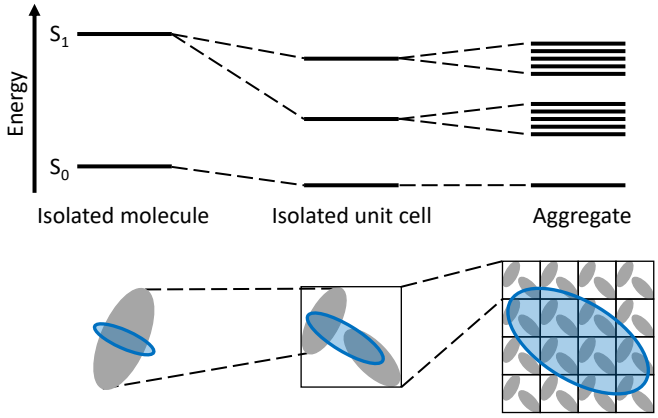

Figure 4.6.: The energetic landscape of an electronic transition is changed by intermolecular interaction. The interaction between two molecules inside a unit cell leads to the Davydov splitting (center) and the interaction between the unit cells leads to the formation of exciton bands (right). The intermolecular interaction leads to a delocalization of the exciton, which is sketched in the lower part of the figure. Moving from the isolated molecule (left) to the isolated unit cell (center) and further to the aggregate (right), the excited state (blue oval) delocalizes over an increasing number of molecules (grey ovals). Inspired by Ref. [53].

within one band compared to the Davydov splitting is that the distance between two unit cells is significantly larger than the one between the two molecules inside one unit cell and hence the interaction between unit cells is smaller than within a unit cell. Depending on the orientation of the molecules, excited-state delocalization can lead to an increase or suppression of luminescence, the effect of which is weakened for vibronic replica of the emission due to symmetry breaking caused by the vibrational quanta [73, 74].

Exciton migration

In an aggregate, the exciton is not bound to the site of initial excitation but can spatially migrate through the sample. There are two mechanisms used to describe this migration, which are namely Dexter energy transfer and Förster resonance energy transfer (FRET) [53]. The transfer rate of FRET

$$k_{\mathrm{FRET}} = k_{\mathrm{rad}} \left(\frac{R_{\mathrm{F}}}{R} \right)^{6} \tag{4.6}$$

depends on the inverse of the sixth power of the distance R between the two molecules involved in the transfer, on the radiative decay rate of the initially excited molecule k_{rad}

and on the Förster radius R_F. The Förster Radius is defined as

$$R_\mathrm{F}^6 = \frac{9\log(10)\,\kappa^2}{128\,\pi^5 n^4 N_\mathrm{A}} \cdot \int_0^\infty I_D(\lambda)\epsilon_A(\lambda)\lambda^4\,\mathrm{d}\lambda \tag{4.7}$$

with the orientation factor κ between the initially and finally excited molecule, the refractive index n, Avogadro's constant N_A, the normalized emission spectrum of the initially excited molecule $I_D(\lambda)$ and the molar extinction coefficient of the finally excited molecule $\epsilon_A(\lambda)$ [75]. The integral in Equation 4.7 depends on the spectral overlap of the emission and absorption of the energy donor and acceptor, respectively, and hence this process can only play a significant role for excited states with dipole allowed transitions from and to the ground state. For other excited states, such as triplets, the Dexter energy transfer is the dominating mechanism, which is based on electron transfer and hence orbital overlap, making it short-ranged compared to FRET [53].

Due to energetic considerations, a migration of excitons to low-energy sites, which are typically impurities in a neat film and are called trap sites, is expected [76]. Migration away from trap states is only possible by thermal activation, which results in kinetic trapping of excitons in energetically deep traps or at low temperatures. Note that kinetic trapping of excitons is already possible in shallow traps at low temperatures, while deeper traps are needed at intermediate temperatures, which means that deep traps play an important role for the photophysics at intermediate temperatures, while the photophysics at low temperatures is dominated by kinetic frustration in shallow traps, making the occupation of deep traps kinetically less likely.

At high excitation densities, an exciton my migrate to a site, which already carries an excitation. This results in one single higher excitation, which subsequently relaxes via IC, effectively leading to an annihilation of one of the two excitons [77]. Depending on the spin-multiplicity of the two excited states present before the annihilation process, the process is called singlet-singlet (SSA), singlet-triplet (STA) or triplet-triplet annihilation (TTA).

Excimers

Excimer is the short form of the term excited dimer and stands for an excited state that is distributed over two molecules in close proximity [23]. In most cases, the excimer cannot be excited directly, but forms out of the S_1 state. During excimer formation, the two molecules involved exhibit an intermolecular movement toward each other, while at the same time the electronic structure of the excited state changes (top black arrow in Figure 4.7) [23, 24, 26]. This change in electronic structure compared to the S_1 state,

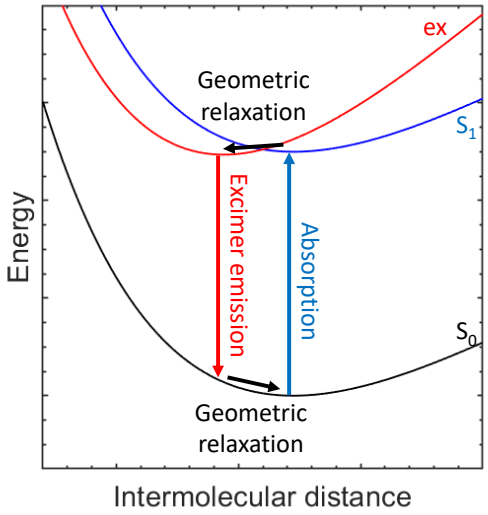

Figure 4.7.: Sketch of the relevant potentials and transitions during excimer formation. The high CT state admixture to the excimer state makes a movement of the molecules toward each other after excitation energetically favorable due to Coulomb attraction. Once the excimer decayed, the ground state geometry with a higher intermolecular spacing is favorable again, leading to one more geometric relaxation following the electronic deactivation. Ground state (S_0) and excited state (S_1) potentials are both Lennard-Jones potentials, for the excimer state (ex) the sum of a Lennard-Jones potential and a Coulomb potential was used. Inspired by Ref. [23].

which is mainly a strong increase in admixture of the diabatic CT state to the adiabatic state, introduces increased Coulomb attraction between the two molecules, stabilizing the excimer state and its distorted geometry (compare the red excimer potential with the blue S_1 potential in Figure 4.7) [23, 78]. Due to the strong geometric distortion in the excimer state, the main decay channel of excimers is IC, which means that most of the luminescence is quenched [23, 79], however, luminescent excimer decay is possible as well [31]. Once the electronic excitation of the excimer is decayed, the involved molecules move away from each other again and reposition themselves in the geometry found before the excimer formation (lower black arrow in Figure 4.7). The enormous geometric distortion associated with excimer formation has two effects on the luminescence of excimers. First, the geometric changes during excimer formation and after excimer emission are both energetic relaxations, which in turn means that the photon energy of excimer emission is significantly lower than the photon energy associated with the excitation or emission of the S_1 state [27]. Second, the intermolecular movement between excimer state and ground state leads to a strong involvement of intermolecular

phonons into the vibronic progression. This leads to a strong asymmetric broadening of the excimer luminescence [24], since thermal broadening makes it impossible to spectrally resolve the intermolecular phonons [23]. The intermolecular movement associated with excimer formation also strongly reduces the mobility of this state compared to the S_1 state [23].

Singlet fission

Singlet fission is an excitation multiplying multimolecular spin-allowed photophysical process, which converts one singlet excitation into two triplet excitations [18, 19]. The process can be divided into several steps, which are (i) the spin-allowed conversion of a singlet excited state ($S_1 + S_0$) into an electronically coupled triplet-pair state with a total singlet spinfunction (^{1}(TT)), (ii) a loss of electronic coupling from the triplet-pair state (^{1}(TT)) to the only spin coupled triplet-pair state (^{1}(T···T)) and finally (iii) a further loss of any coherence between the triplets, resulting in two independent triplets ($T_1 + T_1$) [22]. All processes are in principle also possible backwards, resulting in the equilibrium equation

$$S_1 + S_0 \overset{\text{(i)}}{\rightleftharpoons} {}^1(\text{TT}) \overset{\text{(ii)}}{\rightleftharpoons} {}^1(\text{T}\cdots\text{T}) \overset{\text{(iii)}}{\rightleftharpoons} T_1 + T_1. \tag{4.8}$$

The reverse process to singlet fission is called triplet fusion. Singlet fission can only be efficient if the singlet state is of the order of at least two times the triplet energy [19], otherwise an energetic barrier hinders the process.

In the following all three steps will be discussed in more detail. Starting with the most intriguing one, triplet-pair formation (step (i) in Equation 4.8) can occur on fast timescales since the two triplets in the final state couple to an overall singlet, making the process spin-allowed [18, 19]. However, a transition from the diabatic $S_1 + S_0$ state to the diabatic ^{1}(TT) state requires a transfer of two electrons (center part of Figure 4.8), resulting in a very small direct coupling between the two states. Importantly, this model ignores the admixtures of the diabatic CT state to the adiabatic S_1 or ^{1}(TT) state as well as a possible admixture of the diabatic ^{1}(TT) state to the adiabatic S_1 state and *vice versa*. If the diabatic S_1 and ^{1}(TT) states are mixed in the adiabatic states, the adiabatic S_1 state can evolve coherently into the ^{1}(TT) state and the process is called coherent singlet fission (lower part of Figure 4.8) [80]. In the case of the adiabatic S_1 and ^{1}(TT) states only carrying shared admixtures of the diabatic CT state in a relevant amount, the coupling between the states occurs indirectly via the diabatic CT state and the process is called incoherent singlet fission (upper part of Figure 4.8) [81]. The mediation by the CT state in incoherent singlet fission circumvents the necessity of a simultaneous transfer of two

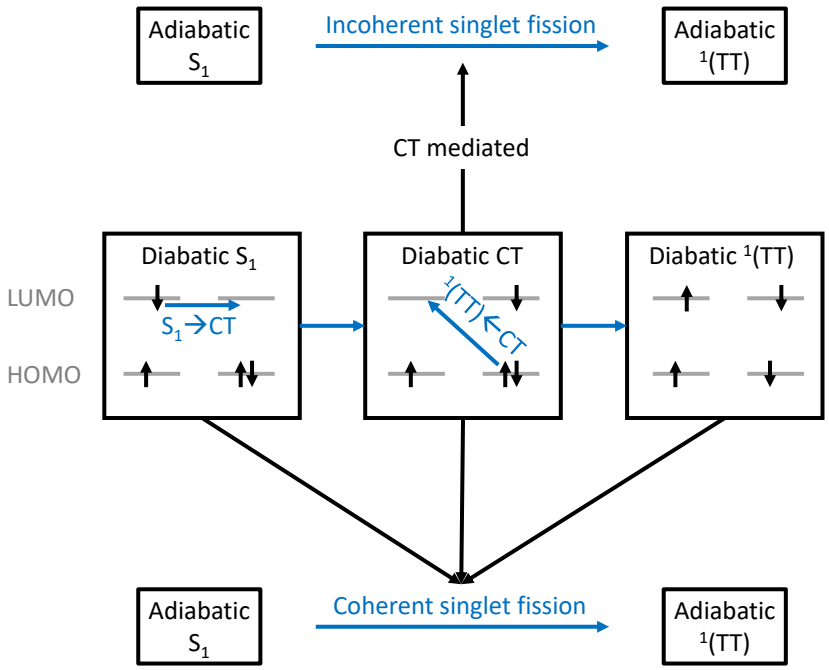

Figure 4.8.: Sketch of the different singlet fission mechanisms. In the center the diabatic states are sketched and the blue arrows indicate the two-electron transfer necessary in the picture of diabatic states. Note that in this picture both electrons have to be transferred simultaneously since the CT state is energetically inaccessible. The upper part displays the incoherent singlet fission mechanism, where only the diabatic CT state is mixed into both adiabatic states and mediates singlet fission. In contrast, all adiabatic states in the coherent singlet fission mechanism (lower part of the figure) have admixtures of all three diabatic states. Inspired by Ref. [82].

electrons between the diabatic S_1 and ^{1}(TT) state, explaining the high efficiency also found for incoherent singlet fission [81].

After triplet-pair formation, the two triplets are electronically bound to each other [83]. This electronic interaction is lost in the next step (step (ii) in Equation 4.8), which can be seen as a spatial separation of the two triplet excitations. There are two possible sources for the energy needed for this step, one is thermal activation of the process, the other facilitator for triplet separation is the introduction of energy fluctuations by structural imperfections[84]. Note that spin coherence is maintained during the second step. The two triplet excitations can in principle not only couple to an overall singlet, but there are also triplet and quintet states [85], however, the transition between the spin manifolds requires a spin flip and is therefore slow. An important decay channel of the ^{1}(TT) state that is not included in Equation 4.8 is luminescent decay to the ground state. Although the ^{1}(TT)$\rightarrow S_0 + S_0$ transition is symmetry forbidden, the sym-

metry can be broken by adding a vibrational quantum to the final state. This means that the transition

$$^1(\mathrm{TT}) \rightarrow \mathrm{S}_0^* + \mathrm{S}_0 + h\nu \tag{4.9}$$

with the vibrationally excited electronic ground state S_0^* is allowed and can be detected in photoluminescence (PL) measurements [30, 86].

In the final step (step (iii) in Equation 4.8), the two triplets lose spin coherence and the final state, two completely independent triplets, is reached.

Singlet fission is not only possible with two molecules of the same kind but can also work with two different molecular species if the requirements considering energy balance and coupling strength are met [87]. Since the term singlet fission is mostly associated with the process between two molecules of the same kind (singlet homofission), the mechanism between two molecules of different species will always be called singlet heterofission in this work.

5. Experimental techniques

In this chapter, the principles of the experimental methods used in this work are explained. It contains techniques for sample preparation, for structural, morphological and optical characterization and for time-resolved measurements. Further details of each technique can be found in the references given in the corresponding section.

5.1. Organic molecular beam deposition

The sample preparation in this work was done by means of organic molecular beam deposition (OMBD) [88–91]. OMBD is based on a Knudsen cell which can be resistively heated. A crucible with a temperature sensor in close proximity is placed inside the Knudsen cell to observe and control the temperature of the crucible during OMBD [91]. Prior to the deposition, the organic compound in form of a crystalline powder is placed inside the crucible [88, 90]. The Knudsen cell is facing a quartz crystal microbalance (QCM) and a sample holder with substrates mounted on it. Silicon with a native silicon oxide layer and quartz glass were used as substrates in this work. This setup is fitted into an ultra-high vacuum chamber [88, 89] with a base pressure of 10^{-8} mbar as sketched in Figure 5.1. By controlling the temperature of the crucible, the sublimation rate of the organic compound inside can be adjusted, which determines the flux of the molecular beam outside the crucible and hence the deposition rate of the organic molecules on the substrate. The growth rate on the substrate is precisely measured by the QCM [91], which has to be calibrated first because the QCM itself only measures changes in vibration frequency due to mass deposited on it. For the calibration of the QCM, a sample is prepared, and its thickness is determined, either by X-ray reflectivity (XRR, see Section 5.2.1) or by comparison of the absorbance spectrum with that of a film of the same compound and known thickness (see Section 5.3.1). This calibration method also respects the fact that the QCM is placed geometrically at a different position in the setup than the sample holder.

OMBD can be used to prepare binary films by depositing two different compounds [58]. For that, each compound is placed in an individual Knudsen cell and heated individually. Each Knudsen cell has its corresponding QCM, which means that

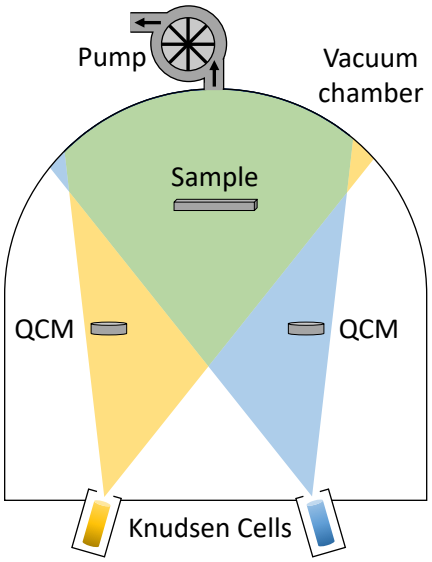

Figure 5.1.: Sketch of a basic OMBD setup for co-deposition of two compounds.

the growth rate of each compound can be monitored independently, while the sample holder is placed in the path of both molecular beams. In this work, the setup sketched in Figure 5.1 has been used to prepare series of samples, in each of which the same two compounds were co-deposited with the same total deposition rate, but the ratio between the two compounds was varied from sample to sample.

The volume ratio of each compound in a sample can be calculated from the growth rates, which are given in thickness per time and were always kept constant during sample preparation, without greater efforts. The molar ratio, however, is more predestined to be linked to changes in the photophysics of the samples, especially for samples that contain two compounds, which intermix statistically [92]. The calculation of the molar fraction of compound $i \in \{1, 2\}$ in a film containing compounds 1 and 2 is based on the number of molecules of species i, N_i, in the sample, which is calculated by

$$N_i = \frac{r_i \, A \, t}{V_i} \tag{5.1}$$

with the growth rate r_i, the sample surface A, the deposition time t and the volume per molecule V_i in the respective neat thin film structure, which was the relevant structure for the calibration of the QCMs. Based on that, the molar fraction of compound i, $p_{\mathrm{mol},i}$, can be calculated by

$$p_{\mathrm{mol},i} = \frac{N_i}{N_1 + N_2} = \frac{r_i}{r_i + \frac{V_i}{V_j} r_j} \tag{5.2}$$

with $i \neq j \in \{1, 2\}$. If not stated otherwise, the given fraction of a binary film in this work is the molar percentage of the singlet fission compound with the lowest bandgap in the film.

5.2. Structural and morphological characterization

Changes to the structure and the molecular arrangement can have a significant impact on the optical properties and photophysics of an OSC [47, 93, 94]. Therefore, it is key for the understanding of the photophysics of an OSC to also gain insight into the structure and morphology of the corresponding samples. For this purpose, X-ray diffraction (XRD) and scanning electron microscopy (SEM) are employed in this work.

5.2.1. X-ray diffraction

The use of XRD for structural investigation of solid OSCs is common [55]. Since all XRD experiments in this work have been performed on samples with a crystalline structure, only this case will be discussed in the following. If an X-ray beam is directed onto a crystalline sample, the X-ray phonons scatter elastically at the electrons in the sample [95]. Due to the crystalline nature of the sample, the electrons are distributed periodically, leading to interference effects in the scattered X-ray intensity, governed by the crystal structure of the sample [95, 96]. For a known crystal structure, the conditions under which constructive interference is expected can be calculated. In order to do so, it is helpful to introduce the reciprocal lattice vectors, which are calculated from the primitive real space lattice vectors $\vec{a}_i$ with $i \in \{1, 2, 3\}$ by

$$\vec{b}_i = \sum_{j,k \in \{1,2,3\}} \epsilon_{ijk}\, \pi\, \frac{\vec{a}_j \times \vec{a}_k}{\vec{a}_1 \cdot \vec{a}_2 \times \vec{a}_3} \tag{5.3}$$

with the Levi-Civita symbol ϵ_{ijk} [95, 96]. With this definition, $|\vec{b}_i|$ is 2π divided by the distance between two neighboring lattice planes, which are constructed by the real space vectors $\vec{a}_j$ and $\vec{a}_k$ with $j, k \neq i$ and $j \neq k$, and is oriented orthogonal to this plane. Hence, a linear combination of reciprocal lattice vectors with $h, k, l \in \mathbb{Z}$,

$$\vec{b}_{hkl} = h\,\vec{b}_1 + k\,\vec{b}_2 + l\,\vec{b}_3\,, \tag{5.4}$$

results in an integer multiple of 2π divided by the distance between two neighboring lattice planes, which are both oriented perpendicular to $\vec{b}_{hkl}$.

Now, for constructive interference, the incoming angle Θ of the X-rays with respect to the lattice plane of interest has to be the same as the outgoing angle. Additionally, the difference in path length between two paths, which include scattering events at directly neighboring lattice planes, has to be an integer multiple of the wavelength λ. This results in Bragg's law,

$$2d \sin\Theta = n\lambda\,, \tag{5.5}$$

with the spacing between two neighboring lattice planes d and an integer number n. By introducing the wave vector of the X-ray beam before ($\vec{k}_{\text{in}}$) and after ($\vec{k}_{\text{out}}$) the scattering event and the scattering vector $\vec{q} = \vec{k}_{\text{out}} - \vec{k}_{\text{in}}$, Equation 5.5 becomes

$$|\vec{q}| = 2\sin\Theta\,|\vec{k}| = \frac{2\pi}{\lambda}\,2\sin\Theta = n\,\frac{2\pi}{d} = |\vec{b}_{hkl}|\,. \tag{5.6}$$

Based on the geometric condition that the angle of the incoming X-ray beam with respect to the lattice plane has to be the same as the outgoing angle, it can be concluded that $\vec{q}$ is oriented orthogonal to the lattice plane, and that $|\vec{q}| = 2\sin\Theta\,|\vec{k}|$, which results in the condition

$$\vec{q} = \vec{b}_{hkl} \tag{5.7}$$

for constructive interference.

This means that, in principle, the diffracted intensity not only depends on the scattering angle and wavelength of the X-ray beam, but also on the orientation of the incoming beam compared to the sample. This is indeed the case for single crystals [96]. However, since the samples characterized in this work consist of many crystallites with uniaxial anisotropy orthogonal to the sample surface or completely isotropic orientation, only the angle of incidence compared to the sample surface needs to be considered in the XRD experiments done in this work. From a mathematical perspective, orientational isotropy simplifies Equation 5.7 to $|\vec{q}| = |\vec{b}_{hkl}|$ and uniaxial anisotropy orthogonal to the sample surface, which is defined as the z-axis, simplifies the equation to the following two equations

$$q_z = \vec{b}_{hkl} \cdot \vec{e}_z \tag{5.8}$$

$$q_{xy} = \sqrt{q_x^2 + q_y^2} = \sqrt{(\vec{b}_{hkl} \cdot \vec{e}_x)^2 + (\vec{b}_{hkl} \cdot \vec{e}_y)^2}. \tag{5.9}$$

Additionally to the position of a Bragg peak, which carries information about the microstructure of a sample, the width of it can be used to extract information about the mesostructure. This can be understood by employing a simplified picture of N coherently scattering lattice planes. In this scenario the structure factor, which depends on

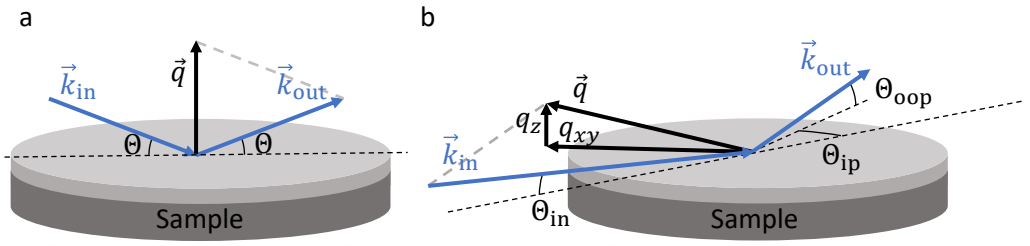

Figure 5.2.: Geometries for (a) XRR and (b) GIWAXS measurements with the construction of the scattering vector $\vec{q} = \vec{k}_{out} - \vec{k}_{in}$. In XRR the angle Θ of the incoming and scattered beam is the same, resulting in $\vec{q}$ orthogonal to the sample surface, while in GIWAXS the angle of the incoming beam Θ_{in} is fixed and an area detector is used to measure the scattered intensity at varying in-plane (Θ_{ip}) and out-of-plane (Θ_{oop}) angles. Inspired by Refs. [99, 100].

q perpendicular to the lattice planes, and hence the full width half maximum (FWHM) of the corresponding Bragg peak, can be calculated [97]. For this system, the relation between the coherently scattering size L, which is N times the lattice spacing a, and the FWHM of the Bragg peak Δq as given by

$$L = N\,a = \frac{5.56}{\Delta q} \tag{5.10}$$

can be found. In the case of a spherical coherently scattering particle with a cubic lattice, which is the assumption used in this work, the calculation is more demanding and one receives

$$L = N\,a = \frac{6.96}{\Delta q}. \tag{5.11}$$

This is the equation used to estimate the coherently scattering size in this work [98]. Note that, since the finite coherently scattering size is not the only contribution to the Bragg peak width, the results for the coherently scattering size in this work have to be treated as lower limits.

X-ray reflectivity

The thin film structure orthogonal to the substrate surface can be analyzed by XRR. In XRR the X-ray source and the detector are positioned in a way that the angle of the incoming beam Θ always equals the angle of the outgoing beam. This results in the scattering vector oriented perpendicular to the surface (see Figure 5.2a), which is defined as the z-axis. In XRR a measurement is done in this geometry under varying Θ with the same photon energy, which results in a scan along q_z.

At very small q_z the beam is completely reflected by the sample due to total reflection at small angles [101]. Once the total reflection edge is passed, Kiessig fringes appear due to interference between the beams reflected at the sample surface and the sample-substrate interface. The periodicity of these fringes contains information about the sample thickness, which was *inter alia* used for the QCM calibration described in Section 5.1, and its damping about the roughness of the sample surface [101]. At higher q_z values Bragg peaks appear due to diffraction at lattice planes. The positions of the Bragg peaks give insight into the lattice spacing. For binary systems, changes of this spacing and of the Bragg peak intensity upon changes in the molar ratio of the compounds can be used as insight into the mixing behavior [58, 102].

The XRR measurements in this work were performed on a diffractometer (3303TT, GE) using CuK$_{\alpha 1}$-radiation ($\lambda = 1.541$ Å) and a 1D detector (Meteor 1D, XRD Eigenmann).

Grazing incidence X-ray diffraction

Complementary to XRR, which gives insight into the out-of-plane structure, grazing incidence wide-angle X-ray scattering (GIWAXS) is used to investigate the in-plane structure [103].

In GIWAXS the X-ray beam penetrates the sample under a shallow angle and an area detector is used to detect the diffracted intensity under various scattering angles, which is sketched in Figure 5.2b. For a known geometry, each point of the detector can be unambiguously assigned to a $\vec{q}$ vector [104]. Due to the in-plane isotropy of the samples studied in this work, $\vec{q}$ is simplified into the components q_z and q_{xy}. The q_{xy}-positions of the Bragg peaks at small q_z contain information about the in-plane structure of the sample, which can be extracted via a comparison of simulated and measured data in a 'trial-and-error' fashion. Additionally, information about the isotropy of the sample can be gained by GIWAXS. While the Bragg peaks of an isotropic sample are smeared out over all points with the same absolute scattering vector,

$$|\vec{q}| = \sqrt{q_z^2 + q_{xy}^2}, \tag{5.12}$$

resulting in ring-like diffraction features on the area detector, the Bragg peaks of a sample with uniaxial anisotropy are only found at discrete q_z and q_{xy} values.

If not specified differently, the GIWAXS measurements of this work were done using a Xeuss 2.0 system (Xenocs) with a Dectris Pilatus3 R 300K detector and CuK$_\alpha$-radiation ($\lambda = 1.542$ Å). In all other cases, beamline P08 of the *Deutsches Elektronen-Synchrotron* (DESY) in Hamburg has been used with a wavelength of 0.689 Å and a Perkin Elmer XRD 1621 flat panel detector.

5.2.2. Scanning electron microscopy

The morphology of the samples prepared in this work was accessed by SEM. For SEM measurements a highly focused electron beam is directed on the sample. This electron beam releases secondary electrons from the sample, which are detected by an electron detector (see Figure 5.3) [105, 106]. Once the focus point of the electron beam is scanned over an area of the sample surface, the intensity of the secondary electrons is measured depending on the position on which the electron beam hits the sample. Since more secondary electrons can be released from the sample if the electron beam hits an edge of the sample [106], the intensity of the secondary electrons contains *inter alia* information about the morphology of the sample.

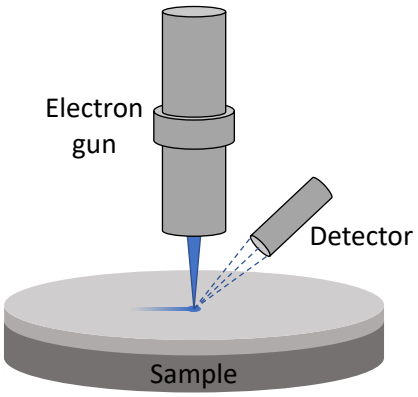

Figure 5.3.: Sketch of a typical SEM setup. The focus of the electron gun is scanned over the sample while the backscattered electrons are detected.

In this work the SEM data are displayed as 2D maps, where the position of a pixel represents the position of the electron beam on the sample and the brightness of the pixel represents the amount of secondary electrons collected by the detector.

The SEM measurements in this work were done with a JEOL JSM 6500F filed emission scanning electron microscope with 5 kV acceleration voltage.

5.3. Optical characterization

In this work, which focuses on the investigation of multimolecular photophysical processes, the interaction of OSC samples with light plays a key role. In the following, absorbance spectroscopy and PL spectroscopy are introduced, which are basic techniques used for optical characterizations.

5.3.1. Absorbance spectroscopy

With absorbance spectroscopy insight into the optically allowed ground state transitions of an OSC can be gained [107]. In a typical setup, a monochromator is used to block the entire spectrum of a white light source except a narrow spectral band. The intensity of this almost monochromatic light is measured by a photodetector after passing through the sample.

By dividing this intensity by the intensity measured by the detector without a sample in the beam path, the transmittance of the sample, which depends on the wavelength λ, can be calculated as

$$T(\lambda) = \frac{I(\lambda)}{I_0(\lambda)} \tag{5.13}$$

with the intensity with the sample in the beam path $I(\lambda)$ and without the sample in the beam path $I_0(\lambda)$. Based on the transmission, the absorbance

$$A(\lambda) = -\log T(\lambda) \tag{5.14}$$

can be calculated.

Three main sources contribute multiplicatively to the transmission and hence additively to the absorbance, namely absorption, scattering and refraction [108]. Absorption is the most interesting quantity of the three for this work, as the spectral shape of the absorption contains critical information for the photophysics of a sample. In order to extract the contribution of the absorption from the absorbance, however, it is important to roughly quantify the other two contributions. Since in all absorbance measurements of this work the film thickness is less than the wavelength of interest, it can be assumed that the refraction of an unknown sample is the same as that of the corresponding blank substrate [108]. This refraction can further be quantified in an appropriate reference measurement. The absorbance due to scattering at the rough film surface is proportional to λ^{-2} [109] and the magnitude can be quantified by fitting the low-energy range of an absorbance spectrum, in which absorption is not present. Note that for very smooth films Rayleigh scattering ($\sim \lambda^{-4}$) is the dominant scattering source, but in this case the contribution of scattering to the absorbance is often negligible. The remaining part of the absorbance, which is absorption, can be used to calculate the thickness of a thin film sample if a reference sample with known thickness exists. For that the Beer-Lambert law,

$$A_{\text{abs}} = \log(e)\,\alpha(\lambda)\,d \tag{5.15}$$

with the attenuation coefficient $\alpha(\lambda)$ and the film thickness d is used. Note that the crystallites of the polycrystalline samples investigated in this work have a size compa-

rable to the wavelength of the light in the absorption measurement and that the attenuation coefficient differs between the individual crystallites [110]. This means that the thickness dependent absorption is a linear combination of multiple exponentially decaying functions, which is clearly different from a single exponential decay. However, for $\alpha(\lambda)\,d < 0.5$, which is roughly the same as $A_{\mathrm{abs}} < 0.2$, the exponential decay of the Beer-Lambert law can be approximated linearly, which makes the law hold true in this limit even for polycrystalline samples.

All absorbance experiments were conducted on a Lambda 950 spectrometer (Perkin Elmer). The system was utilized to cover a spectral range from 200 nm to 1300 nm. A deuterium lamp was employed for wavelengths shorter than 319.2 nm, while a halogen lamp was used for longer wavelengths. In addition, a lead sulfide detector was inserted for wavelengths beyond 820 nm, replacing the photomultiplier tube that was used for shorter wavelengths.

5.3.2. Photoluminescence spectroscopy

Conducting PL experiments gives a first insight into the excited-state behavior of an OSC by spectrally resolving the photoemission after photonic excitation [111, 112]. In a typical PL setup, a laser excites the sample continuously at a fixed wavelength. After excitation, some of the possible deactivation pathways include radiative decay, which leads to photonic emission of the sample. This emission is collected by a lens and guided to a detector. Between the lens and the detector, a bandpass filter is installed to protect the detector from laser radiation and a grid is installed for spectral resolution.

A Jacobian conversion is used to convert the measured wavelength-dependent luminescence spectrum into an energy-dependent spectrum [113]. The spectral shape and energetic position of emission features contain information about the relaxation pathway of the OSC after photonic excitation and prior to emission, which is an important keystone in understanding the photophysics of an OSC.

In this work, the steady-state PL experiments have been conducted with a pulsed laser diode LDH-P-C-470 and an Acton SP300 spectrometer with a PIXIS 100 camera (Princeton Instruments) for laser excitation at 470 nm and with a frequency-doubled Nd:YAG laser with a LabRam HR 800 spectrometer (HORIBA Jobin Yvon) for laser excitation at 532 nm.

5.4. Time-resolved photoluminescence spectroscopy

While PL spectroscopy resolves the luminescence signal only spectrally, time-resolved photoluminescence spectroscopy (TRPL) can be used to simultaneously resolve the signal spectrally and time-dependent. This enables insight into the evolution of an electronically excited state with time, which is key for the understanding of the photophysics of OSCs and, hence, for the development of organic photoelectronic devices [112].

The basis to get access to the time evolution of an excited state is a simultaneous excitation, which, in the case of TRPL, is done by a pulsed laser [114]. In a standard TRPL setup the wavelength of this laser can be chosen from a wide range to ensure direct excitation of the sample. The laser pulses are usually a few hundred fs long and the repetition rate of the pulsed laser is in the kHz to MHz range. The laser is focused on the sample and the emitted light of the sample is collected, spectrally resolved by a grating and temporally resolved by a streak camera [112]. In a streak camera a photocathode converts the photons into electrons, which then pass through deflection plates onto a phosphor screen. The deflection plates sweep through a high voltage and this sweep is synchronized with the laser pulse [115]. The trajectory of the photoelectrons depends on the voltage between the deflection plates. Due to the high voltage sweep, this voltage depends on the time after excitation by the laser pulse. As a result, the position, at which the photoelectrons hit the phosphor screen, contains information about the time, which has passed between photoexcitation of the sample and the corresponding photoemission. The grating is used for spectral resolution along the axis of the phosphor screen, which is not used for time resolution. The combination of a grating and deflection plates results in a two-dimensional map on the phosphor screen, in which one axis represents the time passed since the laser pulse and the other axis represents the wavelength of the emitted photons (see Figure 5.4). This map on the phosphor screen is recorded by a CCD camera. The setup can be further extended [115], for example by the use of multichannel plates for signal enhancement.

Two different TRPL setups have been used for this work. For the data presented in Section 7 the output of an 80 MHz Coherent Vitesse Ti:Sapphire oscillator was frequency doubled to a wavelength of 400 nm. A Pockels cell controlled by a ConOptics pulse-picking system was used to adjust the repetition rate to 100 kHz. The pulse fluence was below 1.2 $\mu J/cm^2$. The samples were mounted into a vacuum cryostat with a base pressure of 10^{-5} Torr during measurement. A long wave-pass filter was used to protect the streak camera from laser scattering light. The TRPL data in Sections 8-10 were collected with a tunable pulsed Ti:Sapphire laser with 80 MHz repetition rate and a wavelength output of 960 nm, which was frequency doubled to 480 nm. The pulse fluence was kept

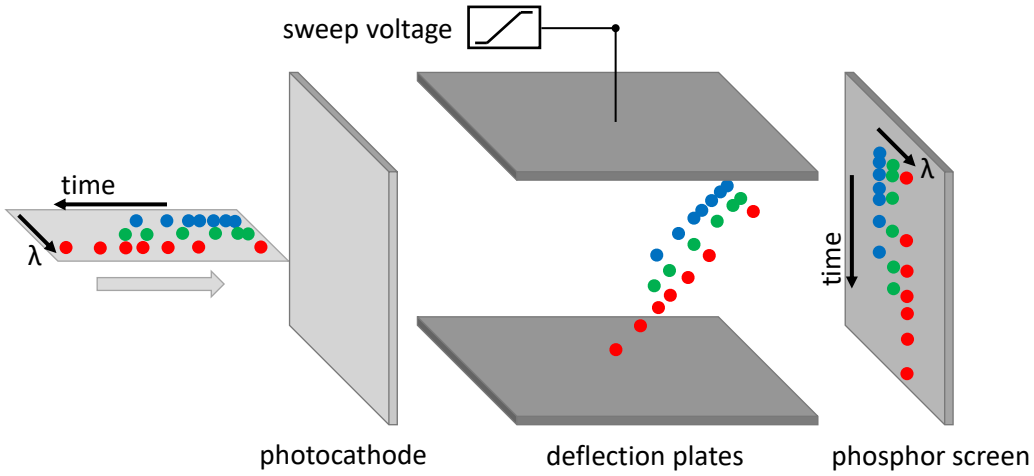

Figure 5.4.: Sketch of the working principle of a streak camera. After passing through a spectrometer, the photons are converted into electrons by the photocathode. A sweep voltage applied to the deflection plates deflects the electrons differently depending on their time of passing through the plates. Afterwards, the electrons are converted back into photons by a phosphor screen, which is recorded by a CCD camera. Inspired by Ref. [116].

at 40 µJ/cm^2. The samples were mounted into a vacuum cryostat with a base pressure of 10^{-5} Torr and were cooled with liquid helium during the measurement. In this setup, a long wave-pass filter was used to protect the streak camera from laser scattering light.

5.5. Analysis of time-resolved excited-state data

The analysis of TRPL data is demanding for multiple reasons. On one side, the data that is already acquired with a single TRPL measurement contains a lot of information due to its simultaneous spectral and temporal resolution. On the other side, since many excited-state species can contribute to the photophysics of a sample and generally neither the total number of excited-state species nor the relation between them is known before the measurement, there can be a host of physical models describing a given dataset with comparable accuracy [117, 118].

Because of that, knowledge about the spectral fingerprints of possible species involved in the photophysics of a sample and about corresponding decay channels has to be gained prior to the analysis of time-resolved data [118]. This can be done by an analysis of the absorbance spectrum of the corresponding film, from where an estimate about the spectral shape of the S_1 emission, including its vibronic progression, can be

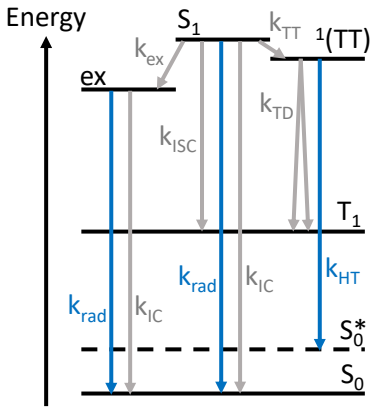

Figure 5.5.: Sketch of possible decay channels of the S_1 state and their decay rates. Radiative channels are printed in blue, nonradiative channels in gray. Additionally, a selection of decay channels for the triplet-pair state (^{1}(TT)) and the excimer state (ex) with their decay rates are given as well. Excimer formation (k_{ex}), triplet-pair state formation (k_{TT}), ISC (k_{ISC}) from the S_1 state, radiative (k_{rad}) and nonradiative (k_{IC}) decay of the S_1 state and excimers to the ground state, luminescence from the ^{1}(TT) state via Herzberg-Teller coupling (k_{HT}) and triplet dissociation from the ^{1}(TT) state (k_{TD}) are the most relevant channels for this work. Inspired by Ref. [66].

deducted. Additionally, a comparison of the steady-state PL spectrum of the film with the spectrum of the compound in dilute solution, where multimolecular states and multimolecular decay channels are not accessible, helps in understanding the PL spectra. Also comparing the steady-state PL spectra of a film and of a single crystal, in which trap states are expected to play an insignificant role, supports a disentanglement of spectral contributions. Other approaches are density functional theory (DFT) calculations, which can be used for example to have a first insight on the triplet energy, which is an important parameter for singlet fission. Also, a careful analysis of the temperature dependent steady-state PL spectra can lead to indications about the existence of multiple excited-state species and their respective spectral shapes. Another option is to employ PL measurements with different excitation densities, since the efficiency of multi-exciton decay channels strongly depends on the excitation density.

In the TRPL experiments of this work, the excitation photon energy is chosen in a way that the S_1 state is primarily excited. Therefore, this state is considered as the starting point for the analysis of the excited-state evolution. From there, multiple decay channels are possible, for example excimer formation, triplet-pair formation, IC, ISC or radiative decay, with their respective decay rates k_{ex}, k_{TT}, k_{IC}, k_{ISC} and k_{rad} [112], which are all shown in Figure 5.5. The initial decay rate of the S_1 state equals the sum over all decay

rates of these channels,

$$k_{\text{prompt}} = k_{\text{ex}} + k_{\text{TT}} + k_{\text{IC}} + k_{\text{ISC}} + k_{\text{rad}}. \tag{5.16}$$

Due to relaxation mechanisms inside the S_1 state like vibrational relaxation, geometric relaxation of the molecule, loss of excited-state delocalization, or occupation of trap sites at lattice defects or grain boundaries, the spectral shape of the S_1 state and its decay rate can change with time after excitation, which *inter alia* causes the decay to be non-exponentially [119].

Some of the possible decay paths of the S_1 state, such as excimer formation and triplet-pair formation, include other luminescent states. These are namely excimer luminescence and ^{1}(TT) luminescence, which occurs via Herzberg-Teller coupling. Hence, the TRPL data do not only contain the emission of the S_1 state, but also emission of other states such as the excimer or the ^{1}(TT) state. Lastly, also population back-transfer from the excimer or ^{1}(TT) state to the S_1 state [120], causing delayed fluorescence of the S_1 state, or population transfer between the excimer and the ^{1}(TT) state is possible, further complicating the analysis of TRPL data.

Since accounting for all these effects in a fitting model would lead to overfitting, some simplifications have to be made. One simplification is that the decay of each state is approximated by a single exponential decay or by the sum of two exponential decays. Another one is that the spectral shape of the luminescence of a state does not change with time. This means that each decay trace is approximated by a sum of (convoluted) exponential decay functions. The number of exponential functions used and whether they are summed up or convoluted depends on the physical model used to describe the present photophysics. Since there are physical and technical limits of a TRPL setup, such as the duration of the excitation pulse or limited resolution of the streak camera, this decay function is again convoluted with a Gaussian function, which represents these effects in the fitting model. By fitting the resulting function to multiple decay traces at different wavelengths, the decay rates associated with each species involved can be calculated.

To get the most precise result for the decay rates possible, this fit is done for every wavelength simultaneously in a global analysis (GA) [121]. Additionally, the resulting prefactors at all wavelengths can be used to create spectra, from which each one is assigned to one of the decay rates. These calculated spectra and their decay rates can then be assigned to the emission of distinct electronic states [118] by combination with the knowledge gained in previous experiments. The spectral contribution of each electronic state can also be disentangled from the TRPL data by analyzing the change in spectral

shape between different time frames. This approach, however, demands even more foreknowledge about the sample than the application of a GA.

6. Materials

In this work, binary films of ADT with a second organic compound were investigated. For the second compound, a host of different compounds were chosen to cover a wide range of structural, morphological, and electronic environments. In the following, these compounds and their most important properties in the context of this work will be introduced briefly.

6.1. Anthradithiophene

ADT ($C_{18}H_{10}S_2$) and its derivatives exhibit a high hole mobility in the solid state, stimulating research for possible application of ADT in organic field effect transistors (OFETs) [122–126]. Derivatization of ADT to improve solubility is very common [125, 127], which results in most studies investigating ADT derivatives [30]. Singlet fission has been found as an accessible decay channel in studies of ADT derivatives [30, 44, 128] and even luminescence from the ^{1}(TT) state was found [30]. However, for the exact material, which is used in this work, only few studies exist.

The used material consists of a mixture of two isomers, namely anti-ADT and syn-ADT, which differ in the position of the sulfur atoms within the molecule (see Figure 6.1

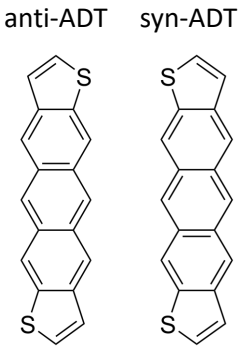

Figure 6.1.: The chemical structures of the two ADT isomers, namely anti-ADT and syn-ADT, differ in the relative positions of the sulfur atoms.

Table 6.1.: Single crystal structure of each of the two ADT isomers.

Material	a(Å)	b(Å)	c(Å)	$\alpha(^\circ)$	$\beta(^\circ)$	$\gamma(^\circ)$	Reference
anti-ADT	5.92	7.77	13.99	86.6	78.3	86.4	[122]
syn-ADT	5.89	7.51	14.35	96.1	94.3	90.4	[122]

for both chemical structures). From the synthesis pathway an equimolar mixture of the two isomers is expected [125] and the crystal structures of the two pure isomers are very similar with both having two molecules incorporated in each unit cell in a herringbone fashion [122]. Both respective unit cell parameters are given in Table 6.1. Thin films of ADT show a split Bragg peak in XRD experiments, indicating the existence of a thin film phase and a bulk phase [126].

In order to focus on ADT in binary films, a good basic understanding of neat ADT films is necessary, which is gained in Appendix E in the Appendix by varying the growth conditions and the isomerical purity of ADT thin films and analyzing the resulting structural and spectroscopic changes.

6.2. [6]-phenacene

The high field effect mobility and good chemical stability in [6]-phenacene (6Ph, fulminene, $C_{22}H_{14}$, chemical structure given in Figure 6.2) thin films makes this compound an interesting candidate for OFET applications [129–131].

One reason for its good chemical stability is the high bandgap of the compound [132], which is also one of the reasons for choosing 6Ph as a compound in the binary films of this work. One further reason for the choice of 6Ph is its thin film structure [130], which exhibits unit cell parameters that are similar to those of ADT, indicating that 6Ph also shares an in-plane herringbone arrangement (see Table 6.2 for unit cell parameters).

With these conditions met, 6Ph has the potential to act as an inactive spacer compound in ADT films by statistically replacing ADT molecules with 6Ph in the crystal lattice. In binary mixtures, the high bandgap of 6Ph thereby not only enables a selective optical excitation of just one molecular species, but also leads to more drastic changes in the polarizability upon admixture of the spacer compound as compared to the admixture of a spacer compound with a comparatively smaller bandgap such as tetracene (TET) [133].

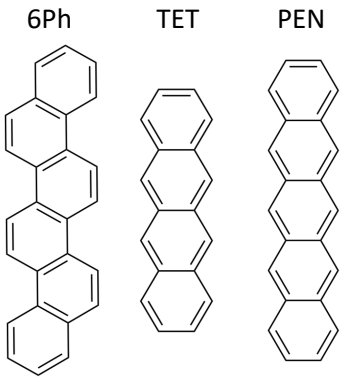

Figure 6.2.: The chemical structures of 6Ph, TET and PEN indicate high geometric similarity of each of the three molecules with ADT.

6.3. Tetracene

TET ($C_{18}H_{12}$, chemical structure given in Figure 6.2) is a prototypical OSC for studying singlet fission. The fact that TET maintains a high singlet fission rate and hence high triplet yields through a wide temperature range [134], although the singlet fission process is strongly endothermic in TET, has stimulated plenty of research in this regard [47, 135–138]. The singlet fission process of TET has also been shown to pivotally depend on the structure, which can be influenced by changes in the growth conditions [47, 135].

TET thin films exhibit two different structures, that of the thin film phase and of the bulk phase, the unit cell parameters of which are given in Table 6.2. Both structures contain two molecules per unit cell in a herringbone arrangement and the structure of the bulk phase is also present in the single crystal [139].

In this work, TET is used as spacer compound in binary mixtures with ADT. Hence, it complements 6Ph as spacer compound and, since TET has a smaller bandgap than 6Ph, it can be used to disentangle the contributions of changing polarizability and changing mixing ratio in thin mixed films. Importantly, ADT and TET both exhibit singlet fission and have a comparable S_1 energy, which makes this system interesting for the investigation of singlet heterofission [87].

6.4. Pentacene

Pentacene (PEN, $C_{22}H_{14}$, chemical structure given in Figure 6.2) is one among the most studied OSCs. The puzzling quantum-mechanical mechanism responsible for the ultra-

Table 6.2.: Selected single crystal (sc) and thin film (tf) structures of 6Ph, TET and PEN.

Material	Structure	a(Å)	b(Å)	c(Å)	$\alpha(^\circ)$	$\beta(^\circ)$	$\gamma(^\circ)$	Reference
6Ph	sc	7.94	12.13	15.40	86.8	90.0	90.0	[131]
6Ph	tf	8.4	6.2	32	90	98	90	[130]
TET	sc	6.04	7.92	13.10	76.6	72.0	86.0	[139]
TET	tf	5.92	7.60	13.20	79.8	86.4	89.6	[139]
PEN	sc	6.06	7.90	16.01	112.6	78.1	94.2	[140]
PEN	sc	6.27	7.78	14.51	76.7	87.5	84.6	[141]
PEN	tf	5.96	7.60	15.61	81.3	86.6	89.8	[142]

fast singlet fission rate in PEN stimulated a lot of theoretical and experimental investigations of the material [30, 45, 143–146].

For PEN multiple different crystal structures have been reported in thin films and for the single crystal [140–142], which are summarized in Table 6.2. All structures share a herringbone arrangement of the molecules in the unit cell, which makes the unit cell structure comparable to that of ADT.

In this work, the comparable lattice parameters are used to statistically replace ADT molecules by PEN molecules in thin films of ADT [45], but, unlike TET or 6Ph, PEN has a smaller bandgap than ADT [45]. This means that PEN does not act like an inactive spacer compound since energy transfer from ADT to PEN is energetically favorable. Instead, the idea is to introduce energy accepting units into the ADT lattice by incorporating small amounts of PEN. In this regard, PEN molecules act as low-energy traps in a material with a higher bandgap.

6.5. Zinc phthalocyanine

While the high absorption coefficient of zinc phthalocyanine (ZnPC, $C_{32}H_{16}N_8Zn$, chemical structure given in Figure 6.3) in the low-energy spectral region [147] has stimulated research for application in solar cells [148, 149], the excellent spectral tunability of the photonic emission of ZnPC makes the compound also an interesting candidate for application in organic light emitting diodes (OLEDs) [93].

The optical tunability of the material is based on the presence of two polymorphs in thin films, namely the α-phase and the β-phase. While the meta-stable α-phase is predominantly formed after vapor deposition, thermal annealing leads to the formation of the stable β-phase [150]. The crystal structures of both polymorphs are given in Table 6.3 and both significantly differ from the structures of the materials introduced

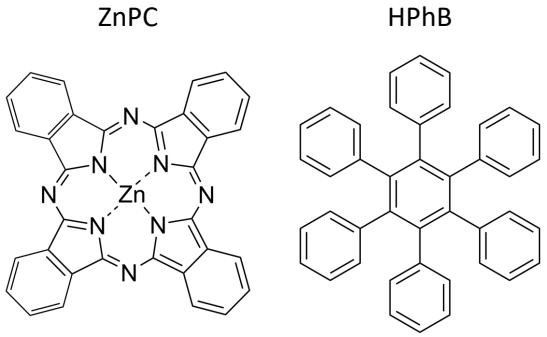

Figure 6.3.: The chemical structures of ZnPC and HPhB indicate limited intermixing between each of them and ADT due to low geometric similarity. Note that the outer rings of HPhB are generally expected not to be in the same plane as the central ring.

Table 6.3.: Selected single crystal structures of copper phthalocyanine (CuPC) and HPhB. Due to its similar chemical structures, ZnPC and CuPC are expected to exhibit the same structures [148].

Material	Structure	a(Å)	b(Å)	c(Å)	$\alpha(^\circ)$	$\beta(^\circ)$	$\gamma(^\circ)$	Reference
CuPC	α-phase	25.9	3.80	24.7	90.0	90.1	95.6	[151]
CuPC	β-phase	19.41	4.79	14.63	90	120.9	90	[152]
HPhB	sc	12.18	11.79	20.86	90	90	90	[153]
HPhB	sc	12.55	11.08	21.78	90	90	90	[153]

previously.

This, in addition to the low geometric similarity of ADT and ZnPC, makes a phase-separation of the two compounds very likely. Although the phase-separation leads to the formation of neat ADT domains and neat ZnPC domains, changes in the photophysics between the neat material and phase-separated binary films can be expected. Among other factors, this is due to the co-deposition, which leads to changes in the growth conditions, and due to the presence of a low bandgap compound, which changes the photophysics of ADT at grain boundaries.

6.6. Hexaphenylbenzene

Hexaphenylbenzene (HPhB, $C_{42}H_{30}$, chemical structure given in Figure 6.3) is known for its interesting geometric properties due to the rotational freedom of the peripheral phenyl groups [153, 154]. This geometric flexibility makes the prediction of the structural behavior challenging.

Two polymorphs were found in thin films of HPhB [153], with their unit cell parameters given in Table 6.3.

Binary systems of ADT and HPhB are investigated in this work and the resulting structural behavior is hard to predict due to the geometric flexibility of HPhB. On the one hand, the bad steric similarity of the two molecules supports a phase-separating scenario, but, on the other hand, a closer look into the unit cell parameters of ADT and HPhB uncovers that the two structures are not as different as they intuitively seem. Four unit cells of ADT can be arranged in a fashion that the resulting supercell has similar parameters as the HPhB unit cell. This is a first indication of the possibility of the formation of a common lattice, where one HPhB molecule can replace two neighboring ADT molecules in the lattice. The high bandgap of HPhB enables selective excitation in excited-state experiments, where HPhB then acts as an electronically inactive compound.

In this work, the complex structural interaction between ADT and HPhB is used to probe the influence of a variety of structural modifications on the photophysics of ADT.

7. Results I: Excimeric emission in blends with spacer molecules

In this chapter the nature of a state causing a red-shifted luminescence (RSL) signal and its role in the singlet fission process of ADT is investigated. It is based on Ref. [155], which was published in collaboration with C. J. Bardeen's research group (UC Riverside, USA) and J. Pflaum's research group (Würzburg, Germany).

Maximizing the quantum yield of singlet fission is critical for its application in organic solar cells [17, 18]. One possibility to maximize the yield of singlet fission is reducing the efficiency of competitive loss channels. To do this in an analytic way, an understanding of the working principle of not only the singlet fission process, but also of the competitive loss channels plays a crucial role. In many cases, for example in excimer formation [23] or in the occupation of trap sites [156], the channels competing with singlet fission include multiple relaxation steps. In case of the excimer, it is the formation of the excimer prior to the relaxation of the excimer back to the ground state [23, 24, 26] and in the case of trap states, the occupation of the trap state represents the first step and its decay to the ground state the second step [156]. This multi-step relaxation leads to emission features redshifted compared to the energy of the initially excited electronic state. Hence the low-energy spectral region is of high interest in PL experiments for the understanding of the photophysics of a material. Unfortunately, luminescence from trap states [136, 156–158], from excimers [30, 31, 41, 46, 48, 159, 160] and from the ^{1}(TT) state [30, 83, 136, 161, 162] can all occur in this spectral region, which leads to ambiguous spectral features and ultimately to speculative assignments [158]. Resolving this spectral ambiguity is an important step, since the nature of the state assigned to the feature partially defines its potential role in the singlet fission process. While trap sites in this spectral region create a loss channel for singlet fission [136, 156–158], the ^{1}(TT) state mediates singlet fission [18, 30] and for excimers there are reports of excimers mediating singlet fission [33–35], but also of excimer formation being detrimental for singlet fission [31, 36–41].

In this chapter, blends of the singlet fission compound ADT with two different spacer molecules, 6Ph or TET, are produced. Additionally to singlet fission, ADT also shows

pronounced RSL in PL spectra. Spacer blends are used to alter the intermolecular interaction, which influences multimolecular photophysical processes such as singlet fission [92, 146], while at the same time the introduction of spacer molecules changes the polarizability of the film [45], which leads to characteristic spectral shifts of PL features that allow for an unambiguous assignment. The two main effects of the introduction of spacer molecules, the reduction of the intermolecular interaction [92] and the reduction of the polarizability of the film [45, 133], are disentangled from each other by investigating blends of ADT with different spacer molecules. By employing TRPL, the photodynamical role of the state causing RSL, including its role in singlet fission, is uncovered as well as details about the singlet fission process itself in ADT.

7.1. Structural characterization

The mixing-ratio dependent structure of both systems has been investigated by combining the two XRD methods XRR and GIWAXS. The XRR curves of the ADT:6Ph mixtures all show two Bragg peaks, which can be assigned to the first (located between 0.4 and 0.5 $Å^{-1}$) and second order (located between 0.8 and 1.0 $Å^{-1}$) Bragg peak. In case of neat ADT both Bragg peaks have a distorted peak shape, which is explained by an overlap of two peaks, originating from the presence of two different phases, namely the thin film phase and the bulk phase of ADT [126] with the thin film phase corresponding to the dominant Bragg peak at smaller scattering vectors (see Appendix E for details). The Bragg peaks of all other films do not show a distorted shape and the Bragg peak positions of all mixtures are in between the Bragg peak positions of neat 6Ph and the thin film phase of neat ADT. Using the formula $d_z = 4\pi/q_z$ for the position of the second order Bragg peak, the d_z spacings can be calculated for all films and can be found in Figure 7.1e. Based on the values of the d_z spacing and the known structures of neat ADT [122, 126] and neat 6Ph [130], a standing-up orientation of the molecules against the surface can be concluded for all samples.

For an analysis of the mixing-ratio dependent changes of the in-plane structure, the grazing incidence diffraction (GID) maps have been integrated along q_z from 0.1 to 0.3 $Å^{-1}$ in order to find the q_{xy} position of the vertically extended features. In all resulting GID linescans of the ADT:6Ph mixtures (Figure 7.1b) three Bragg peaks can be found. Since it is known that neat 6Ph [130] and neat ADT [122, 126] both exhibit an in-plane herringbone structure, this structure is also assumed to analyze the in-plane lattice spacing of both neat films and all mixtures, leading to an assignment of the Bragg peaks to the (11l), (02l) and (12l) reflection in increasing order of q_{xy} [163]. The (11l) peak of neat ADT consists of two peaks, which is another indication of the coexistence of thin

film and bulk phase in neat ADT (Appendix E). Comparable to those from XRR, also the Bragg peaks of the GID scans change continuously with the mixing ratio and the positions of the Bragg peaks in the mixed films are in between those of the corresponding neat films. Under the assumption of a rectangular in-plane unit cell, the positions of the Bragg reflections have been used to calculate the in-plane lattice vectors a and b, which are displayed in Figure 7.1f,g. Note that the assumption of a rectangular in-plane unit cell, which is based on the in-plane unit cells of all neat films being almost rectangular as well (Tables 6.1 and 6.2), is a rather rough assumption.

In case of the ADT:TET system, in XRR again Bragg peaks of first and second order are present (Figure 7.1c). For neat TET two Bragg peaks are visible for each order, which can be assigned to the known thin film and bulk structure of TET [139] with a domination of the thin film phase. The Bragg peak positions of the mixtures are located in between the positions of the thin film phases of neat ADT and neat TET. Also in this system, the positions of the second order Bragg peaks are used to calculate the d_z spacing in Figure 7.1e, the values of which agree with a preferred standing-up orientation of the molecules against the surface. Note that for both systems in some of the XRR scans Kiessig fringes or Laue oscillations can be seen, which can be used to draw conclusions about the roughness of the surface and the sample thickness [58, 102]. However, a detailed analysis of these parameters is not the focus of this work. For the analysis of the GID Bragg peaks of ADT:TET (Figure 7.1d), a herringbone structure is assumed for all samples due to the similarity of the respective GID maps with the GID maps of the known in-plane herringbone structures of neat TET [139] and neat ADT [122, 126], resulting in an assignment of the three visible Bragg peaks to the (11l), (02l) and (12l) reflections. Once again, a rectangular in-plane unit cell is assumed to calculate the in-plane lattice parameters a and b in Figure 7.1f,g.

The out of plane lattice spacing d_z (Figure 7.1e) and the in-plane lattice parameters a (Figure 7.1f) and b (Figure 7.1g) are calculated based on the positions of the Bragg peaks. The estimation of the error in both dimensions is based on $\pm 10\,\%$ FWHM of the respective Bragg peaks (vertical error bars) and on $\pm 10\,\%$ of the measured absolute QCM values during film preparation (horizontal error bars) as confidence intervals. This means that, for the in-plane parameters, two noteworthy effects are not respected in the error bars, which are the assumption of a rectangular in-plane unit cell and the artificial shift of the Bragg peaks in GIWAXS by small deviations in the exact sample placement for the measurement. In some of the films, a split Bragg peak was found, which was then fitted with two Gaussian functions, resulting in two values for this lattice parameter. In these cases, both resulting values are plotted, and for the value, which is based on the Bragg peak component of lower intensity and further assigned to the bulk phase, a faded

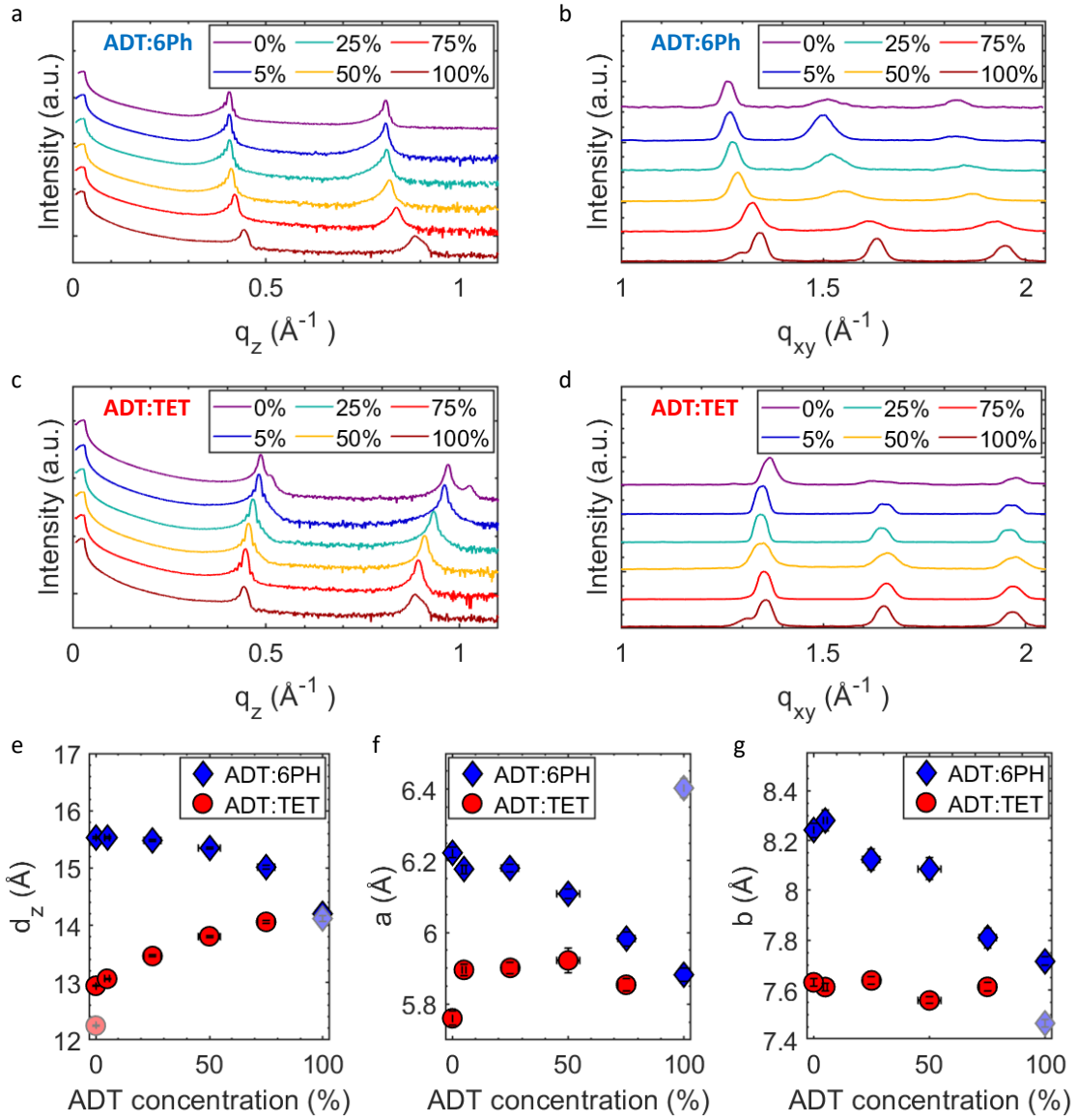

Figure 7.1.: XRD results of binary mixtures of ADT with 6Ph or TET. The XRR (a,c) and GID (b,d) curves of the ADT:6Ph (a,b) and ADT:TET (c,d) blends are vertically offset for clarity. The y-axis of the XRR curves are scaled logarithmically while for the GID data the y-axis are scaled linearly. The scans along q_{xy} (b,d) were calculated by integrating each GID map, which are all shown in Figures A.1 and A.2, along q_z in the range $0.1\,\text{Å}^{-1} < q_z < 0.3\,\text{Å}^{-1}$. The respective binary systems are given in the panels and the ADT concentrations are given in mol-% in each legend. Under the assumption of a rectangular in-plane lattice, the d_z-spacing (e) and the in-plane lattice parameters (f,g) have been calculated based on the Bragg peak positions.

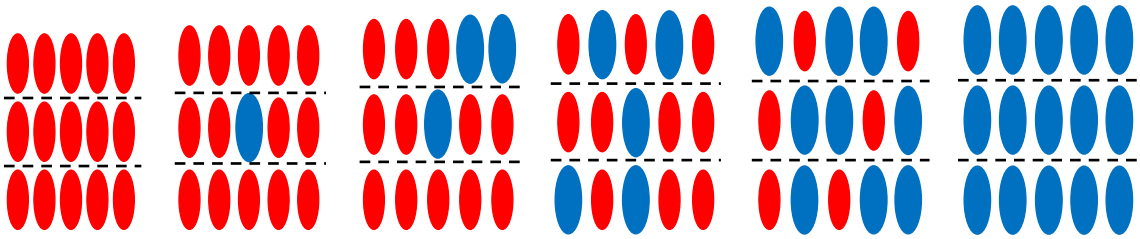

Figure 7.2.: Expected changes in lattice parameters when two compounds with different lattice sizes intermix [164]. An admixture of small amounts of the compound with the greater lattice size has a bigger impact on the resulting structure compared to the inverse scenario [165]. The lattice parameters are expected to change continuously with changing mixing ratios [92].

color type is used.

The ADT:6Ph system (blue markers) shows a continuous decrease in all three calculated parameters with increasing amounts of ADT. An increase in the parameter d_z is found for the ADT:TET system (red markers) with increasing amounts of ADT. The in-plane parameters of the latter system, however, show no clear trend with changing ADT concentrations. Bearing in mind that the errorbars of the in-plane parameters are underestimated, it is likely that no significant change occurs in these parameters with changing ADT concentrations. In both systems the evolution of the d_z-spacing with changing ADT concentrations is not linear, but the d_z-spacings of the mixtures are greater than a linear dependence would suggest.

The continuous evolution of the lattice spacings in the ADT:6Ph system suggests statistical intermixing of the two compounds [92, 102]. In this scenario the incorporation of molecules of one compound into the lattice of the second compound leads to a distortion of the lattice of the second compound toward the lattice of the first one, which explains the continuous evolution in lattice spacings. This effect occurs for the in-plane structure as well as for the d_z-spacing. Since the electromagnetic repulsion of molecules is more sensitive to changes in the molecular distance than the attraction [165], the lattice parameters of mixed films are comparatively closer to the neat film structure of the compound with the greater lattice parameters, explaining the nonlinear trend of the d_z-spacing in both systems (see Figure 7.2) [164]. For the in-plane lattice parameters the same would be expected, but the errors of the calculated values are too large for a clear statement in this regard. In case of the ADT:TET system the evolution of the d_z values also suggests statistical intermixing. Unfortunately, the in-plane parameters of neat ADT [122] and neat TET [139] are too similar to each other to resolve a concentration-dependent trend in the mixtures in this regard. However, also for this system statistical

intermixing is assumed, which will be further proven in the analysis of the absorbance and PL spectra in the following.

7.2. Optical characterization

Absorbance spectra of ADT:6Ph and ADT:TET blends are shown together with the neat films in Figure 7.3a and b, respectively. The absorption spectrum of neat ADT is dominated by the $S_0 \rightarrow S_1$ transition at 2.3 eV, which is split into two Davydov components. The existence of a Davydov splitting indicates the presence of two molecules in the unit cell, which is the case for herringbone structures [72, 166]. Toward higher energies two peaks of the vibronic progression of the $S_0 \rightarrow S_1$ transition are visible at 2.5 and 2.7 eV. Neat 6Ph has its lowest energy optical transition at 3.18 eV with a vibronic replica at 3.35 eV. For this peak no Davydov splitting is visible since the transition dipole moment (TDM) of 6Ph is along the long axis [167] of the molecule and hence the coupling to other molecules does not depend significantly on the orientation of the short molecular axis. In all mixtures features assignable to ADT and to 6Ph coexist and the higher the ADT concentration in the films, the higher the absorption strength of the feature assignable to ADT and the weaker the feature assignable to 6Ph. This can be explained by a change in the absolute amount of each respective molecule in the film with changing mixing ratios. The most important observation in the absorbance spectra is the change in peak shape and peak position of the $S_0 \rightarrow S_1$ transitions with changing mixing ratios, which is more clearly visible for the ADT feature than for the 6Ph feature. For the ADT feature, the low-energy Davydov component loses relative intensity compared to the high-energy component with decreasing amounts of ADT, while both components continuously blueshift at the same time. Also, the feature assigned to 6Ph blueshifts with decreasing amounts of ADT, although in case of this feature the shift is much weaker.

There are two reasons for the spectral shift with changing mixing ratios. One is that materials with a higher bandgap have a lower polarizability [133], which means that the admixture of 6Ph reduces the polarizability of the film, which then increases the energy of delocalized states more strongly than of localized states, hence increasing the energy difference between the S_0 and the S_1 state. This in the end leads to a blueshift of all absorption peaks with decreasing amounts of ADT. The second effect is that statistical intermixing of ADT and 6Ph increases the average distance between neighboring ADT molecules with decreasing amounts of ADT. Because the coupling between molecules is weaker with increasing distance between the molecules, the replacement of molecules leads to a decrease in intermolecular coupling which in the end increases the excitation energy [92]. For the ADT feature this means that the excitation energy is increasing

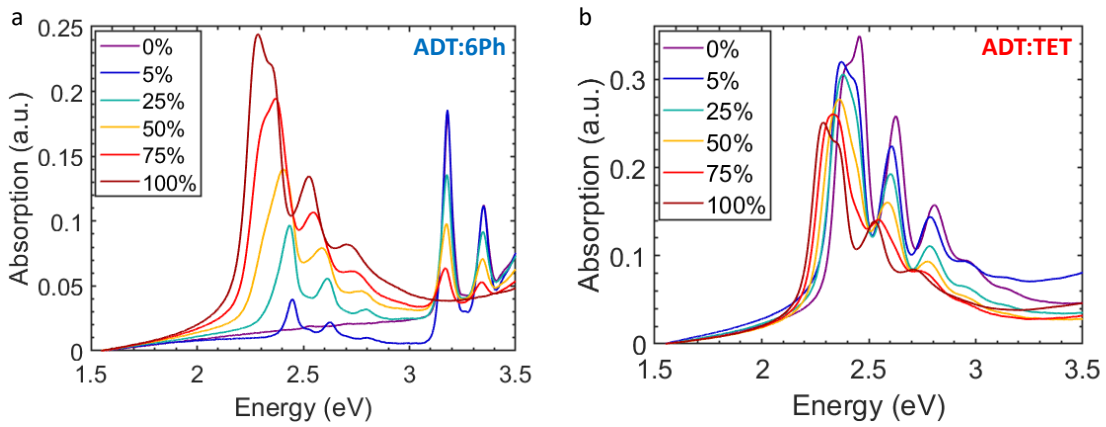

Figure 7.3.: The absorbance spectra of ADT:6Ph (a) and ADT:TET (b) are set to zero at 1.5 eV. The ADT concentration of each film is given in mol-% in the legend. A blueshift of the lowest ADT transition with decreasing amounts of ADT can be seen due to changes in polarizability and electronic structure, confirming statistical intermixing.

with decreasing amounts of ADT, amplifying the effect of the changes in polarizability. For 6Ph, the intermolecular coupling is partially compensating the effect of changes in the polarizability since the intermolecular interaction between 6Ph molecules increases with decreasing amounts of ADT. Note that the intermolecular interaction between ADT and 6Ph can be neglected due to the alignment of the HOMO and LUMO energies [155]. Combining both these effects explains why the blueshift of the ADT features is more pronounced than for the 6Ph features. Finally, it has to be discussed why the low-energy Davydov component is affected more strongly by the blueshift than the upper Davydov component (the two Davydov components move closer with decreasing amounts of ADT). This can be rationalized by the fact that the lower Davydov component has a higher amount of CT admixture than the upper one [166]. Hence the lower component is assigned to a more delocalized state than the upper one and therefore more strongly affected by the changes in polarizability with changing ADT concentration. Also, the extension of the unit cell with decreasing amounts of ADT affects the energy of the CT state more strongly. Lastly, note that for films with very low amounts of ADT it is very unlikely that two ADT molecules directly neighbor each other and since the coupling between molecules of different species is considered weak, the remaining ADT molecules in this film can be considered electronically isolated. Since the electronic interaction of two molecules in the unit cell is the foundation of the Davydov splitting [72], these films with low amounts of ADT do not exhibit a Davydov splitting at all.

Moving on to the absorbance spectra of the ADT:TET mixtures, the deciding difference here is that both compounds have very similar bandgaps. Neat TET has its $S_0 \rightarrow S_1$

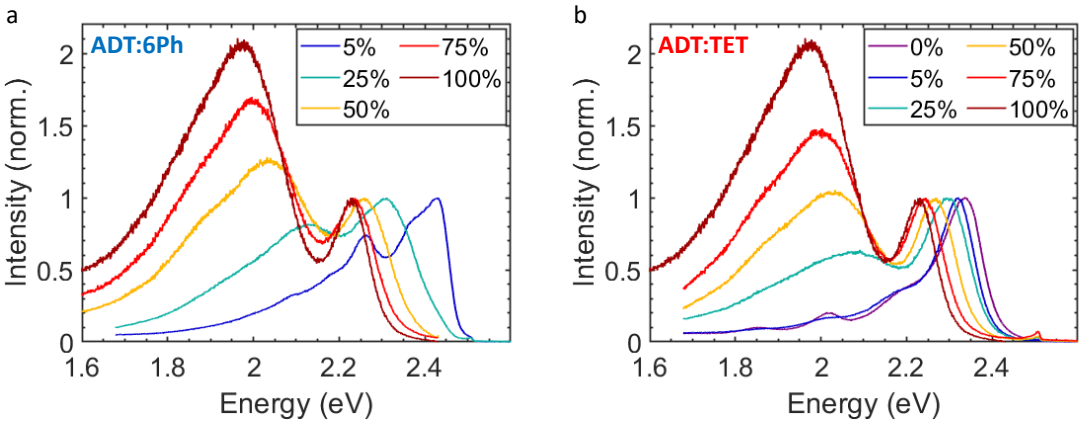

Figure 7.4.: The quasi steady-state PL spectra of ADT:6Ph (a) and ADT:TET (b) are normalized with respect to the free exciton emission. The photon energy of the excitation was 2.54 eV. The ADT concentration of each film is given in mol-% in the legend. In both systems all features blueshift with decreasing amounts of ADT. The blueshift is more pronounced in case of the RSL.

transition at 2.4 eV, which also exhibits a Davydov splitting and two peaks of the vibronic progression at 2.6 and 2.8 eV. Due to both neat materials having comparable bandgaps, it is impossible to disentangle contributions of each compound in the mixtures. However, the explanations made for the other system are not in conflict with the spectra of the ADT:TET mixtures. Also for this system a continuous blueshift of the absorption features with decreasing amounts of ADT can be found. Additionally, the spectral shape changes between the mixtures.

The spectral changes found in both systems are explained by the effect of continuous changes in the polarizability and in the intermolecular interaction. Both these effects are short range effects and hence it is necessary that the films resemble the macroscopic mixing ratio on a microscopic scale. This is only possible for a statistical mixing behavior since limited intermixing scenarios would lock the microscopic mixing ratio to certain preferred ratios.

The focus of this chapter is put on the photoluminescent behavior, into which the quasi steady-state PL spectra (Figure 7.4) give a first insight. The spectrum of neat ADT consists of two peaks, one narrow one at 2.23 eV and one broad one at 1.97 eV. The low-energy peak has a distorted shape with a stronger tail at the low-energy end compared to its high-energy tail. The peak at 2.23 eV can be assigned to the free exciton emission based on its energetic position, which is energetically in close proximity to the absorption edge of the same film in the absorbance spectrum. The reason for the emission peak of the free exciton peak being slightly red-shifted compared to the energetically lowest

absorption peak is the Stokes shift, which is rationalized by an intramolecular geometric relaxation of the molecule after absorption and before photonic emission. The nature of the second, broad, strongly redshifted emission peak of neat ADT is more complicated and will be discussed later on. For now, this emission feature will be called RSL. In both systems, ADT:6Ph and ADT:TET, the free exciton peak and the RSL are visible in all mixtures with an ADT concentration of 25 % or more. In this range, the RSL loses relative intensity compared to the free exciton peak with decreasing amounts of ADT. Both peaks blueshift with decreasing amounts of ADT, which is the same qualitative trend as found for the lowest energy absorption of ADT in mixtures. Just like in absorption, also the emission peaks are blueshifted more strongly in the ADT:6Ph system compared to the ADT:TET system. The blueshift of the peaks can be assigned to changes in polarizability and to changes in the number of direct neighbors of the same species, in the same way as explained for the absorbance spectra. Hence, this spectral shift of the emission features once more underlines the presence of statistical intermixing in both systems. Note that in both respective systems the spectral position of the RSL peak is affected more strongly by changes in the mixing ratio than the position of the free exciton emission. This will be discussed and analyzed in a quantitative and detailed way in the discussion part of this chapter.

Interestingly, in both systems the mixtures with 5 % ADT and less show a distinct spectral shape. The ADT:6Ph sample with 5 % ADT does not exhibit an RSL anymore, instead a new, sharp peak at 2.25 eV arises, which can be assigned to a vibronic replica of the free exciton peak. The free exciton peak has shifted to such high energies, that the bandpass filter, protecting the detector from scattering light of the excitation laser, also distorts the shape of the free exciton peak. Note that the low amount of ADT molecules in the film makes it unlikely to find directly neighboring ADT molecules and hence the behavior of this film is closer to the behavior of electronically isolated ADT molecules in dilute ADT solutions (see Figure A.6a in Appendix A for an ADT solution spectrum) than to the behavior of strongly interacting ADT molecules in the solid state, explaining the dramatic differences in spectral shape. Due to the high bandgap of 6Ph, the excitation laser can only excite ADT molecules, which is why luminescence of neat 6Ph is omitted in Figure 7.4a. In contrast, in the ADT:TET system the bandgaps of both compounds are too similar for a selective excitation of only ADT. For mixtures with 25 % ADT and more, this does not play a significant role since fast energy transfer from TET to ADT can be expected, which will be explained under the use of TRPL data later on. However, in the mixture with 5 % ADT this argument does not hold anymore for two reasons. First, the decrease in ADT concentration slows down the energy transfer from TET to ADT, possibly making internal TET decay channels competitive to it. Second, the lowest

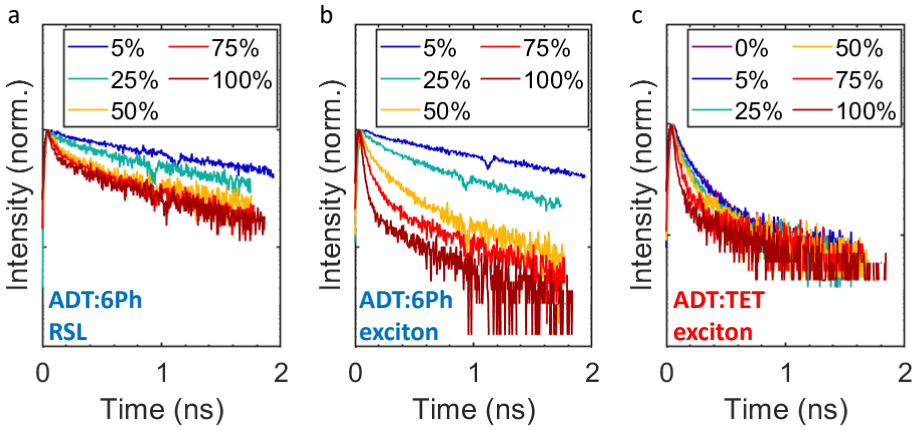

Figure 7.5.: The decay traces of the RSL (a) and the free exciton emission (b) of the ADT:6Ph system and of the free exciton emission of the ADT:TET system (c) are normalized to the intensity immediately after excitation. The y-axis is scaled logarithmically. The photon energy of the exciting laser was 3.10 eV. The spectral integration interval of each time trace can be found in Table 7.1 and was adapted to the spectral position of each emission feature for each sample. The dip in the data around 1 ns is an artifact of the setup. The ADT concentration of each film is given in mol-% in the legend.

energy transition energies of ADT and TET move closer to each other with decreasing amounts of ADT, as explained during the discussion of the absorbance data, which can lead to the energy transfer from TET to ADT being energetically less favorable, while the opposite transfer becomes energetically more favorable (see Figure A.7). Although a more detailed discussion of this film is shifted to the discussion part, this short explanation should allow to understand why the luminescence spectrum of this film is more similar in shape to the neat TET film than to those of the other mixtures. The PL spectrum of neat TET is dominated by the free exciton peak with a vibronic replica toward lower energies. The weak, sharp peak at 2.02 eV and its vibronic replica at 1.85 eV is an artifact due to contamination of the neat TET film with minor amounts of PEN during preparation.

7.3. TRPL spectroscopy

To get a deep insight into the photophysics of the samples, the spectral evolution with time and the temporal evolution of spectral features is tracked with TRPL. In Figure 7.5 time traces of the RSL and the free exciton emission have been extracted for the ADT:6Ph mixtures as well as time traces of the free exciton emission in case of the ADT:TET mixtures. Generally, the free exciton emission decays faster than the RSL and all decays are

Table 7.1.: The spectral integration intervals of the TRPL time traces shown in Figure 7.5 are given in eV.

ADT amount	0 %	5 %	25 %	50 %	75 %	100 %
ADT:6PH RSL		2.09-2.32	2.02-2.23	1.97-2.17	1.94-2.14	1.93-2.12
ADT:6PH exciton		2.32-2.60	2.23-2.49	2.18-2.42	2.15-2.38	2.13-2.37
ADT:TET exciton	2.26-2.39	2.26-2.39	2.26-2.39	2.23-2.35	2.21-2.34	2.16-2.28

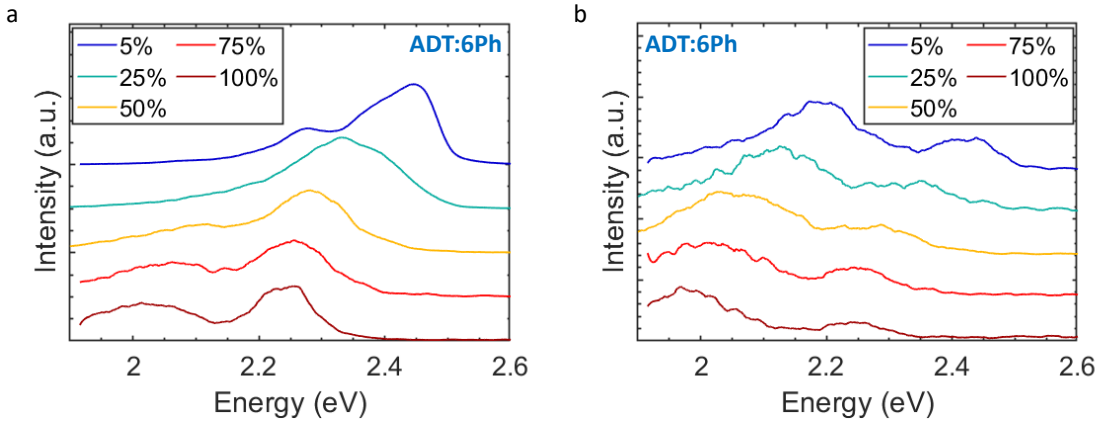

Figure 7.6.: TRPL spectra of ADT:6Ph blends time-integrated (a) from 0 to 2 ns and (b) time-integrated over all accessible times longer than 4 ns (100 %, 75 %), 8 ns (50 %) or 40 ns (25 %, 5 %), depending on the sample. The photon energy of the excitation was 3.10 eV. The ADT concentration of each film is given in mol-% in the legend. All spectra have been noise filtered. The RSL has a higher relative intensity and is redshifted at late times (b) compared to early times (a).

faster in mixtures with higher ADT concentrations. The only exception are the samples with 5 % ADT and less, however, these show a different photophysics compared to the other mixtures as will be explained in detail in the discussion part. Note that the slow decay of the RSL shows weak traces of the fast free exciton decay at short times and that the decay traces of the free exciton emission also have a weak contribution of the long-lived RSL decay. This is due to both features having spectral overlap, making a complete spectral disentanglement impossible. The features are further disentangled in the discussion part by fitting all traces with a biexponential decay and assigning the fast component to the decay of the free exciton emission and the slower component to the decay of the RSL.

Lastly, the spectral evolution of the blends with time is investigated. For this purpose, in Figure 7.6a,b the spectra are time-integrated over short and long delay times, respectively. The time window for the short times was chosen to range from 0 to 2 ns, which includes the time domain which is dominated by the decay of the free exciton

emission. The starting time for the time integration for the later time window was chosen in such fashion, that the free exciton emission has almost fully decayed at that point and hence that the RSL dominates those spectra. Since the decay rates of the free exciton emission vary between the samples (see Figure 7.5), also the starting time of the according time window varies between the samples. All time windows are listed in the caption of Figure 7.6. As one would have expected from the time traces, the early time window is dominated by the free exciton emission with only weak contributions by the RSL, while in the late time window the RSL depicts the dominant contribution and the free exciton emission contributes only weakly. Interestingly, the mixture with 5 % ADT also clearly exhibits RSL in the late time window, although this feature was not visible in the quasi steady-state spectra (compare with Figure 7.4a). This is an indication that the state related to the RSL (X_{RSL}) even has a longer lifetime than the electronically isolated ADT molecules, the luminescence of which dominates the spectrum in the steady-state due to its high luminescence at shorter times. Remember that in the mixture with 5 % ADT it statistically occurs that two molecules neighbor each other, it is just less likely than having one ADT molecule surrounded by only 6Ph molecules, in other words, only 81 % of the ADT molecules are surrounded exclusively by 6Ph molecules, but not all ADT molecules. Although the spectra at early times are dominated by the free exciton emission, the films with 50 % ADT and more still exhibit RSL to a visible amount in Figure 7.6a. Hence, in the case of these three films, the spectral position of the RSL can be compared between the spectra at early times and the spectra at later times. In all three cases (50 %, 75 % and 100 % ADT) the RSL feature is redshifted in the spectra taken at later times compared to the spectra at early times. This means that the RSL redshifts with time on a nanosecond timescale.

7.4. Discussion

The decay traces plotted in Figure 7.5 were fitted biexponentially and the resulting dominant rate of each fit is shown in Figure 7.7. The decay traces were monitored multiple times on different timescales (see Figures A.3 and A.4 in Appendix A), which was used as basis of the error estimation in Figure 7.7. For the ADT:6Ph system the exciton decay rate increases almost linearly with increasing amounts of ADT. The same trend can also be found for the ADT:TET mixtures with more than 25 % ADT, however, the mixtures with little amounts of ADT clearly deviate from the linear trend. All this behavior will be explained in the following with the replacement effect of singlet fission [146]. In case of ADT:6Ph mixtures, the admixture of 6Ph into an ADT film leads to a decrease of the statistical number of direct ADT neighbors, which is, of course, linear with the molar

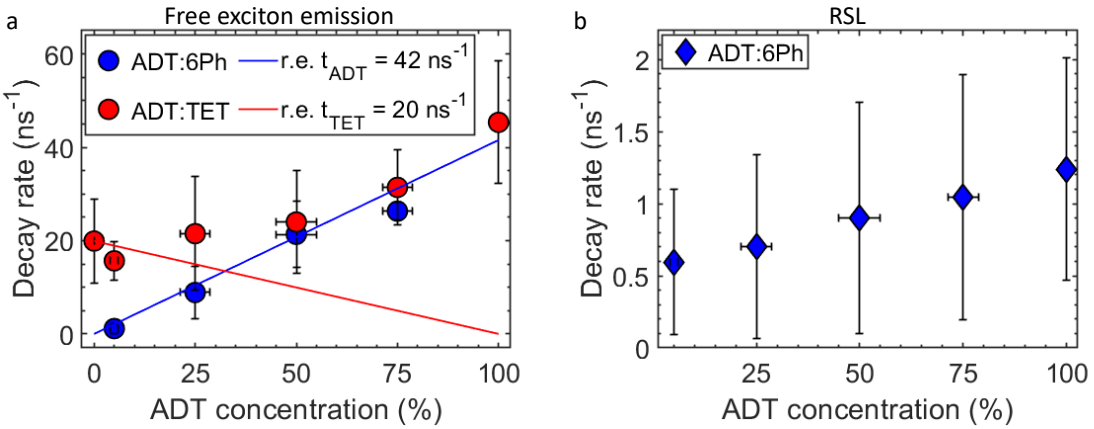

Figure 7.7.: The decay rates of the free exciton emission (a) and the RSL (b) were calculated by biexponentially fitting the respective decay traces in Figure 7.5. The blue (red) line represents the mixing ratio dependent decay rate expected from singlet fission of ADT (TET) based on the replacement effect (r.e.) and suggests incoherent singlet fission for ADT and TET [146].

ADT concentration remaining in the sample [146]. For incoherent singlet fission, the singlet fission rate at one lattice site also depends linearly on the amount of next neighbors [146]. Hence, a linear dependence of the singlet fission rate on the mixing ratio is found in case of statistical intermixing of one compound that exhibits incoherent singlet fission with an inactive spacer compound. Since this is the case in the ADT:6Ph system, it can be concluded that singlet fission occurs via the incoherent process in ADT. Note that the data point at 5 % ADT cannot be used for an analysis of singlet fission because in this mixture most ADT molecules are surrounded by exclusively 6Ph molecules, which means that for most ADT molecules singlet fission is not accessible as decay channel and hence it is very unlikely that singlet fission is the dominant decay channel of this sample.

The incoherent singlet fission mechanism of ADT is also in line with the linear behavior of the singlet decay rate found in the ADT:TET system for high ADT amounts. Interestingly, however, the behavior is clearly not linear at low ADT concentrations. This can be rationalized by the fact that TET excitations also play a role in the mixtures with low amounts of ADT. As has been found in the absorbance spectra, the free exciton of ADT and TET are in close energetic proximity for films with low amounts of ADT. Hence, it is not sufficient to only consider ADT excitations, since an excitation of exclusively ADT is not possible and, due to the energetic proximity, the assumption of downward energy transfer from TET to ADT outcompeting all other TET decay channels does not hold either. Instead, it is assumed that energy transfer between ADT and TET is

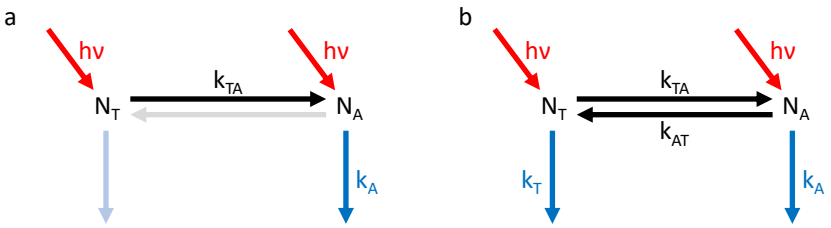

Figure 7.8.: For the ADT:TET blends a complex decay model has to be used. Initially $N_T(t_0)$ TET molecules and $N_A(t_0)$ ADT molecules are excited. Then, energy transfer from ADT (TET) to TET (ADT) occurs with a rate of k_{AT} (k_{TA}) and excitations of ADT (TET) can decay into non-luminescent states with a rate of k_A (k_T), which is expected to be dominated by singlet fission. The reduced model (a) is used for blends with 50 % ADT and more, where k_{TA} and k_A are expected to outcompete k_T and k_{AT}, respectively. For the blends with 5 and 25 % ADT the model with all four rates (b) has to be used.

significant in both directions and the decay mechanisms of both components have to be respected to understand the photophysics of these blends. While for neat TET the high singlet decay rate can be simply rationalized by singlet fission common for thin films of TET [47], for the understanding of the blends a more complex photophysical model is needed, which is sketched in Figure 7.8.

For the blends with high amounts of ADT we use the model sketched in Figure 7.8a, since efficient energy transfer from TET to ADT and inefficient transfer from ADT to TET is expected due to the energy of the TET singlet being higher than the energy of the ADT singlet in these cases. Additionally assuming that the energy transfer from TET to ADT outcompetes both singlet fission rates, we find that the decay of the luminescence is dominated by ADT singlet fission, which explains the same behavior as for ADT:6Ph mixtures in this regime. A deeper insight into the energy transfer rates and hence a justification of the latter assumption can be found in Chapter 8. For the blends with low amounts of ADT, differential equations of the decay based on the more complex model of Figure 7.8b have to be considered since energy transfer in both directions is expected to be relevant. By summing up the two equations of each excited-state species, namely

$$\frac{\mathrm{d}N_\mathrm{T}}{\mathrm{d}t} = -N_\mathrm{T}\,k_\mathrm{T} - N_\mathrm{T}\,k_\mathrm{TA} + N_\mathrm{A}\,k_\mathrm{AT} \tag{7.1}$$

and

$$\frac{\mathrm{d}N_\mathrm{A}}{\mathrm{d}t} = -N_\mathrm{A}\,k_\mathrm{A} - N_\mathrm{A}\,k_\mathrm{AT} + N_\mathrm{T}\,k_\mathrm{TA}\,, \tag{7.2}$$

we get

$$\frac{\mathrm{d}N}{\mathrm{d}t} = -N_\mathrm{T}\,k_\mathrm{T} - N_\mathrm{A}\,k_\mathrm{A} \tag{7.3}$$

with $N = N_T + N_A$ for the evolution of the total amount of luminescent excitations. All other variables used are defined in the caption of Figure 7.8. Since $N_T + N_A = N$, it can be concluded from Equation 7.3 that the value of the overall decay rate of all luminescent species, $\mathrm{d}N/\mathrm{d}t$, has to be between the two values of the decay rates k_A and k_T.[1] Note that $N_A(t)$ and $N_T(t)$ depend on the unknown rates k_{AT} and k_{TA}, which makes solving Equation 7.3 not possible.

This estimation for Equation 7.3 is perfectly in line with the free exciton decay rate of the mixture with 5 % ADT, where the data point is between the expected values of ADT singlet fission and TET singlet fission respecting the replacement effect (blue and red line in Figure 7.7a). In a microscopic picture, energy transfer between ADT and TET slows down the main decay channel, which is TET singlet fission. However, looking at the error bar, this slowdown compared to the expectation from the replacement effect of TET singlet fission is insignificant. For the mixture with 25 % ADT, surprisingly, the decay rate is higher than both expected values from the replacement effect, but its errorbar still extends over both values predicted by the replacement effect.

Since both compounds, ADT and TET, exhibit singlet fission and have comparable singlet energies, this system is a candidate for singlet heterofission [87], which will be discussed in the following. If singlet heterofission is present, an additional decay channel is available to the excited state, resulting in an increase of the related decay rate, i.e. k_A or k_T, or both, are enhanced, depending on the state(s) from which singlet heterofission can occur. Hence the presence of singlet heterofission would lead to decay rates higher than the expectation from the replacement effect. Although this would be in line with the surprisingly high value of the decay rate in the mixture with 25 % ADT, the fact, that the decay rate of the 5 % ADT blend is not enhanced compared to the predictions of the replacement effect alone, strongly suggests that singlet heterofission plays no significant role in the photophysics of the ADT:TET blends. In other words, since all decay rates in Figure 7.7a can be explained by the replacement effect of singlet homofission together with energy transfer between ADT and TET, there is no hint for the presence of singlet heterofission.

In addition to the free exciton decay rates, also the decay rates of the RSL state in the ADT:6Ph system are shown in Figure 7.7b. Compared to the free exciton decay rates, the decay rates of the RSL are far lower, underlining the longer lifetime of the RSL compared to the free exciton emission. Due to the large errorbars, no statement about the evolution of the RSL decay rates with changing mixing ratios can be made.

So far, the discussion of the photophysics of ADT was centered around the decay

[1] For $k_T \leq k_A$, the right side of Equation 7.3 can be estimated by $N\,k_T = N_A\,k_T + N_T\,k_T \leq N_A\,k_A + N_T\,k_T \leq N_A\,k_A + N_T\,k_A = N\,k_A$.

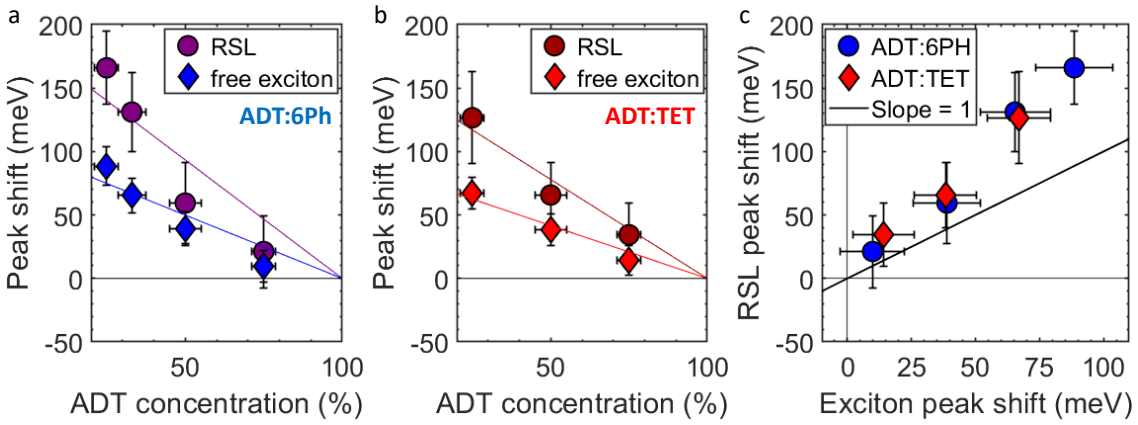

Figure 7.9.: The peak positions of the free exciton emission and the RSL were evaluated using Gaussian fits of the luminescence peaks and are plotted relative to the respective positions in neat ADT for the ADT:6Ph (a) and ADT:TET (b) system. The colored lines serve as guide to the eye and have no physical interpretation. (c) For each mixture, the shift of the RSL peak position compared to the position in neat ADT has been plotted against the respective shift of the free exciton emission. A slope of unity is indicated, which represents the case of X_{RSL} and the free exciton state reacting the same way to changes in polarizability. The fact that all data points are above this line indicates a higher sensitivity of X_{RSL} to changes in polarizability compared to the free exciton.

of the free exciton band and explained with the incoherent singlet fission mechanism. However, this does not depict the complete photophysics of ADT, since it proposes no explanation for the RSL present in most blends. In the following, the nature and dynamics behind the RSL, including the role of X_{RSL} for singlet fission in ADT will be discussed. The nature of X_{RSL} is investigated by analyzing the spectral shift of the RSL upon changes in the polarizability of the environment and comparing it to the spectral shift of the free exciton emission. For that, the peak positions of the free exciton emission and of the RSL were evaluated by applying Gaussian fits to the spectra. For both systems, ADT:6Ph and ADT:TET, and both features, the free exciton emission and the RSL, a continuous blueshift with lowering amounts of ADT compared to the peak positions in neat ADT is found and plotted in Figure 7.9a,b. In both systems and for all mixing ratios the spectral shift of the RSL is greater than the shift of the free exciton emission. Under the assumption that changes in polarizability are the driving force for the blueshift with changing mixing ratios, it can be concluded that X_{RSL} reacts more sensitively to changes in polarizability than the free exciton emission. To further visualize this, the changes in the spectral position of the free exciton emission has been used as a measure for the changes in polarizability in Figure 7.9c and used as x-axis. The y-axis of this plot shows the shift of the RSL, which means that for each mixture the relative position of

the free exciton emission and the relative position of the RSL determine the position of the data point in the plot. In the resulting plot, the slope of unity is indicated, which depicts the case of X_{RSL} and the free exciton exhibiting the same sensitivity to changes in polarizability. If the data points are below this slope, X_{RSL} is less sensitive to changes in the polarizability than the free exciton, while an accumulation of data points above the slope of unity, as in the present case, means that X_{RSL} is more sensitive to changes in the polarizability than the free exciton. Localized states, like triplets and the triplet-pair state [168, 169], exhibit a very low sensitivity to changes in the polarizability, while delocalized states, like excimers [23], are more sensitive to changes in polarizability. This can be understood by the fact that more delocalized states have a higher average spatial separation of electron and hole, leading to a higher fluctuating dipole moment, which can then polarize the local environment to a higher degree [96], in the end leading to a stronger dependence of the energy of the respective state on the polarizability of the surrounding medium compared to a more localized state [53]. Based on the high sensitivity to changes in polarizability which has been found for X_{RSL}, additionally to its typical broad shape and its redshifted position in the emission spectrum [78], it can be concluded that X_{RSL} is an excimer [23]. Since excimer formation is an intermolecular process [24, 26], the assignment to an excimer is also in line with the suppression of the RSL in mixtures with 5 % ADT, where most of the molecules are electronically isolated.

For mixtures with more than 5 % ADT, the lower RSL intensity at lower ADT amounts (Figure 7.4) can be explained by the change in singlet fission rate. Since singlet fission is a luminescence quenching channel, the probability for luminescent decay is higher the lower the singlet fission rate. This effect can be taken into account by normalizing the PL spectra to the free exciton emission multiplied by the singlet fission rate, which is shown in Figure 7.10. If the excimer decay rates are also included in the normalization process, the resulting RSL intensity is proportional to the excimer formation rate. The resulting RSL intensity (Figure 7.10) is of comparable intensity in all mixtures, which indicates that the excimer formation dynamics do not alter between the mixtures. This is a quite interesting result since excimer formation is an intermolecular process and hence needs a neighbor to proceed [23, 24] but at the same time reducing the number of neighbors does not seem to induce changes to the process. One possible explanation for this stability in the photodynamics is that excimer formation occurs in a coherent process, which exhibits nearly the same efficiency, independent of the number of nearest neighbors [146] and a coherent process would also be in line with the fast timescale expected for excimer formation [24].

After identifying X_{RSL} as an excimer, one of the main remaining questions is if and how the excimer influences the singlet fission dynamics. There are two possible sce-

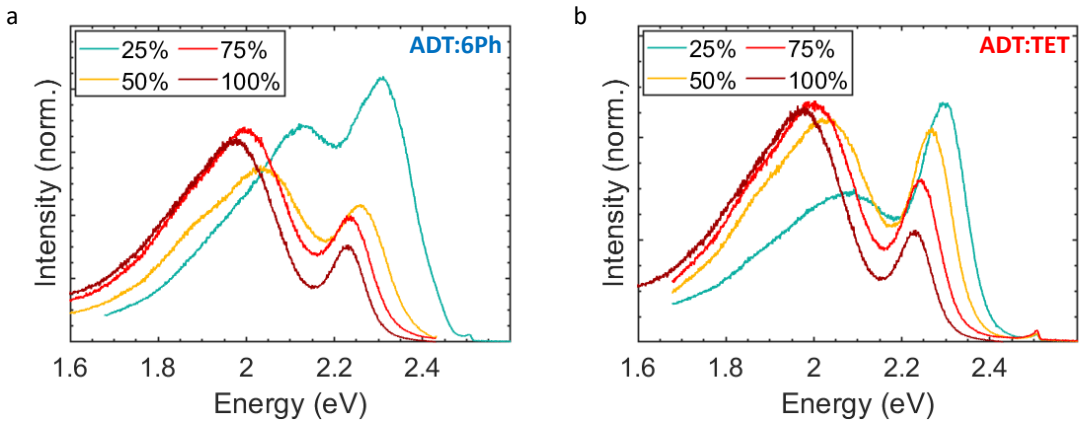

Figure 7.10.: The quasi steady-state PL spectra of ADT:6Ph (a) and ADT:TET (b) are normalized with respect to (a) the free exciton emission times the singlet fission rate divided by the excimer decay rate and (b) to the free exciton emission times the singlet fission rate. The mixtures with 5 % ADT and less are omitted since they do not exhibit RSL. The photon energy of the excitation was 2.54 eV. The ADT concentration of each film is given in mol-% in the legend. The data are the same as in Figure 7.4, normalized differently. All mixtures show comparable RSL intensities besides the ADT:TET mixture with 25 %. In the latter case the RSL is weaker because the luminescence of this mixture is expected to be a superposition of ADT luminescence, which exhibits RSL, and TET luminescence, which does not exhibit RSL.

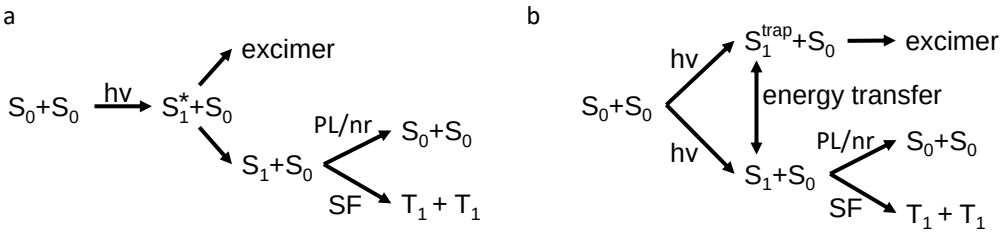

Figure 7.11.: Possible decay mechanisms of ADT including excimer formation and singlet fission as competing channels. Scenario (b) is considered less likely since energy transfer would be expected to couple the singlet decay rate and the excimer formation rate.

narios, one is that excimer formation competes with singlet fission as decay channel, which means that the pathway via excimer formation is a loss channel for singlet fission [31, 46, 47]. The second scenario is that the excimer, which has a high quantum-mechanical admixture of the diabatic CT state, is an intermediate in the singlet fission process, meaning that the initially excited free exciton decays into an excimer, which subsequently decays into the ^{1}(TT) state [33, 35]. For the latter scenario it would be necessary that the free exciton emission decays on the timescale of excimer formation and further that triplet-pair formation occurs on the timescale of the excimer decay. In the present case, the found decay rate for the free exciton emission fits neither the excimer formation rate, nor the excimer decay rate, making the latter scenario unlikely. Instead, it is more likely that excimer formation works as a loss channel for singlet fission. Assuming this scenario, there remain two possible decay mechanisms for ADT that are both sketched in Figure 7.11. A scenario, in which excimer formation and singlet fission affect exactly the same state can be excluded since this would also require the excimer formation rate and the free exciton decay rate to be the same. Instead, excimer formation and singlet fission have to occur from different starting points to explain why both processes coexist with differing rates. Remember that the excimer formation rate is faster than the time resolution of the TRPL setup (10 ps), while the decay of the free exciton emission can be resolved (Figure 7.5). The scenario in Figure 7.11a proposes that excimer formation is only possible for the unrelaxed free exciton. Since excimer emission is also visible under excitation only slightly above the band edge (Figure E.6b in Appendix E shows PL spectra of neat ADT under excitation at 2.33 eV), this cannot be a higher electronic excitation (S_n) or a vibronic excitation, but, for example, this could be the state related to the absorption of the higher Davydov component or an excitation in k-space of a given band. In this case, excimer formation would directly compete with IC to the lowest excited singlet state immediately after excitation, but would not be possible anymore once the relaxed S_1 state is reached. Hence singlet fission would be the dominant decay channel for the free exciton band after relaxation to the lowest excited singlet state. The alternative scenario, Figure 7.11b, proposes that trap states facilitate excimer formation. One example for such trap states would be states at grain boundaries, where, due to the identical orientation of the long molecular axis in all grains, it is very likely that two molecules are oriented to each other in a fashion that is closer to face-to-face stacking than the herringbone structure present in the bulk. Since the face-to-face geometry is most prone to excimer formation [23, 26], it is very likely that excimer formation is facilitated at grain boundaries. However, there are two critical arguments that make the latter scenario, i.e. the one in Figure 7.11b, very unlikely. First, excimers can also be observed to a similar extend in single crystals, in which grain boundaries and trap

states play a negligible role (see Figure A.6b in Appendix A for an ADT single crystal PL spectrum). Second, energy transfer between bulk states and trap states can be expected to be efficient, which means that the bulk states, which facilitate singlet fission, and the trap states, which facilitate excimer formation, would be coupled, which would result in the excimer formation rate being (partially) coupled to the singlet fission rate. However, since no increase in excimer emission intensity is found on the same timescale as singlet fission occurs, such a coupling can be ruled out. This means that the first scenario, in which excimer formation competes with the internal relaxation within the S_1 state and hence indirectly acts as a loss channel for singlet fission, is the most likely one.

Lastly, the spectral redshift of the excimer emission with time has to be discussed. This redshift has been found when comparing the spectral shape of the excimer emission in mixtures with high amounts of ADT at early and late times, i.e. when comparing the spectra in Figure 7.6a and b. This redshift occurs on the nanosecond timescale and can be assigned to the diffusion of excimers [23] to defect sites such as grain boundaries. Due to the uniaxial anisotropy, the long axis of the molecules are also aligned at grain boundaries and, since the inclination angle between neighboring molecules is almost 90° in the herringbone structure of the bulk [122], it is likely that the inclination angle is smaller at grain boundaries. This means that the geometric arrangement at grain boundaries is more favorable for excimers and further that excimers have a lower energy at grain boundaries, explaining the observed redshift. Note that, due to the fast timescale of excimer formation [24, 170, 171] and the low density of defect sites, the defect sites only play a significant role after excimer formation and prior to excimer emission, but not during ultrafast excimer formation.

7.5. Conclusion

In this chapter, ADT blends with different spacer compounds have been used to investigate the nature of the state responsible for the RSL and to uncover its role in the singlet fission process of ADT. Detailed insight into the photophysics of ADT, which is dominated by singlet fission and by the formation and decay of excimers, is gained by employing TRPL spectroscopy.

By preparing binary blends of ADT with TET or 6Ph, which are two different spacer compounds with different bandgaps, the role of the amount of the spacer compound was disentangled from the role of the size of the bandgap. For both systems, a continuous change in unit cell parameters with changing mixing ratio was revealed by XRD, while absorbance and PL spectroscopy additionally revealed a continuous change in polarizability with changing mixing ratios. Based on these results, statistical intermixing

can be concluded for both systems. Combining the data acquired from both systems, changes in polarizability were disentangled from changes in mixing ratio, leading to the finding that the state assigned to the RSL is highly sensitive to changes in polarizability and hence was identified as an excimer. The decay traces extracted from TRPL measurements yield mixing ratio dependent singlet decay rates that suggest incoherent singlet fission of ADT, but no sign of singlet heterofission in the ADT:TET blends were found, although the energetic requirements are met. Since neither the ultrafast formation of excimers, nor their decay on a ns timescale matches the found singlet fission rates, it was concluded that excimer formation is an indirect loss channel for singlet fission in ADT.

8. Results II: Singlet fission in the presence of energetically low-lying states

In this chapter energy transfer in ADT in presence of small amounts of the lower bandgap compound PEN is investigated. The chapter is based on Ref. [172], which will be published in collaboration with M. Gerhard's research group (Marburg, Germany).

Most architectures of organic photovoltaic cells consist of multiple layers with different functions [173–176]. Hence, the device can only work efficiently if the layers are electronically connected with each other, which means that excitations can travel through the layers with high yields [177, 178]. This is achieved by creating structures with energetic landscapes that make the desired transition energetically favorable and kinetically reachable for the excitation [179–183]. Since each such transition reduces the remaining energy of the excitation, it is desirable to make the gradient in the energetic landscape as small as possible [184, 185]. At the same time, small differences in the excitation energy between the layers can reduce the yield of transitions between the layers, since layer-intrinsic loss channels, such as exciton quenching [182, 186, 187], the occupation of trap states [177] or excimer formation [31, 155], can then compete with the desired pathway of the exciton. This multitude of photophysical pathways available in a multicompound system can make it challenging to disentangle the contributions of each channel to the efficiency losses of a given solar cell and hence complicate further improvements of a device.

In this chapter ADT is used as the basic compound, which already as a neat material exhibits a complex photophysics including two concurrent multimolecular decay channels, namely singlet fission and excimer formation [155]. ADT is then blended with low amounts of PEN, which has a lower bandgap than ADT, to enable energetically favorable energy transfer from ADT to PEN. The admixture of PEN leads to drastic changes in the photodynamics of the sample that have been tracked using TRPL. The spectral fingerprint of the PL of neat ADT, which consists of luminescence from the free exciton and the excimer, is drastically reduced in intensity already under the presence of

small amounts of PEN, which is rationalized by fast downward energy transfer from ADT to PEN. For PEN excitations, efficient energy transfer followed by singlet fission was found over a wide temperature range, making the investigated system a prototypical system for efficient and controlled exciton funneling in the presence of a complex photophysics exhibited by ADT. This funneling mechanism results in a system that combines the absorption properties of ADT with the excellent singlet fission yield of PEN, bypassing intrinsic loss channels of neat ADT. Such a funneling mechanism can also be used to combine photon harvesting materials with materials possessing promising exciton transport properties in device applications [188].

8.1. Structural characterization

The structures of the neat films and mixtures of ADT and PEN were investigated by combining XRR and GIWAXS, enabling insight into the out-of-plane and in-plane structure. The data gained by these measurements for the present system appear very comparable to those analyzed in Chapter 7, hence the same analysis procedure was applied in both cases. For this reason, the structural characterization is kept short in this chapter and a more detailed description of the analysis pathway to structurally investigate such a type of system can be found in the structural and optical characterization of the systems investigated in Chapter 7. In the XRR scans (Figure 8.1a) Bragg peaks of first and second order are visible for all films. The neat ADT film exhibits a split peak in both Bragg peak orders, which is assigned to the coexistence of thin film and bulk phase with the thin film phase being the dominant component at smaller q_z-values (see Appendix E for details) [122, 126]. The split Bragg peak in ADT is better visible for the second order Bragg peak. In the same way, the PEN Bragg peak is split in both orders, which is also in this case assigned to the coexistence of thin film and bulk phase [189, 190]. Compared to ADT, all Bragg peaks are at smaller scattering vectors in case of PEN, indicating a higher d_z spacing for PEN compared to ADT. Also, the differences in d_z spacing between the thin film and the bulk phase are greater for PEN, making the split peak in case of the neat PEN film visible for both Bragg peak orders. For all mixtures, a splitting is observed in case of both respective Bragg peaks, indicating a coexistence of thin film and bulk phase in the mixtures as well. The positions of the Bragg peaks in the mixtures are in between those of the neat films in all cases. For a more precise estimation of the peak positions the second order Bragg peak has been fitted with two Gaussians. The position of the higher intensity peak was assigned to the dominant thin film phase and the position of the other peak to the bulk phase. The d_z spacing was calculated in Figure 8.1c using the formula $4\,\pi/q_z$ with the Bragg peak position q_z. The error bars in Figure 8.1c

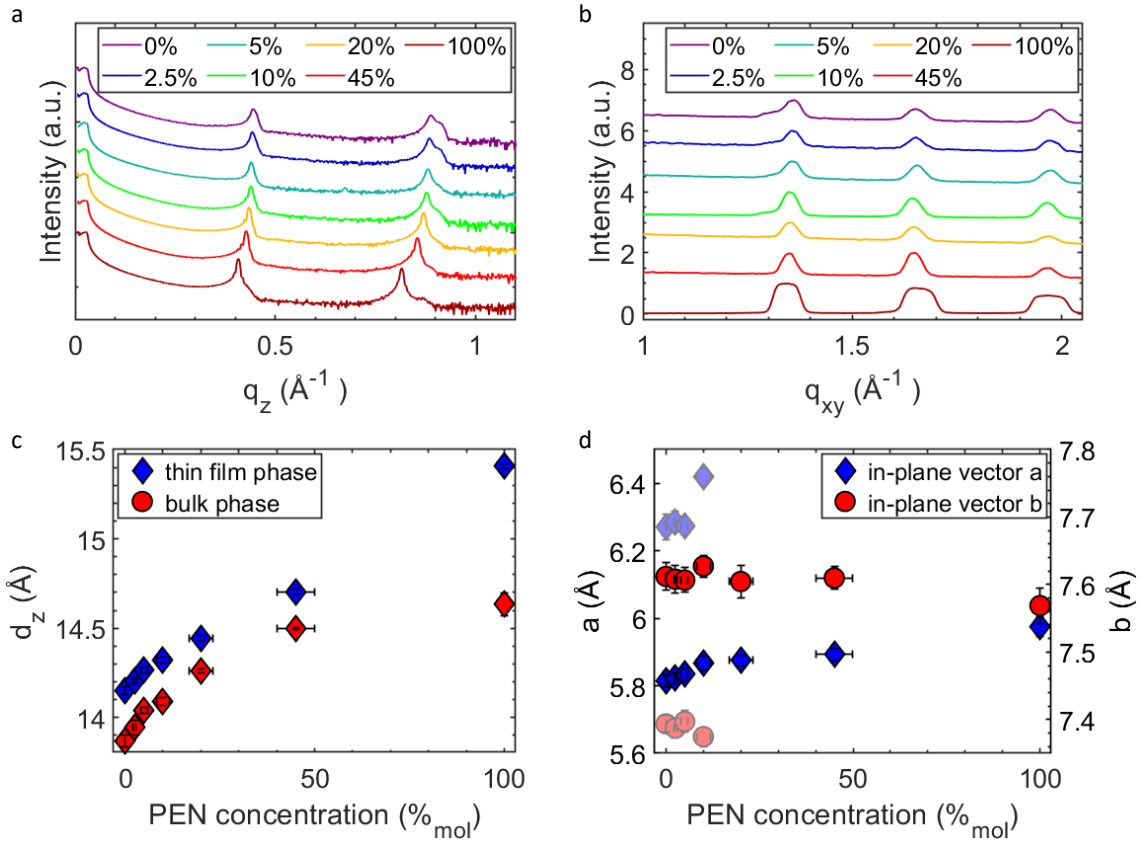

Figure 8.1.: XRD results of ADT:PEN mixtures. The XRR (a) and GID (b) curves are vertically offset for clarity. The y-axis of the XRR curves is scaled logarithmically while for the GID data the y-axis is scaled linearly. The scans along q_{xy} (b) were calculated by integrating each of the GID maps shown in Figure B.1 along q_z in the range $0.1\,\text{Å}^{-1} < q_z < 0.3\,\text{Å}^{-1}$. The peaks of neat PEN are broader because for this sample a substrate of 10 mm was used instead of 5 mm, which was used in all other cases. The PEN concentrations are given in mol-% in each legend. Under the assumption of a rectangular in-plane lattice, the d_z-spacing (c) and the in-plane lattice parameters (d) have been calculated based on the Bragg peak positions. The (11l) peak is split in the GID data of the films with low amounts of PEN. Using the lower intensity component for the calculation leads to the faded data points in (d). All Bragg peaks in XRR are split due to the coexistence of thin film and bulk phase [126, 189, 190] and the d_z spacings of both phases are calculated in (c).

were calculated based on taking 10 % of the Bragg peak width as uncertainty. For both phases, the thin film and bulk phase, a continuous increase in d_z spacing with increasing amounts of PEN was found, which is a first sign of statistical intermixing of the two compounds [58, 92], as found in the literature [45]. The d_z spacings found for the neat films agree well with the c axis of the respective unit cells [122, 140], suggesting a preferred standing-up orientation of the molecules against the substrate surface [126, 190]. Note that Kiessig oscillations are not visible in any of the scans and also Laue oscillations are only weak if visible at all, indicating a high roughness of all films [102]. However, a detailed morphological analysis of the samples is beyond the scope of this chapter.

Additionally to XRR, which gives access to the out-of-plane structure, GIWAXS has been employed for the following analysis of the in-plane structure. Since all GID maps exhibit vertically extended features (see Figure B.1), the maps were integrated along small q_z values to determine and compare the in-plane positions of the Bragg peaks of the different samples in Figure 8.1b. Since both neat compounds are known to arrange in a herringbone structure [122, 189], a herringbone structure is assumed for all films, resulting in an assignment of the three visible peaks to the (11l), (02l) and (12l) reflection moving from lower to higher q_{xy} values. Note that the reason for the Bragg peaks of neat PEN being broader compared to all other samples is that the substrate used for the GIWAXS measurement with neat PEN had a longer extension along the incoming beam path compared to the other samples. This increases the footprint of the X-ray beam on the sample, which leads to a peak broadening (see Figure B.2 in combination with the measurement geometry of GIWAXS, which is sketched in Figure 5.2b). The (11l) peak of neat ADT is split in two peaks with a low intensity component at smaller q_{xy}, which is assigned to the coexistence of thin film phase and bulk phase, where the more intensive component is assigned to the thin film phase and the less intensive component to the bulk phase (see Appendix E for details). This peak splitting is also present in mixtures with low amounts of PEN and assigned to the same effect there. Overall, no clear trend in Bragg peak position with changing mixing ratios can be found, which is validated by fitting the Bragg peaks with Gaussian functions. Using the assumption of a rectangular in-plane unit cell, a rough estimation of the in-plane lattice parameters a and b can be made, and the result is shown in Figure 8.1d. Both lattice parameters only change very little between the mixtures and they change continuously within the error bar, once more indicating statistical intermixing of ADT and PEN [45, 58]. The data points plotted in faded colors are extracted by using the position of the low intensity component of the (11l) peak as basis for the calculation.

8.2. Optical characterization

For a first insight into the optical properties of the mixtures, absorbance spectra of the neat films and blends are shown in Figure 8.2a. Both neat films have a very similar spectral shape, which is composed of a Davydov splitting of the $S_0 \rightarrow S_1$ transition with multiple consecutive peaks at higher energies that are assigned to a vibronic progression. The small differences in intensity ratio and energetic spacing between the two Davydov components of ADT and PEN can be assigned to small differences in intermolecular interaction, to which the Davydov splitting is very sensitive [71, 92, 166, 191]. The biggest difference between the absorbance spectra of the neat compounds is the energetic position of the lowest possible transition, which peaks at 1.86 eV for neat PEN and at 2.29 eV for neat ADT. This large difference in excitation energy makes it possible to distinguish contributions of PEN and ADT in the absorption spectra of the mixed films, which are discussed in the following. Analyzing the changes of the $S_0 \rightarrow S_1$ transition of PEN in the mixed films upon a decrease in the amount of PEN, three trends can be found. The first one is a decrease in intensity of the absorption peak, which is assigned to a reduction of the overall amount of PEN in the sample. Second, the Davydov splitting becomes smaller and vanishes in mixtures with low amounts of PEN. This can be rationalized by the Davydov splitting being steered by the interaction of two translationally inequivalent molecules the following way. At low amounts of PEN, the average distance between two PEN molecules is high and hence their interaction becomes negligible, leading to a decrease in Davydov splitting [92]. The third trend is a spectral blueshift (best visible in case of the first vibronic replica), which can be explained by a change in electronic structure of the S_1 state due to reduced intermolecular interaction [71, 92] and a reduction of polarizability of the environment [133] with decreasing amounts of PEN. For the ADT absorption peak very similar trends are found. With decreasing amounts of ADT, the intensity of the absorption peak and the Davydov splitting both decrease for the same reasons as discussed in the case of the PEN absorption feature. However, no clear spectral shift can be found for the ADT absorption peak with decreasing amounts of ADT, which is most likely because of the effect of changes in electronic structure of the S_1 state and the effect of changes in polarizability compensating each other. While the electronic changes of the S_1 state of ADT are expected to blueshift the spectrum with decreasing amounts of ADT [71, 92], the admixture of PEN increases the polarizability of the environment at the same time [133], leading to a redshift. Note that evaluating the exact values of absorption intensity, Davydov splitting and spectral position of the ADT features from the absorbance spectra is hard in case of the mixtures because here the ADT absorption overlaps with the vibronic progression of PEN. Since the continuous

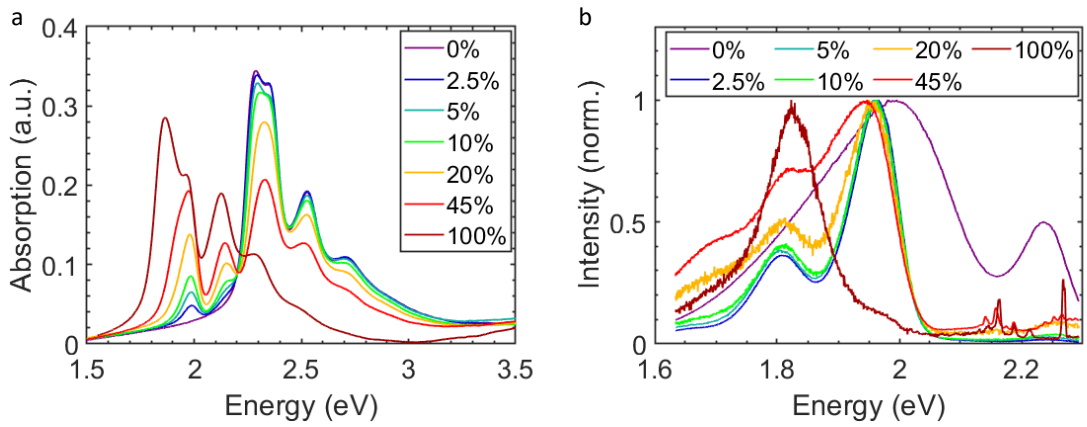

Figure 8.2.: Absorbance (a) and normalized PL (b) spectra of the ADT:PEN mixtures and neat films. The absorbance spectra have been set to zero at 1.5 eV. In the steady-state PL photonic excitation occurred at 2.33 eV. The sharp peaks visible in the high-energy region of the mixtures with high amounts of PEN are Raman peaks [192]. PEN concentrations are given in mol-% in each legend. In the mixtures the free exciton emission of ADT at 2.23 eV and the broad excimer emission of ADT at 2.02 eV are suppressed and PEN monomeric emission at 1.96 eV dominates the spectrum instead.

spectral changes have been explained with changes in intermolecular interaction and in polarizability, which are both short-range effects, the compound ratio has to be represented on a microscopic scale, once more strongly suggesting statistical intermixing of ADT and PEN [45, 92].

PL experiments have been performed using a photon energy of 2.33 eV for excitation, which means that, according to the absorbance spectra, ADT is dominantly excited in the mixtures. As discussed previously in Chapter 7, the spectrum of neat ADT is dominated by two peaks, one sharp peak of the free exciton emission at 2.23 eV and one broad, asymmetric excimer emission peak at 2.02 eV. Neat PEN is known for ultrafast singlet fission [80, 193, 194], which is a luminescence quenching channel. This leads to a very low intensity free exciton peak at 1.81 eV, which has a tail toward higher energies. Due to the low overall intensity of the PEN emission, sharp Raman peaks are clearly visible in the high-energy range [192]. A detailed discussion of the photophysics of neat PEN is beyond the scope of this chapter and can be found elsewhere [80, 81, 193, 194]. Surprisingly, the spectra of all mixtures exhibit a spectral shape that is clearly different from the spectra of the neat films of both contributing compounds. For example, the ADT excimer luminescence is not visible in any of the mixtures, which is rationalized by energy transfer to PEN in the discussion part. All mixtures with 10 % PEN and less have an almost identical spectral shape which is dominated by a sharp peak at 1.96 eV

with a vibronic replica at 1.81 eV. Additionally, these mixtures carry a very weak peak at 2.23 eV. The latter peak is assigned to free exciton emission of ADT based on its energetic position which is the same as in neat ADT. By taking the absorbance spectra into account, the peak at 1.96 eV is assigned to PEN emission based on the following argumentation. Due to statistical intermixing, the probability of a PEN molecule being surrounded by only ADT molecules is high for films with low amounts of PEN [146]. These PEN molecules, which will be called isolated in the following, show only weak electronic interaction [92, 146], leading to an increase in S_1 energy compared to PEN molecules with next neighbors of the same kind [71]. Also for isolated PEN molecules singlet fission is not available as a luminescence quenching channel [92, 146], which means that excitations of PEN molecules without direct PEN neighbors have a much higher luminescent yield compared to sites at which singlet fission is possible. This results in the PEN luminescence being fully dominated by isolated PEN molecules in the mixtures with 10 % PEN and less. A more detailed photophysical model will be discussed later on using the TRPL data to get insight into the time-dependent evolution of the excited state. The peak at 1.81 eV is assigned to a vibronic replica of the peak at 1.96 eV based on the energetic spacing between the two peaks, which fits well with the energy of a characteristic vibration and with the energetic spacing of the vibronic progression in the absorbance spectra. The mixtures with 20 % PEN and 50 % PEN exhibit the same features as the mixtures with lower amounts of PEN, but with small spectral distortions, which are namely a blueshift of the ADT free exciton emission peak to 2.27 eV and a more pronounced low-energy tail of the PEN emission. The blueshift of the ADT free exciton peak can be explained by ultrafast energy transfer from ADT to PEN which outcompetes thermal relaxation inside the free exciton band after excitation. The reason for the spectral distortion of the PEN emission in the mixtures with higher amounts of PEN is that in these samples isolated PEN molecules are rare and hence luminescence from these molecules does not fully dominate the luminescence from lattice sites which are capable of singlet fission. As a result, the spectral shape of the PEN emission in these mixtures is similar to a superposition of the emission of mixtures with low amounts of PEN (emission from isolated PEN molecules) and neat PEN (emission from PEN molecules neighbored by further PEN molecules). Note that it is not exactly a superposition since a superposition would assume that PEN molecules with 1, 2 or 3 PEN neighbors behave the same as PEN molecules with 4 neighbors and a superposition does not take changes in polarizability into account either. Since there are even less isolated PEN molecules in the mixture with 50 % PEN compared to the one with 20 % PEN, the spectrum of the former has an even more pronounced low-energy tail. Once again, this will be discussed in further detail using TRPL data later on. Remember that the steady-state PL data in

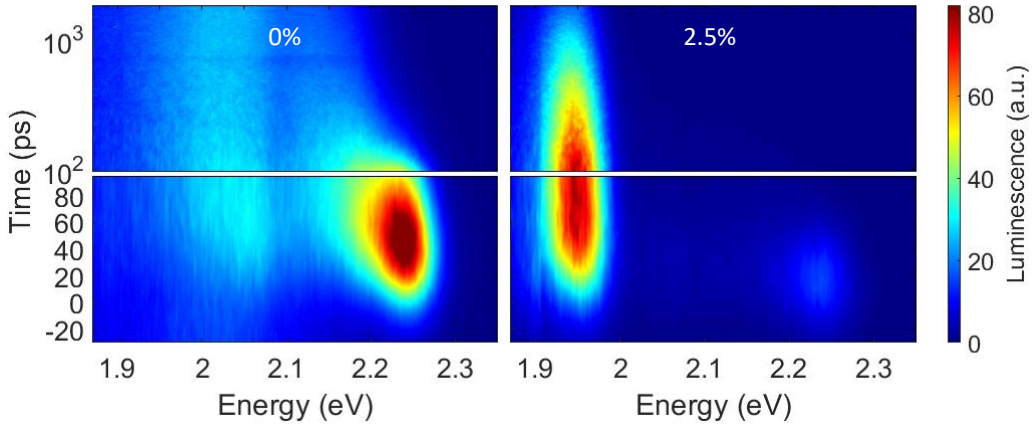

Figure 8.3.: The time axis of the TRPL maps at 70 K of neat ADT and one representative mixture are displayed semilogarithmic. PEN concentrations are given in mol-% inside each map. Neat ADT is dominated by free exciton emission at 2.23 eV with weak excimer emission around 2 eV, while the mixture is dominated by monomeric PEN emission at 1.96 eV.

Figure 8.2b are normalized, which means that, although the mixtures with high amounts of PEN have a higher ADT free exciton emission peak in the figure, this does not mean that the absolute ADT luminescence intensity is also higher in these mixtures.

8.3. TRPL spectroscopy

Insight into the time-dependent evolution of the excited states is gained by employing TRPL. In Figure 8.3 TRPL maps of neat ADT and the mixture with 2.5 % PEN are shown. While neat ADT exhibits a fast decay of the free exciton band at 2.23 eV due to singlet fission [30, 83, 128, 155, 195] and a spectrally broad, redshifted, long-lived excimer emission around 2.02 eV, the mixture exhibits an even faster decay of the free exciton emission of ADT and in the low-energy region long-lived luminescence from isolated PEN is visible instead of excimer luminescence.

Time traces have been extracted for the ADT free exciton (Figure 8.4a) and for the PEN emission (Figure 8.4b) for all mixtures to enable a comparison of the time evolution of these features. Although neat ADT has no PEN emission, time traces of the same spectral region have been taken for this sample, which covers the excimer emission in this case. In all samples, the ADT free exciton emission decays fast and for all mixtures this decay is clearly faster than for neat ADT. In case of the mixtures the lifetime of the ADT free exciton emission is in the order of a few picoseconds, which at the same time is

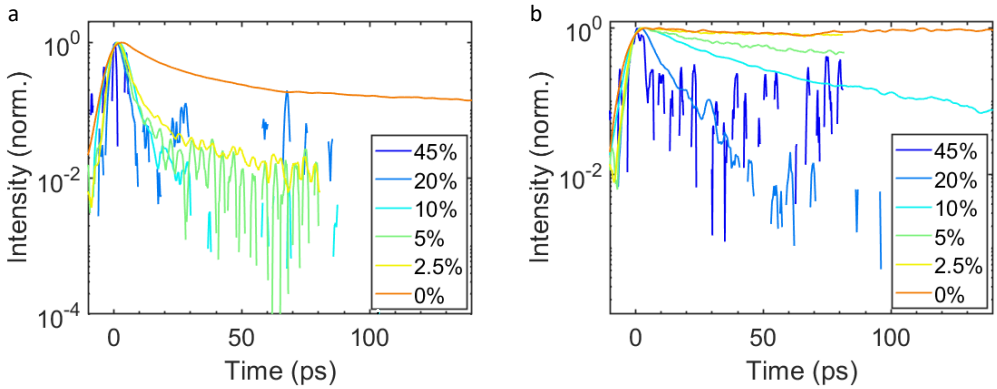

Figure 8.4.: Decay traces of the ADT (a) and PEN (b) emission were extracted by spectrally integrating the TRPL maps recorded at 70 K from 2.12 to 2.36 eV and from 1.86 to 2.05 eV, respectively. Due to the logarithmic y-axis, negative values, resulting from background corrections, were omitted. PEN concentrations are given in mol-% in the legend. Note that in (a) all decay rates of the mixtures are on the order of the instrument response time. Also note that in (b) for neat ADT the excimer decay is shown instead of the PEN decay.

the time resolution limit of the present setup. This makes the quantification of the ADT free exciton decay challenging, which will be explained in more detail later on when employing GA. Compared to the ADT free exciton emission, the PEN luminescence has a longer lifetime in all samples and here a clear trend in the evolution of lifetimes can be found between the samples. With increasing amounts of PEN, the lifetime of the PEN luminescence decreases continuously. Remember that in this spectral region neat ADT exhibits excimer luminescence, which has a lifetime of a few nanoseconds [155] but is a different species than the PEN luminescence exhibited by all mixtures. Hence in this spectral region the decay trace of neat ADT should not be directly compared to those of the mixtures. The fact that the time traces get more noisy with increasing amounts of PEN can be explained by energy transfer to PEN followed by PEN singlet fission, which is a luminescence quenching channel that becomes more efficient with increasing amounts of PEN. This point will be examined in more detail in the discussion part.

TRPL experiments also have been carried out with all samples over a wide temperature range (between 10 K and 295 K). For neat ADT, the sample temperature affects the photodynamics strongly, which will be discussed in detail in Chapter 10. However, in case of the mixtures, the photodynamics do not change strongly with changing temperatures as can be seen exemplary for the mixture with 2.5 % PEN in Figure 8.5. The weak tendency to higher decay rates with increasing temperature, which can be seen in both plots of Figure 8.5, is most pronounced in this mixture and is more difficult to observe in mixtures with higher amounts of PEN. A broader insight into the temperature depen-

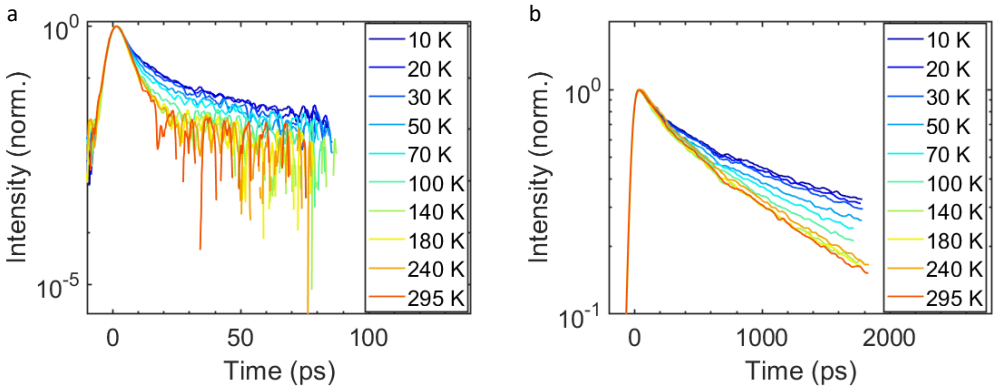

Figure 8.5.: Decay traces of the ADT (a) and PEN (b) emission were extracted from the TRPL maps of the sample with 2.5 % PEN by spectrally integrating from 2.12 to 2.36 eV and from 1.86 to 2.05 eV, respectively. Due to the logarithmic y-axis, negative values, resulting from background corrections, were omitted. Sample temperatures are given in the legend.

dence of the mixtures can additionally be found in Figure 8.6, where PEN decay rates are given depending on temperature and PEN concentration.

For a quantitative analysis of the TRPL data, GA has been employed [121]. Since in the mixtures the emission of ADT and the emission of PEN have no spectral overlap, the two species could be disentangled before applying GA. This has been done by analyzing the high-energy part ($E_{\text{photon}} > 2.14\,\text{eV}$), which contains only ADT luminescence, and the low-energy part ($E_{\text{photon}} < 2.00\,\text{eV}$), containing only PEN luminescence, separately. Since all mixtures exhibit very similar spectral features, this kind of analysis could be applied to almost all mixtures and sample temperatures, however, increasing amounts of PEN and increasing temperatures lead to more efficient luminescence quenching, resulting in some cases in an overall signal, which is too weak for a quantitative analysis. Both features, ADT luminescence and PEN luminescence, exhibit barely any spectral change with time in the mixtures and can be well described with a monoexponential decay. The instrument response function was fitted with a Gaussian function and has a width of around 2 ps. This duration of the instrument response function is comparable to the lifetimes of the ADT excitations in most mixtures and in mixtures containing high amounts of PEN also the decay of PEN luminescence occurs on a comparable timescale. This results in a high uncertainty in the exact decay constants in case of such high decay rates. In case of neat ADT, the TRPL data uncover significant spectral changes with time and with changing sample temperatures. The temperature-dependent photophysics of neat ADT will be discussed in detail in Chapter 10, while in this chapter the data of neat ADT (Figure 8.6a) are analyzed with the same method as the mixtures and the results here should be used only for comparison with the mixtures. Due to spectral overlap

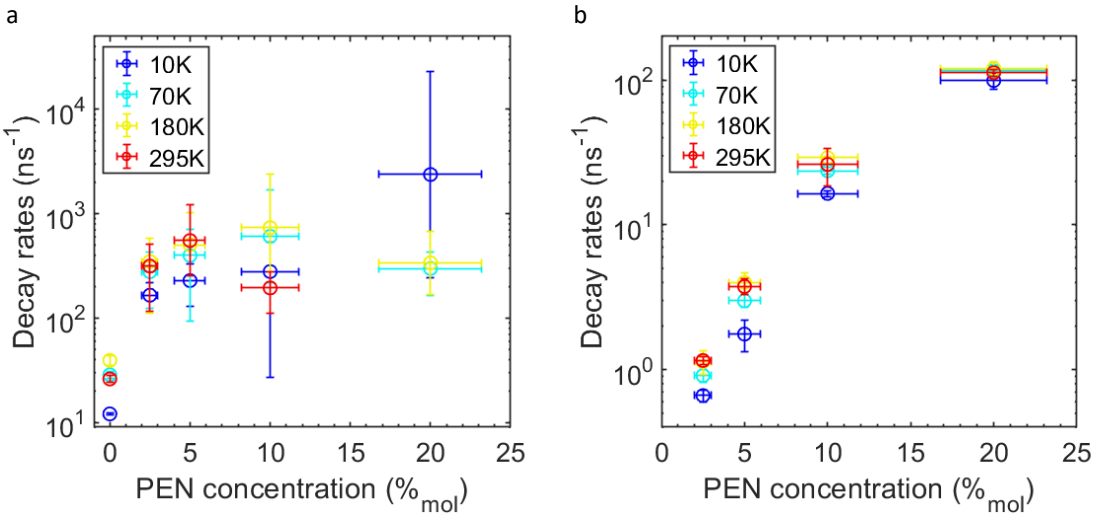

Figure 8.6.: Decay rates of the ADT (a) and PEN (b) emission at different sample temperatures and mixing ratios were evaluated by applying GA as described in the text. Sample temperatures are given in the legend. Remember that in the case of neat ADT the used model and hence the resulting decay rates do not accurately describe the actual photophysics. The data in (b) are compared with a model based on FRET in Figure 8.8.

of the free exciton emission and excimer emission in ADT and due to strong spectral changes with time, the model applied to neat ADT in this chapter is insufficient to correctly describe the entire photophysics behind the data of neat ADT. Note that in case of the neat PEN film. the photophysics is known to be dominated by singlet fission on a sub-picosecond timescale [80, 81, 193, 194], which is far below the instrument response of the present TRPL setup. This results in the luminescence of neat PEN being quenched almost entirely, making an analysis with TRPL impossible. Hence, the data of neat PEN are omitted in the following.

In Figure 8.6 the decay rates of the ADT and PEN emission resulting from GA [121] of the TRPL data are shown for different sample temperatures. If the decay rate is above 500 ns^{-1}, the luminescence mostly decays during the instrument response time and hence the corresponding values have to be treated carefully. While no clear trend can be found for the decay of ADT luminescence upon changes in temperature or mixing ratio due to the decay occurring within the instrument response time for all mixing ratios and sample temperatures, a clear trend in decay rates can be found for the PEN luminescence. For the latter, the luminescence decays significantly faster at higher PEN concentrations. Additionally, it can be speculated about a weak trend to higher decay rates with increasing temperatures, which, however, is not truly continuous and in many cases the errorbars of different temperatures overlap.

8.4. Discussion

The photon energy of the excitation in the PL experiments was chosen at a point where ADT is the dominantly absorbing material. Hence an initial excitation of almost exclusively ADT can be expected. Considering this fact, it is surprising that the emission spectra of all mixtures are strongly dominated by PEN emission and only weak traces of ADT emission are found. Even more striking is the fact that the excimeric emission of ADT is not visible at all in the mixtures. This can be rationalized since excimers generally have a high quenching rate, which means a low luminescence yield [23, 79]. At the same time, the emission spectrum of the excimer has a pronounced spectral overlap with the absorption features of PEN (see Figure 8.7), suggesting efficient FRET from the excimer to PEN, hence drastically reducing the lifetime of the excimer [196, 197]. In Appendix B the average distance of the initially excited ADT molecule to the closest PEN molecule is estimated to be around 1.363 nm for the mixture with only 2.5 % PEN, a value small enough to explain the suppression of ADT excimer luminescence in mixtures exclusively by FRET to PEN molecules. Unfortunately, the strong suppression of ADT excimer luminescence in mixtures means that it is not possible to track the time-dependent luminescence of the excimers in the mixtures, prohibiting us to experimentally track the energy transfer from ADT excimers to PEN with TRPL. As will be discussed later, also the ADT free exciton, which is a state comparable to the precursor of the excimer, transfers its energy extremely efficient to PEN. For the excimer, this means that energy transfer to PEN not only competes with the luminescent decay of the excimer, but also with the initial formation of the excimer on a sub-picosecond scale [26, 170]. This potential competition between excimer formation and energy transfer to PEN could reduce the excimer formation yield. Note that detecting a very weak ADT excimer luminescence in the mixtures might also be difficult since PEN luminescence is spectrally overlapping with the potential ADT excimer emission in the mixtures. Since clear excimer luminescence has been found in ADT:6Ph and ADT:TET mixtures [155], it is very unlikely that the fate of the excimer is strongly influenced by the structural changes introduced by the incorporation of PEN. Instead, due to the high bandgap of 6Ph and TET, FRET from the ADT excimer to these molecules is not possible, explaining why excimer luminescence is not suppressed in these systems.

Next, the other emission feature of neat ADT, which is the free exciton emission, is analyzed in the neat ADT film and the mixtures. Here, one realizes a strong reduction of the feature's luminescence in mixtures compared to the neat film. Importantly, in contrast to the excimer emission, the emission of the free exciton is still visible in the mixtures, which allows a deeper analysis of the photodynamics. Using GA to fit the ADT

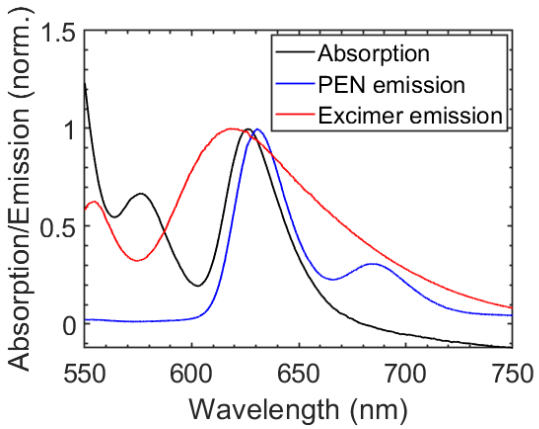

Figure 8.7.: Normalized absorption spectrum of a mixture with 20 % PEN (Absorption), normalized emission spectrum of the mixture with 2.5 % PEN (PEN emission) and normalized emission spectrum of neat ADT (Excimer emission). Note that the spectral shape of the PEN absorption and PEN emission does not change significantly between the mixtures containing 20 % PEN and less (see Figure 8.2). The emission signatures of the ADT excimer and of the PEN emission strongly overlap with the absorption features assigned to PEN, suggesting efficient FRET in both cases.

free exciton emission feature of the TRPL data with a monoexponential decay, it can be clearly seen that the decay rates drastically increase when moving from neat ADT to the mixtures (Figure 8.6a). Although the decay dynamics of neat ADT are not described properly by the monoexponential fit, especially at lower temperatures due to trap state population [44], the increase in decay rates when moving from neat to mixed films is so drastic that it cannot be assigned solely to the use of an incomplete model. Instead, energy transfer from ADT to PEN is available as an additional decay channel for ADT excitations in mixtures compared to neat ADT. Since ADT and PEN intermix and the energy transfer to PEN is energetically favorable, the channel is expected to be efficient (Binary films of ADT and a lower bandgap compound forming a phase-separating system are discussed in Chapter 9). In the statistically mixing system, it is expected that the energy transfer from ADT to PEN becomes more efficient with increasing amounts of PEN in the mixtures, since higher PEN concentrations result in more proximate PEN molecules available for possible energy transfer. Unfortunately, it is only possible to speculate about this mixing-ratio dependent trend using the data in Figure 8.6a, since the decay rates of all mixtures are on the order of 1 ps^{-1} (10^3 ns^{-1}), which equals a time frame shorter than the instrument response. This fact is also responsible for the large errorbars in Figure 8.6a. In addition, the large errorbars prohibit a deeper analysis of the energy transfer, for example by employing a model of diffusing excitations, which,

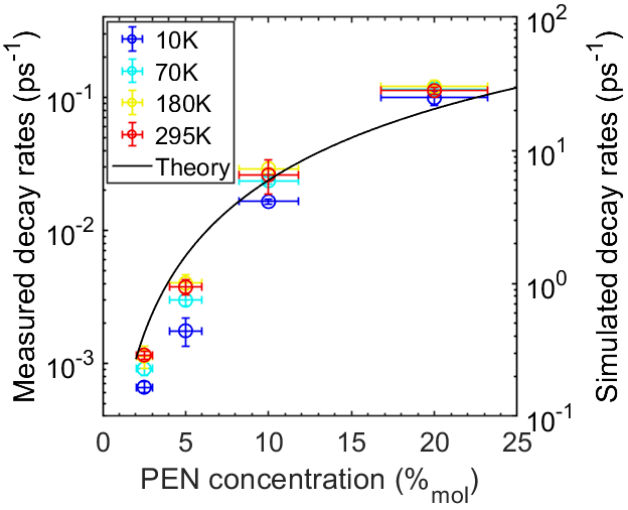

Figure 8.8.: Experimental decay rates of the PEN emission at different sample temperatures and mixing ratios are replotted from Figure 8.6b. Sample temperatures are given in the legend. Additionally, the simulated decay rates based on the model described in Appendix B are shown. Note that a factor of 250 lies between the y-axis of the simulated (right y-axis) and measured (left y-axis) decay rates. The reasons for this difference are discussed in the text.

in agreement with our data, would result in lifetimes below the instrument response function for all mixtures [49].

Summing up, a complete change is found in the photophysics of mixtures of ADT and PEN compared to the photophysics of neat ADT. While in neat ADT the free exciton emission decays due to singlet fission with a rate of 40 ns^{-1} and with an even lower rate at low temperatures due to trap state population [44], the ADT free exciton emission decays more than an order of magnitude faster in the mixtures due to ultrafast energy transfer to PEN, meaning that the free exciton decay channels intrinsic to neat ADT play an insignificant role in the mixtures. The same is the case for the ADT excimer, the luminescence of which is quenched drastically by energy transfer to PEN in the mixtures, making it impossible even to detect excimer luminescence in the mixtures.

Since we determined that the ADT excitations predominantly decay by energy transfer to PEN in the mixtures, an analysis of the decay pathways of excited PEN molecules in the mixtures is of interest. Excitations in bulk phase PEN are known to predominantly decay via singlet fission on a sub-picosecond timescale [80, 81, 193, 194]. Although neither luminescence from the resulting triplets nor luminescence from the triplet-pair state of PEN are visible in the present data, since these features are located at lower photon energies [30, 158], PEN singlet fission is still considered to be the dominant lumines-

cence quenching channel in the mixtures based on literature [45, 92, 146]. However, since PEN singlet fission is a multimolecular process, two neighboring PEN molecules are needed [92, 146]. Hence, luminescence quenching by singlet fission is only expected for PEN molecules at lattice sites that additionally have a directly neighboring PEN molecule. For isolated PEN molecules, i.e. PEN molecules that are surrounded by ADT molecules, PEN luminescence is expected to be a more relevant decay channel [92]. Consistent with this idea, PEN monomer luminescence is the dominant contribution to the PL spectra of the mixtures. With this in mind, the following model is used to understand the decay of PEN luminescence. Excited isolated PEN molecules transfer energy to proximate PEN molecules via FRET [197]. Due to the isolation of the initially excited molecule and the strong spectral overlap of PEN emission and PEN absorption (Figure 8.7), FRET is assumed to be the dominant energy transferring mechanism on this length scale [53]. The accepting molecule can then either be isolated as well, meaning that the situation is the same as before, or the energy accepting molecule can be part of a PEN agglomerate and hence have one or more PEN neighbors. In the latter case, the model assumes singlet fission to occur, which quenches the luminescence at this site [146]. More details on the model can be found in Appendix B, which provides the relation

$$k_{\mathrm{qu}} \sim c \left(1 - (1-c)^4\right) \tag{8.1}$$

between the PEN emission quenching rate k_{qu} due to FRET to PEN agglomerates followed by singlet fission and the molar PEN concentration c in the sample. While this relation describes the mixing ratio dependent evolution of the PEN emission decay rates well over the entire investigated concentration range (see Figure 8.8), the applied model can also be used to predict numeric values for k_{qu}. Here, the prediction is wrong by a factor of about 250 (compare right and left y-axis in Figure 8.8), which is most likely due to the approximation of $\kappa^2 = 2/3$ and approximating the crystal as a gas of same density, which breaks down at short FRET ranges. It might also be that the volume, in which no other PEN molecule is allowed to be for the molecule to count as isolated, is misjudged in the simulation. Since the applied model describes the change in PEN decay rates with changing mixing ratios well, it can be considered unlikely that singlet heterofission, starting with a PEN singlet state and ending with one ADT triplet and one PEN triplet, plays a significant role [87]. Especially at low PEN concentrations, where the PEN monomer excitations maintain relatively long, a significant contribution of singlet heterofission would boost the decay rates to a value that cannot be described solely by FRET to PEN agglomerates, which the applied model, however, does.

Lastly, the temperature dependence of the decay rates of the PEN luminescence has to

be discussed. While for higher PEN concentrations there is no clear dependence of the decay rate on temperature, at lower PEN concentrations there might be an indication of the decay rates increasing with temperature (Figure 8.8). Although it has no explicit temperature dependence, this can be explained by the FRET mechanism in the following way. At higher PEN concentrations, the probability of a PEN molecule being isolated is relatively low (e.g. for 10 % PEN this probability is only 66 %), meaning that the chances of the first FRET transition ending at an agglomerate, and undergoing singlet fission there, is high. Due to intermolecular interaction the spectral shape of the absorbance of a PEN agglomerate is relatively broad and slightly redshifted compared to isolated PEN molecules, leading to a good spectral overlap with the emission spectrum of isolated PEN molecules at all temperatures. In the case of low amounts of PEN, however, the probability of a PEN molecule being isolated is high, which makes it more likely that multiple FRET transitions between isolated PEN molecules occur before an excitation is transferred to an agglomerate. This means that FRET between two isolated molecules plays a more important role in the samples with low amounts of PEN. In this transition the emission spectrum is slightly redshifted compared to the absorbance due to the Stokes shift [197]. Hence, the overlap between the absorption and emission spectrum is higher the broader the spectra are. One effect broadening both spectra is thermal broadening, which is stronger at higher temperatures. Hence FRET between two isolated PEN molecules is expected to be more efficient at elevated temperatures. This temperature-dependent effect plays an insignificant role for FRET from an isolated PEN molecule to a PEN agglomerate, since in an agglomerate the Davydov splitting leads to a broadening and a redshift of the absorption spectrum. One more temperature dependent effect is the population of trap states in thin films. Energy transfer from these states to a neighboring isolated PEN molecule is upward in energy, which means that this process has to be thermally activated. As stated earlier on, these arguments only hold for energy transfer between two isolated PEN molecules and not for transfer from an isolated PEN molecule to a PEN agglomerate, explaining why the temperature dependence of the PEN emission decay rates is more pronounced in mixtures with low amounts of PEN.

8.5. Conclusion

In this chapter mixtures of ADT and PEN have been investigated. It was found that already small amounts of PEN change the photophysics of ADT drastically. While the photophysics of neat ADT is dominated by the parallel channels of singlet fission and excimer formation [30, 44, 155], the admixture of very small amounts of PEN already results in energy transfer from ADT to PEN clearly outcompeting singlet fission and

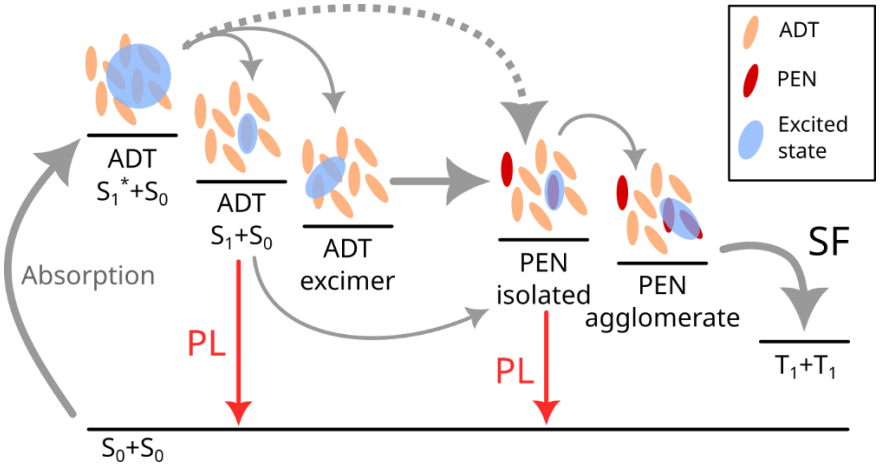

Figure 8.9.: Sketch of the photophysical model for the ADT:PEN mixtures. After photonic excitation, a precursor state can either relax to the free exciton or form an excimer. Both these states then efficiently transfer energy to PEN molecules, leading to a strong quenching of ADT luminescence. Excited isolated PEN molecules transfer their energy to PEN agglomerates, where singlet fission takes place. The energy transfer from the ADT free exciton to PEN and the energy transfer from isolated PEN to PEN agglomerates was recorded by their PL fingerprints (red arrows). An ultrafast energy transfer from the ADT precursor state to PEN is expected as well but could not be resolved based on the present data. Figure reprinted from Ref. [172].

fully quenching excimer luminescence. After the energy transfer to PEN, the excitation decays via singlet fission in PEN [92, 146]. Excited isolated PEN molecules, which are no singlet fission sites, transfer energy to proximate PEN molecules until the excitation ends up at a PEN agglomerate, where singlet fission can occur. The PEN concentration dependence of the energy transfer to agglomerates is well described by a simulation, which assumes FRET to be the driving force. The full photophysical model found for the ADT:PEN blends, starting as the precursor state prior to ADT excimer formation and ending with PEN singlet fission, is sketched in Figure 8.9. Lastly, the temperature dependence of the energy transfer from isolated PEN to agglomerates has been investigated and it has been found that, in case of low amounts of PEN, the energy transfer is slightly more efficient at elevated temperatures, which can be assigned to increased spectral overlap of emission and absorbance at elevated temperatures due to thermal broadening.

Importantly, it was shown that already very small amounts of PEN lead to ultrafast energy transfer to PEN followed by efficient exciton transport between PEN molecules, which might help in the design of devices, which use different materials for photon harvesting and exciton transport [188].

9. Results III: Excited-state delocalization and singlet fission

In this chapter, the fate of the triplet-pair state in ADT is investigated. It is based on Ref. [198], which was published in collaboration with M. Gerhard's research group (Marburg, Germany) and J. Pflaum's research group (Würzburg, Germany).

Finding and understanding ways to manipulate the quantum mechanical steps of singlet fission is an important step in bringing singlet fission toward application [18]. This refers to both steps of singlet fission, the initial formation of the triplet-pair state as well as the second step, triplet separation, where two independent triplet excitons are produced from the triplet-pair state. For example, the first step, triplet-pair state formation, is the more important one for the application of singlet fission in solar cells [83], while triplet separation is the crucial step for applying singlet fission in regards in which quantum mechanical entanglement plays the crucial role, such as quantum computing [20]. A common way to manipulate the singlet fission dynamics in aggregates is by changing the molecular arrangement in the unit cell. This can be achieved by chemical modifications of the molecule [39, 43, 44, 199–201] or by changes in the growth conditions [45, 47, 48, 92, 94, 128, 135, 200–202], which both potentially lead to changes in the unit cell structure and hence in the molecular arrangement. Most studies following this idea support the expectation that the triplet-pair state formation rate can be increased by increasing the structural order [39, 44, 47, 200, 201] and the intermolecular coupling [43, 48, 199, 201, 202].

These experimental results can be explained by current theoretical models, which link strong intermolecular interaction to a higher admixture of the diabatic CT state to the adiabatic singlet state, S_1 [203–205]. Since singlet fission is mediated by CT states [81], the higher admixture of the diabatic CT state promotes triplet-pair state formation [81]. The reason why high structural order is beneficial for triplet-pair state formation is because structural defects lead to exciton migration ending at energetically low-lying trap sites at which the exciton can be inaccessible for singlet fission [44].

For the second step, separation of triplets from the triplet-pair state, the electronic coupling between the two triplets in the triplet-pair state is expected to be in the same

energy range as the thermal energy at room temperature for typical singlet fission materials [83]. Hence, energy fluctuations of this order, e.g. by static or dynamic disorder, can be catalysts for enhanced triplet separation [84, 206–209].

In the following chapter, binary films of the singlet fission material ADT and the low band gap material ZnPC are prepared and the phase-separation between the compounds is used to introduce mesostructural changes into the ADT crystallites. The results of a structural and morphological investigation of the samples allow us to introduce a growth model that can explain the photophysical changes resulting from the introduction of ZnPC into the ADT films. The most important photophysical changes are a suppression of excimer luminescence in all binary films and the visibility of luminescence from the triplet-pair state, ^{1}(TT) luminescence, in binary films with small ADT fractions. Interestingly, ^{1}(TT) luminescence is only visible in binary films, that also maintain a high excited-state delocalization, which was extracted from the spectral shape of the PL spectrum, over time. Both findings, the visibility of the ^{1}(TT) luminescence and the high excited-state delocalization, can be linked to an increased structural order in the corresponding samples.

9.1. Structural characterization

For the structural characterization of the neat and binary films of ADT and ZnPC, XRD has been used. In Figure 9.1 GIWAXS data of the films are shown. The three vertically extended peaks at q_{xy} values of 1.36, 1.66 and 1.96 Å^{-1} for neat ADT confirm the preferred standing-up orientation with an in-plane herringbone arrangement [122, 126], which was analyzed in more detail in Chapter 7. Neat ZnPC shows a vertically extended peak at $q_{xy} = 1.85$ Å^{-1} and a peak at $q_{xy} = 1.0$ Å^{-1} and $q_z = 0.55$ Å^{-1}, which both agree well with the meta-stable α-phase that is known to dominate thin films of ZnPC [150–152]. The XRD features found in neat ZnPC are also present in the binary films and both features continuously lose intensity with increasing amounts of ADT. Since the features do not change position and shape upon the addition of ADT, it can be concluded that the ZnPC crystallites are not affected by the presence of ADT which is a first sign of phase-separation between the two compounds [210, 211]. A phase-separation is also in line with the evolution of the ADT features with changing mixing ratios although less obvious in this case since the ADT features in binary films are different to those in the neat ADT film. While the neat ADT film has vertically extended peaks at distinct q_{xy}-values, the ADT features in the binary films are diffraction rings at distinct values of $q_r = \sqrt{q_{xy}^2 + q_z^2}$. The values at which ring-like diffraction features can be found in the binary films are $q_r = 1.36$ Å^{-1}, $q_r = 1.66$ Å^{-1} and $q_r = 1.96$ Å^{-1} and in some cases

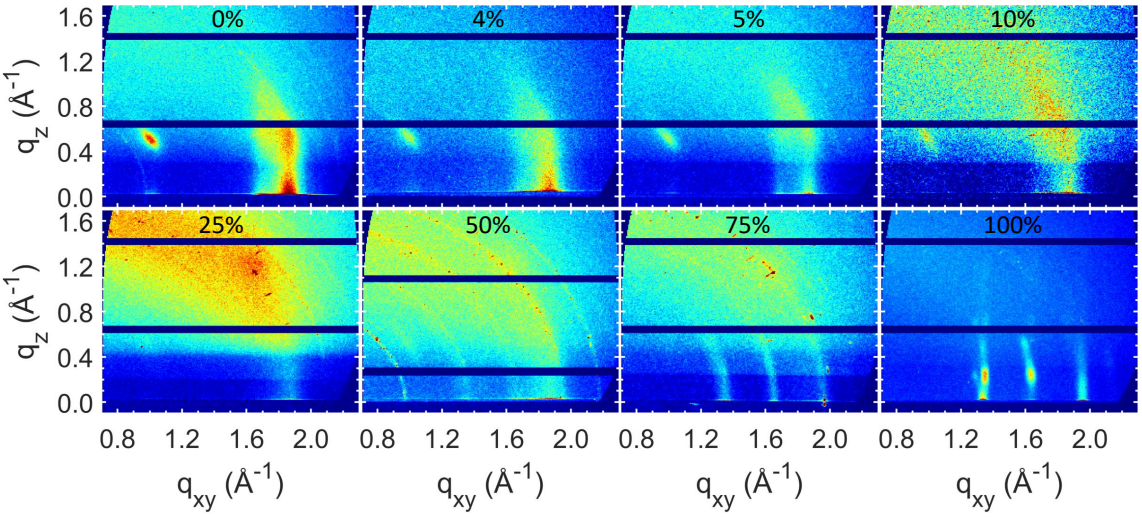

Figure 9.1.: The GIWAXS q-maps of the binary films show coexisting features of neat ADT and neat ZnPC. In binary films, the ADT crystallites lose their preferred standing-up orientation, resulting in ring-like features. ADT concentrations of the films are given in mol-% in each panel.

at $q_r = 0.95\,\text{Å}^{-1}$ and $q_r = 2.15\,\text{Å}^{-1}$. The shape and position of all these features can be explained with the structure known from the ADT thin film [122, 126] and a powder-like orientation of the crystallites, i.e. a loss of the uniaxial anisotropy of ADT in binary films [212]. With this assumption, the Bragg peaks at $q_r = 1.36\,\text{Å}^{-1}$, $q_r = 1.66\,\text{Å}^{-1}$, $q_r = 1.96\,\text{Å}^{-1}$, $q_r = 0.95\,\text{Å}^{-1}$ and $q_r = 2.15\,\text{Å}^{-1}$ can be assigned to the (110), (020), (120), (002) and (200) reflection, respectively. Since the position and shape of the Bragg peaks assigned to ADT is the same in all binary films and the intensity gradually decreases with decreasing amounts of ADT, also the investigation of these features is in line with a phase-separation of ADT and ZnPC [210, 211]. In films with 10 % ADT and less, the intensity of the ADT features drops below the scattering background, resulting in only the ZnPC features being visible in the according q-maps.

The XRR curve of neat ADT (Figure 9.2a) shows two Bragg peaks at 0.44 and $0.88\,\text{Å}^{-1}$, which are both distorted in shape due to the coexistence of thin film and bulk phase [126] as explained in Appendix E. Neat ZnPC exhibits one distorted Bragg peak at $0.50\,\text{Å}^{-1}$, which is in line with the known domination of the α phase in thin films of ZnPC [150–152]. In all binary films, this peak is visible, again indicating a phase-separation of the two compounds since the addition of ADT does not influence the shape and position of the ZnPC feature. The fact that the Bragg peaks of ADT are not visible in the scans of the binary films can be rationalized by the loss of uniaxial anisotropy, which drastically reduces the intensity of Bragg peaks in XRR. Remember that the (002) peak of ADT, which

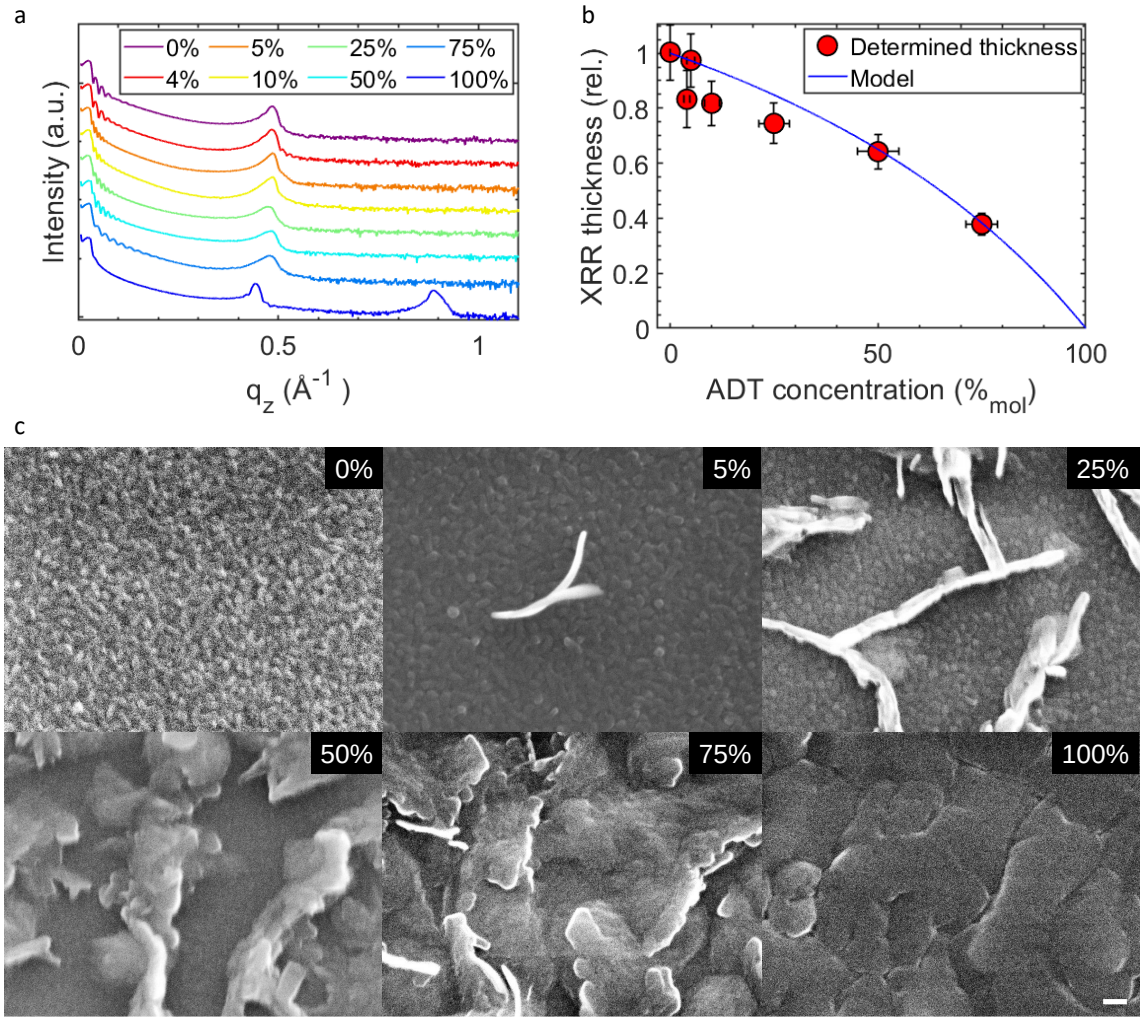

Figure 9.2.: (a) The XRR scans of the binary and neat films show Bragg peaks and, except for neat ADT, strong Kiessig fringes. ADT concentrations are given in mol-% in the legend. (b) Film thickness calculated based on the Kiessig fringes divided by the film thickness measured by the QCMs during film preparation. The blue line indicates the share of the total thickness covered by the ZnPC compound. The line is nonlinear because of the differences in volume per molecule between ADT and ZnPC (see Chapter 6). (c) The SEM images show needle-like crystallites on a smooth surface in case of the binary films. The scale bar in the lower right corner is valid for all images and equals 100 nm. ADT concentrations of the films are given in mol-% in each image.

is visible in XRR scans of neat ADT, is visible as a ring in the GID map of the binary film with 50 % ADT, proofing that the same crystalline structure is still present (Figure 9.1). Summing up the structural analysis with XRD, ADT and ZnPC phase-separate and ADT loses its uniaxial anisotropy when going from the neat film to binary films, while the ZnPC crystallites seem not to be affected by the presence of ADT in binary films. This model will be confirmed during the analysis of the absorbance spectra below, but before that, the morphology of the films is explained briefly.

The spacing of the Kiessig fringes in the XRR scans (Figure 9.2a) was used to calculate the thickness of the films and the result was divided by the thickness measured by the QCMs during growth (Figure 9.2b). Note that neat ADT shows no Kiessig fringes and hence no thickness could be calculated from XRR. Surprisingly, this ratio is not around a value of 1 for all films, but decreases with increasing amounts of ADT. From the QCM data during preparation the contribution of only the ZnPC compound to the overall thickness can be calculated and this contribution describes the evolution of the thickness determined by the Kiessig fringes reasonably well (blue line in Figure 9.2b). This suggests a morphological model in which ZnPC forms a smooth layer covering the substrate and surrounding the pronounced ADT islands. The SEM images of the films (Figure 7.1c) also show needles in a smooth layer for the binary films, supporting the proposed morphology.

Note that one would expect a different morphology and structure if a bilayer of the two compounds would be prepared instead of co-evaporating, because in the former case, ADT would be expected to form more dulled needles and a have better surface coverage, comparable to a neat ADT film [58]. In other words, the co-evaporation of ADT and ZnPC influences the growth of the compounds although phase-separation occurs. Further theoretical details on this topic can be found in Appendix C.

9.2. Optical characterization

The absorbance spectrum of ADT with the Davydov splitting of the $S_0 \rightarrow S_1$ transition at 2.3 eV and a vibronic progression at higher energies is in line with the in-plane herringbone arrangement and has been discussed in more detail in Chapter 7. For neat ZnPC, the high absorbance in the low-energy range is characteristic in thin films [147] and its spectral shape confirms the domination of the α-phase [213]. All binary films are also dominated by absorption attributable to ZnPC, which loses intensity with increasing amounts of ADT and shows minor changes in spectral shape which can be assigned to subtle structural variations in the ZnPC grains [213]. Absorption features assignable to ADT can also be found in the spectra of the binary films with high amounts of ADT

and no clear spectral change or shift is observed. The visual shifts of the peak position of the ADT absorption can be assigned to an overlap with the high-energy tail of the strong ZnPC absorption. In the films with low amounts of ADT, it is almost impossible to disentangle the ADT absorption features from this high-energy tail. Since neither the ZnPC absorption features nor the ADT absorption features show strong spectral changes between the binary films besides a change in intensity, also the absorbance spectra are in line with a phase-separation of ADT and ZnPC. The decrease in absorption strength when moving from the neat ADT film to the binary films is surprisingly high. Although it is hard to disentangle the ADT absorption features from the ZnPC absorption tail in binary films, it can be roughly estimated that the binary film with 75 % ADT only has roughly 50 % of the ADT absorbance strength of the neat film instead of the expected 62 % (One would not expect 75 % of the absorption strength since film thickness was kept constant and not the total number of molecules, which results in films having a higher total number of molecules the higher the molar fraction of the smaller ADT molecule, see Figure 9.2b). This surprisingly low ADT absorption strength once more confirms the powder-like orientation of the ADT crystallites in binary films based on the following argumentation. In the used geometry, the incident light is unpolarized and normal to the sample surface while the ADT molecules have their TDM oriented roughly along their short molecular axis (DFT calculations in Appendix E). For the neat ADT films with uniaxial anisotropy, this means that the light polarization and the ADT TDM are almost in the same plane for all grains, while in the powder-like case the TDMs of ADT molecules are oriented randomly with respect to the polarization of the incident light, resulting in a reduced absorption strength.

The small band gap of ZnPC makes a selective excitation of ADT impossible in PL experiments, *inter alia* due to energy transfer from ADT to ZnPC. Crucially, bulk phase ZnPC does not show luminescence in the investigated spectral region (Figure 9.3b) [93], which enables an assignment of most spectral features present in the binary films to ADT. The small sharp peaks visible in the spectrum of neat ZnPC are Raman peaks [214]. While neat ADT shows the free exciton emission at 2.27 eV (marked FE in Figure 9.3b) and excimer emission at 2.02 eV (marked EX in Figure 9.3b), binary films are dominated by the free exciton emission and excimer luminescence is not visible in the corresponding spectra. However, this makes other spectral features in the low-energy range visible, which are namely a vibronic replica of the free exciton emission at 2.1 eV (FE* in Figure 9.3b), luminescence from the triplet-pair state at 1.97 eV (TT in Figure 9.3b) with a vibronic replica at 1.80 eV (TT* in Figure 9.3b) and luminescence from electronically isolated ZnPC molecules (the reason for the existence of isolated molecules in a phase-separating system is explained in Appendix C) at 1.78 eV (ZnPC in Figure 9.3b). The

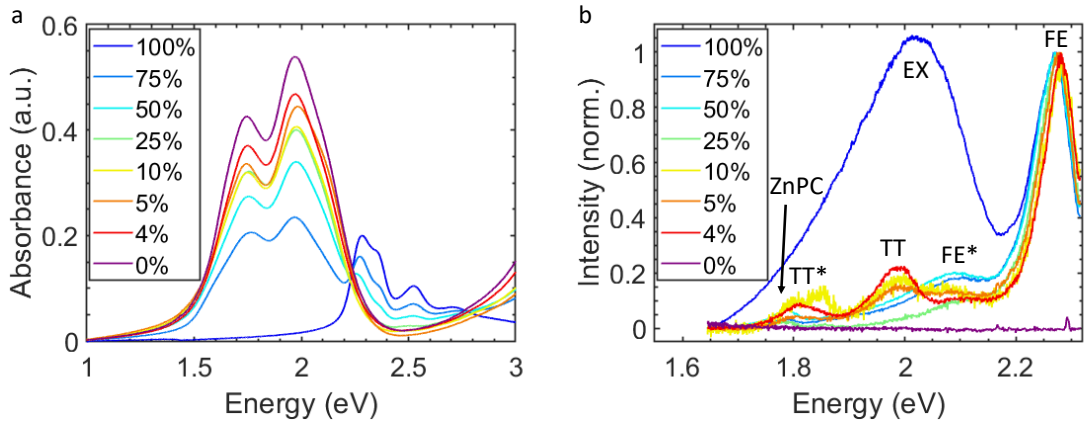

Figure 9.3.: (a) The absorbance spectra of neat and binary films of ADT and ZnPC are set to 0 at 1 eV. Neither the ADT nor the ZnPC features clearly shifting with changing mixing ratios confirms phase-separation. (b) The PL spectra of the neat and binary films are normalized with respect to the free exciton emission (FE). The photon energy of the exciting laser was 2.33 eV. The ADT concentrations are given in mol-% in the legend. In the binary films, the ADT excimer luminescence (EX) is suppressed and the vibronic replica of the ADT free exciton emission (FE*), and, depending on the ADT concentration, triplet-pair state emission (TT) and its vibronic replica (TT*), or monomeric ZnPC emission (ZnPC), becomes visible.

proposed peak assignments will be justified in the discussion part.

For a phase-separating system, there are surprisingly strong spectral differences between the binary films. One is that the intensity ratio between the free exciton emission and its vibronic replica is higher for films with low amounts of ADT. A second difference is the visibility of the triplet-pair state emission, which is only visible in binary films with low amounts of ADT and in samples, in which the triplet-pair state emission is visible, also its vibronic replica is present at lower energies.

9.3. TRPL spectroscopy

To better understand the PL spectra, TRPL spectroscopy has been employed, which resolves the luminescence not only spectrally but also temporally. Hence it is possible to separate the features based on their luminescent lifetime. Note that for a better signal-to-noise ratio, the TRPL measurements were carried out at 200 K sample temperature, a temperature at which the overall photophysics is barely changed compared to room temperature, but non-luminescent quenching is significantly reduced (Figure C.5 shows TRPL data at room temperature for comparison). The temperature dependence of ADT

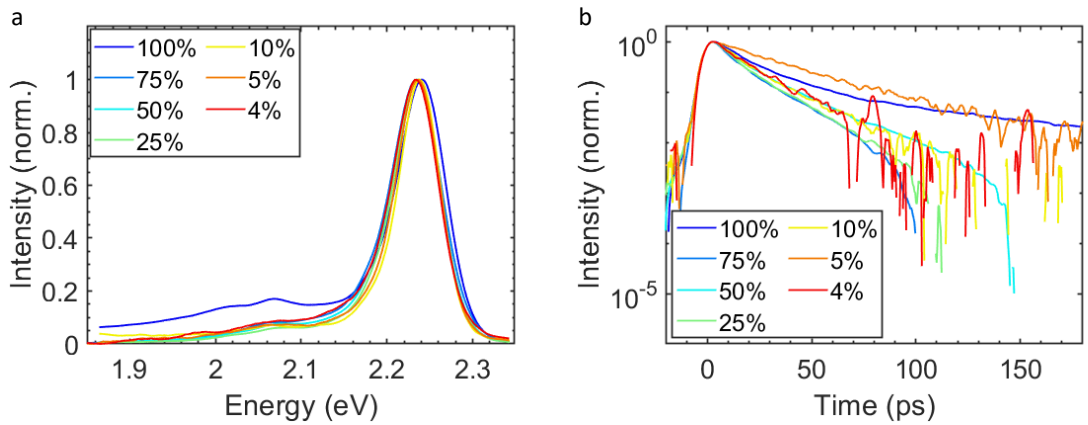

Figure 9.4.: (a) The spectra were extracted by time-integrating the TRPL data (Figure C.4) from 0 to 50 ps before noise filtering and normalizing the data. (b) The time traces were extracted from the TRPL data (Figure C.4) by spectrally averaging from 2.12 to 2.36 eV before noise filtering and normalizing. ADT concentrations are given in mol-% in the legend. The measurements were carried out at 200 K sample temperature and with a photon energy of the exciting laser of 2.58 eV.

luminescence will be discussed in detail in Chapter 10. The use of a different photon energy for excitation and the limited time frame of the TRPL setup after excitation leads to slight spectral shifts of the features in TRPL compared to the positions in steady-state. On short timescales (Figure 9.4a), the spectra are dominated by the free exciton emission, which peaks at 2.24 eV, and has a vibronic replica at 2.07 eV. The spectrum of neat ADT has a higher relative intensity in the low-energy range due to pronounced excimer emission in this range, which is not present to a comparable extend in the binary films (remember the excimer suppression in binary films proposed based on Figure 9.3b). In contrast to the steady-state spectra, where the ratio between the free exciton emission and its vibronic replica differs between the binary films, this ratio between the free exciton peak and its vibronic replica is comparable in all binary films at short times (compare Figure 9.4a and Figure 9.3b). Also, the vibronic replica has a lower relative intensity at short times (Figure 9.4a) compared to the steady-state (Figure 9.3b) in all binary films. No statement can be made in this regard for neat ADT due to excimer emission dominating the spectral region of the vibronic progression of the free exciton in all time domains.

Decay traces of the free exciton emission feature, which dominates all spectra at short times, are shown in Figure 9.4b and show a fast decay on a timescale of around 20 ps. With the exception of the film with 5 % ADT, the free exciton emission of the binary films decays slightly faster than in the neat ADT film. The decay constants will be analyzed more precisely later using GA [121].

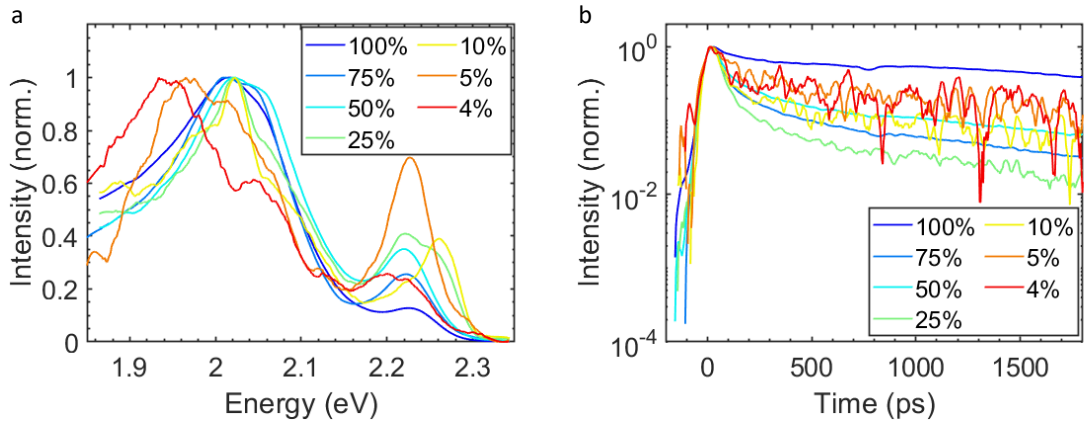

Figure 9.5.: (a) The spectra were extracted by time-integrating the TRPL data (Figure C.3) from 0.5 to 2 ns before noise filtering and normalizing the data. The redshift of the low-energy emission visible at low amounts of ADT is assigned to the presence of triplet-pair state emission. (b) The time traces were extracted from the TRPL data (Figure C.3) by spectrally averaging from 1.92 to 2.12 eV (> 5 % ADT), from 1.88 to 2.07 eV (5 % ADT) or from 1.85 to 2.03 eV (4 % ADT), depending on the sample, before noise filtering and normalizing. ADT concentrations are given in mol-% in the legend. The measurements were carried out at 200 K sample temperature and with a photon energy of the exciting laser of 2.58 eV.

The spectral shape of the luminescence looks drastically different at longer times (Figure 9.5a), in which redshifted features dominate the spectra instead of the free exciton emission. Note that the noisy spectra in combination with the application of a noise filter can lead to an artificial distortion of the peak shape. In all spectra, luminescence from the free exciton peak is visible, however, the spectral position and shape varies between the films, which might be due to luminescence from trap states. The focus of the analysis of the spectra at late times will be put on the feature at low photon energies, where the peak is found to shift from 2.02 eV to 1.94 eV with decreasing amounts of ADT. While the position is constant at 2.02 eV for the neat film and all binary films with more than 10 % ADT, it starts to continuously redshift at 10 % ADT and for the film containing 4 % ADT the peak position has shifted to 1.94 eV. Note that the shift of the film with 10 % ADT is hard to see, since the distorted peak shape results in the peak being at the same position as for films with higher amounts of ADT, however, the flanks of the peak indicate the redshift that is found for the center of mass of the peak.

Time traces of the dominant feature in the low-energy range are shown in Figure 9.5b, for which the spectral integration range depends on the sample as detailed in the figure caption. At short times, a fast decay of a part of the intensity is found in the time traces that can be assigned to the decay of the free exciton emission and its vibronic

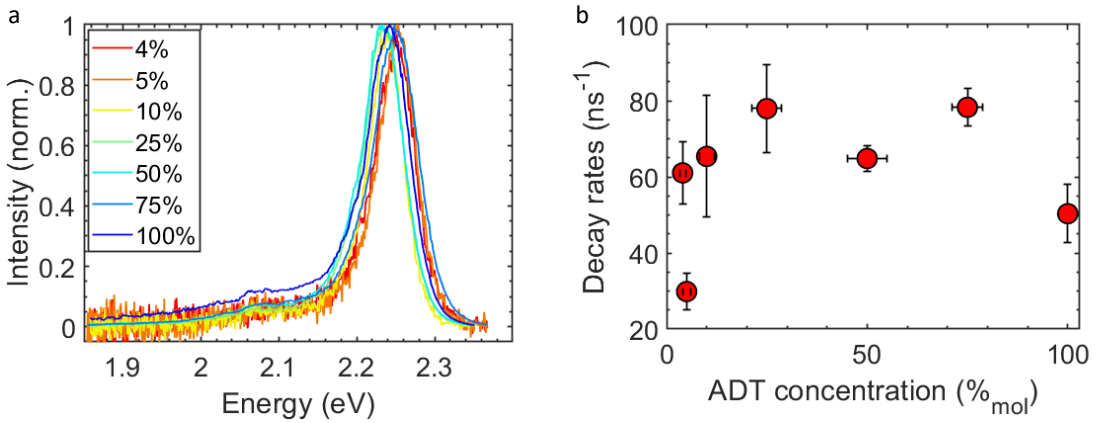

Figure 9.6.: (a) The spectra are calculated by a GA of the TRPL data in Figure C.4 with two decay species. The dominant, fast-decaying species is shown. ADT concentrations are given in mol-% in the legend. (b) The decay rates of the free exciton emission calculated by a GA with two species are assigned to the fast-decaying spectra shown on the left.

progression. At longer times, the decay slows down drastically, and the slowly decaying part can be assigned to the features visible in the low-energy range of the spectra of Figure 9.5a based on their long lifetime. Note that due to the presence of the fast decay of the free exciton emission in the time traces, the slope of the traces at longer times has to be used to compare the decay rates of the long-lived redshifted features and not the absolute intensity. A precise estimation of the decay rates will be extracted by the application of GA in the following.

For the decay rates of the free exciton emission, GA with two species has been applied to the TRPL maps in Figure C.4. While the rate of the fast-decaying dominant species is assigned to the decay of the free exciton, the second, slower decay is used to disentangle the signal of the free exciton emission from the weak contribution of the long-lived species. Since the TRPL maps are strongly dominated by the free exciton emission, which decays not perfectly monoexponentially due to effects such as SSA, TTA and trap state emission, it is hard to extract the decay of the species luminescent in the low-energy region by GA. In order to do that, GA has been applied to only the spectral region energetically below 2.12 eV of the TRPL maps shown in Figure C.3. With this selection, a large part of the intensity of the free exciton emission is cut out of the data on which the GA is applied and therefore the GA is more sensitive to the remaining spectral features.

The resulting spectra and decay constants assigned to the free exciton emission and the species causing redshifted emission are shown in Figures 9.6 and 9.7. The redshift of the long-living species with decreasing amounts of ADT is found in the TRPL data as well as in the spectra calculated by GA.

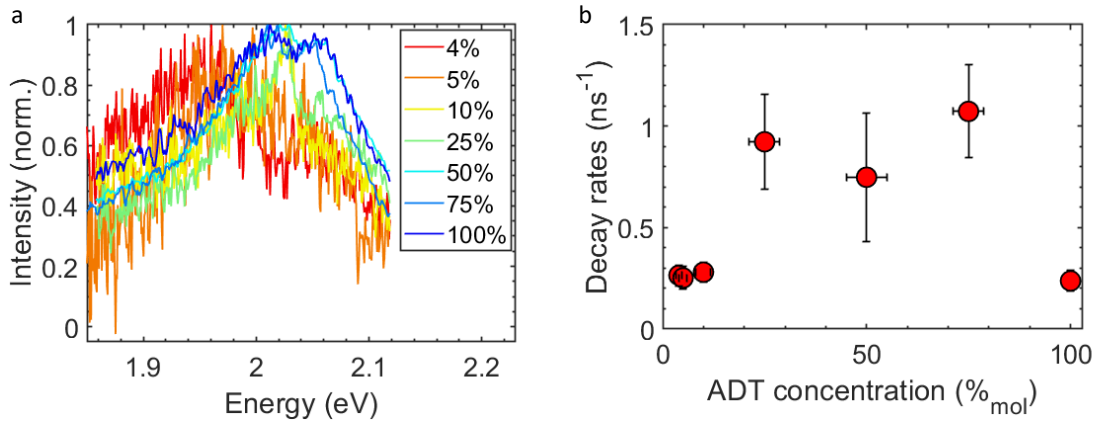

Figure 9.7.: (a) The spectra are calculated by a GA of the low-energy region (< 2.12 eV) of the TRPL data in Figure C.3 with two decay species. The long-living species, which cannot be assigned to the free exciton, is shown. ADT concentrations are given in mol-% in the legend. (b) The decay rates were calculated by a GA with two species and are assigned to the long-living species with the spectra shown on the left. At low amounts of ADT, a spectral redshift and a reduction of the decay rate are found.

For the decay rates, an interesting behavior is found with changing ADT concentration. In case of the fast decay rate assigned to the free exciton emission (Figure 9.6b) a slight increase of decay rates might be visible when moving from neat ADT to binary films, which, however, is speculative due to the increase being insignificant. The binary film with 5 % ADT has a surprisingly low free exciton decay rate, which might indicate problems with the thermal contact during the measurement or differences in the growth conditions that might lead for example to a higher amount of ADT molecules in ZnPC grains (see section C for details), which would decrease the exciton decay rate. However, also in this film the absolute value of the free exciton decay rate is still high, strongly suggesting that also in this sample singlet fission is the dominant free exciton decay channel.

In the decay rates of the emission at low energies (Figure 9.7b) a clear trend can be found. Moving from neat ADT to binary films with more than 10 % ADT, a strong enhancement of the decay rate can be found. This is in the region where no spectral changes were found. When now moving from the binary films with more than 10 % ADT to those with 10 % ADT and less, the decay rate decreases again and this decrease in decay rate is accompanied by a spectral redshift of the corresponding emission feature.

9.4. Discussion

The proposed assignment of the peaks visible in the steady-state PL data (Figure 9.3b) is justified in the following. In Chapter 7 the assignment of the free exciton peak is explained based on the small Stokes shift, the spectral shape and the high decay rate due to singlet fission, and also a detailed discussion of the assignment of the low-energy peak in neat ADT to an excimer can be found there. While the free exciton emission is also present in the binary films with the same spectral shape and position, the excimer emission is suppressed in all binary films. The suppression of the excimer emission is a surprising result since ADT and ZnPC phase-separate and from single crystal PL data (Figure A.6b) it is known that excimer emission is possible without the presence of defects or grain boundaries. Contradicting to this fact, the main impact of the presence of ZnPC on the photophysics of ADT is expected to be based on changes in crystallite quality and the existence of grain boundaries between ADT and ZnPC. On the other hand, however, the redshift found for excimer emission with time in Chapter 7 might be due to excimer diffusion to grain boundaries, indicating that grain boundaries can indeed have an influence on excimer emission. With these findings from Chapter 7 in mind, the following reasoning can be found for the suppression of the excimer emission in binary ADT:ZnPC films. Compared to neat ADT, the ADT crystallites lose the uniaxial anisotropy in binary films, which means that at grain boundaries between two neighboring ADT crystallites it is highly unlikely that the long molecular axis of ADT molecules of two different crystallites are aligned. This means that, in contrast to films with uniaxial anisotropy, in case of ADT:ZnPC films the sites at grain boundaries are energetically unfavorable for excimers instead of being favorable [23, 26, 215–217]. Hence excimer emission from grain boundaries, that seems to play an important role in the excimer luminescence of neat ADT, is unlikely in binary films. An additional effect is the presence of ZnPC, which makes not only grain boundaries between two ADT grains possible, but also grain boundaries between ADT and ZnPC. In the latter case one can expect efficient ADT excimer quenching by energy transfer to ZnPC, since the spectral emission of the ADT excimer almost perfectly overlaps with the strong absorption of ZnPC (see Figure C.7). Both these effects combined explain the strong suppression of ADT excimer emission. Note that, although excimer emission is not visible in the steady-state PL spectra of the binary films, it can still occur and is in some cases even visible e.g. in some of the integrated TRPL spectra in Figure 9.5a.

The suppression of the excimer luminescence makes new peaks visible in this spectral range, which are assigned to a vibronic progression of the free exciton emission and to triplet-pair state emission and its vibronic progression in the following by the use of the

TRPL data. GA links the peak at 2.1 eV and the free exciton emission to the same decay constant (Figure 9.6a), which indicated that both features come from the same species. Additionally, the energetic spacing between the free exciton emission and the peak at 2.1 eV is with 0.17 eV exactly the energy of a characteristic vibration, which makes the peak clearly assignable to a vibronic replica of the free exciton emission.

In order to find out to which state the emission at 1.97 eV is linked, the decay rates and spectra assigned to the long-living component are used (Figures 9.5 and 9.7). The case of neat ADT has been analyzed in Chapter 7 and will be used as a starting point with its excimer emission peak at 2.02 eV and a decay rate of approximately 0.25 ns^{-1}. Moving from the neat film to binary films with 25 % ADT or more, no significant spectral change is found, and the decay rate assigned to the feature increases to around 1 ns^{-1}. Due to the same spectral shape as in the neat ADT film, the feature of these binary films is also assigned to excimer emission. The increased decay rate of the excimer emission in binary films compared to neat ADT can be explained by the following two arguments that have already been listed in context of the suppression of excimer luminescence in binary films. Grain boundaries seem to play an important role for the excimer luminescence in the nanosecond time domain [155] and the role of grain boundaries changes drastically when moving from the neat film to binary films as explained earlier. Additionally, energy transfer to ZnPC is an excimer quenching channel that is only available in binary films and increases the decay rate there. So far, only the films with more than 10 % ADT have been discussed, in which the emission feature at 1.97 eV is not visible in the steady-state. Moving on to the films with 10 % ADT and less, two changes happen at the same time, which are namely a continuous redshift of the emission with lowering amounts of ADT (Figure 9.5a) and, compared to the binary films with higher ADT concentrations, a decrease in decay rate of the feature to approximately 0.25 ns^{-1} (Figure 9.7b). Both, the redshift and the decrease in decay rate cannot be explained by still assigning the luminescence to excimer emission, since the same photophysical arguments should count for excimers in all binary films. Instead, the luminescence at low amounts of ADT is assigned to a different species, namely the ^{1}(TT) state. The assignment to the ^{1}(TT) state can explain both observations, the redshift and the decrease in decay rate, since on the one hand the decay rate of the ^{1}(TT) state is expected to be low [120, 208, 218, 219] and on the other hand the luminescence from the ^{1}(TT) state is expected to be located spectrally at 1.93 eV [30] based on the following calculation. Since luminescent decay from the ^{1}(TT) state is symmetry forbidden, a vibrational quantum has to be present for symmetry breaking [30, 220], resulting in the photon energy of ^{1}(TT) state emission being equal to two times the triplet energy minus the energy of one (characteristic) vibrational

quantum [30], i.e.

$$h\nu_{\mathrm{TT}} = 2 \cdot E(T_1) - \hbar\omega_{\mathrm{vib}} \approx 2 \cdot 1.05\,\mathrm{eV} - 0.17\,\mathrm{eV} = 1.93\,\mathrm{eV}. \tag{9.1}$$

The ADT triplet energy has been estimated based on the energy published for an ADT derivative [83] and the energy of the vibrational quantum was chosen to be 0.17 eV, since this is the vibronic spacing found in the absorption spectra and for the free exciton emission. Additionally, all films that show ^{1}(TT) state emission at 1.97 eV in the steady-state also show a weaker emission peak at 1.80 eV which can be assigned to a vibronic replica of the ^{1}(TT) state and is also exactly 0.17 eV below the ^{1}(TT) peak. Remember that, due to setup differences between TRPL and steady-state PL, the peak positions are not exactly the same in both measurements.

With the assignment of the ^{1}(TT) state emission and its vibronic structure, the last emission feature left to discuss is the peak at 1.78 eV, which is easiest to see in the binary films with more than 10 % ADT since it does not spectrally overlap with the vibronic progression of the ^{1}(TT) state emission there (in Figure C.8 the steady-state PL spectra are vertically offset to make feature identification easier). This feature is assigned to luminescence from ZnPC molecules that are incorporated into ADT crystallites [221]. This happens since entropic and kinetic limitations prohibit perfect phase-separation (see Appendix C for details) [58]. These ZnPC molecules that are surrounded by ADT are electronically isolated and are hence expected to behave comparable to ZnPC molecules in solution [148, 222] or in an isolating matrix [221]. For such systems, luminescence from ZnPC is found at energies comparable to 1.78 eV [221]. Note that the exact energy of the luminescence depends on the polarizability of the environment (Chapter 7), i.e. on the solvent or the material used for the isolating matrix structure.

Now, after justifying the assignment of all peaks visible in the PL spectra of the neat and binary films, a closer look will be taken into changes in spectral shape between the samples. For that, two important features will be tracked, which are the relative intensity of the vibronic replica of the free exciton peak compared to the free exciton peak itself, and the visibility of the ^{1}(TT) state emission. Starting with the relative intensity of the vibronic replica, the free exciton emission will be called 0-0 emission and its first vibronic replica 0-1 emission in the following, hence the intensity ratio between them can be written as $I^{0\text{-}0}/I^{0\text{-}1}$. This ratio can be linked to excited-state delocalization and the more delocalized the excited state is, the stronger $I^{0\text{-}0}/I^{0\text{-}1}$ deviates from its value in solution (Figure C.6a) [73, 74], where the molecules are isolated and hence the excitation located on one molecule. In all PL spectra of the binary films, $I^{0\text{-}0}/I^{0\text{-}1}$ has a higher value than in solution, which means that the excitation is delocalized over multiple molecules

in all cases and the higher $I^{0\text{-}0}/I^{0\text{-}1}$, the stronger the excited-state delocalization [73]. The fact that $I^{0\text{-}0}/I^{0\text{-}1}$ does increase with increasing excited-state delocalization and not decrease means that the free exciton emission is assigned to a J-type aggregation [73, 223]. In the steady-state PL, $I^{0\text{-}0}/I^{0\text{-}1}$ and hence the excited-state delocalization increases with decreasing amounts of ADT. This is best visible between the films with more than 25 % ADT compared to the film with 25 % ADT. Note that for films with less than 25 % ADT, ^{1}(TT) state emission is present and coupling the triplet-pair state to a typical symmetry breaking mode for Herzberg-Teller coupling (318 cm^{-1}) [224] ends at a photon energy of 2.07 eV for ^{1}(TT) state emission, which overlaps with the 0-1 emission. Also for neat ADT, $I^{0\text{-}0}/I^{0\text{-}1}$ cannot be estimated since the 0-1 emission overlaps with the dominant excimer emission of neat ADT. One possible explanation for the excited-state delocalization in ADT increasing with decreasing amounts of ADT, is that, counterintuitively, the crystallite quality of the ADT crystallites increases with decreasing ADT concentrations due to a reduced growth rate of the ADT compound. This idea is explained in further detail in Appendix C. Interestingly, differences in $I^{0\text{-}0}/I^{0\text{-}1}$ between the binary films can only be seen in the steady-state PL data, but not in the TRPL spectra extracted at short times (Figure 9.4a). In the latter spectra, $I^{0\text{-}0}/I^{0\text{-}1}$ is at roughly the same value for all binary films. And in all cases $I^{0\text{-}0}/I^{0\text{-}1}$ has a higher value there than in the corresponding steady-state PL spectra. In case of neat ADT, again, no statement can be made in this regard due to overlap with excimer emission. This means that, for binary films, the excited-state delocalization is equally high in all films during the first 50 ps and in all films the excited-state delocalization decreases after 50 ps. However, this decrease at longer timescales is different depending on the sample. The samples with high amounts of ADT show a stronger loss of excited-state delocalization at later times. The latter statement and the underlying working principle of the extraction of values of the excited-state delocalization on different timescales is supported and explained by the use of simulations incorporating singlet fission and the loss of excited-state delocalization with time in Appendix C.

As a last step in the discussion, differences in the singlet fission mechanism between the binary films are examined and brought into context of other photophysical and structural properties. The most intriguing insight the present data give into singlet fission in ADT comes from the luminescence of the singlet fission mediating ^{1}(TT) state. This luminescence is only visible in some of the binary blends, namely exclusively those with 10 % ADT and less, while all other films do not show ^{1}(TT) luminescence. This finding can be rationalized by a better crystallite quality at low ADT concentrations and would thereby be in line with the findings before considering the excited-state delocalization. From a theoretical perspective, it is expected that energy fluctuations, which can

be caused by static or dynamic disorder, cause localization of excited states [225, 226] and help to separate the triplets from the triplet-pair state [84, 85, 120, 206–209]. Hence a better crystallite quality would lead to an increased excited-state delocalization and hamper the separation of triplets from the triplet-pair state [84], making luminescent decay a competitive channel for the ^{1}(TT) state. Looking at this mechanism from the other perspective, at higher ADT concentration the higher density of trap states leads to an enhanced separation of triplets from the triplet-pair state [84], resulting in the luminescent decay being outcompeted by triplet separation. Remember that a growth model which explains how ADT crystallites of higher quality can be formed at lower ADT concentrations is given in Appendix C. This reasoning for the visibility of ^{1}(TT) luminescence is also well in line with the PL spectrum of ADT single crystals (Figure C.6b), in which an extremely high crystallite quality is expected and pronounced ^{1}(TT) luminescence is found. Note that the excited-state delocalization extracted from $I^{0\text{-}0}/I^{0\text{-}1}$ considers the S_1 state [73] while for ^{1}(TT) luminescence the fate of the triplet-pair state is crucial [30], which means that both parameters cannot be directly connected.

This is in principle different for the first step of singlet fission, the triplet-pair state formation, which starts in the S_1 state. However, the singlet fission rate of all binary films is higher than $20\,\mathrm{ns}^{-1}$, which means that the excited-state delocalization during this period has to be considered. This is done by taking a closer look into the spectra extracted during the first 50 ps (Figure 9.4a). As stated earlier on, in this period no difference in excited-state delocalization is found between the binary films, which means that no statement of the influence of changes in excited-state delocalization on triplet-pair state formation dynamics can be made with the present data. Looking into the decay rates of the free exciton, with the exception of the binary film with 5 % ADT, a minor, insignificant rise in decay rates might be present when moving from the neat film to the binary films. However, assuming this increase is true, it is more reasonable to assign it to energy transfer from the ADT S_1 state to ZnPC boosting the free exciton decay rate, since it works as an additional, parallel decay path in the binary films, than assigning it to an actual change in singlet fission rates.

9.5. Conclusion

In this chapter, binary films of ADT and ZnPC have been prepared and the two compounds have been shown to phase-separate. The addition of phase-separated ZnPC crystallites influenced the photophysics of the ADT crystallites in multiple ways. In binary films, the ADT crystallites lose the uniaxial anisotropy, leading to changes in the role of grain boundaries for the photophysics already at small amounts of ZnPC in the sample,

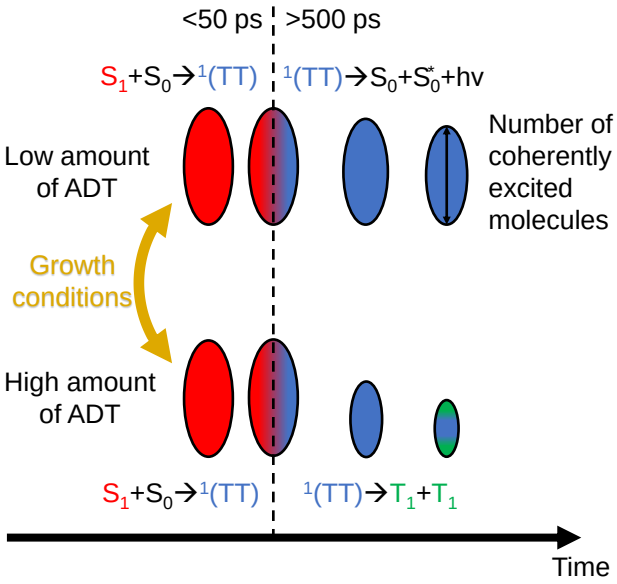

Figure 9.8.: Sketch of the photophysics of binary films of ADT and ZnPC. The size of the ovals qualitatively represents the number of coherently excited molecules. The time since initial excitation increases from left to right. During the first 50 ps after excitation, no difference in the photophysical behavior is found between the samples, and triplet-pair state formation is the dominant process in this time frame. However, after 500 ps, differences in the photophysics are found experimentally. While the binary films with low amounts of ADT maintain a higher excited-state delocalization and at the same time show ^{1}(TT) luminescence via Herzberg-Teller coupling (top part of the sketch), the films with higher amounts of ADT lose excited-state delocalization more rapidly and other decay channels (such as triplet dissociation) outcompete ^{1}(TT) luminescence (lower part of the sketch).

effectively leading to a suppression of excimer luminescence in binary films. Mesostructural changes of the ADT crystallites were introduced by the presence of ZnPC and led to changes in excited-state delocalization and triplet separation. A comparison of the intensity of the free exciton peak with the intensity of its first vibronic replica gives access to the excited-state delocalization and, while this parameter could not be influenced in the timescale of triplet-pair state formation, it was possible to increase the excited-state delocalization on longer timescales by reducing the amount of ADT in the film. Correlating to this result, no changes were found between the binary films for the first step of singlet fission, triplet-pair state formation, while for the second step, triplet separation, ^{1}(TT) luminescence was only found in samples which also exhibit a high excited-state delocalization. The photophysical model found in this chapter, including the correlation between excited-state delocalization and ^{1}(TT) luminescence, which is suggested to originate from differences in crystalline quality, is sketched in Figure 9.8.

10. Results IV: Impact of thermal energy on singlet fission

In this chapter, the impact of mesostructural changes on the temperature dependent photophysics of binary films containing ADT and HPhB is investigated.

The photophysics of solid organic materials can be strongly influenced by the sample temperature [55, 227]. This is due to multiple photophysically relevant properties changing upon changes in the temperature. One example is the presence of phonons, i.e. intramolecular or intermolecular vibrations, which can be activated by thermal energy [228, 229]. These vibrations facilitate intramolecular processes such as IC [230, 231], or multimolecular processes such as singlet fission [232, 233], energy transfer [197, 234] or excimer formation [235, 236]. Also the efficiency of endotherm processes, i.e. in which the product has a higher energy than the educt, increases with increasing temperature [237]. One more example of thermal effects is thermal restructuring, where the structure and hence the molecular arrangement changes with temperature, which again can influence the photophysics [93, 238].

For singlet fission, the relation between the efficiency of the process and the temperature is complex [136, 137, 232]. For example, phonons are known to play a critical role in symmetry breaking [239, 240] and energy matching of the initial singlet state and the triplet-pair state [45]. If the triplet-pair state is higher in energy than the singlet state, an increased temperature might be beneficial for singlet fission, but in this regard entropic considerations also play a critical role since singlet fission doubles the number of excitations and hence increases entropy [134]. In solid singlet fission materials with imperfections, the occupation of trap states, which is higher at lower temperatures, can be detrimental [44] or beneficial [47, 84] for singlet fission, depending on the investigated system.

Another process that is influenced by thermal effects is excimer formation, for which the presence of facilitating phonons might help during initial formation [235, 236]. Yet, an increased temperature can also enable a pathway of thermal activation of the excimer to a more localized excited state [235] and increased temperatures also increase non-luminescent excimer quenching via IC [230, 231].

In this chapter, binary films containing ADT and HPhB are investigated. Limited intermixing of the two compounds is found, where neat HPhB phase-separates against a mixed phase below a critical fraction of ADT. In the phase-separating regime, minor structural changes were introduced by changing the compound ratio and the effect of these changes on the photophysics is analyzed by TRPL. Finally, the temperature-dependence of the TRPL data of these differently structured samples is investigated in order to disentangle the multitude of thermal effects on the photophysics. With this approach, it is found that changing the sample temperature displays one possible pathway to influence the balance between excimer formation and singlet fission.

10.1. Structural characterization

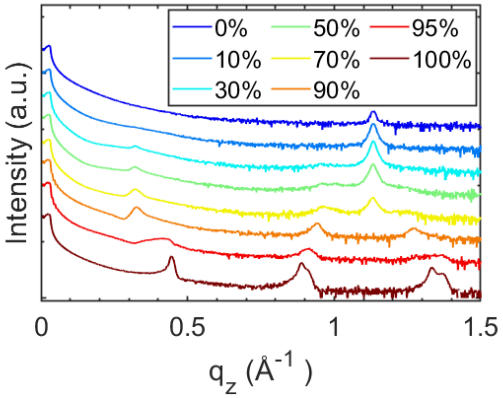

Figure 10.1.: The XRR curves of neat and binary films of ADT and HPhB are plotted with a logarithmic y-axis and vertically offset for clarity. Molar concentrations of ADT are given in the legend.

Binary films containing ADT and HPhB have been structurally investigated using XRD techniques. For the out-of-plane structure, XRR curves of the neat and binary films have been recorded and are plotted in Figure 10.1. Neat ADT, which has already been discussed in the previous chapters, exhibits Bragg peaks of first, second and third order around 0.45, 0.9 and 1.35 $Å^{-1}$, respectively. Each of these peaks is split due to the coexistence of thin film phase and bulk phase [126], which becomes easier to see at higher Bragg peak orders (also see Appendix E). The Bragg peak positions of neat ADT are related to a d_z-spacing of around 14 Å, which indicates a standing-up orientation of the ADT molecules against the surface [122]. Neat HPhB only exhibits one Bragg peak at 1.14 $Å^{-1}$ in the displayed q_z-range, which equals a d_z-spacing of 5.51 Å, corresponding to

half the value of the lattice vector b of the HPhB single crystal structure [153]. Since four HPhB molecules are in each single crystal unit cell [153] (Table 6.3 in Chapter 6), this coincidence suggests a lying-down orientation of the HPhB molecules on the substrate surface in the neat thin film. The XRR curves of the binary films with more than 70 % ADT will be discussed in the following. Moving from neat ADT to binary films with high fractions of ADT, a change in peak position is found for all three Bragg peaks. Surprisingly, the peak, which was assigned to the first order Bragg peak in neat ADT, shifts to lower q_z-values, while the second order Bragg peak of neat ADT seems to shift to higher values. The peak, which was assigned to the third order Bragg peak of ADT, shifts to lower values again, but by a smaller amount compared to the Bragg peak at lowest scattering vectors. Since all Bragg peaks exhibit a different shift upon adding HPhB, the second (third) order Bragg peak of ADT is not anymore at a value of two (three) times the first order Bragg peak in the binary films. As a result, the three Bragg peaks visible in the binary films with more than 70 % ADT cannot be assigned to the first, second and third order anymore, suggesting a more complex out-of-plane structure of these binary films. However, a phase-separation of ADT and HPhB can be excluded in this regime, since neither of the Bragg peak positions in the binary films agrees with the Bragg peak positions in the two neat films and since the Bragg peak positions shift continuously upon changes in the compound ratio, suggesting intermixing [58, 102]. A detailed structural analysis of the binary films with high fractions of ADT is beyond the scope of this work, which will focus on the binary films with 70 % ADT and less. In this latter region, no shifts of the Bragg peak positions can be observed. The film with 70 % ADT shows four peaks, which are positioned at 0.32, 0.97, 1.13 and 1.25 $Å^{-1}$. Moving from there to films with lower fractions of ADT, the peak at 1.13 $Å^{-1}$ gains intensity while the three other peaks gradually lose intensity until they fall below the noise level at 10 % ADT. This behavior of continuous changes in peak intensity with changing compound ratio, but no changes in peak positions, suggests a phase-separation in the range of ADT fractions that are 70 % and less [58]. In this region, the Bragg peak at 1.13 $Å^{-1}$, which is almost exactly at the position of the Bragg peak of neat HPhB, is assigned to one phase, indicating that this phase is neat HPhB. The peaks at 0.32, 0.97 and 1.25 $Å^{-1}$ are assigned to the other phase. These Bragg peak positions might be the same as those, toward which the Bragg peaks of the films with high fractions of ADT converge, when changing the compound ratio towards 70 %. Hence, this is an indication that the other phase in the phase-separating regime is a mixed phase of ADT and HPhB. The volume per molecule in the single crystal unit cell structure of HPhB [153] is almost exactly twice that of ADT [122]. This might be a further indication that a stable HPhB:ADT mixed phase with a ratio of 1:2 or 1:4 is possible, which would equal 66 % ADT or 80 %

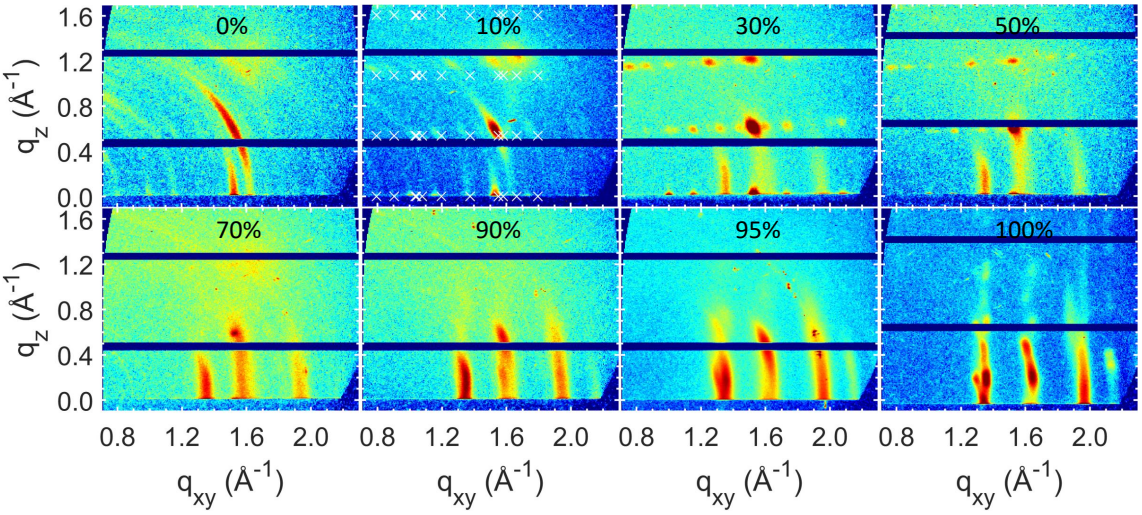

Figure 10.2.: The reciprocal space maps of neat and binary films of ADT and HPhB indicate phase-separation below 70 % ADT, which is in agreement with the XRR data in Figure 10.1. Molar concentrations of ADT are given in each map. In the binary film with 10 % ADT, the expected Bragg peak positions based on the HPhB single crystal structure [153] are indicated with small white crosses.

ADT, respectively. This limited intermixing model of ADT and HPhB will be verified by the analysis of GIWAXS data, absorption spectra and PL spectra in the following.

So far, only the out-of-plane structure has been investigated with XRR. In the following, GIWAXS is used to also access the in-plane structure and the resulting reciprocal space maps are shown in Figure 10.2. Neat ADT shows three vertically extended diffraction features that have been assigned to the (11l), (02l) and (12l) reflections of the in-plane herringbone arrangement in the previous chapters [126, 155] and agree with the preferred standing-up orientation of the ADT molecules [122]. Moving from the neat ADT film to the binary films, these three features stay visible until they fall below the noise level at 10 % ADT. However, when moving from neat ADT to the film with 70 % ADT, small shifts in the q_{xy}-positions of the Bragg peaks are found, indicating intermixing in this range (see Figure 10.3). Below 70 % ADT, the positions of the vertically extended features do not change anymore, only the intensity decreases with decreasing fractions of ADT. Additionally, at 50 % ADT and less, more localized features appear that arrange in horizontal rows at around $q_z = 0\,\text{Å}^{-1}$, $q_z = 0.55\,\text{Å}^{-1}$ and $q_z = 1.1\,\text{Å}^{-1}$ in Figure 10.2. In the map with 10 % ADT, the expected Bragg peak positions for the HPhB single crystal structure [153] are indicated with white crosses and agree reasonably well with the experimentally found positions, indicating that the localized Bragg peaks are assignable to neat HPhB. Neat HPhB exhibits the same Bragg peak positions, but in this

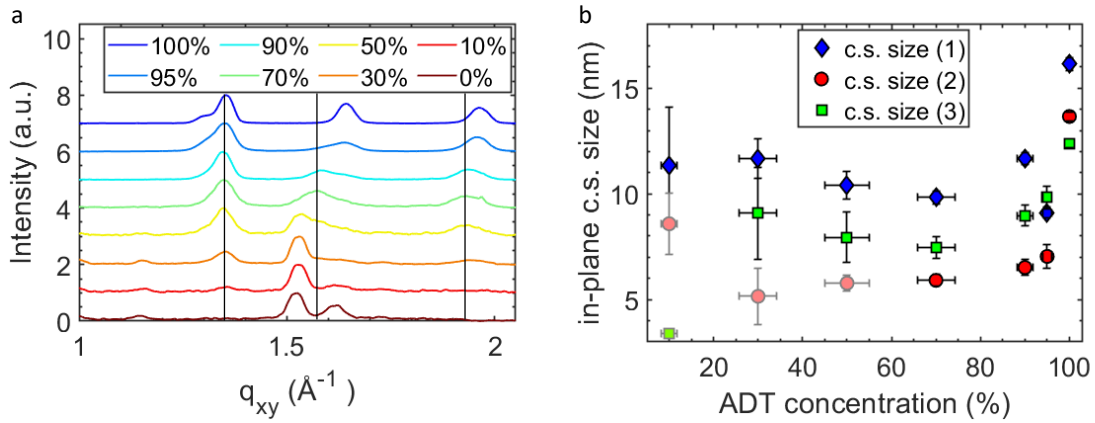

Figure 10.3.: (a) The GID maps in Figure 10.2 have been integrated along q_z in the range $0.1\,\text{Å}^{-1} < q_z < 0.3\,\text{Å}^{-1}$. The molar ADT concentrations are given in the legend. The peaks at 1.35, 1.6 and $1.95\,\text{Å}^{-1}$ (best visible in the films with 70 % ADT and more) are assigned to the mixed phase and named (1), (2) and (3), respectively, in the legend of Figure 10.3b. These three peaks are marked with a vertical black line each to visualize the peak shifts at high ADT fractions. (b) The mentioned peaks have been fitted with Gaussian functions and the widths of the peaks have been used to calculate the coherently scattering size (c.s. size) with Equation 5.11. Unclear fit results due to overlap or low intensity were plotted in faded colors.

case the peaks are azimuthally smeared out, making it more difficult to see and localize the features. This smearing-out indicates a less strictly preferred orientation of the HPhB molecules in the neat film as compared to the binary films with low fractions of ADT. Note that this partial loss of preferred orientation in neat HPhB also explains why the Bragg peak of neat HPhB in the XRR data (Figure 10.1) is weaker than in the binary films with low fractions of ADT. To directly compare the in-plane structure of the films, linescans along q_{xy} have been extracted by integrating the GID maps in the range $0.1\,\text{Å}^{-1} < q_z < 0.3\,\text{Å}^{-1}$ (Figure 10.3a). There, the shifting of the peaks in the range of more than 70 % ADT is visible, while below this value the position of the peaks assigned to the mixed phase stays constant and instead the peaks gradually lose intensity. At the same time, the Bragg features assignable to neat HPhB gain intensity (the most prominent one is at $1.52\,\text{Å}^{-1}$). Note that the Bragg peak of the mixed phase at $1.58\,\text{Å}^{-1}$ overlaps with the Bragg peaks of neat HPhB at $1.52\,\text{Å}^{-1}$ and $1.62\,\text{Å}^{-1}$, making a disentangling of these three peaks in the phase-separating regime difficult.

Since this chapter focuses on the optical properties of the ADT containing mixed phase in the phase-separating regime, the structural properties of this mixed phase in the phase-separating films with 70 % ADT and less is investigated in more detail as basis for the understanding of the optical properties. To achieve this, the Bragg peaks of

the mixed phase have been fitted with Gaussian functions and their widths have been used to calculate the coherently scattering in-plane sizes using Equation 5.11 (see Figure 10.3b). Due to overlap with other features or due to weak peak intensity, some of the fit results have to be handled with care and the corresponding data points are plotted in faded color. For the remaining data points, a weak trend to higher coherently scattering sizes with decreasing fractions of ADT can be found in the phase-separating regime (*i.e.* at ADT concentrations less than 70 %). This finding can be explained with the argumentation presented in context of the ADT:ZnPC films in Appendix C, which suggests a better crystallite quality of the ADT containing phase when the ADT concentration is reduced [58, 198, 241]. The argumentation is based on the idea that a hampered grain formation and slower growth of the ADT containing grains, which is a result of a lower ADT concentration in the film at constant total growth rates, can lead to a higher crystallite quality. Since the intensity of the Bragg peaks assigned to the mixed phase decreases with decreasing fractions of ADT, an accurate fit of the Bragg peak widths is becoming difficult at ADT fractions of 10 % and below. However, based on the described growth model, it is expected that the trend of an increasing coherently scattering size with decreasing ADT fractions, which is found at higher ADT fractions, continues at low ADT fractions.

10.2. Optical characterization

After extracting the hypothesis of limited intermixing between ADT and HPhB from the structural analysis based on XRD in the previous section, the optical properties of this system are analyzed in the following. For this purpose, absorbance spectra of the neat and binary films have been recorded and are shown in Figure 10.4. In the energy range below 3 eV the $S_0 \rightarrow S_1$ transition of ADT with its vibronic progression toward higher photon energies is the only optically allowed transition, which also explains why neat HPhB only shows scattering in Figure 10.4a. In the binary films, the intensity of the ADT absorption peaks decreases with decreasing fractions of ADT. In the range of ADT concentrations above 70 % ADT, also small changes in the spectral shape of the Davydov splitting, including a blueshift of the entire spectrum, can be found. These changes can be assigned to structural changes, to which the Davydov splitting is sensitive [71, 72, 92, 242], and which are induced by the admixture of HPhB as has been found during the structural analysis based on XRD. Additionally, with the admixture of the high bandgap material HPhB, the polarizability of the film decreases [133], leading to the observed increase in transition energy. Below 70 % ADT, no spectral changes or shifts are found besides the decrease in overall intensity, which is in line with the

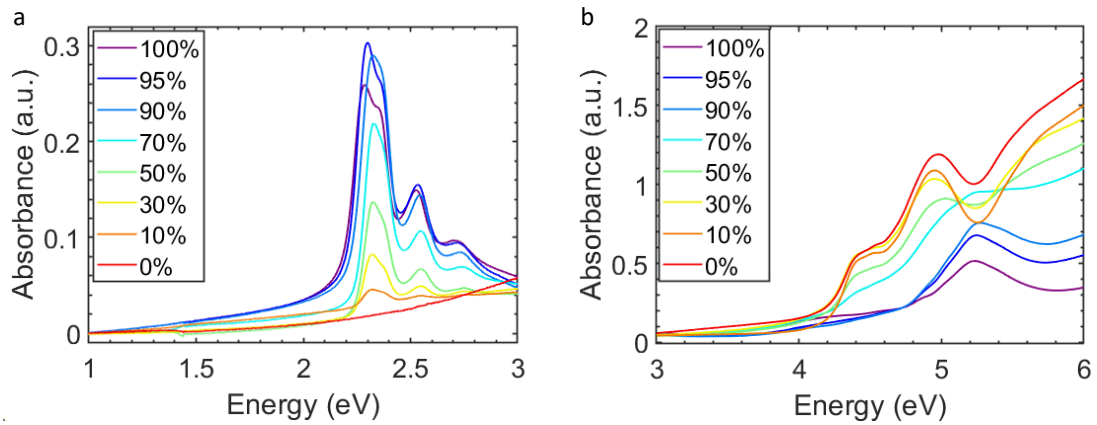

Figure 10.4.: (a) The absorbance spectra of the neat and binary films were set to zero at 1 eV and plotted in the energy region of the $S_0 \rightarrow S_1$ transition of ADT. Significant changes in spectral shape only occur above 70 % ADT, indicating limited intermixing. (b) The high-energy range of the absorbance spectra shows that higher transitions of ADT and the energetically lowest transition of HPhB are all at energies higher than 4 eV. Molar concentrations of ADT are given in the legend.

idea of limited intermixing proposed in the XRD analysis [243]. Note that, surprisingly, neat ADT does not have the highest absorption peak, which can be explained either by varying film thicknesses due to uncertainties of the QCM during film growth or by structural changes upon the admixture of HPhB. This admixture might lead to the TDM of the ADT molecules and the electric field of the probing light being aligned more favorably in mixtures compared to the neat ADT film.

Figure 10.4b shows the absorbance spectra in the energy range above 3 eV, where one can see the absorption of HPhB onsetting at 4.3 eV and higher transitions of ADT at energies above 5 eV. The following PL experiments were carried out with photon energies of the exciting laser far below the latter two energies (namely 2.33 or 2.58 eV), which means that neither excitations of HPhB nor higher electronic excitations of ADT have to be considered relevant in the analysis of the recorded PL spectra [1].

The PL spectra of neat ADT and the binary films are shown in Figure 10.5. All spectra show a sharp peak around 2.25 eV and a broad peak around 2.0 eV, which both blueshift with decreasing fractions of ADT in the range of ADT concentrations of 70 % and more. At concentrations below this value, the spectral position of both features does not change significantly anymore with changing ADT concentrations. As discussed in detail in Chapter 7, the sharp high-energy peak is assigned to the free exciton emission and

[1] Processes such as SSA can lead to higher excitations, but can be considered to play a negligible role for the present excitation densities, at which singlet fission and excimer formation will be shown to dominate the photophysics.

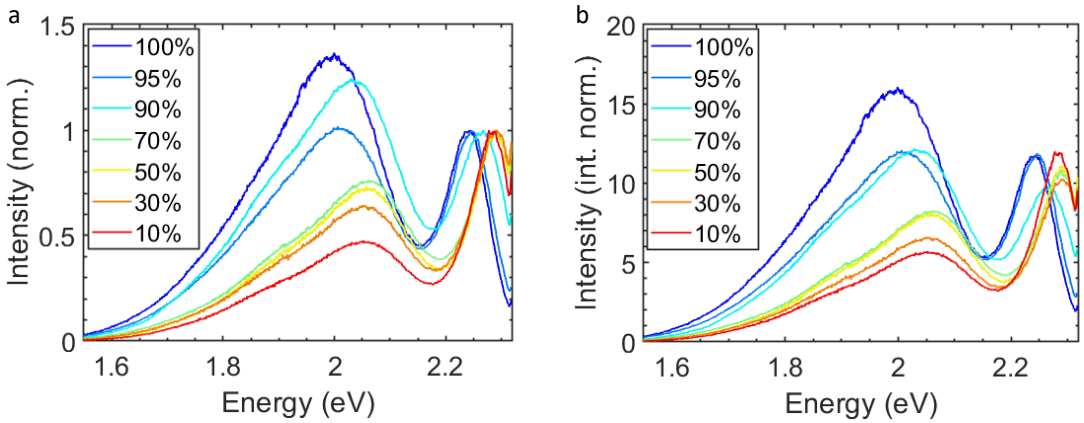

Figure 10.5.: (a) The PL spectra of neat ADT and the binary films are normalized to the peak intensity of the ADT free exciton emission. The photon energy of the exciting laser was 2.33 eV, which makes an excitation of HPhB impossible. For this reason, the PL spectrum of neat HPhB is omitted. (b) The PL spectra are replotted but normalized to the integral (int. norm.) of the intensity of the free exciton emission, which was estimated based on Gaussian fits of the free exciton emission peak. Molar ADT concentrations are given in the legend.

the spectrally broad peak around 2.0 eV is assigned to the excimer emission [155]. The blueshift of the two features with decreasing ADT concentrations is assigned to changes in the polarizability of the film in analogy to Chapter 7. Additionally, the same argumentation as presented in Chapter 7 can be used in the present case to explain why this blueshift is stronger for the excimer emission than for the free exciton emission [155]. The reasoning for that is that in the excimer, electron and hole are more delocalized compared to the situation in the free exciton and more delocalized charges polarize the environment to a higher amount, which ends up in a higher sensitivity of the energy of the corresponding state to changes in polarizability [155]. The absence of spectral shifts at ADT concentrations below 70 % once more supports limited intermixing. At ADT concentrations below this threshold, neat HPhB is expected to phase-separate from a mixed phase, which means that the addition of more HPhB does not change the local environment of the ADT molecules and hence neither the polarizability of their environment.

One further observation is that, with the exception of the film containing 90 % ADT, the relative intensity of the excimer decreases with decreasing fractions of ADT. However, a closer analysis of the PL data reveals that the film with 90 % ADT is no true exception, since in Figure 10.5a the intensity is simply normalized with respect to the peak intensity of the free exciton emission, while the more physical way of normaliza-

tion would be a normalization with respect to the integrated intensity of the free exciton emission. Since not all free exciton emission peaks do have the same width, these two ways of normalization are not equal. Thus, in Figure 10.5b, the spectra have been normalized with respect to the integrated intensity by applying a Gaussian fit to the free exciton emission peak. Now, as a result of the free exciton peak of the film with 90 % ADT being the broadest, the intensity of the excimer emission of this film is no exception anymore and a decreasing excimer luminescence with decreasing fractions of ADT can be generally observed. This means that the relative intensity of the excimer emission does not only decrease when HPhB and ADT are intermixing (at ADT concentrations above 70 %), but also in the range where additional HPhB molecules phase-separate (below 70 % ADT), indicating that the addition of phase-separating HPhB can influence the photophysics of ADT. In the intermixing regime this decrease can for example be assigned to intermixing of ADT and HPhB, which reduces the amount of next ADT neighbors, which then reduces the singlet fission rate. This leads to an increase in luminescent yield of the free exciton and in the end resulting in a decrease of the relative intensity of the excimer. Another reason for this decrease in excimer luminescence could be the structural changes introduced by the incorporation of HPhB, which might result in a structure that is less favorable for excimer formation compared to the structure of neat ADT. A detailed reasoning for the observation that the relative intensity of the excimer also changes in the phase-separating regime will be given later by also taking the TRPL data into account.

10.3. TRPL spectroscopy

The molecular arrangement and hence the microstructure of the film is known to have a significant impact on the photophysics [242], especially on multimolecular processes such as singlet fission [42, 43, 202, 244] or excimer formation [26, 245]. Although the system investigated here shows microstructural changes in the intermixing regime, it does not fit well for such an investigation for multiple reasons. On the one hand a lot of stress, strain, stacking faults and other sources of disorder are introduced into the crystallites due to the heteromolecular nature and the sample preparation procedure, which makes it challenging to extract the structural details. On the other hand, the statistical mixing, which is expected in the intermixing phase, means that every ADT molecule has a slightly different local environment, which might have a comparable or even greater effect on the photophysics than the microstructural changes between two samples. Instead, the phase-separating regime of this system can be used to quantify the effects of mesostructural changes on the photophysics. For this purpose, the ADT concentration

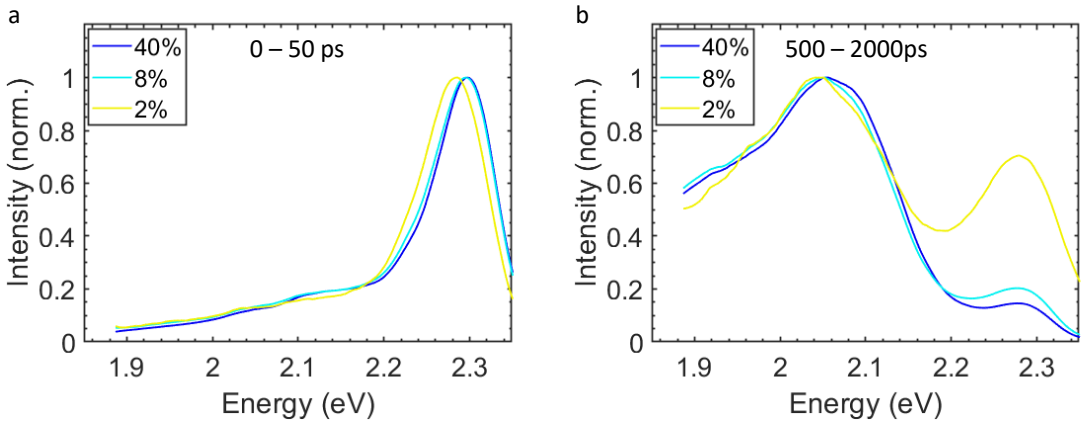

Figure 10.6.: The spectra of binary films were extracted by time integrating the TRPL data recorded at a sample temperature of 200 K (corresponding maps are shown in Figure D.2) (a) over the first 50 ps and (b) in the time range between 500 and 2000 ps, noise filtering and normalizing the data. The photon energy of the exciting laser was 2.58 eV. Molar ADT concentrations of the films are given in the legend.

is only varied within the phase-separating regime, which means that changes in ADT concentration should mainly impact mesostructural parameters, such as for example the grain size, the crystallite quality or the architecture at grain boundaries.

For this reason, in the following only TRPL data of samples in the phase-separating regime will be shown and analyzed. TRPL spectra of the binary films were extracted at early (0 to 50 ps) and late times (500 to 2000 ps) in Figure 10.6a and b, respectively. During the first 50 ps the spectra of all films are fully dominated by the free exciton emission and a slight shift of the free exciton emission peak to lower energies with decreasing fractions of ADT is visible. The excimer emission, which is a dominant contribution in the steady-state PL spectra (Figure 10.5), is not visible during the first 50 ps, but becomes the dominant contribution after 500 ps. Interestingly, the relative intensity of the free exciton emission compared to the excimer emission is low after 500 ps and depends on the ADT concentration, for lower ADT concentrations the relative intensity of the free exciton emission is higher. This is a first indication of an overall fast decay of the free exciton in all samples and a dependence on the ADT concentration of this decay, where the decay of the free exciton emission might slow down with decreasing fractions of ADT. Also for the excimer emission a small redshift of the emission feature with decreasing fractions of ADT might be present, however, this shift might also be an artifact of the noisy data in combination with the applied noise filter.

To get insight into the actual decay, time traces at the energy of the free exciton emission and the excimer emission have been extracted in Figure 10.7a and b. These decay

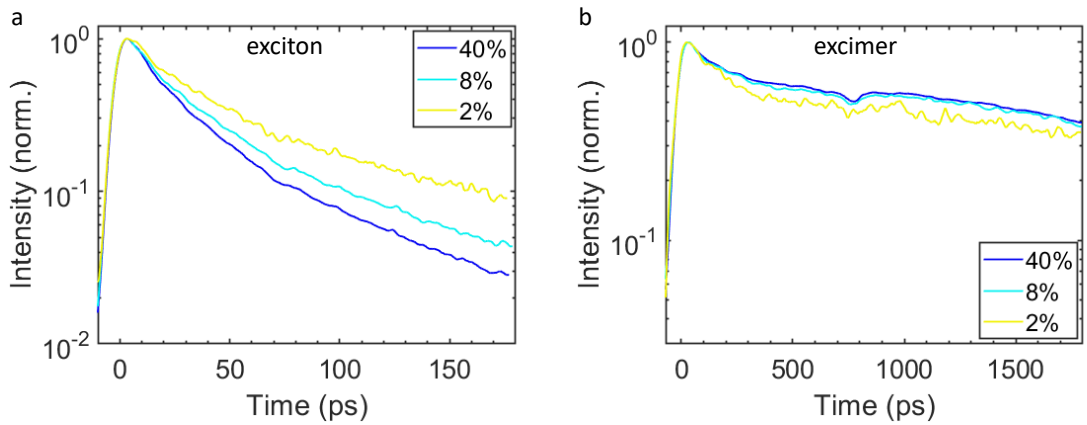

Figure 10.7.: The decay traces of binary films were extracted by spectrally averaging the TRPL data recorded at a sample temperature of 200 K (corresponding maps are shown in Figure D.2) in an energy range above 2.16 eV for the free exciton emission (a) and between 1.89 and 2.08 eV for the excimer emission (b), noise filtering and normalizing the data. The photon energy of the exciting laser was 2.58 eV. Molar ADT concentrations of the films are given in the legend.

traces clearly show that the free exciton emission decays faster than the excimer emission for all investigated samples. In case of the free exciton emission, an acceleration of the decay with increasing fractions of ADT can be found, while the decay rates of the excimer emission are comparable for all samples. The decay rates were precisely analyzed by applying GA [121] on the data, which allows for a better spectral disentanglement of excimer emission and free exciton emission than a multiexponential fit of the presented decay traces. The results gained by this procedure will be presented in the discussion part.

Lastly, the temperature dependence of the TRPL spectra over a wide temperature range (10 K to room temperature) is investigated. For that, the TRPL data at different temperatures were time integrated over the entire timerange of the measurement (0 to 2000 ps) and are presented in Figure 10.8. In all spectra, the free exciton emission is the dominant contribution and at all temperatures the free exciton emission is shifting to the red when the ADT concentration is reduced. This shift between the samples is getting more pronounced at lower temperatures. At temperatures of 110 K and more, excimer emission is clearly visible for all ADT concentration. At lower temperatures, the intensity of the excimer emission decreases to a point, where it cannot be clearly disentangled from the vibronic progression of the free exciton emission anymore, which is expected to be around 2.1 eV based on the results of Chapter 9. Interestingly, there is no continuous trend in the relative intensity of the excimer emission. While it gains

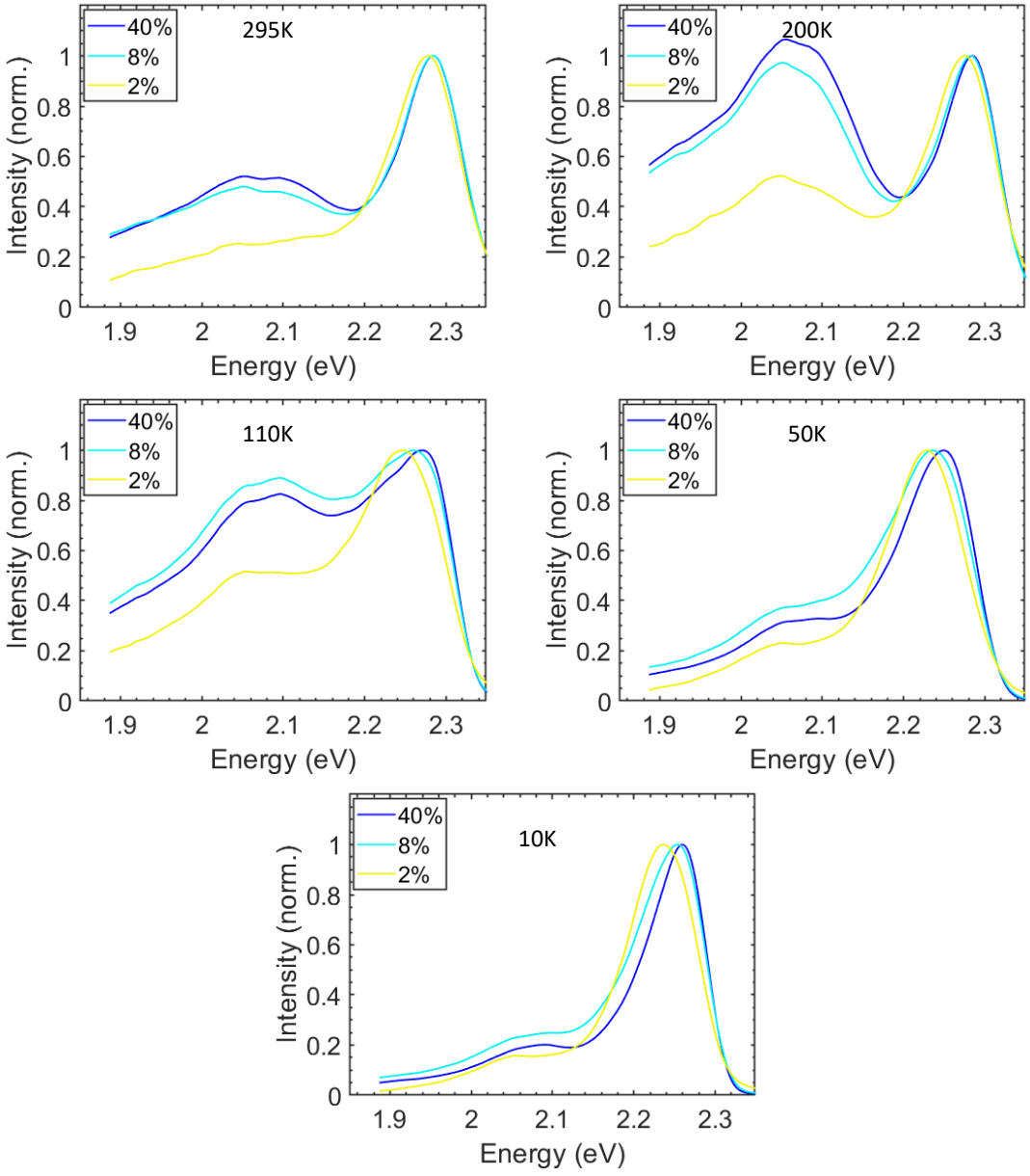

Figure 10.8.: The spectra of binary films were extracted by time integrating the TRPL data recorded at different sample temperatures from 0 to 2000 ps and noise filtering the resulting spectra before normalizing them with respect to the free exciton emission. The photon energy of the exciting laser was 2.58 eV. Molar ADT concentrations of the films are given in the legend, the sample temperature is given inside each plot. With decreasing temperatures, the relative intensity of the excimer emission initially increases, but then strongly decreases, possibly due to a sequential freeze-out of excimer quenching and singlet fission (Figures 10.9 and 10.10 show the corresponding decay traces). The energetic position of the free exciton emission is redshifting with decreasing temperature and with decreasing fractions of ADT, indicating a higher trap state density at low fractions of ADT.

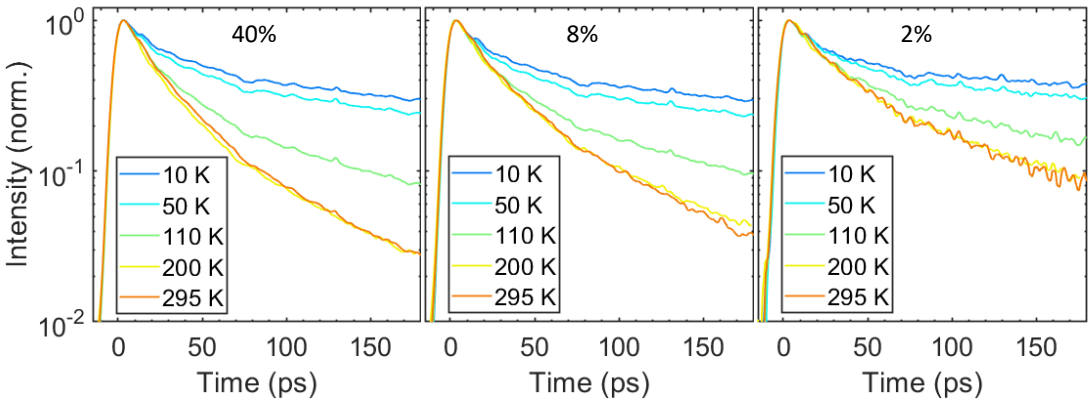

Figure 10.9.: The free exciton decay traces of the different samples at different temperatures are averaged over an energy range above 2.16 eV. The photon energy of the exciting laser was 2.58 eV. The sample temperatures are given in the legend and the molar ADT concentration of the sample inside each plot.

intensity upon reducing the temperature from room temperature to 200 K, the relative intensity decreases again when moving to even lower temperatures.

For each sample, time traces of the exciton are extracted at different sample temperatures in Figure 10.9. Besides a general increase in decay rates with increasing fractions of ADT, all individual samples show the same trend upon changes of the temperature. While barely any changes in decay behavior can be found between 295 and 200 K, a further decrease in sample temperature leads to a continuous decrease in decay rates.

For the decay traces of the excimer (Figure 10.10), no strong differences are found between the samples. However, for each sample, a change in temperature from 295 to 200 K leads to a decrease in excimer decay rate, while further cooling the sample does not show any effects on the decay rate of the excimer. Note that the initial fast decay of the signal is assigned to the low-energy contribution of the free excimer emission *inter alia* due to its vibronic progression, which means that the slope of the logarithmically plotted decay traces after 500 ps is a good measure of the excimer decay rate, but not the absolute intensity at specific times.

10.4. Discussion

By applying GA [121], the decay rates of the free exciton emission and the excimer emission at 200 K are calculated. Due to the strong domination of the TRPL data by the free exciton emission, it was not possible to disentangle the excimer emission in a GA of the entire measured spectrum. Instead, a GA with two species is applied to the energy range

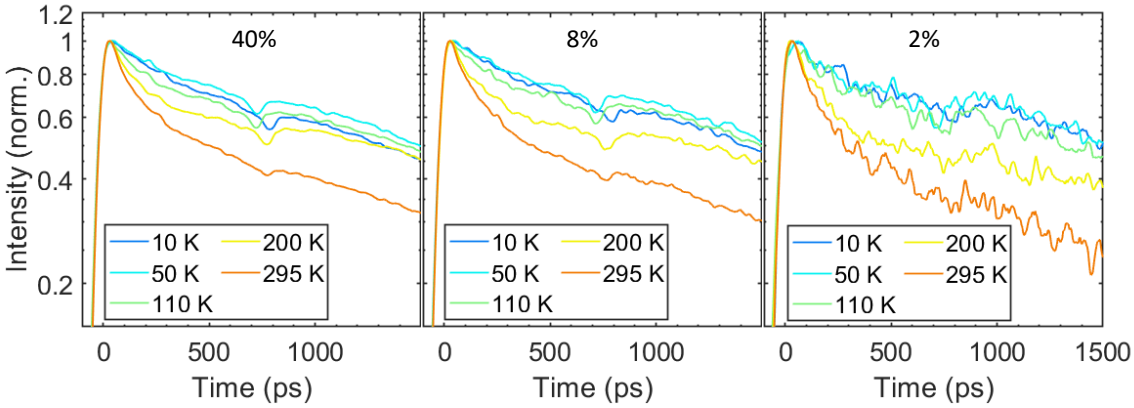

Figure 10.10.: The excimer decay traces of the different samples at different temperatures are averaged over an energy range from 1.89 to 2.08 eV. The photon energy of the exciting laser was 2.58 eV. The sample temperatures are given in the legend and the molar ADT concentration of the sample inside each plot. The initial fast decay visible in some traces is assigned to the exciton emission, while the longer-living signal can be attributed to the excimer.

above 2.21 eV, where the fast decay rate is assigned to the free exciton emission and the slower decay represents traces of the luminescence from trap states and excimers, and to the energy range below 2.16 eV, where the fast rate represents the traces of the free exciton decay and its vibronic progression, so that the slow decay rate is expected to represent the excimer decay rate. The resulting rates in Figure 10.11 clearly show decreasing decay rates of the free exciton emission with decreasing fractions of ADT, while no clear trend is found for the decay rates of the excimer emission. The clear changes in free exciton decay rate with changing ADT concentrations is a intriguing result, since, based on Chapter 9, it is not expected that the addition of phase-separated grains of a different material has a significant impact on the dominant decay channel of ADT excitons, which is singlet fission [198]. However, this observation can be explained with the following model, in which, for simplicity, it is assumed that the mixed phase has an ADT:HPhB stoichiometry of 2:1. The explanation would work equally well for stoichiometries in the mixed phase different from 2:1. As Figure 10.3b indicates, the coherently scattering size of the mixed phase increases with decreasing fractions of ADT, which might mean that the mixed crystallites are better ordered at low fractions of ADT. One possible parameter of better order would be a transition from statistical intermixing to a regularly ordered co-crystal. As sketched in Figure 10.12, for a 2:1 stoichiometry, this would mean in a co-crystal that every ADT molecule has exactly one directly neighboring ADT molecule in-plane (Figure 10.12a), in statistical mixing one ADT molecule can have between one

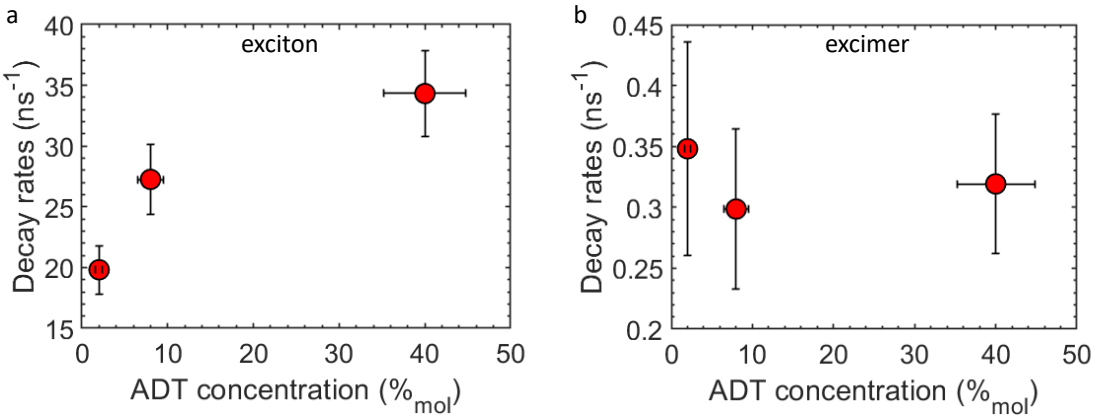

Figure 10.11.: GA has been applied to extract the decay rates of (a) the free exciton emission and (b) the excimer emission based on the TRPL maps at 200 K sample temperature (Figure D.2). In (a), GA has been applied to only the spectral range above 2.21 eV and in (b) to the spectral range below 2.16 eV. In both cases two species have been used to compensate for (a) traces of excimer luminescence and trap state luminescence in the high-energy range and for (b) traces of the free exciton emission and its vibronic progression in the low-energy range.

and four direct ADT neighbors in plane, with a statistical average of 2.66 direct neighbors (Figure 10.12b). Note that the number 2.66 is the number of in-plane neighboring sites (4) multiplied with the ADT concentration (66 %) [49]. Now, the higher average number in the statistical mixed case compared to the co-crystal would explain the higher singlet fission rate at higher fractions of ADT. This is the case because ADT exhibits incoherent singlet fission (Chapter 7) [155], the rate of which linearly increases with the number of nearest neighbors of the same kind [146]. Note that many other common explanations for the decrease in singlet fission rates with decreasing ADT concentrations can be ruled out. For example, an assignment of the slow-down of singlet fission to a higher density of trap states is not in line with the proposed higher crystallite quality at low ADT concentrations. Also, an assignment of the decreased decay rates to ADT molecules incorporated into HPhB crystallites is not possible, since these molecules would experience a lower polarizability of the film, which would lead to a significant blueshift of the free exciton emission peak with decreasing fractions of ADT. With the same argument it can also be excluded that the slow-down is due to changes in the stoichiometry of the mixed phase, since then once again a change in polarizability and hence energy of the free exciton would be observed.

Now, after analyzing the decay of the free exciton, the excimer emission is investigated. GA of the decay rates did not show a clear trend (Figure 10.11b), suggesting

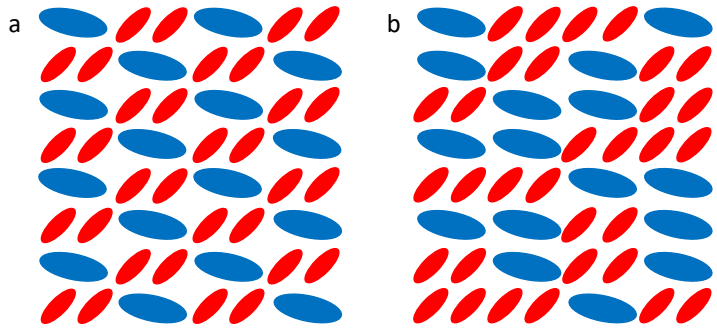

Figure 10.12.: Sketch of the possible in-plane mixing scenarios of the mixed phase. The red ovals represent ADT molecules and the blue ovals HPhB molecules. (a) In a mixed co-crystal every ADT molecule has only exactly one direct ADT neighbor. (b) In the statistically mixed case an ADT molecule has an average of 2.66 directly neighboring ADT molecules, although in both cases the ratio between ADT and HPhB is the same. This model, in combination with the replacement effect of incoherent ADT singlet fission [146, 155] can explain the changes in exciton decay rate in Figure 10.11a.

that the addition of phase-separating HPhB has no strong effect on the excimer decay dynamics. Although the time resolution of the TRPL setup is insufficient to track the excimer formation (typical excimer formation times are 200 fs [24, 170, 171]), a small insight into the formation dynamics can be gained by analyzing the relative intensities. For that, it is assumed that the rate of the fluorescent decay channel of the free exciton is the same in all samples and the same assumption is made for the excimer. It is also assumed that the dominant decay mechanism is non-luminescent for both excited-state species, namely singlet fission for the free exciton [30, 44, 155] and non-luminescent quenching for excimers [23]. Under these assumptions, dividing the spectra normalized to the free exciton emission by the free exciton decay rate results in the spectral intensity representing the absolute luminescence (e.g. if the free exciton decay rate is higher, the luminescence quenching is more efficient and hence the luminescence is lower). Now, multiplying this luminescence per molecule with the decay rate of the excimer leads to the resulting excimer emission intensity being proportional to the excimer density after initial excimer formation. This procedure was applied to the time-integrated TRPL data in Figure 10.13, resulting in the excimer peak being of roughly equal size for all samples, considering the significant error bars in Figure 10.11. This indicates that the excimer formation yield after excitation is the same for all samples and the strong changes in relative intensity between excimer and exciton can be assigned mainly to changes in singlet fission rates between the samples. This is in line with the data of Chapter 7, where the same decrease in relative intensity of the excimer is found and is there also

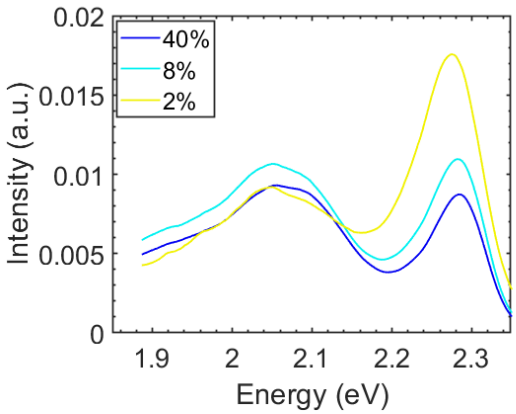

Figure 10.13.: The spectra at 200 K are replotted from Figure 10.8, but instead of normalizing to the maximum intensity of the free excimer emission, the spectra have been divided by the exciton decay rate and multiplied by the excimer decay rate of each film after normalization. Under the assumption of the same free exciton density immediately after excitation in all films, the intensity of the excimer is now representing the excimer density immediately after formation and hence indicating the same excimer formation yields in all films.

assigned to changes in singlet fission rate. As concluded from the data there [155], also the present data agree with the idea of the singlet fission rate in ADT depending on the number of nearest neighbors of the same kind, while the excimer formation rate seems to be equally fast as soon as any nearest ADT neighbor is present.

In the following, the temperature dependence of the TRPL data is discussed. The redshift of the free exciton peak with decreasing temperatures can be assigned to the population of trap states. Assuming a Gaussian distribution of the density of states in energy (remember Section 4.3.3), thermal activation from low-energy sites leads to an increased amount of luminescence from sites with increased energy at elevated temperatures, which in turn leads to a blueshift of the spectral fingerprint with increasing temperature. This model can explain the blueshift when moving from 50 K to 295 K present for all samples in Figure 10.8 (peak positions of the free exciton emission are given in Table 10.1). However, moving from 10 K to 50 K, there is no blueshift to be found, but a small redshift. This can be explained by spatial isolation of trap states [234], which is not taken into account in the model so far. If one trap state of significant energetic depth is populated, it is unlikely that another deep trap state is in close proximity, which means that thermally activated hopping away from this trap state is highly unlikely due to a significant thermal barrier [234]. With decreasing temperature, the thermal energy decreases and hence the energetic depth needed for this mechanism decreases, which

Table 10.1.: Peak positions of the free exciton emission estimated by Gaussian fits.

ADT fraction	295 K	200 K	110 K	50 K	10 K
2 % mol.	2.2773 eV	2.2740 eV	2.2452 eV	2.2282 eV	2.2367 eV
8 % mol.	2.2835 eV	2.2823 eV	2.2590 eV	2.2358 eV	2.2521 eV
40 % mol.	2.2836 eV	2.2842 eV	2.2614 eV	2.2360 eV	2.2588 eV

means the excitations can already be spatially trapped at higher energy sites, i.e. in traps of smaller depth. This mechanism can explain why the energetic position of the free exciton emission is higher at 10 K than at 50 K. The fact that the energetic position of the free exciton emission is lower for samples with lower fractions of ADT at all temperatures can be explained by the trap site density. Expecting a higher trap site density, i.e. a broader energetic distribution of states, at low ADT concentrations not only explains why the energy of the free exciton emission is lower, but also why the differences between the samples are more pronounced at lower temperatures. At low temperatures the part of the luminescence coming from trap sites is higher, hence the density of trap states has a more influential role there. Although the existence of trap sites reduces the coherently scattering size, this is not in contrast to Figure 10.3b due to lattice stress. In the statistically mixed case, which is present at higher ADT fractions, the lattice stress is higher due to geometric differences between the molecules, decreasing the coherently scattering size. In contrast, the regular molecular arrangement in a co-crystal reduces lattice stress and hence increases the coherently scattering size. This effect on the coherently scattering size might compensate the effect of trap sites, explaining the trend in Figure 10.3b.

Lastly, the complex spectral changes with temperature have to be discussed. The initial increase of the relative intensity of the excimer emission upon cooling the sample might be justifiable by a reduced quenching rate of the excimer emission with decreasing temperature. For example, it can be expected that the efficiency of IC decreases with decreasing temperatures [230, 231]. This explanation is well in line with the decay traces of the free exciton emission and excimer emission in this temperature range (Figure 10.9 and 10.10), which shows no change in case of the exciton and a slow-down for the excimer, which indicates a higher luminescent yield of the excimer while it stays constant for the exciton. In other words, a lower decay rate of the excimer agrees with less efficient non-luminescent excimer quenching. Moving to temperatures lower than 200 K, the decrease of relative intensity of the excimer emission is in line with the decreasing exciton decay rates while the excimer decay rates stay constant in this lower temperature range. The decrease in exciton decay rates might be due to the dominant,

non-luminescent singlet fission channel being thermally activated, e.g. by intermolecular motion, which freezes out at low temperatures. Note that the energy of the ^{1}(TT) state is below the energy of the exciton in ADT [30, 83], meaning that triplet-pair formation in ADT is exothermic, but starting the process might still be thermally activated. The same argumentation might also hold true for excimer formation, in the case of which lower temperatures would then lead to smaller excimer formation rates, explaining the strong spectral dominance of the exciton at low temperatures. However, the time resolution of TRPL is insufficient to get insight into the excimer formation dynamics. Note that an excimer deactivation pathway by thermal activation from the excimer to the exciton, followed by singlet fission can be considered to have negligible impact in the investigated temperature range, as demonstrated in Appendix D.

10.5. Conclusion

The photophysics of ADT in the phase-separating regime of binary films containing ADT and HPhB has been analyzed. For films with low fractions of ADT, in which a neat HPhB phase and a mixed phase separate, a slow-down of singlet fission has been found with decreasing fractions of ADT, accompanied by an increase in coherently scattering size. This counterintuitive result has been explained by a transition of the mixed phase from solid-solution to co-crystal with decreasing fractions of ADT, a transition which increases the coherently scattering size, while at the same time decreases the number of neatest neighbors of the same kind, which again leads to a decrease in the incoherent singlet fission rate of ADT [146, 155]. Based on spectral shifts in PL, a higher trap state density has been suggested for films with lower fractions of ADT. Lastly, the temperature-dependence of the photophysics has been analyzed, where spectral shifts with temperature could be explained by a model involving energy transfer to trap states and temperature activated hopping away from trap states. Temperature-dependent changes in the PL transients of the exciton and the excimer, and changes in the spectral intensity ratio between the features of these two, can be explained by a decrease of the excimer quenching rate upon initial cooling from room temperature to 200 K, while further cooling leads to a potential freeze out of single fission. The data also give room for speculations about a possible reduced excimer formation rate at low temperatures.

With these findings, it has been shown that both, structural changes of the sample as well as changes in sample temperature, are successful approaches to tune the balance between excimer formation and singlet fission.

11. Conclusion and outlook

The photophysics of ADT in thin films has been investigated in this thesis. For this purpose, binary films of ADT with multiple different compounds have been produced and can be categorized by their intermixing behavior and bandgap as shown in Figure 11.1. This approach enabled a controlled alteration of the photophysics of the sample, which made it possible to gain insights into the photophysics of ADT. The measured results revealed a significant competition of two multimolecular processes: singlet fission and excimer formation. Furthermore, the investigated systems uncovered a multitude of pathways to influence the balance between excimer formation and singlet fission and hence to tune the photophysics of ADT.

11.1. Conclusion

The first result in this thesis was obtained by statistically mixing ADT with higher bandgap materials in Chapter 7. Here, the linear dependence between the decay rate of the free exciton emission and the ADT concentration strongly suggested that incoherent singlet fission [146] is the dominant decay process of this state [30, 44]. Statistical mixing, however, not only changes the average number of nearest neighbors of the same kind, but also influences the polarizability of the sample [133]. The latter effect was used to analyze the sensitivity to changes in polarizability of a low-energy emission coming from an unknown state. With this approach, a high charge delocalization was found for this state, allowing an assignment of the emission to excimer emission [23, 168, 169]. By also taking the independence of the decay rates of excimer and free exciton into account, a model was developed, which suggests excimer formation and singlet fission as parallel channels that are connected only indirectly via a common precursor state.

The influence of the presence of a low bandgap material on the photophysics of ADT was investigated in Chapter 8. For this investigation the molecule PEN was used, which mixes statistically with ADT. In this system, very fast and efficient energy transfer from ADT to PEN was found for all excited-state species of ADT. The excited-state funneling from ADT to PEN is explainable by a downward energy gradient present for all observed transitions, including the transition from isolated PEN molecules to PEN agglomerates.

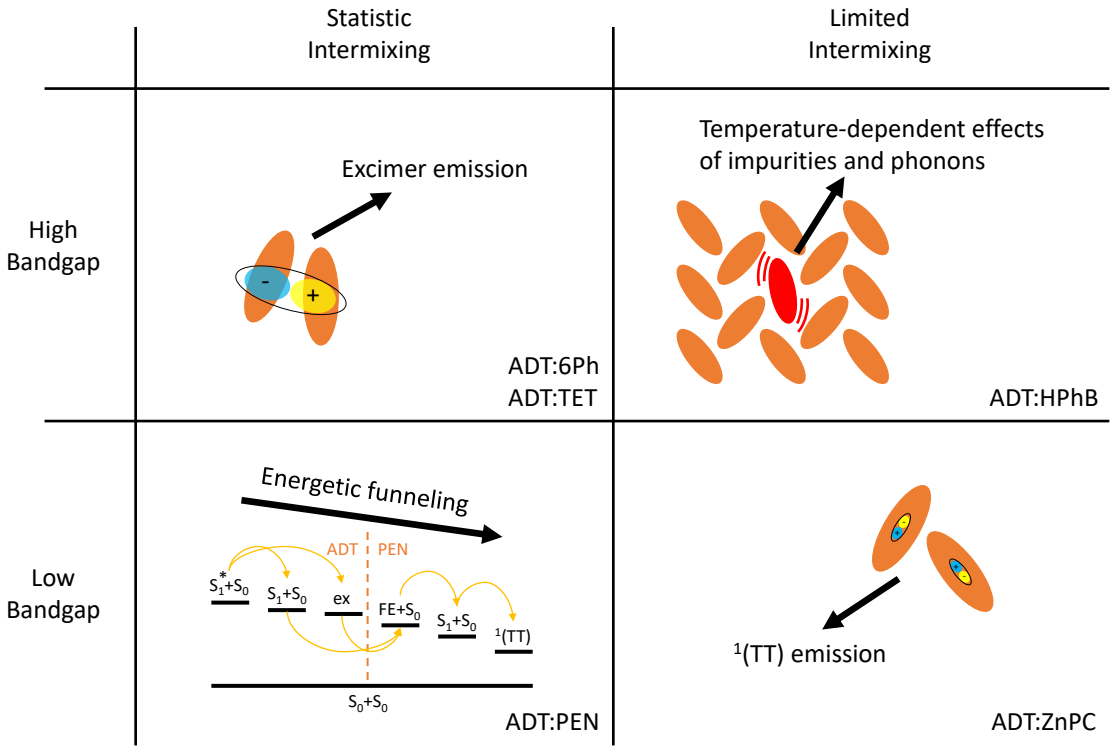

Figure 11.1.: Graphical overview over the results of this thesis. The polarization changes induced by statistical intermixing of ADT with high bandgap materials enables to identify excimer emission in ADT (top left). In the phase-separating regime of ADT and a high bandgap material, the impact of trap states and phonons on the photophysics was studied by varying the sample temperature and trap site density (top right). The singlet fission efficiency of ADT was increased by statistical intermixing with a small bandgap singlet fission material, resulting in energetic funneling to the latter material, followed by singlet fission (bottom left). ADT excimer emission is suppressed in the phase-separating system with a low bandgap material, which made it possible to uncover ^{1}(TT) emission, the visibility of which correlated with excited-state delocalization (bottom right).

PEN is a highly efficient singlet fission material [246, 247], and thus, this system is expected to increase the singlet fission yield compared to neat ADT, as an energetic funnel is installed that opens a pathway toward singlet fission for states which decay in a different pathway in neat ADT.

In the phase-separating system containing ADT and the low bandgap molecule ZnPC changes to the mesostructure were introduced via growth conditions in Chapter 9. This led to a strong suppression of the ADT excimer emission, which in turn made ^{1}(TT) emission in this spectral range visible, which clearly proofs that singlet fission is one dominant decay channel of ADT [30]. The presence of ^{1}(TT) emission was correlated to a high excited-state delocalization [203], which is in line with the pronounced ^{1}(TT) emission in single crystals of ADT. The suppression of the ADT excimer emission in the phase-separating samples once again suggests that grain boundaries and trap states play an important role for the emission of excimers [155].

Complementing the other three parts, in Chapter 10 ADT was combined with a limited intermixing, high bandgap molecule and investigated in the phase-separating regime. In this system, the intrinsic balance between the multimolecular processes singlet fission and excimer formation in ADT was influenced by mesostructural changes and by changes in temperature. While the mesostructural changes influenced the incoherent singlet fission process more heavily than the excimer formation, decreasing the temperature leads to a freeze-out of thermally activated phonons [228], which influences both processes [233, 236]. By also taking the population and thermal activation of trap states into account [237], a picture was drawn in which with decreasing temperatures first excimer quenching is reduced, before the singlet fission rate, and possibly also the excimer formation rate, decreases.

To conclude, binary systems containing ADT have been used to continuously change the structural and energetic landscape and the resulting impact on the photophysics has been analyzed. This approach not only uncovered the complex photophysics intrinsic to ADT [30, 44], but also showed promising ways to tune the photophysical behavior of ADT. Such pathways to continuously change the photophysics of a given material play an important role in bringing OSCs closer to application, where it is critical to adapt the behavior of a material to given desires.

11.2. Outlook

Based on the previously described results, further scientific questions arose and ideas for further projects were elaborated. This section includes these questions and possible experimental pathways to tackle them.

A common precursor state has been proposed for the free exciton band and the excimer in ADT [172], however, the nature of this state is not known yet. This state must not be an intramolecular vibronic excitation, since ADT was excited at the 0-0 and at the 0-1 transition with similar results in this work. The nature of the precursor state could be investigated by tracking changes to the photophysics of neat ADT while scanning through the excitation wavelength in the region of the $S_0 \rightarrow S_1$ transition of ADT. Hypothetically, the balance between singlet fission and excimer formation is strongly impacted once the excitation energy is in the region of the energy of the precursor state. It might be helpful to also execute this experiment with ADT single crystals and at different temperatures to minimize broadening effects.

Further insight into the details about the competition between singlet fission and excimer formation could be gained by employing time-resolved techniques with a resolution in the femtosecond range, which would be sufficient to resolve excimer formation. One possible technique would be transient absorption, for which, however, the data analysis is challenging due to a possible spectral overlap of features assigned to the excimer, the singlet state, the triplet state and the triplet-pair state.

In comparable fashion, transient absorption measurements could also be launched to track the energy transfer between ADT and PEN in mixtures, which occurred faster than the instrument response of the TRPL setup. A disentanglement of the multitude of possible spectral contributions in this system is assumed to be challenging, although the strong suppression of ADT emission in the mixtures might help in this regard.

Alternatively to employing transient absorption, the energy transfer from ADT to PEN could also be tackled by producing mixtures of ADT and PEN with PEN amounts below 2.5 %, which should then slow down the energy transfer from ADT to PEN enough to track it with TRPL. However, due to limited purity of the used materials and limited precision of the QCMs used in OMBD, the preparation of films with such low PEN concentrations is a challenging task.

Transient absorption measurements of ADT:PEN mixtures with low amounts of PEN could also be used to track singlet heterofission in this system with increased sensitivity compared to TRPL. The presence of a ground state bleach of ADT under selective excitation of exclusively the smaller bandgap molecule PEN can be considered a strong indication of the presence of singlet heterofission [87].

In the binary films containing ADT and ZnPC, a higher excited-state delocalization and ^{1}(TT) luminescence was found at low ADT concentrations. Considering this finding, it is unclear whether the compound ratio or the growth rate of the ADT compound is the deciding factor. To disentangle these two parameters, either a series with the same compound ratio, but different growth rates, or a series with the same ADT deposition

rate, but different compound ratios could be produced and analyzed. As an indication, Figure C.9 shows binary films of ADT and ZnPC with the same compound ratios, but with spectral differences in PL. In sample preparation, the samples had slight variations in total growth rate.

Temperature-dependent measurements on ADT single crystals might display an avenue toward further understanding of the possible connection between excited-state delocalization and ^{1}(TT) emission. This is not possible with thin films, since in thin films the low-temperature photophysics is often dominated by trap states.

In Appendix E a thin film and a bulk phase of ADT have been found. It would be of interest to find ways to influence which phase is grown preferentially (e.g. by changing growth conditions, the substrate material, the preparation method or by annealing) and to fully analyze the structure and photophysics of each individual phase. The structural differences between the two phases are expected to influence e.g. the excimer formation rate and singlet fission rate.

Bibliography

[1] Petrova-Koch, V.; Hezel, R.; Goetzberger, A. *High-efficient low-cost photovoltaics*; Springer, Berlin, Heidelberg, 2009.

[2] Dong, P.; Chen, Y.-K.; Duan, G.-H.; Neilson, D. T. Silicon photonic devices and integrated circuits. *Nanophotonics* **2014**, *3*, 215–228.

[3] Moliton, A.; Hiorns, R. C. The origin and development of (plastic) organic electronics. *Polym. Int.* **2012**, *61*, 337–341.

[4] Tsujimura, T. *OLED display fundamentals and applications*; John Wiley & Sons Inc., 2017.

[5] Jeong, E. G.; Kwon, J. H.; Kang, K. S.; Jeong, S. Y.; Choi, K. C. A review of highly reliable flexible encapsulation technologies towards rollable and foldable OLEDs. *J. Inf. Disp.* **2020**, *21*, 19–32.

[6] Yao, H.; Hou, J. Recent advances in single-junction organic solar cells. *Angew. Chem. Int. Ed.* **2022**, *61*, e202209021.

[7] Riede, M.; Spoltore, D.; Leo, K. Organic solar cells — the path to commercial success. *Adv. Energy Mater.* **2021**, *11*, 2002653.

[8] Kaltenbrunner, M.; White, M. S.; Głowacki, E. D.; Sekitani, T.; Someya, T.; Sariciftci, N. S.; Bauer, S. Ultrathin and lightweight organic solar cells with high flexibility. *Nat. Commun.* **2012**, *3*.

[9] Meiss, J.; Menke, T.; Leo, K.; Uhrich, C.; Gnehr, W.-M.; Sonntag, S.; Pfeiffer, M.; Riede, M. Highly efficient semitransparent tandem organic solar cells with complementary absorber materials. *Appl. Phys. Lett.* **2011**, *99*.

[10] Barcelos, D. A.; Leitao, D. C.; Pereira, L. C. J.; Gonçalves, M. C. What is driving the growth of inorganic glass in smart materials and opto-electronic devices? *Mater.* **2021**, *14*.

[11] Anctil, A.; Lee, E.; Lunt, R. R. Net energy and cost benefit of transparent organic solar cells in building-integrated applications. *Appl. Energy* **2020**, *261*, 114429.

[12] Didoné, E. L.; Wagner, A. Semi-transparent PV windows: A study for office buildings in Brazil. *Energy Build.* **2013**, *67*, 136–142.

[13] Xie, Y.; Xia, R.; Li, T.; Ye, L.; Zhan, X.; Yip, H.-L.; Sun, Y. Highly transparent organic solar cells with all-near-infrared photoactive materials. *Small Methods* **2019**, *3*, 1900424.

[14] Cui, Y.; Yao, H.; Zhang, J.; Xian, K.; Zhang, T.; Hong, L.; Wang, Y.; Xu, Y.; Ma, K.; An, C.; He, C.; Wei, Z.; Gao, F.; Hou, J. Single-junction organic photovoltaic cells with approaching 18% efficiency. *Adv. Mater.* **2020**, *32*, 1908205.

[15] Upama, M. B.; Mahmud, M. A.; Conibeer, G.; Uddin, A. Trendsetters in high-efficiency organic solar cells: Toward 20% power conversion efficiency. *Sol. RRL* **2020**, *4*, 1900342.

[16] Dexter, D. L. Two ideas on energy transfer phenomena: Ion-pair effects involving the OH stretching mode, and sensitization of photovoltaic cells. *J. Lumin.* **1979**, *18-19*, 779–784.

[17] Hanna, M. C.; Nozik, A. J. Solar conversion efficiency of photovoltaic and photoelectrolysis cells with carrier multiplication absorbers. *J. Appl. Phys.* **2006**, *100*, 074510.

[18] Smith, M. B.; Michl, J. Recent advances in singlet fission. *Annu. Rev. Phys. Chem.* **2013**, *64*, 361–386.

[19] Smith, M. B.; Michl, J. Singlet fission. *Chem. Rev.* **2010**, *110*, 6891–6936.

[20] Smyser, K. E.; Eaves, J. D. Singlet fission for quantum information and quantum computing: The parallel JDE model. *Sci. Rep.* **2020**, *10*, 18480.

[21] Kim, H.; Zimmerman, P. M. Coupled double triplet state in singlet fission. *Phys. Chem. Chem. Phys.* **2018**, *20*, 30083–30094.

[22] Miyata, K.; Conrad-Burton, F. S.; Geyer, F. L.; Zhu, X.-Y. Triplet pair states in singlet fission. *Chem. Rev.* **2019**, *119*, 4261–4292.

[23] Birks, J. B. Excimers. *Rep. Prog. Phys.* **1975**, *38*, 903.

[24] Hong, Y.; Kim, W.; Kim, T.; Kaufmann, C.; Kim, H.; Würthner, F.; Kim, D. Real-time observation of structural dynamics triggering excimer formation in a perylene bisimide folda-dimer by ultrafast time-domain raman spectroscopy. *Angew. Chem. Int. Ed.* **2022**, *61*, e202114474.

[25] Bialas, A. L.; Spano, F. C. A Holstein–Peierls approach to excimer spectra: The evolution from vibronically structured to unstructured emission. *J. Phys. Chem. C* **2022**, *126*, 4067–4081.

[26] Gao, Y.; Liu, H.; Zhang, S.; Gu, Q.; Shen, Y.; Ge, Y.; Yang, B. Excimer formation and evolution of excited state properties in discrete dimeric stacking of an anthracene derivative: A computational investigation. *Phys. Chem. Chem. Phys.* **2018**, *20*, 12129–12137.

[27] Hinoue, T.; Shigenoi, Y.; Sugino, M.; Mizobe, Y.; Hisaki, I.; Miyata, M.; Tohnai, N. Regulation of π-stacked anthracene arrangement for fluorescence modulation of organic solid from monomer to excited oligomer emission. *Chem. Eur. J.* **2012**, *18*, 4634–4643.

[28] Wu, J.-J.; Wang, X.-D.; Liao, L.-S. Advances in energy-Level systems of organic lasers. *Laser Photonics Rev.* **2022**, *16*, 2200366.

[29] Wu, J.; Ameri, L.; Cao, L.; Li, J. Efficient excimer-based white OLEDs with reduced efficiency roll-off. *Appl. Phys. Lett.* **2021**, *118*, 073301.

[30] Bossanyi, D. G.; Matthiesen, M.; Wang, S.; Smith, J. A.; Kilbride, R. C.; Shipp, J. D.; Chekulaev, D.; Holland, E.; Anthony, J. E.; Zaumseil, J.; Musser, A. J.; Clark, J. Emissive spin-0 triplet-pairs are a direct product of triplet–triplet annihilation in pentacene single crystals and anthradithiophene films. *Nat. Chem.* **2021**, *13*, 163–171.

[31] Dover, C. B.; Gallaher, J. K.; Frazer, L.; Tapping, P. C.; Petty II, A. J.; Crossley, M. J.; Anthony, J. E.; Kee, T. W.; Schmidt, T. W. Endothermic singlet fission is hindered by excimer formation. *Nat. Chem.* **2018**, *10*, 305–310.

[32] Kim, W.; Nowak-Król, A.; Hong, Y.; Schlosser, F.; Würthner, F.; Kim, D. Solvent-modulated charge-transfer resonance enhancement in the excimer state of a bay-substituted perylene bisimide cyclophane. *J. Phys. Chem. Lett.* **2019**, *10*, 1919–1927.

[33] Mauck, C. M.; Hartnett, P. E.; Margulies, E. A.; Ma, L.; Miller, C. E.; Schatz, G. C.; Marks, T. J.; Wasielewski, M. R. Singlet fission via an excimer-like intermediate in 3,6-bis(thiophen-2-yl)diketopyrrolopyrrole derivatives. *J. Am. Chem. Soc.* **2016**, *138*, 11749–11761.

[34] Walker, B. J.; Musser, A. J.; Beljonne, D.; Friend, R. H. Singlet exciton fission in solution. *Nat. Chem.* **2013**, *5*, 1019–1024.

[35] Miller, C. E.; Wasielewski, M. R.; Schatz, G. C. Modeling singlet fission in rylene and diketopyrrolopyrrole derivatives: The role of the charge transfer state in superexchange and excimer formation. *J. Phys. Chem. C* **2017**, *121*, 10345–10350.

[36] Schrauben, J. N.; Ryerson, J. L.; Michl, J.; Johnson, J. C. Mechanism of singlet fission in thin films of 1,3-diphenylisobenzofuran. *J. Am. Chem. Soc.* **2014**, *136*, 7363–7373.

[37] Sandoval-Salinas, M. E.; Casanova, D. The doubly excited state in singlet fission. *ChemPhotoChem.* **2021**, *5*, 282–293.

[38] Huang, Y.; Buyanova, I. A.; Phansa, C.; Sandoval-Salinas, M. E.; Casanova, D.; Myers, W. K.; Greenham, N. C.; Rao, A.; Chen, W. M.; Puttisong, Y. Competition between triplet pair formation and excimer-like recombination controls singlet fission yield. *Cell Rep. Phys. Sci.* **2021**, *2*, 100339.

[39] Dron, P. I.; Michl, J.; Johnson, J. C. Singlet fission and excimer formation in disordered solids of alkyl-substituted 1,3-diphenylisobenzofurans. *J. Phys. Chem. A* **2017**, *121*, 8596–8603.

[40] Liu, H.; Nichols, V. M.; Shen, L.; Jahansouz, S.; Chen, Y.; Hanson, K. M.; Bardeen, C. J.; Li, X. Synthesis and photophysical properties of a "face-to-face" stacked tetracene dimer. *Phys. Chem. Chem. Phys.* **2015**, *17*, 6523–6531.

[41] Feng, X.; Krylov, A. I. On couplings and excimers: Lessons from studies of singlet fission in covalently linked tetracene dimers. *Phys. Chem. Chem. Phys.* **2016**, *18*, 7751–7761.

[42] Aster, A.; Zinna, F.; Rumble, C.; Lacour, J.; Vauthey, E. Singlet fission in a flexible bichromophore with structural and dynamic control. *J. Am. Chem. Soc.* **2021**, *143*, 2361–2371.

[43] Pensack, R. D.; Tilley, A. J.; Grieco, C.; Purdum, G. E.; Ostroumov, E. E.; Granger, D. B.; Oblinsky, D. G.; Dean, J. C.; Doucette, G. S.; Asbury, J. B.; Loo, Y.-L.;

Seferos, D. S.; Anthony, J. E.; Scholes, G. D. Striking the right balance of intermolecular coupling for high-efficiency singlet fission. *Chem. Sci.* **2018**, *9*, 6240–6259.

[44] Mayonado, G.; Vogt, K. T.; Van Schenck, J. D. B.; Zhu, L.; Fregoso, G.; Anthony, J.; Ostroverkhova, O.; Graham, M. W. High-symmetry anthradithiophene molecular packing motifs promote thermally activated singlet fission. *J. Phys. Chem. C* **2022**, *126*, 4433–4445.

[45] Unger, F.; Moretti, L.; Hausch, J.; Bredehoeft, J.; Zeiser, C.; Haug, S.; Tempelaar, R.; Hestand, N. J.; Cerullo, G.; Broch, K. Modulating singlet fission by scanning through vibronic resonances in pentacene-based blends. *J. Am. Chem. Soc.* **2022**, *144*, 20610–20619.

[46] Young, R. M.; Wasielewski, M. R. Mixed electronic states in molecular dimers: Connecting singlet fission, excimer formation, and symmetry-breaking charge transfer. *Acc. Chem. Res.* **2020**, *53*, 1957–1968.

[47] Piland, G. B.; Bardeen, C. J. How morphology affects singlet fission in crystalline tetracene. *J. Phys. Chem. Lett.* **2015**, *6*, 1841–1846.

[48] Kolata, K.; Breuer, T.; Witte, G.; Chatterjee, S. Molecular packing determines singlet exciton fission in organic semiconductors. *ACS Nano* **2014**, *8*, 7377–7383.

[49] Zeiser, C. F. Controlled variation of intermolecular coupling in polycrystalline thin films of singlet fission chromophores. Ph.D. thesis, Universität Tübingen, 2021.

[50] Mei, J.; Diao, Y.; Appleton, A. L.; Fang, L.; Bao, Z. Integrated materials design of organic semiconductors for field-effect transistors. *J. Am. Chem. Soc.* **2013**, *135*, 6724–6746.

[51] Chen, Y.; Shen, L.; Li, X. Effects of heteroatoms of tetracene and pentacene derivatives on their stability and singlet fission. *J. Phys. Chem. A* **2014**, *118*, 5700–5708.

[52] Clayden, J.; Greeves, N.; Warren, S. *Organic chemistry*; Oxford University Press, 2012.

[53] Köhler, A.; Bässler, H. *Electronic processes in organic semiconductors*; John Wiley & Sons, Inc., 2015.

[54] Friederich, P.; Meded, V.; Poschlad, A.; Neumann, T.; Rodin, V.; Stehr, V.; Symalla, F.; Danilov, D.; Lüdemann, G.; Fink, R. F.; Kondov, I.; von Wrochem, F.; Wenzel, W. Molecular origin of the charge carrier mobility in small molecule organic semiconductors. *Adv. Funct. Mater.* **2016**, *26*, 5757–5763.

[55] Brütting, W. *Physics of organic semiconductors*; Wiley VCH, Weinheim, 2005.

[56] Venables, J. A. *Introduction to surface and thin film processes*; Cambridge University Press, 2000.

[57] Heinemeyer, U.; Hinderhofer, A.; Alonso, M. I.; Ossó, J. O.; Garriga, M.; Kytka, M.; Gerlach, A.; Schreiber, F. Uniaxial anisotropy of organic thin films determined by ellipsometry. *Phys. Stat. Sol. (a)* **2008**, *205*, 927–930.

[58] Hinderhofer, A.; Schreiber, F. Organic–organic heterostructures: Concepts and applications. *ChemPhysChem* **2012**, *13*, 628–643.

[59] Corpinot, M. K.; Bučar, D.-K. A practical guide to the design of molecular crystals. *Cryst. Growth Des.* **2019**, *19*, 1426–1453.

[60] Kitaĭgorodskiĭ, A. I. *Organic chemical crystallography*; Consultants Bureau: New York, 1961.

[61] Lin-Vien, D.; Colthup, N. B.; Fateley, W. G.; Grasselli, J. G. *The handbook of infrared and raman characteristic frequencies of organic molecules*; Academic Press: San Diego, 1991.

[62] Volpati, D.; Aoki, P. H. B.; Alessio, P.; Pavinatto, F. J.; Miranda, P. B.; Constantino, C. J. L.; Oliveira Jr., O. N. Vibrational spectroscopy for probing molecular-level interactions in organic films mimicking biointerfaces. *Adv. Colloid Interface Sci.* **2014**, *207*, 199–215.

[63] Pope, M.; Swenberg, C. E. *Electronic processes in organic crystals and polymers*; Oxford University Press, 1999.

[64] Kupka, H. J. *Transitions in molecular systems*; John Wiley & Sons, Inc., 2010.

[65] Coon, J. B.; DeWames, R. E.; Loyd, C. M. The Franck-Condon principle and the structures of excited electronic states of molecules. *J. Mol. Spectrosc.* **1962**, *8*, 285–299.

[66] McGlynn, S. P.; Azumi, T.; Kinoshita, M. *Molecular spectroscopy of the triplet state*; Prentice-Hall, 1969.

[67] Valeur, B.; Berberan-Santos, M. N. *Molecular fluorescence: principles and applications*; John Wiley & Sons, Inc., 2012.

[68] Kanamaru, N. Radiationless transition between randomly fluctuating levels. S1-T2-T1 intersystem crossing in condensed phase. *Bull. Chem. Soc. Jpn.* **1982**, *55*, 3093–3096.

[69] Birks, J. B. *Photophysics of aromatic molecules*; Wiley-Interscience, 1970.

[70] Kasha, M.; Rawls, H. R.; El-Bayoumi, M. A. The exciton model in molecular spectroscopy. *Pure Appl. Chem.* **1965**, *11*, 371–392.

[71] Yamagata, H.; Norton, J.; Hontz, E.; Olivier, Y.; Beljonne, D.; Brédas, J. L.; Silbey, R. J.; Spano, F. C. The nature of singlet excitons in oligoacene molecular crystals. *J. Chem. Phys.* **2011**, *134*, 204703.

[72] Davydov, A. S. The theory of molecular excitons. *Sov. Phys. Uspekhi* **1964**, *7*, 145.

[73] Spano, F. C.; Yamagata, H. Vibronic coupling in J-aggregates and beyond: A direct means of determining the exciton coherence length from the photoluminescence spectrum. *J. Phys. Chem. B* **2011**, *115*, 5133–5143.

[74] Spano, F. C.; Clark, J.; Silva, C.; Friend, R. H. Determining exciton coherence from the photoluminescence spectral line shape in poly(3-hexylthiophene) thin films. *J. Chem. Phys.* **2009**, *130*, 074904.

[75] Förster, T. Transfer mechanisms of electronic excitation energy. *Radiat. Res. Suppl.* **1960**, *2*, 326–339.

[76] Jang, S.; Newton, M. D.; Silbey, R. J. Multichromophoric förster resonance energy transfer. *Phys. Rev. Lett.* **2004**, *92*, 218301.

[77] Greene, B. I.; Millard, R. R. Singlet-exciton fusion in molecular solids: A direct subpicosecond determination of time-dependent annihilation rates. *Phys. Rev. Lett.* **1985**, *55*, 1331–1334.

[78] Birks, J. B.; Kazzaz, A. A. Excimer fluorescence XII. The pyrene crystal excimer interaction potential. *Proc. R. Soc. Lond. A.* **1968**, *304*, 291–301.

[79] Jenekhe, S. A.; Osaheni, J. A. Excimers and exciplexes of conjugated polymers. *Science* **1994**, *265*, 765–768.

[80] Tempelaar, R.; Reichman, D. R. Vibronic exciton theory of singlet fission. III. How vibronic coupling and thermodynamics promote rapid triplet generation in pentacene crystals. *J. Chem. Phys.* **2018**, *148*, 244701.

[81] Monahan, N.; Zhu, X.-Y. Charge transfer–mediated singlet fission. *Annu. Rev. Phys. Chem.* **2015**, *66*, 601–618.

[82] Li, J.; Cao, H.; Zhang, Z.; Liu, S.; Xia, Y. Research progress on singlet fission in acenes and their derivatives. *Photonics* **2022**, *9*.

[83] Yong, C. K. et al. The entangled triplet pair state in acene and heteroacene materials. *Nat. Commun.* **2017**, *8*, 15953.

[84] Tao, G. Energy fluctuations induced quantum decoherence and exciton localization in singlet fission. *J. Phys. Chem. C* **2019**, *123*, 29571–29579.

[85] Tayebjee, M. J. Y.; Sanders, S. N.; Kumarasamy, E.; Campos, L. M.; Sfeir, M. Y.; McCamey, D. R. Quintet multiexciton dynamics in singlet fission. *Nat. Phys.* **2017**, *13*, 182–188.

[86] Lukman, S.; Richter, J. M.; Yang, L.; Hu, P.; Wu, J.; Greenham, N. C.; Musser, A. J. Efficient singlet fission and triplet-pair emission in a family of zethrene diradicaloids. *J. Am. Chem. Soc.* **2017**, *139*, 18376–18385.

[87] Zeiser, C.; Moretti, L.; Lepple, D.; Cerullo, G.; Maiuri, M.; Broch, K. Singlet heterofission in tetracene–pentacene thin-film blends. *Angew. Chem. Int. Ed.* **2020**, *59*, 19966–19973.

[88] Forrest, S. R. Ultrathin organic films grown by organic molecular beam deposition and related techniques. *Chem. Rev.* **1997**, *97*, 1793–1896.

[89] Kowarik, S.; Gerlach, A.; Schreiber, F. Organic molecular beam deposition: fundamentals, growth dynamics, and in situ studies. *J. Phys.: Condens. Matter* **2008**, *20*, 184005.

[90] Schreiber, F. Organic molecular beam deposition: Growth studies beyond the first monolayer. *Phys. Status Solidi A* **2004**, *201*, 1037–1054.

[91] Gutzler, R.; Heckl, W. M.; Lackinger, M. Combination of a Knudsen effusion cell with a quartz crystal microbalance: In situ measurement of molecular evaporation rates with a fully functional deposition source. *Rev. Sci. Instrum.* **2010**, *81*, 015108.

[92] Broch, K.; Dieterle, J.; Branchi, F.; Hestand, N. J.; Olivier, Y.; Tamura, H.; Cruz, C.; Nichols, V. M.; Hinderhofer, A.; Beljonne, D.; Spano, F. C.; Cerullo, G.; Bardeen, C. J.; Schreiber, F. Robust singlet fission in pentacene thin films with tuned charge transfer interactions. *Nat. Comm.* **2018**, *9*, 954.

[93] Hammer, S.; Ferschke, T.; Eyb, G.; Pflaum, J. Phase transition induced spectral tuning of dual luminescent crystalline zinc-phthalocyanine thin films and OLEDs. *Appl. Phys. Lett.* **2019**, *115*, 263303.

[94] Williams, M. L.; Schlesinger, I.; Ramirez, C. E.; Jacobberger, R. M.; Brown, P. J.; Young, R. M.; Wasielewski, M. R. Effect of crystallinity on endoergic singlet fission in perylenediimide single crystals and polycrystalline films. *J. Phys. Chem. C* **2022**, *126*, 10287–10297.

[95] Kittel, C. *Einführung in die festkörperphysik*; Oldenbourg Wissenschaftsverlag, 2013.

[96] Ashcroft, N. W.; Mermin, D. N. *Festkörperphysik*; Oldenbourg Wissenschaftsverlag, 2007.

[97] Warren, B. E. *X-ray diffraction*; Reading, Mass.: Addison-Wesley Pub. Co, 1969.

[98] Patterson, A. L. The Scherrer formula for X-ray particle size determination. *Phys. Rev.* **1939**, *56*, 978–982.

[99] Mocuta, C.; Stanescu, S.; Gallard, M.; Barbier, A.; Dawiec, A.; Kedjar, B.; Leclercq, N.; Thiaudiere, D. Fast X-ray reflectivity measurements using an X-ray pixel area detector at the DiffAbs beamline, Synchrotron SOLEIL. *J. Synchrotron Radiat.* **2018**, *25*, 204–213.

[100] Yoon, H.; Hong, S.; Lee, S. H.; Cho, I. H.; Kim, H. J. GIWAXS Analysis on preferred orientation in metal halide perovskite films via alkylamines. *Electron. Mater. Lett.* **2022**, *18*, 456–464.

[101] Kowarik, S.; Gerlach, A.; Hinderhofer, A.; Milita, S.; Borgatti, F.; Zontone, F.; Suzuki, T.; Biscarini, F.; Schreiber, F. Structure, morphology, and growth dynamics of perfluoro-pentacene thin films. *Phys. Status Solidi Rapid Res. Lett.* **2008**, *2*, 120–122.

[102] Aufderheide, A.; Broch, K.; Novák, J.; Hinderhofer, A.; Nervo, R.; Gerlach, A.; Banerjee, R.; Schreiber, F. Mixing-induced anisotropic correlations in molecular crystalline systems. *Phys. Rev. Lett.* **2012**, *109*, 156102.

[103] Birkholz, M. *Thin film analysis by X-ray scattering*; Wiley VCH, Weinheim, 2006.

[104] Schmidbauer, M.; Schäfer, P.; Besedin, S.; Grigoriev, D.; Köhler, R.; Hanke, M. A novel multi-detection technique for three-dimensional reciprocal-space mapping in grazing-incidence X-ray diffraction. *J. Synchrotron Radiat.* **2008**, *15*, 549–557.

[105] Vernon-Parry, K. D. Scanning electron microscopy: An introduction. *III-Vs Rev.* **2000**, *13*, 40–44.

[106] Flegler, S. L.; Heckman, J. W.; Klomparens, K. L. *Scanning and transmission electron microscopy: An introduction*; Oxford University Press, 1993.

[107] Hestand, N. J.; Spano, F. C. Expanded theory of H-and J-molecular aggregates: the effects of vibronic coupling and intermolecular charge transfer. *Chem. Rev.* **2018**, *118*, 7069–7163.

[108] Stenzel, O. *The physics of thin film optical spectra*; Springer Cham, Heidelberg, New York, Dordrecht, London, 2016.

[109] Poruba, A.; Fejfar, A.; Remeš, Z.; Špringer, J.; Vaněček, M.; Kočka, J.; Meier, J.; Torres, P.; Shah, A. Optical absorption and light scattering in microcrystalline silicon thin films and solar cells. *J. Appl. Phys.* **2000**, *88*, 148–160.

[110] Hofberger, W. Structure and optical properties of polycrystalline evaporated tetracene films. *Phys. Status Solidi (a)* **1975**, *30*, 271–278.

[111] Gauglitz, G.; Moore, D. S. *Handbook of spectroscopy*; John Wiley & Sons, Inc., 2014.

[112] Lakowicz, J. R. *Principles of fluorescence spectroscopy*; Springer, Berlin, Heidelberg, 2006.

[113] Mooney, J.; Kambhampati, P. Get the basics right: Jacobian conversion of wavelength and energy scales for quantitative analysis of emission spectra. *J. Phys. Chem. Lett.* **2013**, *4*, 3316–3318.

[114] Siegman, A. E. *Lasers*; University Science Books, 1986.

[115] Takahashi, A.; Nishizawa, M.; Inagaki, Y.; Koishi, M.; Kinoshita, K. New femtosecond streak camera with temporal resolution of 180 fs. Generation, Amplification, and Measurement of Ultrashort Laser Pulses. 1994; pp 275–284.

[116] Komura, M.; Itoh, S. Fluorescence measurement by a streak camera in a single-photon-counting mode. *Photosynth. Res.* **2009**, *101*, 119–133.

[117] Amesz, J.; Hoff, A. J. *Biophysical techniques in photosynthesis*; Kluwer Academic Publishers, Dordrecht, 1996.

[118] van Stokkum, I. H. M.; Larsen, D. S.; Van Grondelle, R. Global and target analysis of time-resolved spectra. *Biochim. Biophys. Acta Bioenerg.* **2004**, *1658*, 262.

[119] Burdett, J. J.; Müller, A. M.; Gosztola, D.; Bardeen, C. J. Excited state dynamics in solid and monomeric tetracene: The roles of superradiance and exciton fission. *J. Chem. Phys.* **2010**, *133*, 144506.

[120] Burdett, J. J.; Bardeen, C. J. Quantum beats in crystalline tetracene delayed fluorescence due to triplet pair coherences produced by direct singlet fission. *J. Am. Chem. Soc.* **2012**, *134*, 8597–8607.

[121] Snellenburg, J. J.; Laptenok, S.; Seger, R.; Mullen, K. M.; van Stokkum, I. H. M. Glotaran: A Java-based graphical user interface for the R package TIMP. *J. Stat. Software* **2012**, *49*, 1–22.

[122] Mamada, M.; Katagiri, H.; Mizukami, M.; Honda, K.; Minamiki, T.; Teraoka, R.; Uemura, T.; Tokito, S. Syn-/anti-anthradithiophene derivative isomer effects on semiconducting properties. *ACS Appl. Mater. Interfaces* **2013**, *5*, 9670–9677.

[123] Hallani, R. K.; Thorley, K. J.; Mei, Y.; Parkin, S. R.; Jurchescu, O. D.; Anthony, J. E. Structural and electronic properties of crystalline, isomerically pure anthradithiophene derivatives. *Adv. Funct. Mater.* **2016**, *26*, 2341–2348.

[124] Kwon, O.; Coropceanu, V.; Gruhn, N. E.; Durivage, J. C.; Laquindanum, J. G.; Katz, H. E.; Cornil, J.; Brédas, J. L. Characterization of the molecular parameters determining charge transport in anthradithiophene. *J. Chem. Phys.* **2004**, *120*, 8186–8194.

[125] Laquindanum, J. G.; Katz, H. E.; Lovinger, A. J. Synthesis, morphology, and field-effect mobility of anthradithiophenes. *J. Am. Chem. Soc.* **1998**, *120*, 664–672.

[126] Wang, C.-H.; Jian, S.-D.; Chan, S.-W.; Ku, C.-S.; Huang, P.-Y.; Chen, M.-C.; Yang, Y.-W. Enhanced stability of organic field-effect transistors with blend pentacene/anthradithiophene films. *J. Phys. Chem. C* **2012**, *116*, 1225–1231.

[127] Tylleman, B.; Vande Velde, C. M. L.; Balandier, J.-Y.; Stas, S.; Sergeyev, S.; Geerts, Y. H. Synthesis of isomerically pure anti-anthradithiophene derivatives. *Org. Lett.* **2011**, *13*, 5208–5211.

[128] Gish, M. K.; Thorley, K. J.; Parkin, S. R.; Anthony, J. E.; Johnson, J. C. Hydrogen bonding optimizes singlet fission in carboxylic acid functionalized anthradithiophene films. *ChemPhotoChem* **2021**, *5*, 68–78.

[129] Nguyen, T. P.; Roy, P.; Shim, J. H. Remarkable charge-transfer mobility from [6] to [10]phenacene as a high performance p-type organic semiconductor. *Phys. Chem. Chem. Phys.* **2018**, *20*, 8658–8667.

[130] Zwadlo, M.; Hagara, J.; Duva, G.; Hagenlocher, J.; Gerlach, A.; Zaluzhnyy, I.; Hodas, M.; Hinderhofer, A.; Siffalovic, P.; Schreiber, F. Structure of thin films of [6] and [7] phenacene and impact of potassium deposition. *Adv. Opt. Mater.* **2021**, *9*, 2002193.

[131] He, X.; Eguchi, R.; Goto, H.; Uesugi, E.; Hamao, S.; Takabayashi, Y.; Kubozono, Y. Fabrication of single crystal field-effect transistors with phenacene-type molecules and their excellent transistor characteristics. *Org. Electron.* **2013**, *14*, 1673–1682.

[132] Okamoto, H.; Kawasaki, N.; Kaji, Y.; Kubozono, Y.; Fujiwara, A.; Yamaji, M. Air-assisted high-performance field-effect transistor with thin films of picene. *J. Am. Chem. Soc.* **2008**, *130*, 10470–10471.

[133] Hervé, P.; Vandamme, L. K. J. General relation between refractive index and energy gap in semiconductors. *Infrared Phys. Techn.* **1994**, *35*, 609–615.

[134] Chan, W.-L.; Ligges, M.; Zhu, X.-Y. The energy barrier in singlet fission can be overcome through coherent coupling and entropic gain. *Nat. Chem.* **2012**, *4*, 840–845.

[135] Arias, D. H.; Ryerson, J. L.; Cook, J. D.; Damrauer, N. H.; Johnson, J. C. Polymorphism influences singlet fission rates in tetracene thin films. *Chem. Sci.* **2016**, *7*, 1185–1191.

[136] Cruz, C. D.; Chronister, E. L.; Bardeen, C. J. Using temperature dependent fluorescence to evaluate singlet fission pathways in tetracene single crystals. *J. Chem. Phys.* **2020**, *153*, 234504.

[137] Burdett, J. J.; Gosztola, D.; Bardeen, C. J. The dependence of singlet exciton relaxation on excitation density and temperature in polycrystalline tetracene thin films: Kinetic evidence for a dark intermediate state and implications for singlet fission. *J. Chem. Phys.* **2011**, *135*, 214508.

[138] Tayebjee, M. J. Y.; Clady, R. G. C. R.; Schmidt, T. W. The exciton dynamics in tetracene thin films. *Phys. Chem. Chem. Phys.* **2013**, *15*, 14797–14805.

[139] Nahm, R. K.; Engstrom, J. R. Who's on first? Tracking in real time the growth of multiple crystalline phases of an organic semiconductor: Tetracene on SiO_2. *J. Chem. Phys.* **2017**, *146*, 052815.

[140] Campbell, R. B.; Robertson, J. M.; Trotter, J. The crystal structure of hexacene, and a revision of the crystallographic data for tetracene. *Acta Crystallogr.* **1962**, *15*, 289–290.

[141] Siegrist, T.; Kloc, C.; Schön, J. H.; Batlogg, B.; Haddon, R. C.; Berg, S.; Thomas, G. A. Enhanced physical properties in a pentacene polymorph. *Angew. Chem. Int. Ed.* **2001**, *40*, 1732–1736.

[142] Schiefer, S.; Huth, M.; Dobrinevski, A.; Nickel, B. Determination of the crystal structure of substrate-induced pentacene polymorphs in fiber structured thin films. *J. Am. Chem. Soc.* **2007**, *129*, 10316–10317.

[143] Deng, G.-H.; Qian, Y.; Li, X.; Zhang, T.; Jiang, W.; Harutyunyan, A. R.; Chen, G.; Chen, H.; Rao, Y. Singlet fission driven by anisotropic vibronic coupling in single-crystalline pentacene. *J. Phys. Chem. Lett.* **2021**, *12*, 3142–3150.

[144] Rao, A.; Wilson, M. W. B.; Albert-Seifried, S.; Di Pietro, R.; Friend, R. H. Photophysics of pentacene thin films: The role of exciton fission and heating effects. *Phys. Rev. B* **2011**, *84*, 195411.

[145] Tempelaar, R.; Reichman, D. R. Vibronic exciton theory of singlet fission. I. Linear absorption and the anatomy of the correlated triplet pair state. *J. Chem. Phys.* **2017**, *146*, 174703.

[146] Zeiser, C.; Cruz, C.; Reichman, D. R.; Seitz, M.; Hagenlocher, J.; Chronister, E. L.; Bardeen, C. J.; Tempelaar, R.; Broch, K. Vacancy control in acene blends links exothermic singlet fission to coherence. *Nat. Commun.* **2021**, *12*, 5149.

[147] Roy, D.; Das, N. M.; Shakti, N.; Gupta, P. S. Comparative study of optical, structural and electrical properties of zinc phthalocyanine Langmuir–Blodgett thin film on annealing. *RSC Adv.* **2014**, *4*, 42514–42522.

[148] Wöhrle, D.; Schnurpfeil, G.; Makarov, S. G.; Kazarin, A.; Suvorova, O. N. Practical applications of phthalocyanines–from dyes and pigments to materials for optical, electronic and photo-electronic devices. *Macroheterocycles* **2012**, *5*, 191–202.

[149] Ahn, H.; Liou, W.-H.; Chen, H.-M. P.; Hsu, C.-H. Anisotropic exciton relaxation in nanostructured metal (Zn and F_{16}Zn)-phthalocyanine. *Opt. Express* **2015**, *23*, 3230–3235.

[150] Senthilarasu, S.; Hahn, Y. B.; Lee, S.-H. Structural analysis of zinc phthalocyanine (ZnPc) thin films: X-ray diffraction study. *J. Appl. Phys.* **2007**, *102*, 043512.

[151] Hoshino, A.; Takenaka, Y.; Miyaji, H. Redetermination of the crystal structure of α-copper phthalocyanine grown on KCl. *Acta Crystallogr.* **2003**, *B59*, 393–403.

[152] Brown, C. J. Crystal structure of β-copper phthalocyanine. *J. Chem. Soc. A* **1968**, 2488–2493.

[153] Bart, J. C. J. The crystal structure of a modification of hexaphenylbenzene. *Acta Crystallogr.* **1968**, *24*, 1277–1287.

[154] Vij, V.; Bhalla, V.; Kumar, M. Hexaarylbenzene: Evolution of properties and applications of multitalented scaffold. *Chem. Rev.* **2016**, *116*, 9565–9627.

[155] Hausch, J.; Berges, A. J.; Zeiser, C.; Rammler, T.; Morlok, A.; Bredehöft, J.; Hammer, S.; Pflaum, J.; Bardeen, C. J.; Broch, K. Distinguishing between triplet-pair state and excimer emission in singlet fission chromophores using mixed thin films. *J. Phys. Chem. C* **2022**, *126*, 6686–6693.

[156] He, R.; Chi, X.; Pinczuk, A.; Lang, D. V.; Ramirez, A. P. Extrinsic optical recombination in pentacene single crystals: Evidence of gap states. *Appl. Phys. Lett.* **2005**, *87*, 211117.

[157] Aoki-Matsumoto, T.; Furuta, K.; Yamada, T.; Moriya, H.; Mizuno, K.; Matsui, A. H. Excitonic photoluminescence in pentacene single crystal. *Int. J. Mod. Phys. B* **2001**, *15*, 3753–3756.

[158] Anger, F.; Ossó, J. O.; Heinemeyer, U.; Broch, K.; Scholz, R.; Gerlach, A.; Schreiber, F. Photoluminescence spectroscopy of pure pentacene, perfluoropentacene, and mixed thin films. *J. Chem. Phys.* **2012**, *136*, 054701.

[159] Ni, W.; Sun, L.; Gurzadyan, G. G. Ultrafast spectroscopy reveals singlet fission, ionization and excimer formation in perylene film. *Sci. Rep.* **2021**, *11*, 5220.

[160] Stern, H. L.; Musser, A. J.; Gelinas, S.; Parkinson, P.; Herz, L. M.; Bruzek, M. J.; Anthony, J.; Friend, R. H.; Walker, B. J. Identification of a triplet pair intermediate in singlet exciton fission in solution. *P. Natl. Acad. Sci.* **2015**, *112*, 7656–7661.

[161] Thampi, A.; Stern, H. L.; Cheminal, A.; Tayebjee, M. J. Y.; Petty II, A. J.; Anthony, J. E.; Rao, A. Elucidation of excitation energy dependent correlated triplet pair formation pathways in an endothermic singlet fission system. *J. Am. Chem. Soc.* **2018**, *140*, 4613–4622.

[162] Musser, A. J.; Clark, J. Triplet-pair states in organic semiconductors. *Annu. Rev. Phys. Chem.* **2019**, *70*, 323–351.

[163] Dutta, P. Grazing incidence X-ray diffraction. *Curr. Sci.* **2000**, *78*, 1478–1483.

[164] Kitaigorodsky, A. I. *Mixed crystals*; Springer, Berlin, Heidelberg, 1984.

[165] Lennard-Jones, J. E. Cohesion. *Proc. Phys. Soc.* **1931**, *43*, 461.

[166] Beljonne, D.; Yamagata, H.; Brédas, J. L.; Spano, F. C.; Olivier, Y. Charge-transfer excitations steer the Davydov splitting and mediate singlet exciton fission in pentacene. *Phys. Rev. Lett.* **2013**, *110*, 226402.

[167] Gallivan, J. B.; Brinen, J. S. Polarization of electronic transitions of aromatic hydrocarbons. *J. Chem. Phys.* **1969**, *50*, 1590–1595.

[168] Zimmerman, P. M.; Zhang, Z.; Musgrave, C. B. Singlet fission in pentacene through multi-exciton quantum states. *Nat. Chem.* **2010**, *2*, 648–652.

[169] Zeng, T.; Hoffmann, R.; Ananth, N. The low-lying electronic states of pentacene and their roles in singlet fission. *J. Am. Chem. Soc.* **2014**, *136*, 5755–5764.

[170] Sung, J.; Kim, P.; Fimmel, B.; Würthner, F.; Kim, D. Direct observation of ultrafast coherent exciton dynamics in helical π-stacks of self-assembled perylene bisimides. *Nat. Commun.* **2015**, *6*, 8646.

[171] Kaufmann, C.; Kim, W.; Nowak-Król, A.; Hong, Y.; Kim, D.; Würthner, F. Ultrafast exciton delocalization, localization, and excimer formation dynamics in a highly defined perylene bisimide quadruple π-stack. *J. Am. Chem. Soc.* **2018**, *140*, 4253–4258.

[172] Hofeditz, N.; Hausch, J.; Broch, K.; Heimbrodt, W.; Schreiber, F.; Gerhard, M. Efficient Energy Transfer and Singlet Fission in Co-Deposited Thin Films of Pentacene and Anthradithiophene. *Adv. Opt. Mater.* **2024**, 2300922.

[173] Son, H. J.; Carsten, B.; Jung, I. H.; Yu, L. Overcoming efficiency challenges in organic solar cells: rational development of conjugated polymers. *Energy Environ. Sci.* **2012**, *5*, 8158–8170.

[174] Rand, B. P.; Richter, H. *Organic solar cells: fundamentals, devices, and upscaling*; CRC Press, 2014.

[175] Li, Y.; Ji, C.; Qu, Y.; Huang, X.; Hou, S.; Li, C.-Z.; Liao, L.-S.; Guo, L. J.; Forrest, S. R. Enhanced light utilization in semitransparent organic photovoltaics using an optical outcoupling architecture. *Adv. Mater.* **2019**, *31*, 1903173.

[176] Cao, W.; Xue, J. Recent progress in organic photovoltaics: device architecture and optical design. *Energy Environ. Sci.* **2014**, *7*, 2123–2144.

[177] Menke, S. M.; Holmes, R. J. Exciton diffusion in organic photovoltaic cells. *Energy Environ. Sci.* **2014**, *7*, 499–512.

[178] Jiang, K.; Zhang, J.; Peng, Z.; Lin, F.; Wu, S.; Li, Z.; Chen, Y.; Yan, H.; Ade, H.; Zhu, Z., et al. Pseudo-bilayer architecture enables high-performance organic solar cells with enhanced exciton diffusion length. *Nat. Commun.* **2021**, *12*, 468.

[179] Menke, S. M.; Luhman, W. A.; Holmes, R. J. Tailored exciton diffusion in organic photovoltaic cells for enhanced power conversion efficiency. *Nat. Mater.* **2013**, *12*, 152–157.

[180] Menke, S. M.; Mullenbach, T. K.; Holmes, R. J. Directing energy transport in organic photovoltaic cells using interfacial exciton gates. *ACS nano* **2015**, *9*, 4543–4552.

[181] Fratini, S.; Nikolka, M.; Salleo, A.; Schweicher, G.; Sirringhaus, H. Charge transport in high-mobility conjugated polymers and molecular semiconductors. *Nat. Mater.* **2020**, *19*, 491–502.

[182] Hains, A. W.; Liang, Z.; Woodhouse, M. A.; Gregg, B. A. Molecular semiconductors in organic photovoltaic cells. *Chem. Rev.* **2010**, *110*, 6689–6735.

[183] Shtein, M.; Mapel, J.; Benziger, J. B.; Forrest, S. R. Effects of film morphology and gate dielectric surface preparation on the electrical characteristics of organic-vapor-phase-deposited pentacene thin-film transistors. *Appl. Phys. Lett.* **2002**, *81*, 268–270.

[184] Tang, H.; Bai, Y.; Zhao, H.; Qin, X.; Hu, Z.; Zhou, C.; Huang, F.; Cao, Y. Interface engineering for highly efficient organic solar cells. *Adv. Mater.* **2023**, 2212236.

[185] Tress, W.; Inganäs, O. Simple experimental test to distinguish extraction and injection barriers at the electrodes of (organic) solar cells with S-shaped current–voltage characteristics. *Sol. Energy Mater. Sol. Cells* **2013**, *117*, 599–603.

[186] Zou, Y.; Holmes, R. J. Influence of a MoOx interlayer on the open-circuit voltage in organic photovoltaic cells. *Appl. Phys. Lett.* **2013**, *103*, 053302.

[187] Ratcliff, E. L.; Zacher, B.; Armstrong, N. R. Selective interlayers and contacts in organic photovoltaic cells. *J. Phys. Chem. Lett.* **2011**, *2*, 1337–1350.

[188] Yang, L.; Yan, L.; You, W. Organic solar cells beyond one pair of donor–acceptor: ternary blends and more. *J. Phys. Chem. Lett.* **2013**, *4*, 1802–1810.

[189] Nabok, D.; Puschnig, P.; Ambrosch-Draxl, C.; Werzer, O.; Resel, R.; Smilgies, D.-M. Crystal and electronic structures of pentacene thin films from grazing-incidence x-ray diffraction and first-principles calculations. *Phys. Rev. B* **2007**, *76*, 235322.

[190] Ruiz, R.; Mayer, A. C.; Malliaras, G. G.; Nickel, B.; Scoles, G.; Kazimirov, A.; Kim, H.; Headrick, R. L.; Islam, Z. Structure of pentacene thin films. *Appl. Phys. Lett.* **2004**, *85*, 4926–4928.

[191] Spano, F. C. The fundamental photophysics of conjugated oligomer herringbone aggregates. *J. Chem. Phys.* **2003**, *118*, 981–994.

[192] Seto, K.; Furukawa, Y. Study on solid structure of pentacene thin films using Raman imaging. *J. Raman Spectrosc.* **2012**, *43*, 2015–2019.

[193] Chan, W.-L.; Berkelbach, T. C.; Provorse, M. R.; Monahan, N. R.; Tritsch, J. R.; Hybertsen, M. S.; Reichman, D. R.; Gao, J.; Zhu, X.-Y. The quantum coherent mechanism for singlet fission: Experiment and theory. *Acc. Chem. Res.* **2013**, *46*, 1321–1329.

[194] Bakulin, A. A.; Morgan, S. E.; Kehoe, T. B.; Wilson, M. W. B.; Chin, A. W.; Zigmantas, D.; Egorova, D.; Rao, A. Real-time observation of multiexcitonic states in ultrafast singlet fission using coherent 2D electronic spectroscopy. *Nat. Chem.* **2016**, *8*, 16–23.

[195] Dean, J. C.; Zhang, R.; Hallani, R. K.; Pensack, R. D.; Sanders, S. N.; Oblinsky, D. G.; Parkin, S. R.; Campos, L. M.; Anthony, J. E.; Scholes, G. D. Photophysical characterization and time-resolved spectroscopy of a anthradithiophene dimer: exploring the role of conformation in singlet fission. *Phys. Chem. Chem. Phys.* **2017**, *19*, 23162–23175.

[196] Förster, T. Zwischenmolekulare energiewanderung und fluoreszenz. *Ann. Phys.* **1948**, *437*, 55–75.

[197] Mikhnenko, O. V.; Blom, P. W. M.; Nguyen, T.-Q. Exciton diffusion in organic semiconductors. *Energy Environ. Sci.* **2015**, *8*, 1867–1888.

[198] Hausch, J.; Hofeditz, N.; Bredehöft, J.; Hammer, S.; Pflaum, J.; Broch, K.; Gerhard, M.; Schreiber, F. Influence of excited-state delocalization on singlet fission: tuning triplet-pair-state emission in thin films. *J. Phys. Chem. C* **2023**, *127*, 3778–3786.

[199] Margulies, E. A.; Logsdon, J. L.; Miller, C. E.; Ma, L.; Simonoff, E.; Young, R. M.; Schatz, G. C.; Wasielewski, M. R. Direct observation of a charge-transfer state preceding high-yield singlet fission in terrylenediimide thin films. *J. Am. Chem. Soc.* **2017**, *139*, 663–671.

[200] Eaton, S. W.; Miller, S. A.; Margulies, E. A.; Shoer, L. E.; Schaller, R. D.; Wasielewski, M. R. Singlet exciton fission in thin films of tert-butyl-substituted terrylenes. *J. Phys. Chem. A* **2015**, *119*, 4151–4161.

[201] Pensack, R. D.; Tilley, A. J.; Parkin, S. R.; Lee, T. S.; Payne, M. M.; Gao, D.; Jahnke, A. A.; Oblinsky, D. G.; Li, P.-F.; Anthony, J. E.; Seferos, D. S.; Scholes, G. D. Exciton delocalization drives rapid singlet fission in nanoparticles of acene derivatives. *J. Am. Chem. Soc.* **2015**, *137*, 6790–6803.

[202] Dillon, R. J.; Piland, G. B.; Bardeen, C. J. Different rates of singlet fission in monoclinic versus orthorhombic crystal forms of diphenylhexatriene. *J. Am. Chem. Soc.* **2013**, *135*, 17278–17281.

[203] Tao, G. Nonadiabatic simulation of singlet fission dynamics in tetracene clusters: The topology of quantum coherence in a global view. *J. Chem. Phys.* **2019**, *151*, 054308.

[204] Wang, L.; Olivier, Y.; Prezhdo, O. V.; Beljonne, D. Maximizing singlet fission by intermolecular packing. *J. Phys. Chem. Lett.* **2014**, *5*, 3345–3353.

[205] Harcourt, R. D.; Scholes, G. D.; Ghiggino, K. P. Rate expressions for excitation transfer. II. Electronic considerations of direct and through–configuration exciton resonance interactions. *J. Chem. Phys.* **1994**, *101*, 10521–10525.

[206] Jacobberger, R. M.; Qiu, Y.; Williams, M. L.; Krzyaniak, M. D.; Wasielewski, M. R. Using molecular design to enhance the coherence time of quintet multiexcitons generated by singlet fission in single crystals. *J. Am. Chem. Soc.* **2022**, *144*, 2276–2283.

[207] Lee, T. S.; Lin, Y. L.; Kim, H.; Rand, B. P.; Scholes, G. D. Two temperature regimes of triplet transfer in the dissociation of the correlated triplet pair after singlet fission. *Can. J. Chem.* **2019**, *97*, 465–473.

[208] Xu, R.; Zhang, C.; Xiao, M. Magnetic field effects on singlet fission dynamics. *Trends Chem.* **2022**, *4*, 528–539.

[209] Hudson, R. J.; Stuart, A. N.; Huang, D. M.; Kee, T. W. What next for singlet fission in photovoltaics? The fate of triplet and triplet-pair excitons. *J. Phys. Chem. C* **2022**, *126*, 5369–5377.

[210] Banerjee, R.; Hinderhofer, A.; Weinmann, M.; Reisz, B.; Lorch, C.; Gerlach, A.; Oettel, M.; Schreiber, F. Interrupted growth to manipulate phase separation in DIP:C60 prganic semiconductor blends. *J. Phys. Chem. C* **2018**, *122*, 1839–1845.

[211] Banerjee, R.; Novák, J.; Frank, C.; Lorch, C.; Hinderhofer, A.; Gerlach, A.; Schreiber, F. Evidence for kinetically limited thickness dependent phase separation in organic thin film blends. *Phys. Rev. Lett.* **2013**, *110*, 185506.

[212] Wang, C.; Russegger, N.; Duva, G.; Konovalov, O. V.; Jankowski, M.; Gerlach, A.; Hinderhofer, A.; Schreiber, F. Growth, structure and templating of anthradithiophene and its β-methylthiolated derivative. *Mater. Chem. Front.* **2022**, *6*, 3422–3430.

[213] Feng, S.; Wang, Y.-C.; Ke, Y.; Liang, W.; Zhao, Y. Effect of charge-transfer states on the vibrationally resolved absorption spectra and exciton dynamics in ZnPc aggregates: Simulations from a non-Makovian stochastic Schrödinger equation. *J. Chem. Phys.* **2020**, *153*, 034116.

[214] Jennings, C.; Aroca, R.; Hor, A.-M.; Loutfy, R. O. Raman spectra of solid films 3—Mg, Cu and Zn phthalocyanine complexes. *J. Raman Spec.* **1984**, *15*, 34–37.

[215] Sugino, M.; Araki, Y.; Hatanaka, K.; Hisaki, I.; Miyata, M.; Tohnai, N. Elucidation of anthracene arrangement for excimer emission at ambient conditions. *Crys. Growth Des.* **2013**, *13*, 4986–4992.

[216] Flanders, N. C.; Kirschner, M. S.; Kim, P.; Fauvell, T. J.; Evans, A. M.; Helweh, W.; Spencer, A. P.; Schaller, R. D.; Dichtel, W. R.; Chen, L. X. Large exciton diffusion coefficients in two-dimensional covalent organic frameworks with different domain sizes revealed by ultrafast exciton dynamics. *J. Am. Chem. Soc.* **2020**, *142*, 14957–14965.

[217] Casanova, D. Theoretical investigations of the perylene electronic structure: Monomer, dimers, and excimers. *Int. J. Quantum Chem.* **2015**, *115*, 442–452.

[218] Johnson, J. C. Open questions on the photophysics of ultrafast singlet fission. *Commun. Chem.* **2021**, *4*, 85.

[219] Sanders, S. N.; Pun, A. B.; Parenti, K. R.; Kumarasamy, E.; Yablon, L. M.; Sfeir, M. Y.; Campos, L. M. Understanding the bound triplet-pair state in singlet fission. *Chem.* **2019**, *5*, 1988–2005.

[220] Herzberg, G.; Teller, E. Schwingungsstruktur der elektronenübergänge bei mehratomigen molekülen. *Z. Phys. Chem.* **1933**, *21*, 410–446.

[221] Kolb, V.; Pflaum, J. Hybrid metal-organic nanocavity arrays for efficient light outcoupling. *Opt. Express* **2017**, *25*, 6678–6689.

[222] Sandanayaka, A. S. D.; Ito, O.; Zhang, M.; Ajima, K.; Iijima, S.; Yudasaka, M.; Murakami, T.; Tsuchida, K. Photoinduced electron transfer in zinc phthalocyanine

loaded on single-walled carbon nanohorns in aqueous solution. *Adv. Mater.* **2009**, *21*, 4366–4371.

[223] Tempelaar, R.; Spano, F. C.; Knoester, J.; Jansen, T. L. C. Mapping the evolution of spatial exciton coherence through time-resolved fluorescence. *J. Phys. Chem. Lett.* **2014**, *5*, 1505–1510.

[224] Qian, Y.; Zhang, T.; Han, J.; Harutyunyan, A. R.; Chen, G.; Rao, Y.; Chen, H. Symmetry-breaking enhanced Herzberg–Teller effect with brominated polyacenes. *J. Phys. Chem. A* **2021**, *125*, 3589–3599.

[225] Lunt, R. R.; Benziger, J. B.; Forrest, S. R. Relationship between crystalline order and exciton diffusion length in molecular organic semiconductors. *Adv. Mater.* **2010**, *22*, 1233–1236.

[226] Seiler, H.; Krynski, M.; Zahn, D.; Hammer, S.; Windsor, Y. W.; Vasileiadis, T.; Pflaum, J.; Ernstorfer, R.; Rossi, M.; Schwoerer, H. Nuclear dynamics of singlet exciton fission in pentacene single crystals. *Sci. Adv.* **2021**, *7*, eabg0869.

[227] Clark, J.; Silva, C.; Friend, R. H.; Spano, F. C. Role of intermolecular coupling in the photophysics of disordered organic semiconductors: aggregate emission in regioregular polythiophene. *Phys. Rev. Lett.* **2007**, *98*, 206406.

[228] Gierschner, J.; Mack, H.-G.; Lüer, L.; Oelkrug, D. Fluorescence and absorption spectra of oligophenylenevinylenes: Vibronic coupling, band shapes, and solvatochromism. *J. Chem. Phys.* **2002**, *116*, 8596–8609.

[229] Wu, C. C.; Korovyanko, O. J.; Delong, M. C.; Vardeny, Z. V.; Ferraris, J. P. Optical studies of distyrylbenzene single crystals. *Synth. Met.* **2003**, *139*, 735–738.

[230] Zhang, M.; Wang, W.; Yin, S.; Meng, R.; Li, C.; Gao, K. Temperature effect on the internal conversion dynamics following different stimulated absorptions in a conjugated polymer. *Org. Electron.* **2018**, *56*, 201–207.

[231] Litvinenko, K. L.; Webber, N. M.; Meech, S. R. Internal conversion in the chromophore of the green fluorescent protein: temperature dependence and isoviscosity analysis. *J. Phys. Chem. A* **2003**, *107*, 2616–2623.

[232] Tamura, H.; Huix-Rotllant, M.; Burghardt, I.; Olivier, Y.; Beljonne, D. First-principles quantum dynamics of singlet fission: Coherent versus thermally activated mechanisms governed by molecular π stacking. *Phys. Rev. Lett.* **2015**, *115*, 107401.

[233] Miyata, K.; Kurashige, Y.; Watanabe, K.; Sugimoto, T.; Takahashi, S.; Tanaka, S.; Takeya, J.; Yanai, T.; Matsumoto, Y. Coherent singlet fission activated by symmetry breaking. *Nat. Chem.* **2017**, *9*, 983–989.

[234] Athanasopoulos, S.; Hoffmann, S. T.; Bässler, H.; Köhler, A.; Beljonne, D. To hop or not to hop? Understanding the temperature dependence of spectral diffusion in organic semiconductors. *J. Phys. Chem. Lett.* **2013**, *4*, 1694–1700.

[235] Seyfang, R.; Port, H.; Wolf, H. C. Picosecond study on excimer formation in pyrene single crystals II. The excimer precursor state in the high-temperature phase. *J. Lumin.* **1988**, *42*, 127–135.

[236] Walker, B.; Port, H.; Wolf, H. C. The two-step excimer formation in perylene crystals. *Chem. Phys.* **1985**, *92*, 177–185.

[237] Kaiser, C.; Sandberg, O. J.; Zarrabi, N.; Li, W.; Meredith, P.; Armin, A. A universal Urbach rule for disordered organic semiconductors. *Nat. Commun.* **2021**, *12*, 3988.

[238] Cölle, M.; Brütting, W. Thermal, structural and photophysical properties of the organic semiconductor Alq_3. *Phys. Stat. Sol. (a)* **2004**, *201*, 1095–1115.

[239] Xie, X.; Santana-Bonilla, A.; Fang, W.; Liu, C.; Troisi, A.; Ma, H. Exciton–phonon interaction model for singlet fission in prototypical molecular crystals. *J. Chem. Theory Comput.* **2019**, *15*, 3721–3729.

[240] Tao, G. Bath effect in singlet fission dynamics. *J. Phys. Chem. C* **2014**, *118*, 27258–27264.

[241] Andreasson, M.; Ilver, L.; Kanski, J.; Andersson, T. G. Organic molecular beam deposition system and initial studies of organic layer growth. *Phys. Scr.* **2006**, *2006*, 1–5.

[242] Tanaka, S.; Miyata, K.; Sugimoto, T.; Watanabe, K.; Uemura, T.; Takeya, J.; Matsumoto, Y. Enhancement of the exciton coherence size in organic semiconductor by alkyl chain substitution. *J. Phys. Chem. C* **2016**, *120*, 7941–7948.

[243] Theurer, C. P.; Valencia, A. M.; Hausch, J.; Zeiser, C.; Sivanesan, V.; Cocchi, C.; Tegeder, P.; Broch, K. Photophysics of charge transfer complexes formed by tetracene and strong acceptors. *J. Phys. Chem. C* **2021**, *125*, 6313–6323.

[244] Tom, R.; Gao, S.; Yang, Y.; Zhao, K.; Bier, I.; Buchanan, E. A.; Zaykov, A.; Havlas, Z.; Michl, J.; Marom, N. Inverse design of tetracene polymorphs with enhanced singlet fission performance by property-based genetic algorithm optimization. *Chem. Mater.* **2023**, *35*, 1373–1386.

[245] Aster, A.; Licari, G.; Zinna, F.; Brun, E.; Kumpulainen, T.; Tajkhorshid, E.; Lacour, J.; Vauthey, E. Tuning symmetry breaking charge separation in perylene bichromophores by conformational control. *Chem, Sci.* **2019**, *10*, 10629–10639.

[246] Marciniak, H.; Fiebig, M.; Huth, M.; Schiefer, S.; Nickel, B.; Selmaier, F.; Lochbrunner, S. Ultrafast exciton relaxation in microcrystalline pentacene films. *Phys. Rev. Lett.* **2007**, *99*, 176402.

[247] Wilson, M. W. B.; Rao, A.; Clark, J.; Kumar, R. S. S.; Brida, D.; Cerullo, G.; Friend, R. H. Ultrafast dynamics of exciton fission in polycrystalline pentacene. *J. Am. Chem. Soc.* **2011**, *133*, 11830–11833.

[248] Platt, A. D.; Day, J.; Subramanian, S.; Anthony, J. E.; Ostroverkhova, O. Optical, fluorescent, and (photo)conductive properties of high-performance functionalized pentacene and anthradithiophene aerivatives. *J. Phys. Chem. C* **2009**, *113*, 14006–14014.

[249] Xie, X.; Ma, H. Opposite anisotropy effects of singlet and triplet exciton diffusion in tetracene crystal. *ChemistryOpen* **2016**, *5*, 201–205.

[250] Vaubel, G.; Baessler, H. Diffusion of singlet excitons in tetracene crystals. *Mol. Cryst.* **1970**, *12*, 47–56.

[251] Berghuis, A. M.; Raziman, T. V.; Halpin, A.; Wang, S.; Curto, A. G.; Rivas, J. G. Effective negative diffusion of singlet excitons in organic semiconductors. *J. Phys. Chem. Lett.* **2021**, *12*, 1360–1366.

A. Appendix: Excimeric emission in blends with spacer molecules

To support the results in Chapter 7, the following raw data are presented. This includes GID maps of the ADT:6Ph and ADT:TET systems as well as decay traces of the free exciton emission and the RSL from the TRPL maps. Lastly, raw data of the exciton decay traces of ADT in a thin film and in solution are shown, as well as the respective spectra.

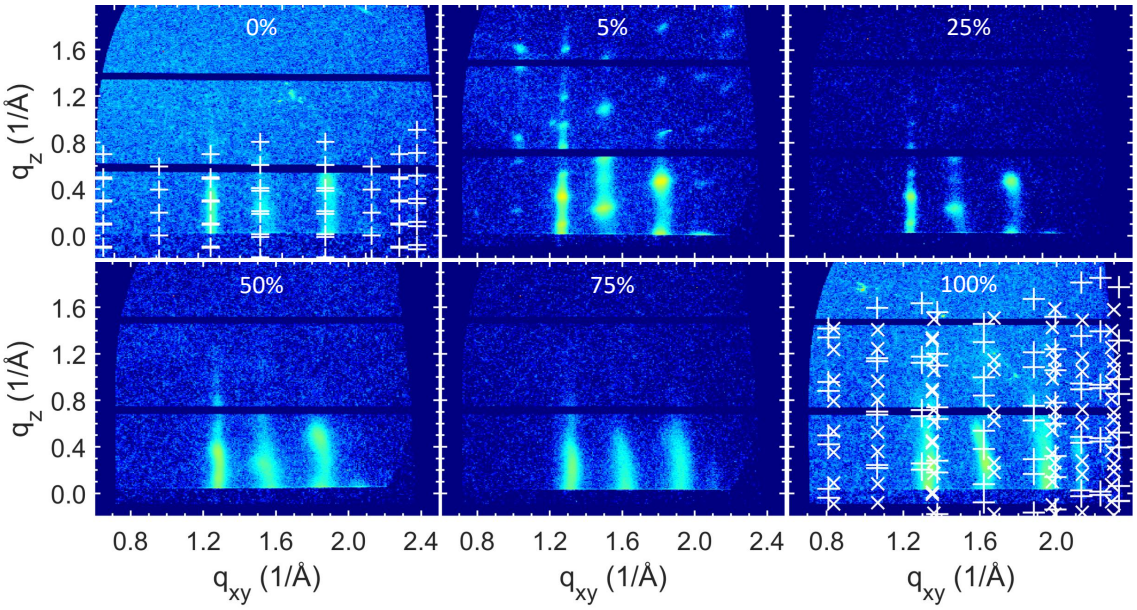

Figure A.1.: All GID maps of mixtures of ADT and 6Ph show features typical for a herringbone structure. The mixing ratio of ADT is given in mol-% in each respective map. In the maps of the neat films, the expected Bragg peak positions of the known structures are given. Namely, for neat 6Ph the thin film structure of Ref. [130] is given and for ADT the single crystal structures of anti-ADT (white +) and syn-ADT (white x) of Ref. [122]. Each map has been intensity integrated along q_z in the range $0.1\,\text{Å}^{-1} < q_z < 0.3\,\text{Å}^{-1}$ to produce Figure 7.1b.

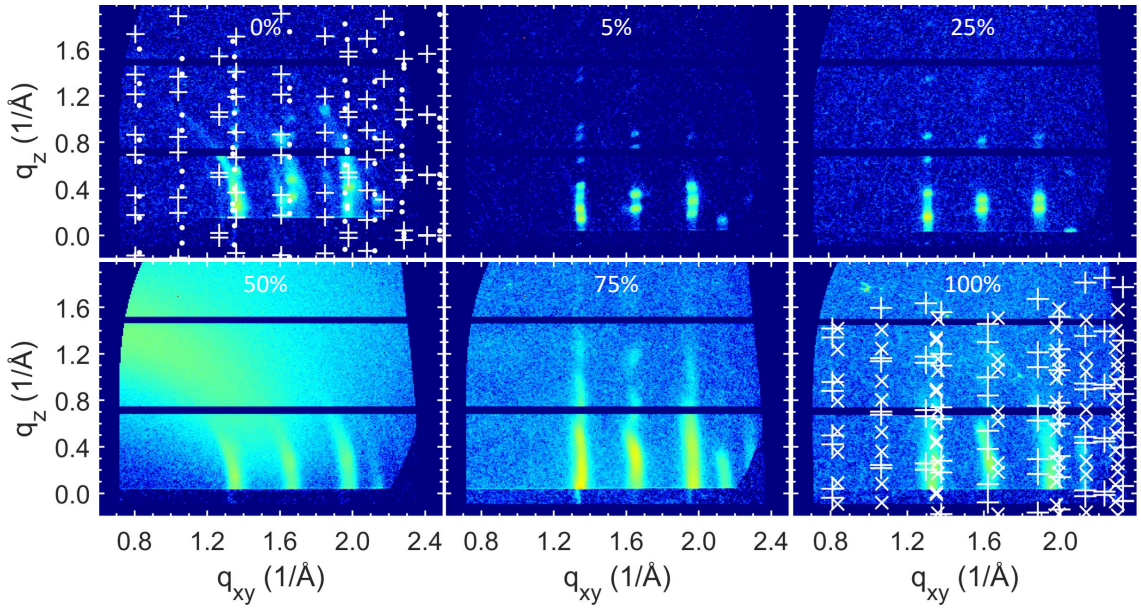

Figure A.2.: All GID maps of mixtures of ADT and TET show features typical for a herringbone structure. The mixing ratio of ADT is given in mol-% in each respective map. In the maps of the neat films, the expected Bragg peak positions of the known structures are given. Namely, for neat TET the thin film structure (white •) and bulk structure (white +) of Ref. [139] is given and for ADT the single crystal structures of anti-ADT (white +) and syn-ADT (white x) of Ref. [122]. Each map has been intensity integrated along q_z in the range $0.1\,\text{Å}^{-1} < q_z < 0.3\,\text{Å}^{-1}$ to produce Figure 7.1d.

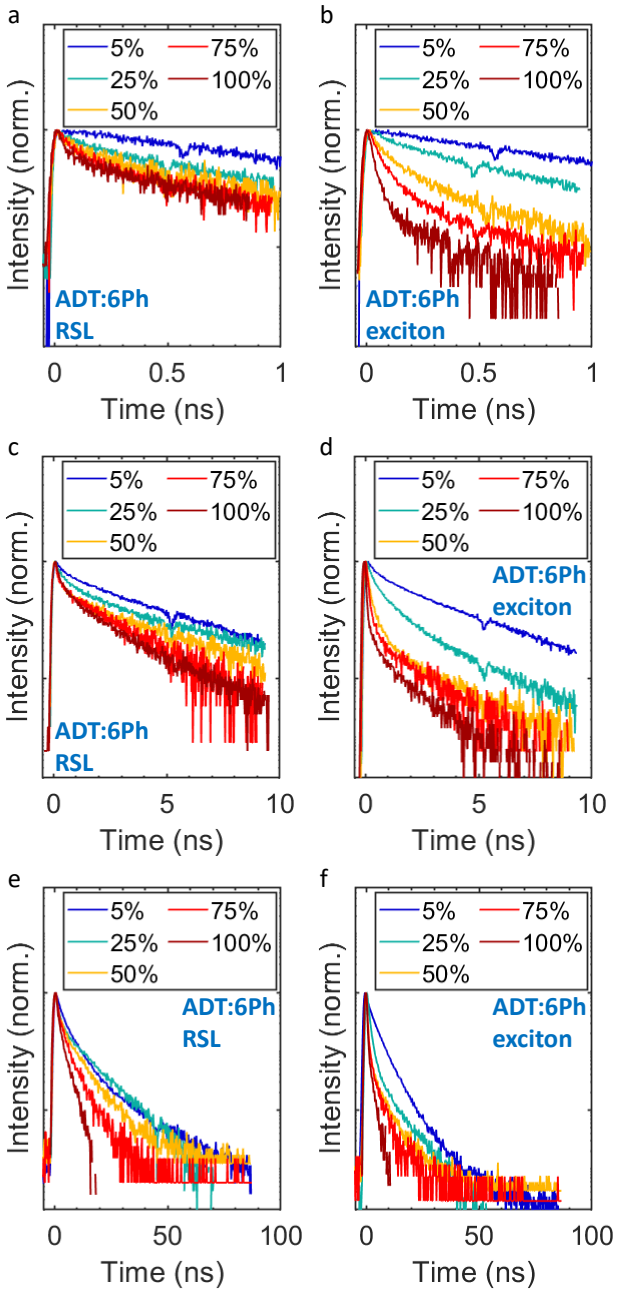

Figure A.3.: The decay traces of the RSL (a,c,e) and the free exciton emission (b,d,f) of the ADT:6Ph system on different timescales are normalized to the intensity right after excitation. The y-axis is scaled logarithmically. The photon energy of the exciting laser was 3.1 eV. The spectral integration interval of each time trace can be found in Table 7.1 and was adapted to the spectral position of each emission feature for each sample. The dip in the data after half the measuring time is an artifact of the setup. The ADT concentration of each film is given in mol-% in the legend.

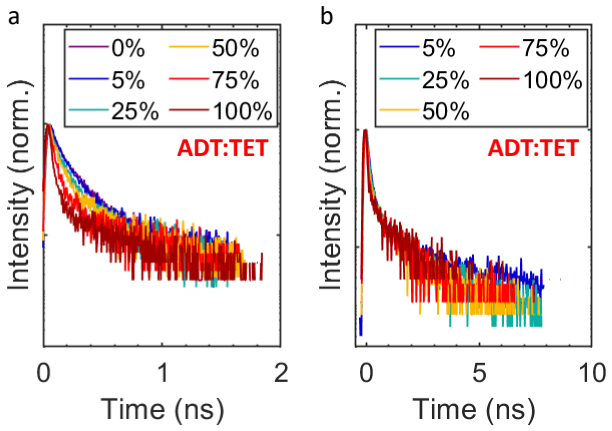

Figure A.4.: The decay traces of the free exciton emission of the ADT:TET system on different timescales are normalized to the intensity right after excitation. The y-axis is scaled logarithmically. The photon energy of the exciting laser was 3.1 eV. The spectral integration interval of each time trace can be found in Table 7.1 and was adapted to the spectral position of the free exciton emission for each sample. The ADT concentration of each film is given in mol-% in the legend.

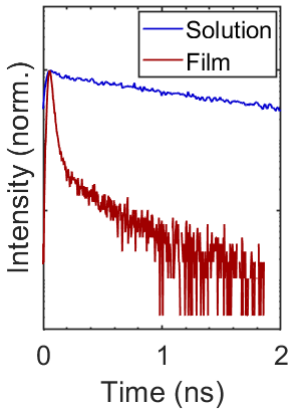

Figure A.5.: The decay traces of the S_1 state of ADT in solution and of the free exciton emission of an ADT thin film are normalized to the intensity right after excitation. The y-axis is scaled logarithmically. The photon energy of the exciting laser was 3.1 eV. The fast-decaying part in the film is not present in solution, indicating that the fast decay might be an intermolecular process such as singlet fission.

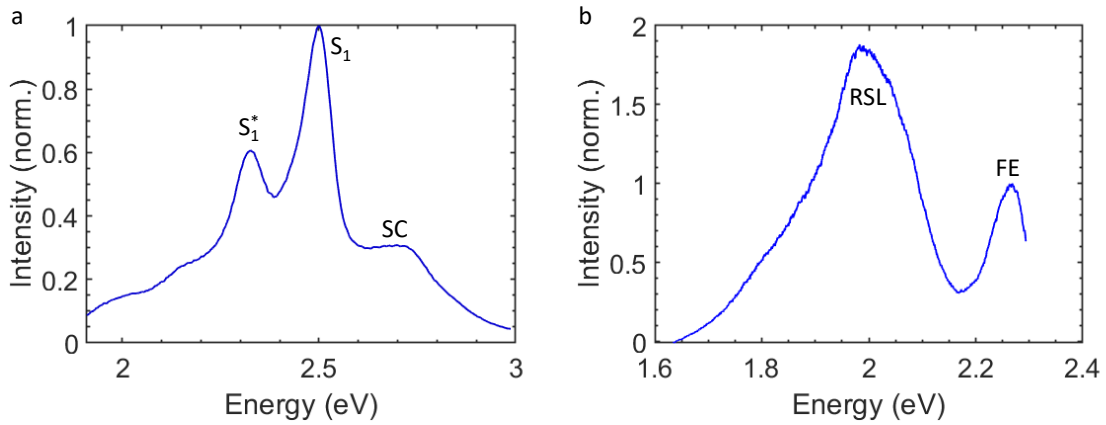

Figure A.6.: (a) The quasi steady-state PL spectrum of ADT in $CHCl_3$ solution is normalized to the S_1 emission. The peak at 2.7 eV (SC) is a scattering peak of the laser, the peak at 2.5 eV (S_1) is assigned to S_1 emission with a vibronic replica at 2.3 eV (S_1^*). The photon energy of the exciting laser was 3.1 eV. (b) The steady-state spectrum of an ADT single crystal is normalized with respect to the free exciton emission (FE) and also shows RSL (RSL), proving that the presence of grain boundaries is not necessary for X_{RSL} formation. The excimer emission is distorted in shape due to ^{1}(TT) emission, which will be discussed in Chapter 9. The photon energy of the exciting laser was 2.33 eV.

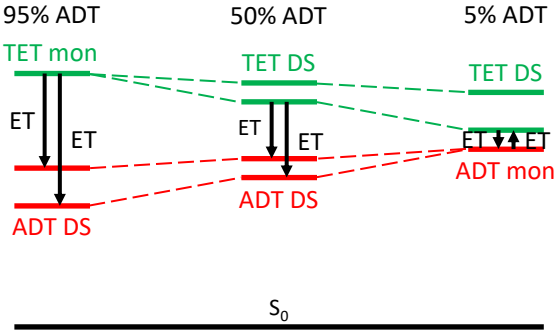

Figure A.7.: Sketch of the changes in the energetic landscape of the S_1 state of ADT (red) and TET (green) with changing mixing ratios in ADT:TET blends. For low amounts of ADT (TET), most ADT (TET) molecules are surrounded by exclusively TET (ADT) molecules, hence no ADT (TET) Davydov splitting is present, resulting in monomer-like (mon) behavior. In all other cases, a Davydov splitting (DS) is present and increases with increasing concentrations of the respective compound [92]. At high and intermediate ADT concentrations, the energy of the TET S_1 state is clearly above the energy of the ADT S_1 state, resulting in only downward energy transfer (ET) from TET to ADT being relevant. In case of low ADT fractions (right side of the figure), the TET S_1 state and the ADT S_1 state move close enough in energy that energy transfer in both directions is relevant. Due to intraband relaxation the energy transfer is always expected to start at the lower energy Davydov component.

B. Appendix: Singlet fission in the presence of energetically low-lying states

In the following GID maps on the basis of which the GID linescans (Figure 8.1b) were extracted are shown. Additionally, statistical calculations are presented, in which the average distance between two neighboring PEN molecules is estimated, as well as an estimation of the PEN luminescence quenching rate due to the decay channel of energy transfer from PEN monomers to PEN agglomerates, followed by PEN singlet fission.

B.1. Estimation of the average distance to the next PEN molecule

For the estimation of the average distance of a given lattice site to the closest PEN molecule, the crystal is represented as a random distribution of molecules with the same molecular density as the crystal. Hence a volume of

$$V_{\mathrm{mol}} = \frac{1}{2}\, a\, b\, d_z \equiv r_0^3, \tag{B.1}$$

with the values of a, b and d_z from Figure 8.1, is assigned to each molecule. Now, the probability of finding the closest PEN molecule in a radial shell $[r, r+\Delta r]$ is

$$P(r,\Delta r) = (1-c)^{\frac{4\pi(r^3-r_0^3)}{3V_{\mathrm{mol}}}} \cdot \left(1-(1-c)^{\frac{4\pi((r+\Delta r)^3-r^3)}{3V_{\mathrm{mol}}}}\right) \tag{B.2}$$

with the molar PEN concentration c. $P(r,\Delta r)$ is the probability of finding no PEN molecule closer to the admolecule than r multiplied with the probability of finding at least one molecule in the radial shell $[r, r+\Delta r]$. The volume r_0^3 is subtracted since it is occupied

by the admolecule. Tayloring Equation B.6 to the first order of Δr results in

$$P_1(r) = (1-c)^{\frac{4\pi(r^3-r_0^3)}{3V_{\mathrm{mol}}}} \cdot (-\frac{4\pi r^2)}{V_{\mathrm{mol}}}) \ln(1-c)\,\Delta r, \tag{B.3}$$

which can be multiplied by r and integrated to calculate the average distance from our admolecule to the closest PEN molecule, resulting in

$$\langle r \rangle = \int_{r_0}^{\infty} (1-c)^{\frac{4\pi(r^3-r_0^3)}{3V_{\mathrm{mol}}}} \cdot (-\frac{4\pi r^3)}{V_{\mathrm{mol}}}) \ln(1-c)\,\Delta r. \tag{B.4}$$

In case of $c = 0.025$ one receives $\langle r \rangle \approx 2.0144\, r_0 \approx 1.363\,\mathrm{nm}$. For higher PEN concentrations this value is even lower.

B.2. Simulation of concentration-dependent PEN luminescence quenching

To find out whether the luminescence decay of PEN in mixtures can be explained accurately by FRET to lattice sites at which singlet fission is possible, simulations have been performed. These simulations start with an excited PEN molecule at a lattice site at which singlet fission is not possible, i.e. surrounded by ADT molecules. From there, FRET occurs to an other PEN molecule, which can be either isolated or have a next neighbor of the same species. In the latter case singlet fission, i.e. luminescence quenching is expected, in the former case one more FRET to another proximate PEN molecules is simulated until a lattice site is occupied at which singlet fission can occur. In the simulation the sample is treated as a heteromolecular gas with the same molecular density and the same PEN concentration as in the crystal structure found in Figure 8.1. Since the excited PEN molecule is not allowed to have a direct PEN neighbor in-plane in the simulation, the distance to the center of the next PEN molecule has to be at least the unit cell parameters (due to two molecules per unit cell the next neighbor in-plane is closer than the unit cell parameters). This results in a volume of

$$V_{\mathrm{iso}} = \pi\, a \left(1 - \frac{1}{2}\sqrt{\frac{1}{2}}\right) b \left(1 - \frac{1}{2}\sqrt{\frac{1}{2}}\right) d_z \approx 0.418\,\pi\, a\, b\, d_z \tag{B.5}$$

with the lattice parameters a, b and d_z from Figure 8.1c–d, in which no PEN molecule can be due to preconditions. The term $1/2\sqrt{1/2}\,a$ ($1/2\sqrt{1/2}\,b$) is subtracted from a (b) in

Equation B.5 due to the in-plane area occupied by the neighboring molecule itself.

In this setup, the statistical average number of PEN molecules in a radial shell of the range $[r, r + \Delta r]$ is

$$N(r, \Delta r) = \frac{4\pi((r + \Delta r)^3 - r^3)}{3V_{\mathrm{mol}}}\, c \tag{B.6}$$

for $r^3 > V_{\mathrm{iso}}$ with the volume V_{mol} occupied per molecule and the PEN concentration c. Tayloring Equation B.6 to the first order of Δr results in

$$N(r, \Delta r) \approx \frac{4\pi r^2}{V_{\mathrm{mol}}}\, c\, \Delta r. \tag{B.7}$$

Multiplying this term with the FRET rate

$$k_{\mathrm{ET}} = k_{\mathrm{D}} \frac{R_0^6}{r^6} \tag{B.8}$$

and the probability of the energy accepting PEN molecule to be on a luminescence quenching site, i.e. having at least one direct PEN neighbor,

$$P_{\mathrm{qu}} = 1 - (1 - c)^4, \tag{B.9}$$

and integrating over r results in the luminescence quenching rate due to FRET from isolated sites to sites that are capable of singlet fission. The resulting equation is

$$k_{\mathrm{qu}} = \int_{\sqrt[3]{V_{\mathrm{iso}}}}^{\infty} \left(1 - (1 - c)^4\right) \left(k_{\mathrm{D}} \frac{R_0^6}{r^6}\right) \frac{4\pi r^2}{V_{\mathrm{mol}}}\, c \;\mathrm{d}r \tag{B.10}$$

with the radial integration starting at $\sqrt[3]{V_{\mathrm{iso}}}$ since only FRET from isolated PEN molecules is considered, which are sites that have no PEN molecules closer to them than $\sqrt[3]{V_{\mathrm{iso}}}$. Solving the integral results in

$$k_{\mathrm{qu}} = \left(1 - (1 - c)^4\right) k_{\mathrm{D}}\, R_0^6\, \frac{4\pi}{V_{\mathrm{mol}}} c\, \frac{1}{3V_{\mathrm{iso}}}, \tag{B.11}$$

which is the term used for the simulations of the quenching rate due to FRET. In the simulations $V_{\mathrm{mol}} = \frac{1}{2}\, a \cdot b \cdot d_z$ and $V_{\mathrm{iso}} = 0.4179\, \pi \cdot a \cdot b \cdot d_z$ is used. The luminescent decay rate of PEN is $k_{\mathrm{D}} = 0.0637\,\mathrm{ns}^{-1}$ [248] and the Förster radius is calculated to be $R_0 = 7.396\,\mathrm{nm}$ using Equation 4.7. In this equation, $\kappa^2 = 2/3$ and $n = 2$ was assumed and the overlap integral was calculated based on the absorption and emission spectra in Figure 8.2.

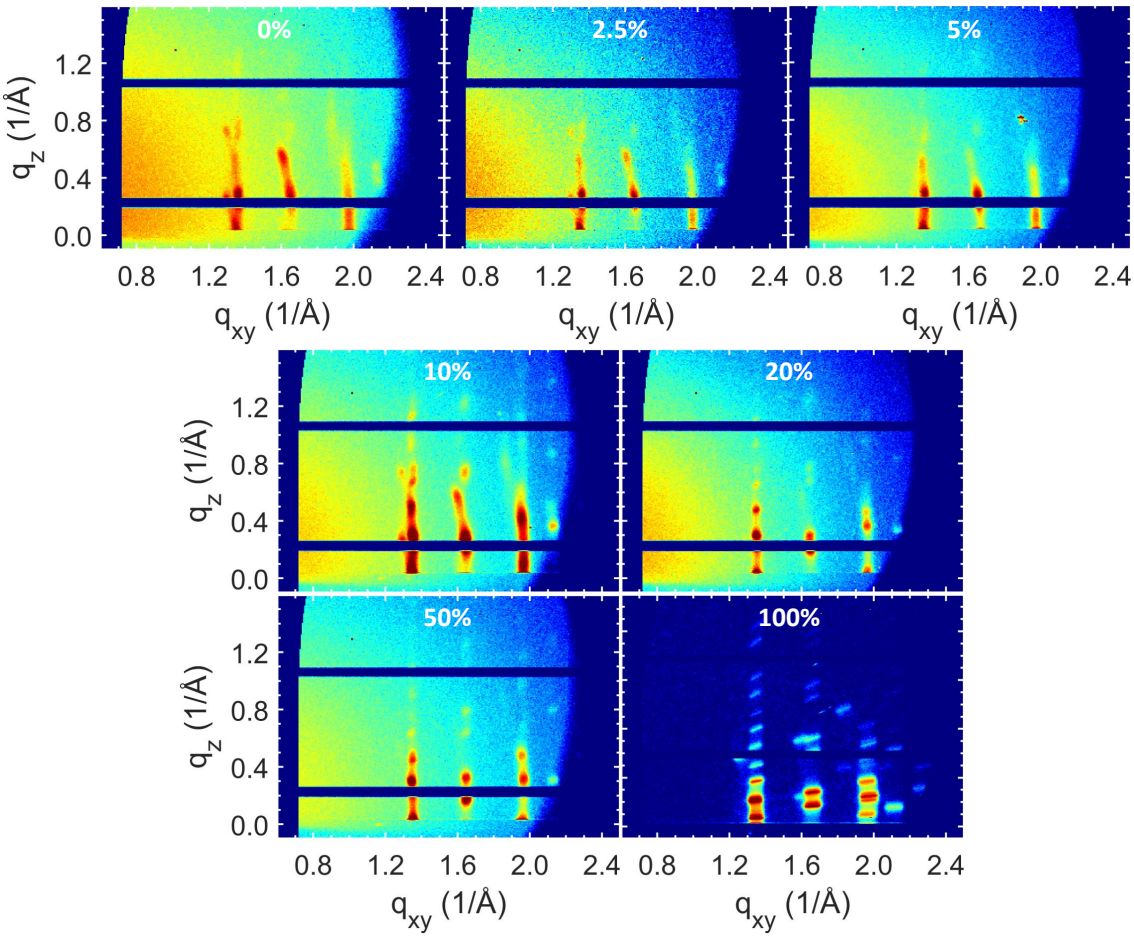

Figure B.1.: All GID maps of mixtures of ADT and PEN show features typical for a herringbone structure. The mixing ratio of PEN is given in mol-% in each respective map. The Bragg peaks of neat PEN have an increased broadness due to the use of a larger substrate, leading to a larger footprint of the incoming beam on the sample, which is projected onto the detector. Each map has been intensity integrated along q_z in the range $0.1\,\text{Å}^{-1} < q_z < 0.3\,\text{Å}^{-1}$ to produce Figure 8.1b.

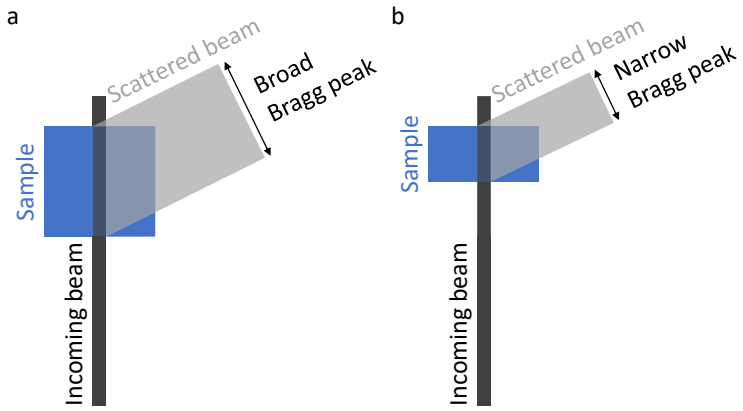

Figure B.2.: Top-view sketch of the Bragg peak broadening in GIWAXS experiments due to the sample extension in beam direction. The larger sample (a) leads to a larger footprint of the incoming beam on the sample compared to the smaller sample (b). The spatial extension of this footprint is then projected on the detector via the scattering angle. This broadening effect is more significant the closer the scattering angle to 90° and the larger the footprint of the incoming beam on the sample.

C. Appendix: Excited-state delocalization and singlet fission

In the following chapter synchrotron-based high-resolution GIWAXS data of the ADT:ZnPC system and the raw TRPL data are shown. Additionally, PL data of an ADT single crystal, of ADT in solution and from multiple series of binary films containing ADT and ZnPC are plotted. Also, the high spectral overlap of ADT excimer emission and ZnPC absorption is highlighted by plotting the respective spectra in the same figure.

Besides this supporting data, a growth model, which supports the hypothesis of a higher ADT crystallite quality at low ADT concentrations is presented. After that, simulations are presented that explain how a time-dependent evolution of the excited-state delocalization can be extracted from TRPL data.

C.1. Growth model for the binary films

The photophysics of the binary films of ADT and ZnPC presented in Chapter 9 suggests that the quality of the ADT crystallites is increased in binary films with low amounts of ADT compared to binary films with higher amounts of ADT. Although this result seems counterintuitive, a physical growth model, which supports this hypothesis, is presented in the following. During preparation of the samples, the total growth rate was kept the same for all films, which means that films with higher concentrations of ADT have a higher ADT deposition rate. In the case of binary films with very low ADT concentrations, the low deposition rate of ADT leads to a hampered formation of ADT grains and to a slow growth velocity of existing ADT crystallites. This can in the end lead to ADT crystallites of higher quality in binary films with low amounts of ADT [58, 241]. The increased crystallite quality might reduce the significance of trap states for the photophysics of the corresponding samples [242] and the hampered grain formation increases the average distance between neighboring ADT crystallites, making the occurrence of boundaries between two ADT grains less frequent.

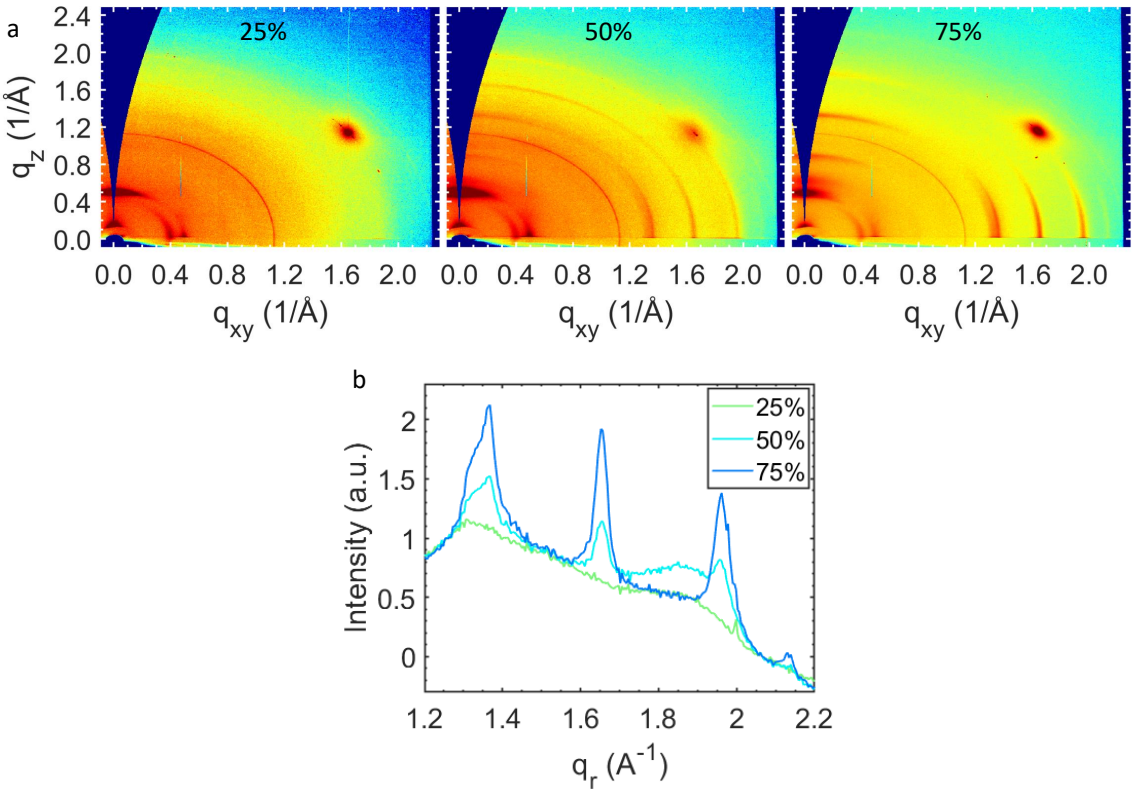

Figure C.1.: (a) The ring-like features at q_r values of 1.35, 1.65 and 1.95 Å^{-1} in the GID maps of binary films are only visible in films with 50 % and 75 % ADT and assigned to ADT. The molar ADT concentrations are given in each map. The measurements were conducted at beamline P08 (DESY, Hamburg) with an incident angle of $\Theta_{inc} = 0.07^\circ$. The ring at $q_r = 1.1$ Å^{-1} is a diffraction peak of the cone used for sample protection and the peak at $q_{xy} = 1.65$ Å^{-1} and $q_z = 1.15$ Å^{-1} is a diffraction peak of silicon oxide from the substrate. (b) The GID maps from (a) have been cut to values of $q_z < 0.8$ Å^{-1} and after that the intensities have then been plotted against the absolute scattering vector q_r to visualize potential trends in the width of the peaks with changing ADT concentrations. Molar ADT concentrations are given in the legend. At 25 % ADT, the Bragg peaks of ADT are overshadowed by the scattering background.

Experimental evidence for this concept has been approached by conducting synchrotron-based high-resolution GIWAXS experiments with the binary films. Since the ADT features in the binary films are ring-like, the GIWAXS intensity has then been plotted against the absolute scattering vector $q_r = \sqrt{q_z^2 + q_{xy}^2}$ in Figure C.1b. Unfortunately, already at 25 % ADT the scattering background of the sample makes the rings visually disappear (Figure C.1a) and for the binary films with higher amounts of ADT the complicated shape of the background made it impossible to get precise fitting results upon application of Gaussian shapes to the Bragg peaks. Hence, for none of the samples an estimation of the Bragg peak width was possible, which could have been then used to draw conclusions on the crystallite size via Equation 5.11 and hence to extract information about the crystallite quality.

Although ADT and ZnPC were found to phase-separate, there are kinetic and entropic arguments for small amounts of ADT in ZnPC crystallites and for small amounts of ZnPC in ADT crystallites [58]. From the kinetic perspective, a molecule of the one species might be kinetically trapped in between molecules of the other species during growth, making a spatial movement of the molecule impossible and leading to the molecule being incorporated into a grain of the other molecular species. The entropic perspective to this phenomenon is based on the free energy of mixing [58]

$$F_{\text{mix}} = k_{\text{B}}T\, x_A \ln x_A + k_{\text{B}}T\, x_B \ln x_B + x_A\, x_B (W_{AA} + W_{BB} - 2\, W_{AB}) \tag{C.1}$$

with the concentration of molecule A (B), x_A (x_B), and the molecular interactions between molecules of identical (W_{AA} and W_{BB}) and different (W_{AB}) molecular species. In order to find a minimum of F_{mix}, its derivative, F'_{mix}, has to be set to zero. Defining $x \equiv x_A$ and using the resulting relation for binary films $x_B = 1 - x$, we get

$$F'_{\text{mix}} = k_{\text{B}}T\, \ln x - k_{\text{B}}T\, \ln(1 - x) + (1 - 2x)(W_{AA} + W_{BB} - 2\, W_{AB}) \tag{C.2}$$

for the derivative of the free energy. Since $\ln x$ diverges for $x \to 0$ and $\ln(1-x)$ diverges for $x \to 1$, F_{mix} cannot have a minimum at $x = 0$ or $x = 1$ and hence perfect phase-separation is entropically not possible. For the phase-separating ADT:ZnPC films this physically means that small amounts of ADT are expected in the ZnPC grains and small amounts of ZnPC are expected in the ADT grains. ZnPC molecules in ADT grains are detected experimentally in the binary films as they cause luminescent features comparable to ZnPC in solution [148, 222] or in an isolating matrix [221] (see Figure C.8).

C.2. Simulations of the time-evolution of the excited-state delocalization

For a better understanding of the conclusions made about the excited-state delocalization based on PL spectra, simulations are presented in the following. The simulation assumes N_0 excitations at time $t = 0$ that decay with a rate of k_{SF}. At the same time, each excitation is coherently delocalized over $M_{coh} + 1$ molecules at $t = 0$ and localizes with a rate of k_{coh} toward a value of 1. This results in

$$N(t) = N_0 \, e^{-k_{SF} t} \tag{C.3}$$

for the evolution of the number of excitations with time and

$$M(t) = 1 + M_{coh} \, e^{-k_{coh} t} \tag{C.4}$$

for the evolution of the excited-state delocalization with time. For molecules in dilute solution, which is the reference case, the excitation is always localized on one molecule, i.e. $M(t) = 1$, which is the same as $M_{coh} = 0$. In this case the time-integrated intensity of the 0-0 peak is

$$I_{00} = \int_{t_1}^{t_2} k_{00} \, N(t) \, \mathrm{d}t \tag{C.5}$$

and for the 0-1 peak the integrated intensity is

$$I_{01} = \int_{t_1}^{t_2} k_{01} \, N(t) \, \mathrm{d}t \tag{C.6}$$

with the time-independent luminescent decay rates k_{00} and k_{01} for the luminescent 0-0 and 0-1 transition, respectively. Using the Franck-Cordon principle and the assumption that I_{00}/I_{01} is proportional to the excited-state delocalization, we get

$$\frac{I_{00}}{I_{01}} = \frac{k_{00}}{k_{01}} = \frac{1}{S} \sim M = 1 \tag{C.7}$$

with the Huang-Rhys factor S [223]. Note that Equation C.7 is only true for electronically isolated molecules and in this case independent of the choice of t_1 and t_2. In analogy to the idea behind Equation C.7, a more general equation can be found for the time-averaged

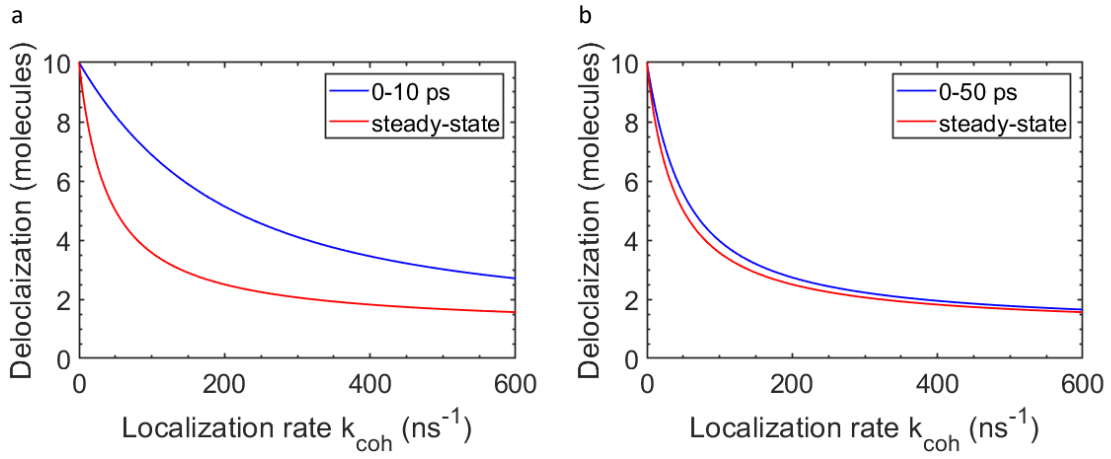

Figure C.2.: The excited-state delocalization depending on k_{coh} is extracted from the simulation when time-integrating the spectral intensities over (a) the first 10 ps or (b) the first 50 ps (blue lines) and compared to an integration over all times, which displays the case of a steady-state measurement (red lines). In all cases, the calculated excited-state delocalization is higher in the simulation, which time-integrates only over short times, compared to the simulation of the steady-state.

excited-state delocalization,

$$\overline{M} = \frac{1}{t_2 - t_1} \int_{t_1}^{t_2} M(t)\,\mathrm{d}t = S\,\frac{I_{00}}{I_{01}}. \tag{C.8}$$

Equation C.8 is also valid in the solid state, where excited-state delocalization plays a significant role, i.e. $M_{\mathrm{coh}} > 0$. Combining the proposed proportionality between I_{00}/I_{01} and the excited-state delocalization with Equation C.7 results in

$$k_{00} = \frac{M(t)}{S}\,k_{01}. \tag{C.9}$$

Plugging this result into Equation C.5 allows to simulate the result of Equation C.8 for different values of t_1, t_2 and k_{coh}. For the simulation N_0, S, k_{01} and M_{coh} are prefactors and chosen to be 1 (1 ns^{-1} in case of k_{01}), with the exception of M_{coh}, which is chosen to be 9.

The two cases, for which experimental data exist, were simulated, which is $t_1 = 0$ ps and $t_2 = 50$ ps (experimental data in Figure 9.4a, simulation in Figure C.2b) and $t_1 = 0$ and $t_2 = \infty$ (experimental data in Figure 9.3b, simulation in Figure C.2b). Independent of the value of k_{coh}, the extracted value for the excited-state delocalization is higher when only considering short times compared to the steady-state case (blue line vs. red line

in Figure C.2). The differences between the two time domains are highest for values of k_{coh} around $50\,ns^{-1}$ and are minor for very high or very low values of k_{coh}. This can be understood by considering the two extreme cases. In case of a very fast localization (large k_{coh}), the emission is dominated by fully localized excitons at all times, while for a very slow localization (small k_{coh}), the exciton decay is faster than the exciton localization, which means that no significant exciton localization occurs within the lifetime of an excitation. In the intermediate case, where k_{coh} is on the order of k_{SF} and the window of time-integration, the most pronounced differences are found. A rough value for k_{coh} is estimated by assuming that excited-state localization occurs at grain boundaries. From the SEM images (Figure 9.1) a grain size of $r = 300\,nm$ is assumed and by assuming an exciton diffusion constant of $D = 5 \cdot 10^{-7}\,m^2/s$ [249–251], one receives

$$t_{loc} = \frac{r^2}{2D} = 90\,ps \tag{C.10}$$

and hence $k_{coh} = 11\,ns^{-1}$ as a rough estimate.

In the simulation, the comparison of the steady-state case with a time integration of only the first 10 ps seems more fruitful (Figure C.2a), however, in the experimental case this time-range is not easily accessible due to the time resolution of the TRPL experiment being limited to 10 ps and an increasing noise level with decreasing integration time. Also the assumption of an exponential decay of the excited-state delocalization with time is rough and speculative, which means that the simulations carried out should only be considered as a support for a qualitative understanding, but not as a trustful basis for quantitative evaluations [223].

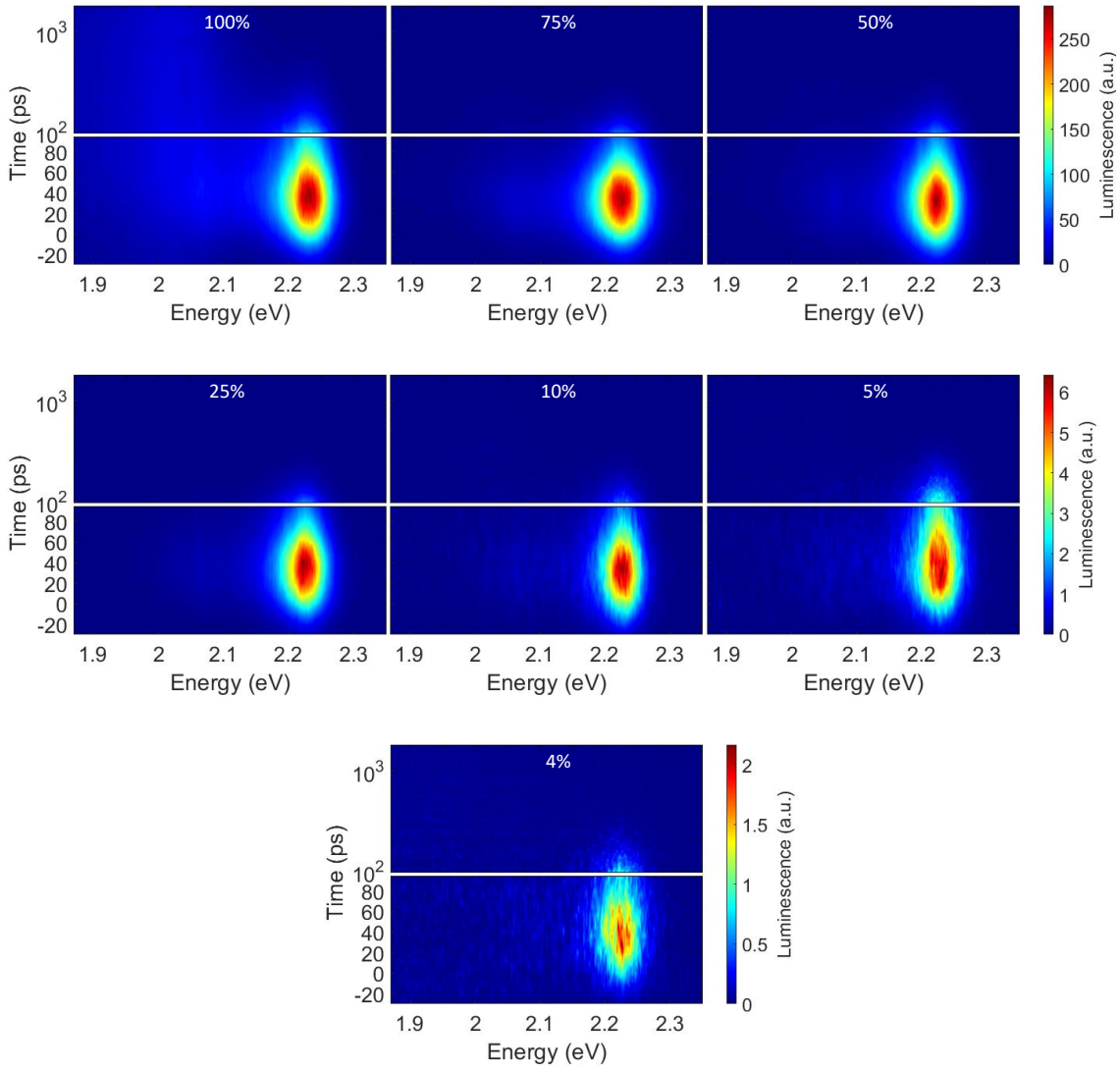

Figure C.3.: The delay times of the TRPL maps are displayed in a linear-logarithmic fashion. The time resolution of the measurement is 100 ps. ADT concentrations are given in mol-% in each map. The measurements were carried out at 200 K sample temperature and with a photon energy of the exciting laser of 2.58 eV.

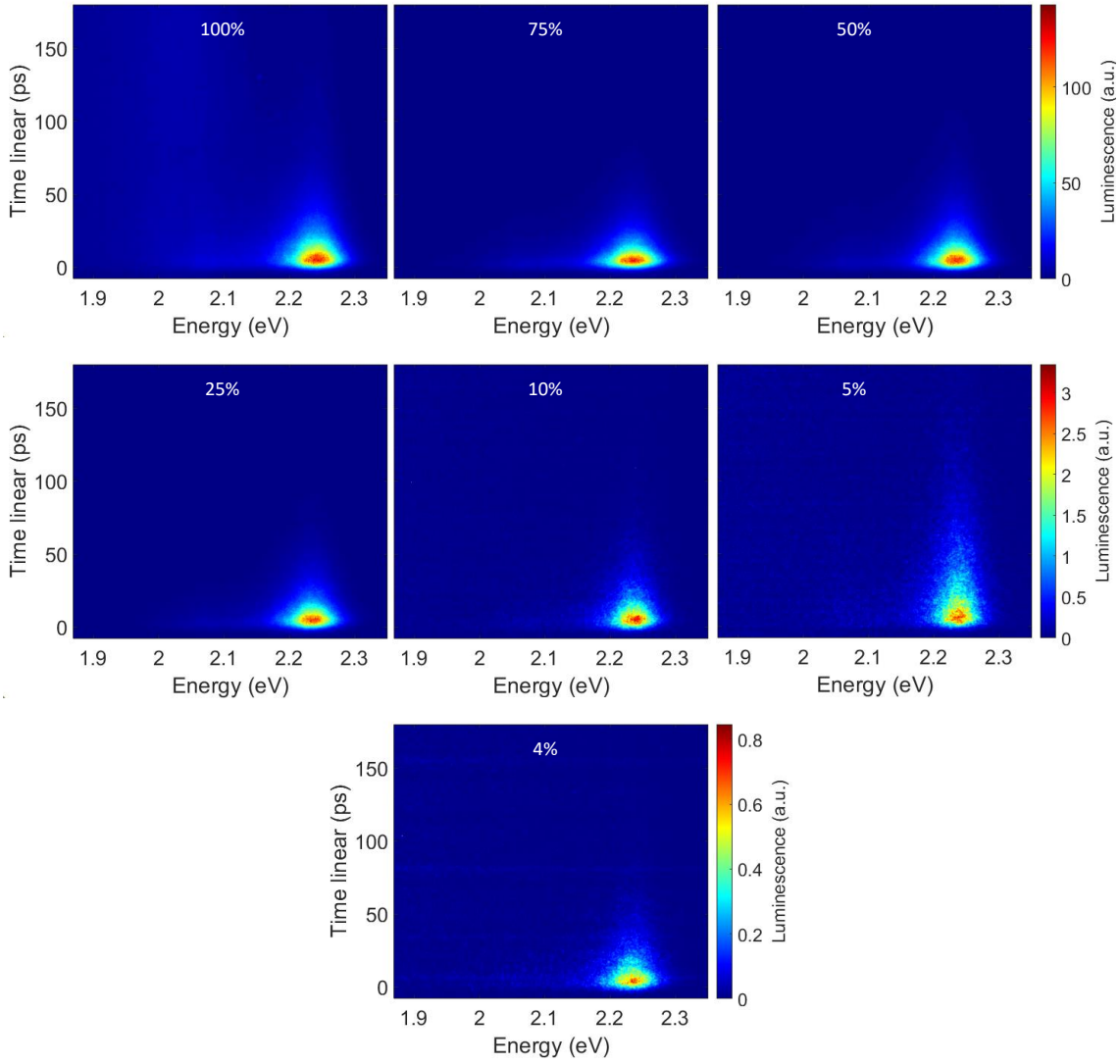

Figure C.4.: The delay times of the TRPL maps are displayed in a linear fashion. The time resolution of the measurement is 10 ps. ADT concentrations are given in mol-% in each map. The measurements were carried out at 200 K sample temperature and with a photon energy of the exciting laser of 2.58 eV.

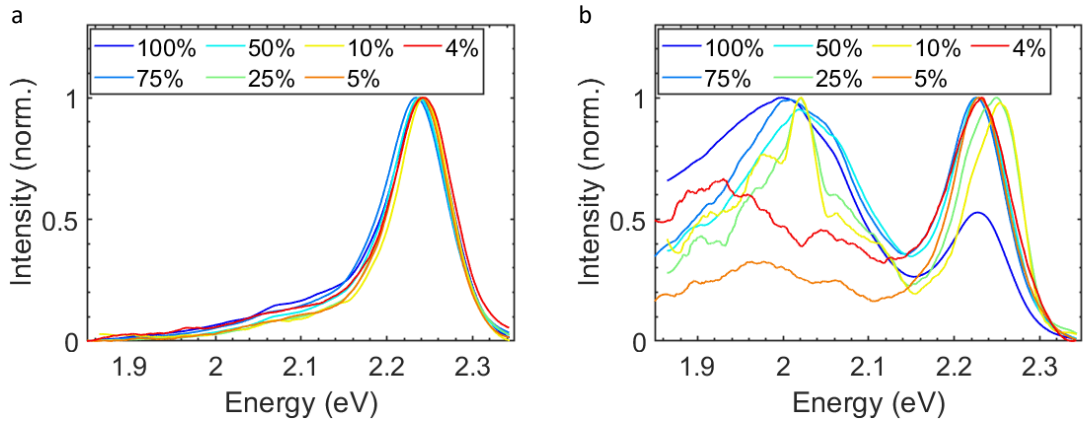

Figure C.5.: The spectra were extracted by time-integrating the TRPL data measured at a sample temperature of 295 K from 0 to 50 ps (a) and from 500 to 2000 ps (b) before noise filtering and normalizing the data. ADT concentrations are given in mol-% in the legend. Excitation occurred at a photon energy of 2.58 eV. The spectra show the same spectral features as the spectra extracted the same way at 200 K sample temperature (Figure 9.4a and 9.5a)

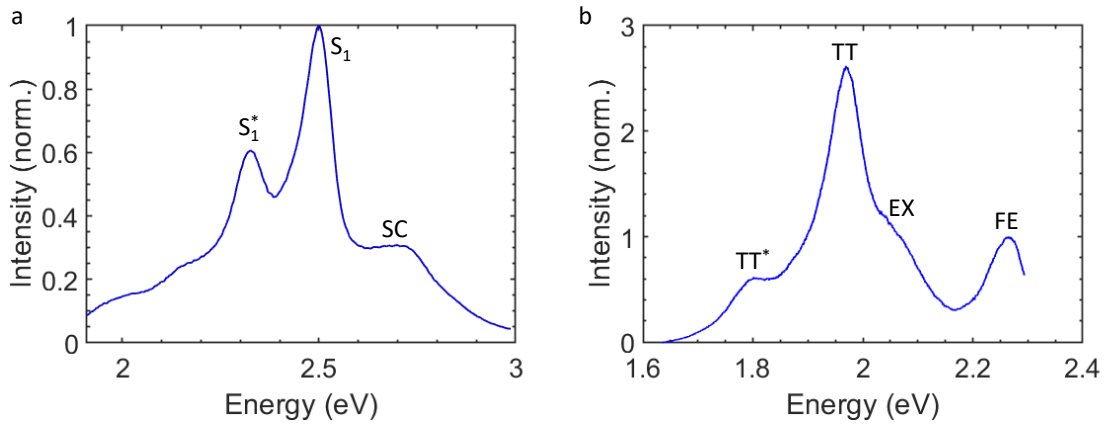

Figure C.6.: (a) The quasi steady-state PL spectrum of ADT in $CHCl_3$ solution is normalized to the S_1 emission. The peak at 2.7 eV (SC) is a scattering peak of the laser, the peak at 2.5 eV (S_1) is assigned to S_1 emission with a vibronic replica at 2.3 eV (S_1^*). The photon energy of the exciting laser was 3.1 eV. (b) The steady-state spectrum of an ADT single crystal is normalized with respect to the free exciton emission (FE) and shows a broad excimer emission (EX). The two sharp peaks in the low-energy region (TT and TT*) are assigned to ^{1}(TT) emission and its vibronic replica based on the peak shape and the energetic position. The photon energy of the exciting laser was 2.33 eV. The differences between the present spectrum and the one in Figure A.6b can be explained by differences in the intensity of the ^{1}(TT) emission, which is expected to depend on the density of imperfections in the single crystal.

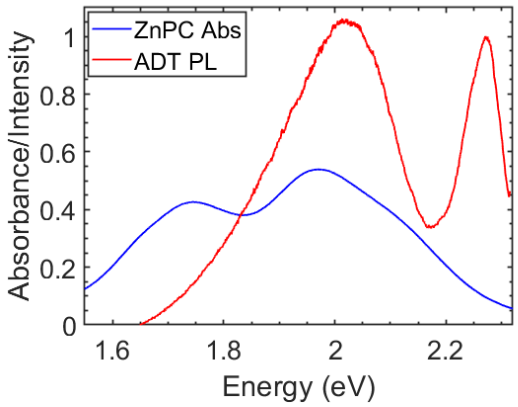

Figure C.7.: The PL spectrum of neat ADT and the absorbance spectrum of neat ZnPC illustrate the pronounced spectral overlap of the excimer emission and the ZnPC absorption, which makes energy transfer from ADT excimers to ZnPC efficient. Spectra are replotted from Figure 9.3.

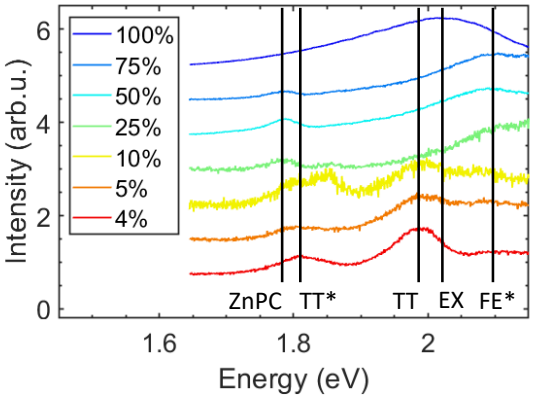

Figure C.8.: The low-energy range of the PL spectra from Figure 9.3b are replotted with an artificial vertical offset to make the individual low-energy features, which are highlighted by black vertical lines, more easily visible to the reader. ADT concentrations are given in mol-% in the legend.

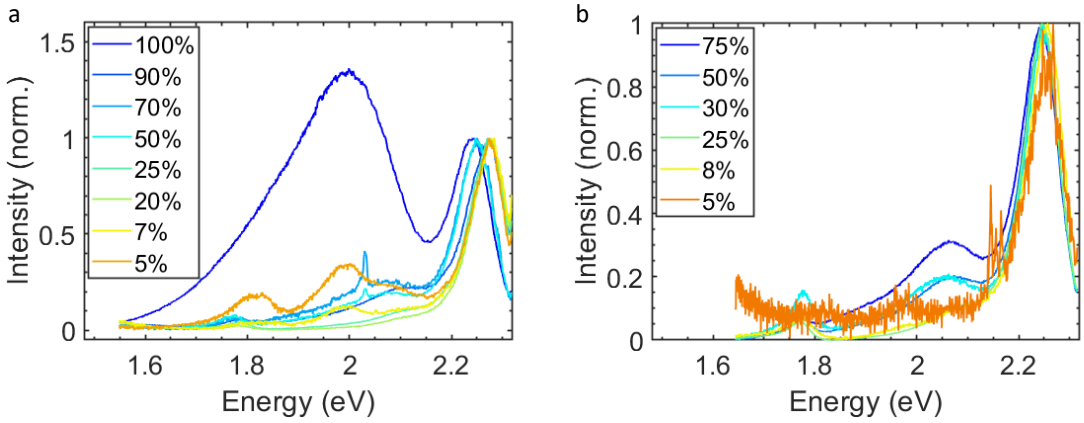

Figure C.9.: The steady-state PL spectra of binary ADT:ZnPC films from (a) an earlier and (b) a later sample series show the same spectral features and concentration-dependent trends as the spectra in Figure 9.3b, but differing relative intensities. ADT concentrations are given in mol-% in the legend.

D. Appendix: Impact of thermal energy on singlet fission

In this chapter, representative TRPL maps are shown. Additionally, a calculation is carried out, which can be used for an estimation of the relevance of the excimer decay pathway via thermal activation compared to other excimer decay mechanisms.

D.1. Calculation of thermal activation of excimers

In the following, the decay rate of excimers by a pathway via thermal activation to the exciton, followed by singlet fission, is calculated. For this calculation, a Lennard-Jones potential

$$V_{\mathrm{LJ}} = 4\,\epsilon \left[\left(\frac{\sigma}{r} \right)^{12} - \left(\frac{\sigma}{r} \right)^{6} \right] \tag{D.1}$$

is assumed with the distance between the molecules r, the potential depth ϵ and the distance σ at which the potential is zero. Additionally, a Coulomb potential

$$V_{\mathrm{C}} = -\frac{q^2}{4\,\pi\,\epsilon_0}\,\frac{1}{r} \tag{D.2}$$

is added with q proportional to the admixture of the diabatic CT state to the adiabatic state and the vacuum permittivity ϵ_0. This leads to a total potential of

$$V_{\mathrm{tot}} = 4\,\epsilon \left[\left(\frac{\sigma}{r} \right)^{12} - \left(\frac{\sigma}{r} \right)^{6} \right] - \frac{q^2}{4\,\pi\,\epsilon_0}\,\frac{1}{r}. \tag{D.3}$$

Next, it is assumed that in ground state geometry the S_1 state and the excimer state have the same energy and it is assumed that the distance between two molecules is the same for the ground state and the S_1 state, while it reduces by a factor of $(1/2)^{(1/6)}$ in the relaxed excimer geometry compared to the ground state geometry, which agrees roughly with calculations [26]. Assuming no diabatic CT state admixture to the adiabatic S_1 state (i.e. $q = 0$), enables us to calculate the energy difference between the S_1 state and the

excimer state. For the S_1 state, the minimum of V_{tot} with $q = 0$ is calculated by setting its derivative to zero,

$$V'_{\text{tot}} = 4\,\epsilon \left[-12 \left(\frac{\sigma^{12}}{r^{13}}\right) + 6 \left(\frac{\sigma^{6}}{r^{7}}\right)\right] + \frac{0^2}{4\,\pi\,\epsilon_0}\,\frac{1}{r^2} \stackrel{!}{=} 0 \tag{D.4}$$

$$4\,\epsilon \left[-12 \left(\frac{\sigma^{6}}{r^{6}}\right) + 6\right] = 0 \tag{D.5}$$

$$2\,\sigma^6 = r^6, \tag{D.6}$$

and inserting the result for r^6 into V_{tot}, resulting in

$$V_{\text{tot, S}_1}(r = 2^{\frac{1}{6}}\sigma) = 4\,\epsilon \left[\frac{\sigma^{12}}{4\,\sigma^{12}} - \frac{\sigma^6}{2\,\sigma^6}\right] = -\epsilon. \tag{D.7}$$

With a similar procedure the energy of the excimer state is calculated, but here the minimum of the potential is assumed to be at $r = \sigma$, which means that V'_{tot} has to be zero at $r = \sigma$, leading to the relation

$$V'_{\text{tot}} = 4\,\epsilon \left[-12 \left(\frac{\sigma^{12}}{r^{13}}\right) + 6 \left(\frac{\sigma^{6}}{r^{7}}\right)\right] + \frac{q^2}{4\,\pi\,\epsilon_0}\,\frac{1}{r^2} \stackrel{!}{=} 0 \tag{D.8}$$

$$\frac{q^2}{4\,\pi\,\epsilon_0}\,\frac{1}{\sigma^2} = 4\,\epsilon \left[\frac{12}{\sigma} - \frac{6}{\sigma}\right] \tag{D.9}$$

$$\frac{q^2}{4\,\pi\,\epsilon_0} = 24\,\epsilon\,\sigma \tag{D.10}$$

between the coefficients of the Lennard-Jones and Coulomb potential. Inserting this result in V_{tot} at the assumed minimum position $r = \sigma$ results in

$$V_{\text{tot,ex}}(r = \sigma) = 4\,\epsilon \left[\left(\frac{\sigma}{\sigma}\right)^{12} - \left(\frac{\sigma}{\sigma}\right)^{6}\right] - 24\,\epsilon\,\sigma\,\frac{1}{\sigma} = -24\,\epsilon, \tag{D.11}$$

meaning that an energy of $23\,\epsilon$ is relieved during excimer formation.

For the energy relieved during geometric relaxation in the ground state after exciton emission, the change in V_{tot} when moving from $r = \sigma$ to $r = 2^{\frac{1}{6}}\sigma$ is used. Since the ground state has no CT state admixture, $q = 0$ is assumed for the calculation. Hence, the geometric relaxation after excimer emission relieves an energy of only

$$V_{\text{tot}}(r = \sigma) - V_{\text{tot}}(r = 2^{\frac{1}{6}}\sigma) = 4\,\epsilon \left[\left(\frac{\sigma}{\sigma}\right)^{12} - \left(\frac{\sigma}{\sigma}\right)^{6}\right] - 4\,\epsilon \left[\frac{\sigma^{12}}{4\sigma^{12}} - \frac{\sigma^6}{2\sigma^6}\right] = \epsilon, \tag{D.12}$$

which is lower than the relaxation in the excited state by a factor of 23.

Inserting experimental values for the S_1 energy and the energy of the excimer relaxation from the photon energies in PL experiments (2.23 and 2.02 eV, respectively), results in a geometric relaxation during the excimer pathway of 0.21 eV, 0.2016 eV of which then occur in the electronically excited state. Hence, this energy is needed as thermal activation energy for the excimer deactivation pathway via the S_1 state, followed by singlet fission. The rate of this process can then be calculated via

$$k_{\text{ex via S}_1} = k_{\text{SF}} \exp\left(-\frac{0.2016\,\text{eV}}{k_\text{B}\,T}\right) = 0.0151\,\text{ns}^{-1} \tag{D.13}$$

at room temperature $T = 295\,\text{K}$ with the singlet fission rate of ADT $k_{\text{SF}} = 42\,\text{ns}^{-1}$ [155] and the Boltzmann constant $k_\text{B} = 8.6173 \cdot 10^{-5}\,\text{eV/K}$.

This value is almost two orders of magnitude smaller than the experimentally found decay rates of the excimer [155], suggesting that this decay channel has no significant effect on the excimer decay dynamics. Note that there must be an additional barrier for the transition between the free exciton state and the excimer state that hinders the downward-transition from the free exciton to the excimer and hence decouples the decay of both states [155]. This barrier is likely to also effect the reverse transition, i.e. the transition from the excimer to the free exciton, additionally to the energetic barrier taken into account here.

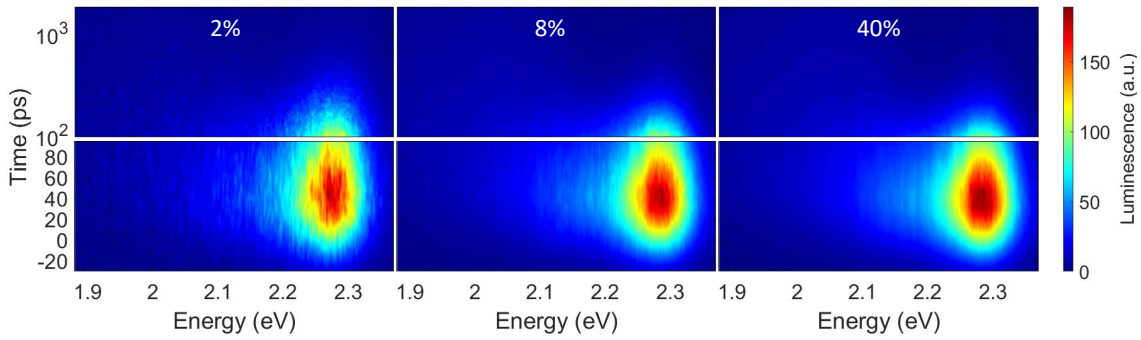

Figure D.1.: The TRPL data were recorded at a sample temperature of 295 K and the time axis is displayed in a linear-logarithmic fashion. Molar ADT concentrations are given inside the respective maps. The photon energy of the exciting laser was 2.58 eV.

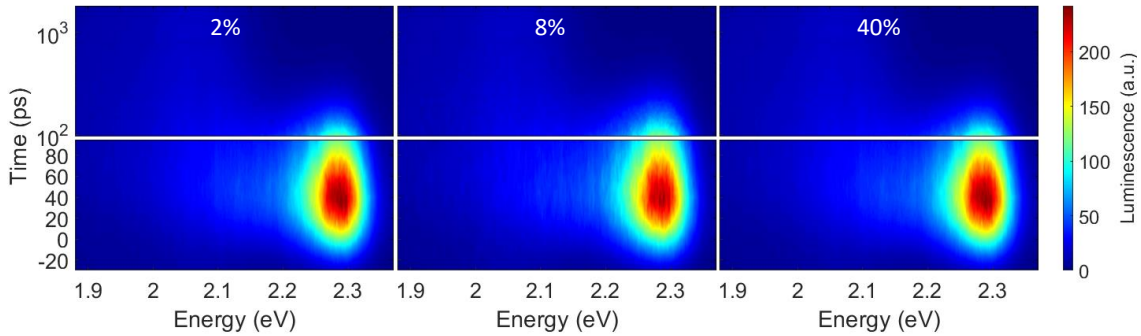

Figure D.2.: The TRPL data were recorded at a sample temperature of 200 K and the time axis is displayed in a linear-logarithmic fashion. Molar ADT concentrations are given inside the respective maps. The photon energy of the exciting laser was 2.58 eV.

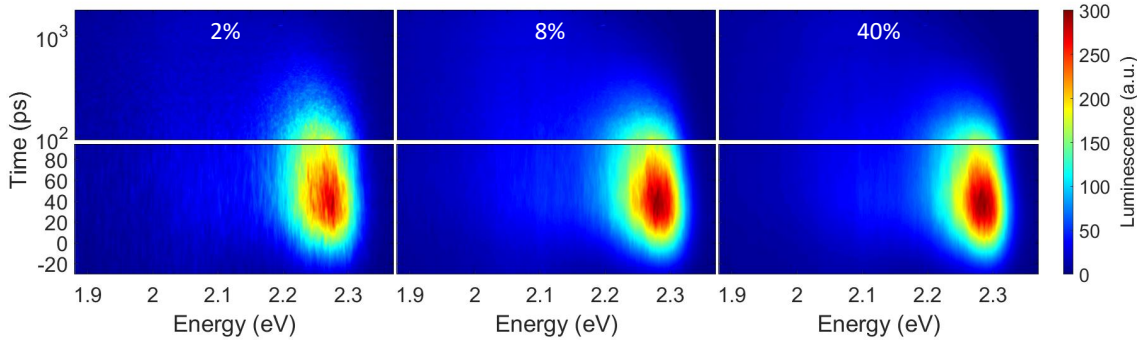

Figure D.3.: The TRPL data were recorded at a sample temperature of 110 K and the time axis is displayed in a linear-logarithmic fashion. Molar ADT concentrations are given inside the respective maps. The photon energy of the exciting laser was 2.58 eV.

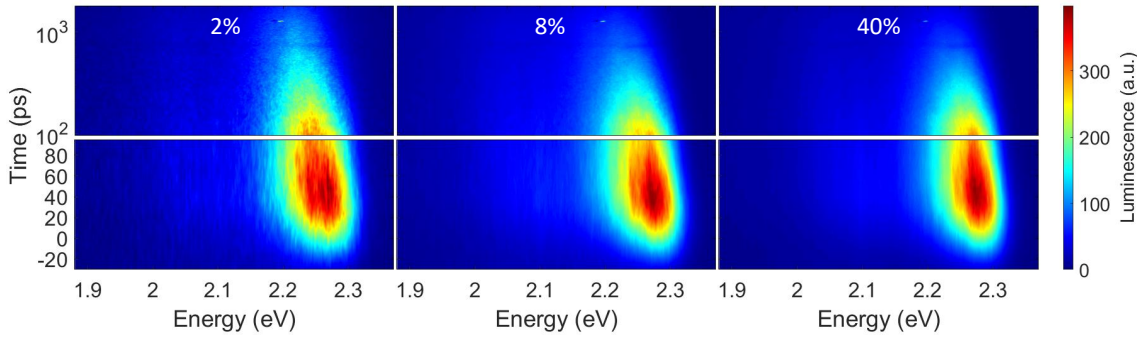

Figure D.4.: The TRPL data were recorded at a sample temperature of 50 K and the time axis is displayed in a linear-logarithmic fashion. Molar ADT concentrations are given inside the respective maps. The photon energy of the exciting laser was 2.58 eV.

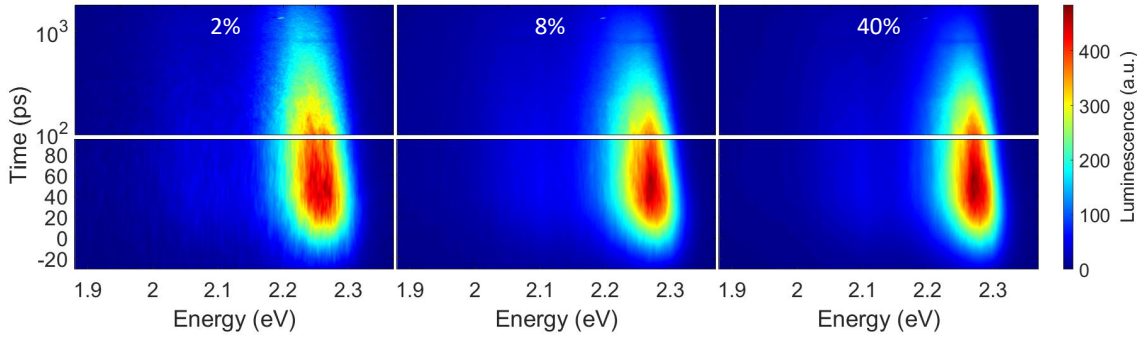

Figure D.5.: The TRPL data were recorded at a sample temperature of 10 K and the time axis is displayed in a linear-logarithmic fashion. Molar ADT concentrations are given inside the respective maps. The photon energy of the exciting laser was 2.58 eV.

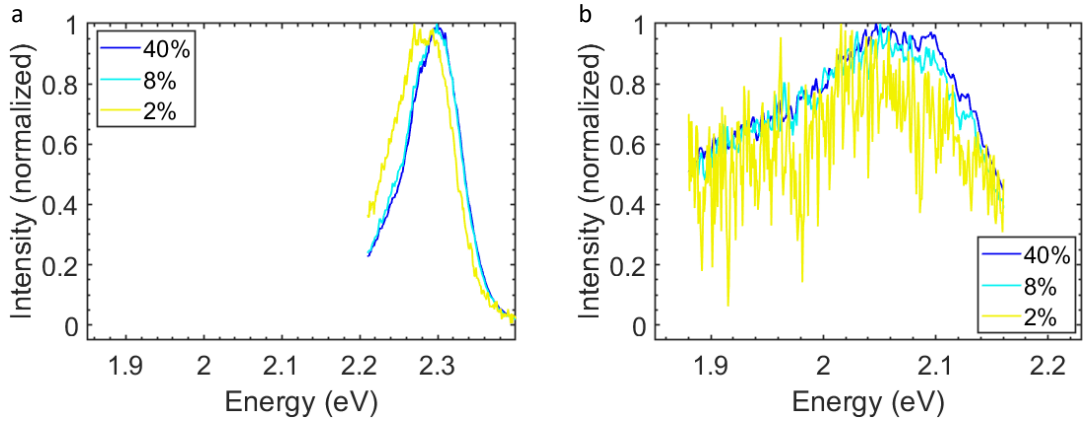

Figure D.6.: Spectra associated to the decay rates shown in Figure 10.11. The spectra were calculated by GA as described in the figure caption of Figure 10.11.

E. Appendix: Influence of growth conditions and isomeric purity on the photophysics of ADT

As a basis of this thesis, which focuses on binary films containing ADT, it is important to also investigate the influence of changes in the preparation procedure on the structure and photophysics of neat ADT. For this purpose, the film thickness, growth rate and substrate temperature have been varied between the prepared samples and ADT of different isomeric compositions has been used. The produced samples have then been analyzed structurally and optically to find possible effects of a variation of the above-mentioned parameters. In the following, the effects of a variation of the film thickness are discussed first, before analyzing changes introduced by variations of the remaining parameters. Note that the effects of a variation of the film thickness only play a minor role for this thesis, since almost all films in this thesis have a nominal thickness of 80 nm.

E.1. Variation of the film thickness

Effects introducible by changes in the film thickness have been investigated by preparing films of different thickness. The structure of the films was investigated by means of XRD, where XRR has been used to analyze the out-of-plane structure and GIWAXS was employed for the analysis of the in-plane structure.

The XRR scans of the films of different thickness are displayed in Figure E.2. All scans show very similar shapes, neither of the scans exhibits clear Kiessig fringes or Laue oscillations and all films exhibit Bragg peaks of first and second order around 0.45 and 0.9 $Å^{-1}$, respectively. Two clear differences between the scans can be found. One is that the Bragg peaks are becoming sharper with increasing thickness, which can be explained by an increasing number of lattice planes contributing to the diffraction with increasing film thickness, which is known from the Scherrer equation (Equation 5.11). The second difference is the appearance of a split Bragg peak at increased film thickness, which is best visible for the second order Bragg peak. It is assumed by Wang et

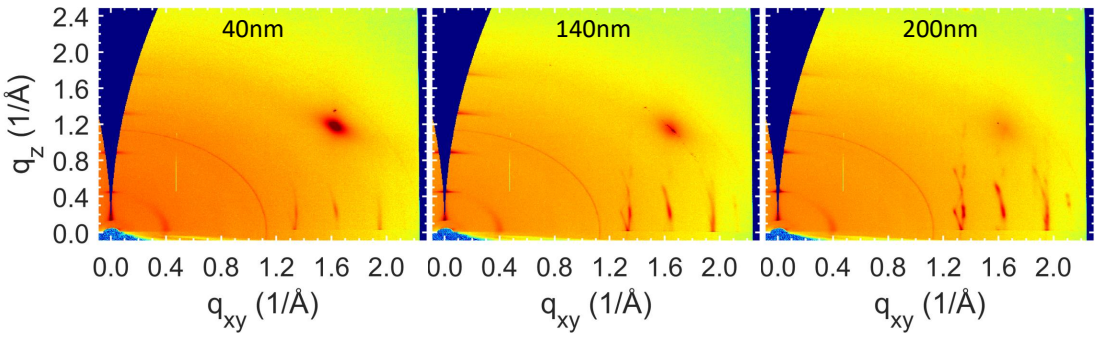

Figure E.1.: GIWAXS maps of neat ADT films of different thickness. The thickness of each film is given in the respective map. With increasing thickness, the bulk phase features of ADT gain relative intensity. The measurements were conducted at DESY with an incident angle of $\Theta_{inc} = 0.1^{\circ}$.

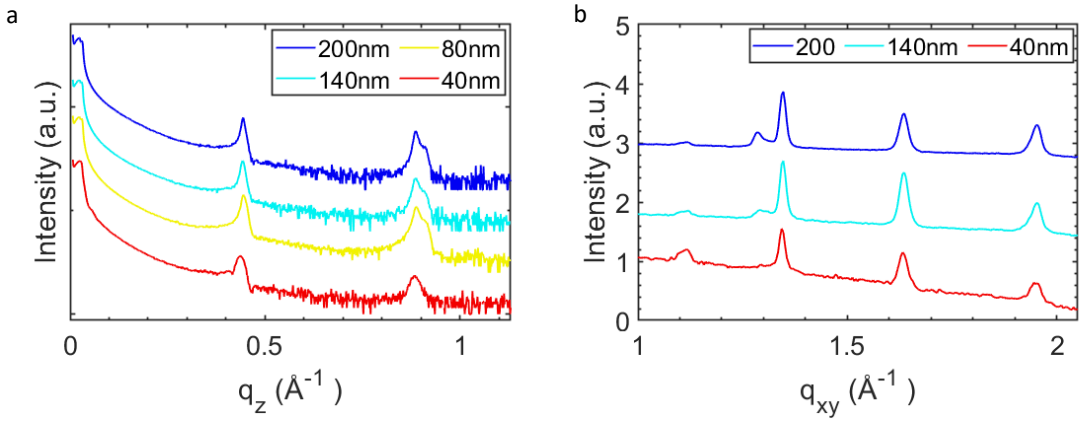

Figure E.2.: (a) The XRR scans of neat ADT are plotted logarithmically and vertically offset for clarity. (b) The GID scans of neat ADT are plotted linearly and are vertically offset for clarity. The GID scans were created by integrating the GIWAXS maps in Figure E.1 along q_z in the range $0.1\,\text{Å}^{-1} < q_z < 0.3\,\text{Å}^{-1}$. The film thickness is given in the legend.

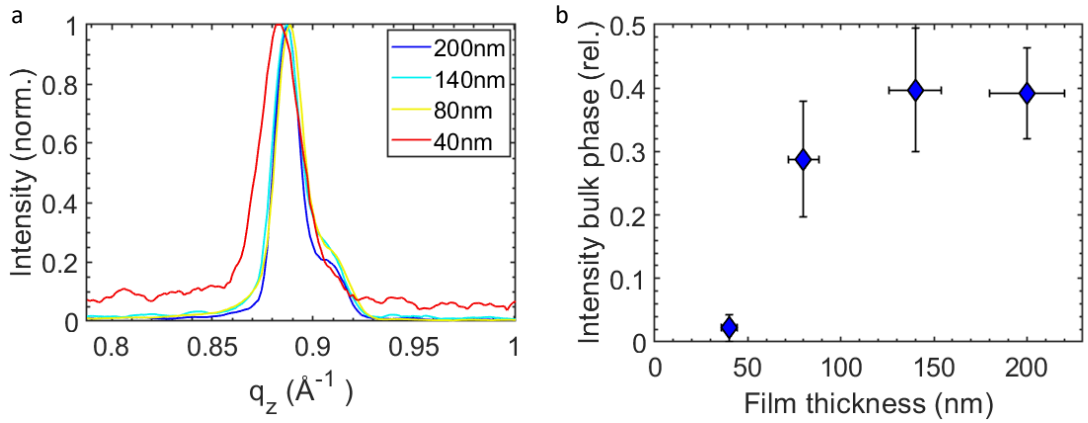

Figure E.3.: (a) The second order Bragg peak is replotted from Figure E.2 with a linear y-axis and normalized after applying a noise filter. The thickness of the neat ADT film is given in the legend. (b) The integrated intensity of the Gaussian fit of the part of the Bragg peak assigned to the bulk phase has been divided by the analogous intensity assigned to the thin film phase and plotted against the nominal film thickness, showing a higher relevance of the bulk phase for thicker films.

al. [126] that the part of the peak at higher q_z-values belongs to a bulk phase of ADT, while the dominant component at smaller values is assigned to the thin film phase. If this assignment is correct, one should be able to track an increase in relative intensity of the bulk phase compared to the thin film phase with increasing film thickness [139]. Hence, the second Bragg peak is replotted in a linear fashion (Figure E.3a) and fit with a function containing two Gaussians, one for the thin film phase and one for the bulk phase. By integrating the intensity of each of the two contributing Gaussian functions and dividing the area assigned to the bulk phase by the one assigned to the thin film phase, the relative contribution of the bulk phase was calculated. The result is displayed in Figure E.3b and shows that the contribution of the bulk phase increases with increasing film thickness, although this trend might saturate at high film thickness. This trend supports the statement made by Wang et al. [126], which explains the splitting of the Bragg peak by a coexistence of thin film and bulk phase.

In Chapter 7 and 8 a split peak was also found in in-plane scattering experiments, namely the (11l) peak was an overlap of a low-intensity peak at smaller q_{xy} values and a higher-intensity peak at a slightly higher scattering vector, which will be assigned to the coexistence of thin film and bulk phase in the following. For this, GIWAXS experiments were executed with neat ADT films of different thickness. The resulting q-maps are shown in Figure E.1 and were integrated along q_z in the range $0.1\,\text{Å}^{-1} < q_z < 0.3\,\text{Å}^{-1}$ to produce Figure E.2b. In this Figure, the samples of higher thickness show a split (11l)

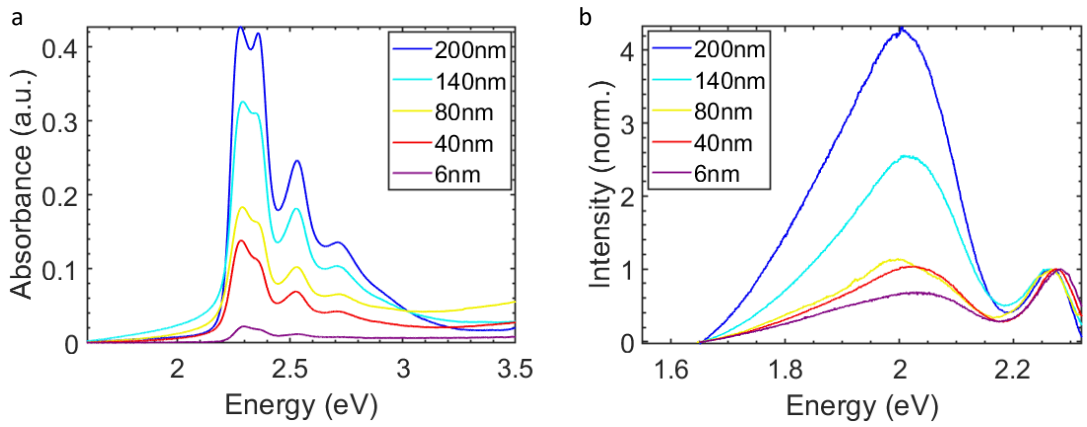

Figure E.4.: (a) In the absorbance spectra of the neat ADT films a change in relative intensity between the two Davydov compounds is observed upon variations of the film thickness. (b) The PL spectra of neat ADT films show an increasing relative intensity of the excimer peak compared to the free exciton peak and a slight redshift of all features with increasing film thickness. The nominal film thickness is given in the legend.

peak, but with decreasing film thickness, the part of the (11l) peak at low q_{xy} values loses intensity until it visually vanishes at a film thickness of 40 nm. Such a thickness-dependent behavior suggests an assignment of the more intense part of the (11l) peak to the thin film phase and of the part carrying lower intensity to the bulk phase. Additionally, such an assignment is in line with the XRR data discussed previously and with the work of Wang et al. [126]. A detailed analysis of the structure of the thin film and bulk phase of ADT is beyond the scope of this work. Note that in Figure E.1 the diffraction ring at $q_r = 1.12\,\text{Å}^{-1}$ is a feature of the cone, which has been used to protect the sample from beam damage during the measurement and the peak at $q_{xy} = 1.65\,\text{Å}^{-1}$ and $q_z = 1.2\,\text{Å}^{-1}$ is a feature of the native silicon substrate and hence both features can be ignored for the analysis of the film structure.

Additionally to the structural investigations with XRD, also a basic optical characterization of the neat ADT films of different thickness has been done by employing absorbance and PL spectroscopy (Figure E.4). Due to an increasing thickness of the absorbing material, the absorption features get more pronounced with increasing film thickness. Interestingly, the intensity ratio between the two Davydov compounds also changes, namely the higher energy component gains relative intensity with increasing thickness. This can, in principle, be connected to the higher amount of bulk phase ADT at higher film thickness, since the bulk phase contains a different in-plane structure and the in-plane structure strongly influences the photophysics [242]. However, most likely the more important reason is that at higher thicknesses the dependence of film thickness

and transmittance cannot be approximated linear anymore (according to Lambert-Beer's law the dependence is exponential), but not exponential either, since, for grain sizes that are at least of the order of the probing wavelength, the overall transmittance is a linear combination of the transmittance of multiple grains. Hence, the absorption of the two Davydov components can be seen as linear combinations of exponential functions with different prefactors, resulting in each Davydov component reacting differently to changes in thickness. This idea is explained in more detail in Ref. [110].

More intriguing results can be found in the PL spectra, which are normalized with respect to the free exciton emission in Figure E.4b. Here, a strong increase in relative intensity of the excimer emission with increasing film thickness is found. Additionally to this increase in relative intensity of the excimer, the free exciton emission shows a small, but continuous redshift with increasing film thickness. For these observations, multiple possible explanations are available, one of which is self-absorption. Since the lowest energy allowed optical transition of ADT is at 2.28 eV, the excimer emission, which is at far lower energies, is expected not to be affected by self-absorption. In contrast, the free exciton emission with its peak intensity at 2.27 eV is redshifted compared to the lowest absorption peak by such a little amount that the two spectra clearly overlap, which means that self-absorption plays a role for this peak. Due to the slight redshift of the emission compared to the absorption, self-absorption has two effects on the free exciton emissio. These are a reduction of the overall intensity of the free exciton emission and, since the high-energy region of the free exciton emission peak is affected more strongly by self-absorption, a redshift of the emission. With increasing film thickness, both these effects gain relevance, leading to the redshift of the free exciton emission peak and, since the spectra are normalized to the free exciton peak, the reduction of the free exciton emission intensity leads to an increase in relative intensity of the excimer emission. The second explanation bases on changes in the ratio between thin film and bulk phase with changing thickness, which has been found earlier in this chapter. We also expect the bulk phase of ADT to have a higher molecular packing density than the thin film phase, since this is the case in PEN [140, 142] and TET [139]. This higher packing density of the bulk phase in likely to increase the intermolecular interaction and the polarizability, which are both changes that lead to an energetic decrease of the S_1 state, explaining the redshift of the free exciton emission with increasing film thickness. Consistently, a redshift can also be found in the excimer emission with increasing thickness. Since the bulk phase has a different packing motive than the thin film phase, it might be the case that the molecular arrangement in the bulk phase is more favorable for excimer formation, explaining the drastic increase in relative intensity of the excimer emission with increasing film thickness. Lastly, it might also be the case that the packing motive of the bulk

phase is more favorable for singlet fission, which means that in the bulk phase singlet fission is quenching the free exciton emission more efficient than in the thin film phase, leading to a decrease in free exciton emission with increasing film thickness, which, due to the normalization, results in an increased excimer emission peak in Figure E.4b.

E.2. Variation of the isomeric composition, growth rate and substrate temperature

In most samples prepared during this work, commercially available ADT is used as a material. This commercially available ADT, however, is a mixture of two isomers, namely anti-ADT and syn-ADT, that differ in the relative position of the two sulfur atoms in the molecule (see Figure 6.1 for both chemical structures and Section 6.1 for details). From the synthesis pathway, we expect an equimolar mixture of the two isomers in the commercially available material [125]. Due to the bad solubility of the material, a separation of the isomers with established methods was not possible with high yields [122, 127]. The chemical structures suggest a permanent dipole moment for syn-ADT, but not for anit-ADT, which might cause differences in the photophysics between the two isomers. In this chapter, we compare the structure and photophysics of isomerically mixed ADT with that of isomerically pure anti-ADT to show that both materials exhibit barely any differences and hence that the use of isomerically mixed ADT in this work is not concerning. To complement this experimental approach, both isomers have also been investigated theoretically using DFT, where the first electronic transition shows a comparable excitation energy and a comparable orientation of the TDM. Additionally, samples of isomerically mixed ADT were prepared at different substrate temperatures and growth rates to test the influence of a variation of growth conditions on the structure and photophysics of thin ADT films. Also for this chapter, if not specified differently, the term ADT is related to the commercially available, isomerically mixed ADT.

The results of the DFT calculations can be found in Table E.1 for the energetically lowest six allowed optical ground state transitions. Since in this work ADT is never directly excited to an electronic state energetically higher than S_1, in the following the focus is put on the results for the $S_0 \rightarrow S_1$ transition of both isomers. Under this aspect, the respective transitions of anti-ADT and syn-ADT are at comparable energies with comparable oscillator strength and the orientation of the TDM is roughly along the short axis for both molecules. These similar results in *ab initio* calculations for both isomers is a first indication that both isomers might exhibit comparable photophysics.

For the complementing experimental investigations, films of isomerically pure anti-

Table E.1.: Energy, oscillator strength and TDM orientation for the energetically lowest six allowed optical ground state transition. DFT calculations were made after geometry optimization using the B3-LYP exchange correlation function and ref-TZVP as a basis function. [a] The given angle is the angle between the TDM of the respective transition and the long axis of the anthracene core of the molecule. For all transitions the TDM is in the molecular plane.

Molecule	Electronic transition	Energy	Osc. strength	TDM orientation[a]
anti-ADT	$S_1 \leftarrow S_0$	2.449 eV	0.0641	58°
anti-ADT	$S_2 \leftarrow S_0$	3.372 eV	0	–
anti-ADT	$S_3 \leftarrow S_0$	3.411 eV	0.00093	72°
anti-ADT	$S_4 \leftarrow S_0$	3.796 eV	0	–
anti-ADT	$S_5 \leftarrow S_0$	4.293 eV	0.458	4°
anti-ADT	$S_6 \leftarrow S_0$	4.342 eV	1.849	1°
syn-ADT	$S_1 \leftarrow S_0$	2.457 eV	0.0436	90°
syn-ADT	$S_2 \leftarrow S_0$	3.310 eV	0.00510	0°
syn-ADT	$S_3 \leftarrow S_0$	3.418 eV	0.0118	0°
syn-ADT	$S_4 \leftarrow S_0$	3.888 eV	0.2789	0°
syn-ADT	$S_5 \leftarrow S_0$	4.288 eV	0.00211	87°
syn-ADT	$S_6 \leftarrow S_0$	4.424 eV	2.1697	0°

ADT and of isomeric ADT have been prepared by means of OMBD and the preparation conditions of each sample are summarized in Table E.2. XRD experiments have been carried out with these samples and the resulting XRR scans and GIWAXS maps can be found in Figure E.5a and b–f, respectively. The XRR scans of all samples exhibit Bragg peaks of first and second order at 0.44 and 0.88 $Å^{-1}$, respectively, and in all cases the second Bragg peak is distorted in shape, indicating that the feature might be composed of multiple peaks. None of the curves exhibits Kiessig fringes and only in some of the scans weak Laue oscillations can be found near the first Bragg peak, which indicates an overall high roughness of the films. The GIWAXS maps of all films look very similar, with three vertically extended peaks at q_{xy} = 1.35, 1.65 and 2.0 $Å^{-1}$ dominating the map, which can be assigned to the (11l), (02l) and (12l) diffraction, respectively. The (01l) and (10l) diffraction features are not visible in all cases, indicating an in-plane herringbone arrangement [102].

These peak positions in GID are consistent with a preferred standing-up orientation of the ADT molecules against the sample surface and an in-plane herringbone structure as has been found previously [122, 126]. Importantly, no clear structural differences can be examined between the films based on the GID data. The only minor difference that can be found is that the second Bragg peak in XRR looks slightly different in shape for the

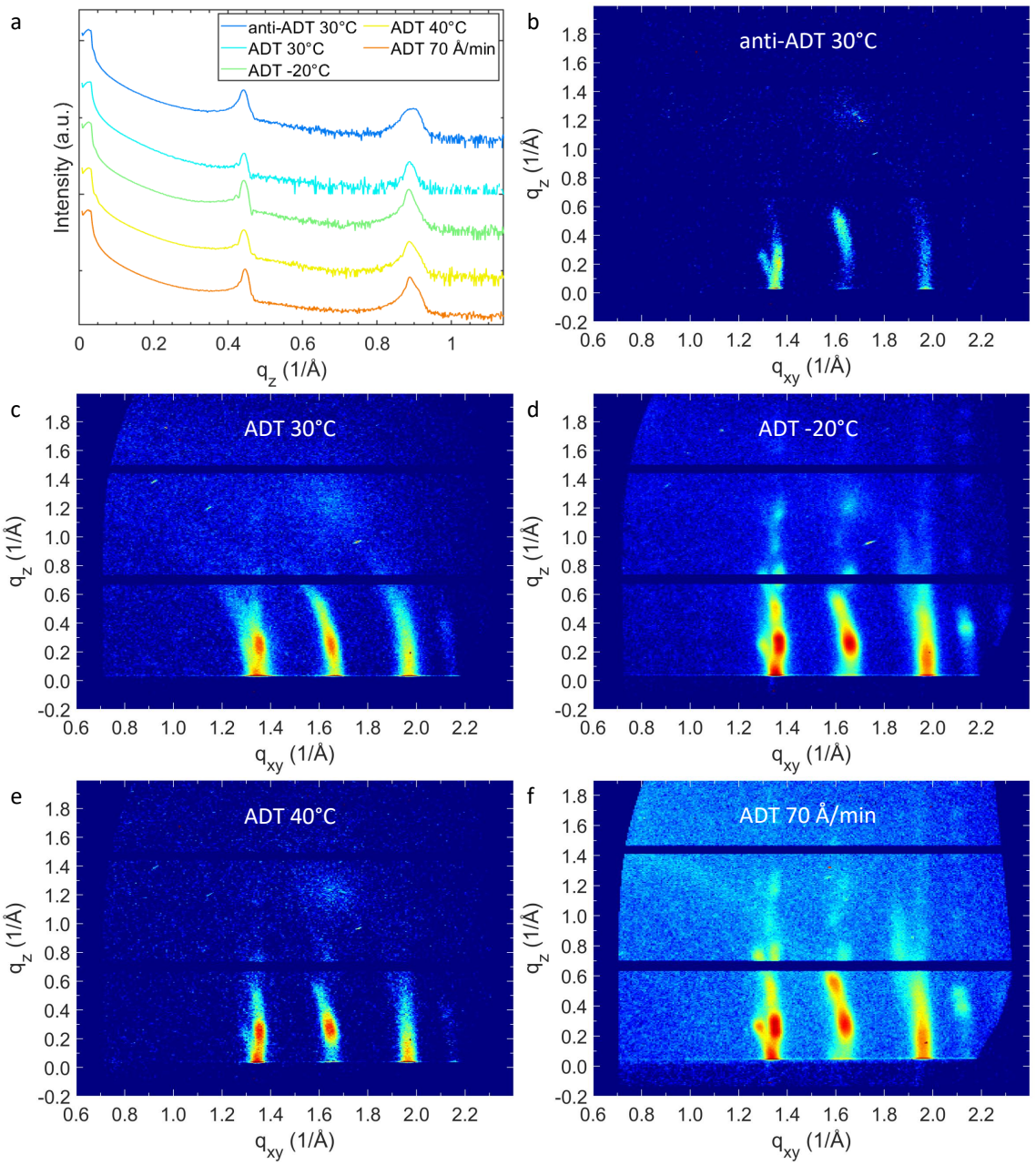

Figure E.5.: (a) XRR scans are vertically offset for clarity. (b-f) GIWAXS maps of ADT films with different stoichiometries of the isomers and prepared under different conditions as identified in each GIWAXS map. The same identifiers are used in the legend of the XRR plot and the meaning of each can be found in Table E.2.

anti-ADT film compared to all other films that were prepared based on mixed isomers. This difference in peak shape can be explained by differences in the ratio between thin film phase and bulk phase [126], where in case of the anti-ADT film the bulk phase has a higher share compared to the other films. However, this difference in structure cannot be solely traced back to the fact that only one isomer is present in the one case, but, more likely, is due to a higher density of imperfections in the anti-ADT film. Further evidence for the hypothesis of the anti-ADT film having more imperfections, and hence more trap states, will be found later in this chapter by analyzing the PL spectra. One possible reason for the higher trap site density in the anti-ADT film might be the purity of the used material.

Next, the optical properties of the samples are discussed. For this purpose, absorbance and PL spectra are shown in Figure E.6. Starting with the absorbance spectra, all samples show very similar spectral features, which are namely the $S_0 \rightarrow S_1$ transition around 2.3 eV, which is split into two Davydov components in all cases and exhibits two peaks of the vibronic progression toward higher energies, which are found as weaker peaks at 2.5 and 2.7 eV in all samples. However, small differences between the spectra can be found, which are variations of the absolute intensity of the absorption peaks, minimal changes of the intensity ratio between the two Davydov components and differences in the slope of the low-energy tail at energies lower than the $S_0 \rightarrow S_1$ transition energy. Note that the small step in the absorption data at around 3.3 eV is an artifact of the setup.

The differences in absorption peak intensity between the samples can be explained by differences between the respective film thicknesses. The strongest difference in this parameter can be found in case of the film grown at high growth rates, where the following two effects made it hard to precisely control the thickness. First, the high growth rate multiplies the effect of a small mistiming during the start and the end of film growth and, second, for the high growth rate a higher temperature is needed in the crucible, which results in more radiative heat that potentially changes the temperature of the QCM. This increase in temperature might lower the sticking factor of the QCM and can hence lead to a thicker film on the substrate as expected based on the QCM data. The QCM is ex-

Table E.2.: Identifiers, material and growth conditions of the samples in this chapter.

Identifier	Isomers	Substrate temp.	Growth rate	Film thickness
anti-ADT 30°C	anti	30°C	6 Å/min	80 nm
ADT 30°C	mixed	30°C	6 Å/min	80 nm
ADT -20°C	mixed	−20°C	6 Å/min	80 nm
ADT 40°C	mixed	40°C	6 Å/min	80 nm
ADT 70 Å/min	mixed	30°C	70 Å/min	80 nm

pected to be affected more strongly by the radiated heat of the crucible than the sample holder since the QCM is geometrically closer to the crucible than the sample holder. The second strongest deviation in absorption peak intensity is found for the isomerically pure anti-ADT film. For the preparation of this film, the same scaling factor has been used for the QCM as for ADT with mixed isomers. Since these two materials are in principle different, the use of the same scaling factor might be slightly inaccurate, resulting in small deviations in sample thickness. Although the substrate temperature during growth effects the sticking coefficient of the substrate, which can influence the final sample thickness, this effect seems to play very little role in the present case, since the absorption peaks of the samples grown at different substrate temperatures are almost of identical height. The Davydov splitting, that is exhibited by all films, confirms the presence of an in-plane herringbone arrangement [72], which has been suggested during the analysis of the XRD data. The ratio between the intensities of the two Davydov components varies a little between the samples. Two effects can explain this variation. One effect is the film thickness, a change of which can change the ratio between the two peaks if the grain size is at least of the order of the wavelength [110]. The other source for these changes might be minimal changes in structure. This latter point is well in line with the anti-ADT film showing the strongest deviation from the other films in the shape of the Davydov splitting and at the same time, in case of the anti-ADT film, the XRR data suggested that exactly this film might incorporate a higher relative amount of bulk phase compared to the other samples. Lastly, the differences in the shape of the low-energy tail in the absorbance spectra can be explained by scattering at the rough film surface. For a higher sample surface roughness, a higher scattering intensity is expected. This is in line with the XRR data, in which the ADT films grown at $-20^{\circ}C$ and at $30^{\circ}C$ substrate temperature show Laue oscillations and are hence expected to be smoother than the other films. These two films are also the two films that show the lowest surface scattering intensity in the absorbance spectra.

The PL spectra of the films (Figure E.6b) all show free exciton emission at 2.27 eV and a broad excimer emission at 2.02 eV. The ratio between the intensity of the free exciton emission and of the excimer emission differs between the samples. The samples with a low relative intensity of the excimer also exhibit a distorted shape of the excimer emission, which can be described as a high-energy shoulder at 2.1 eV.

The fact that all samples exhibit luminescence from the free exciton and from the excimer at the same time suggests comparable photophysics in all cases. Since additionally all spectra have a comparable shape, it is likely that both channels, singlet fission and excimer formation, are available in all samples. Note that the difference in spectral shape between the sample with the highest relative excimer luminescence and the one with the

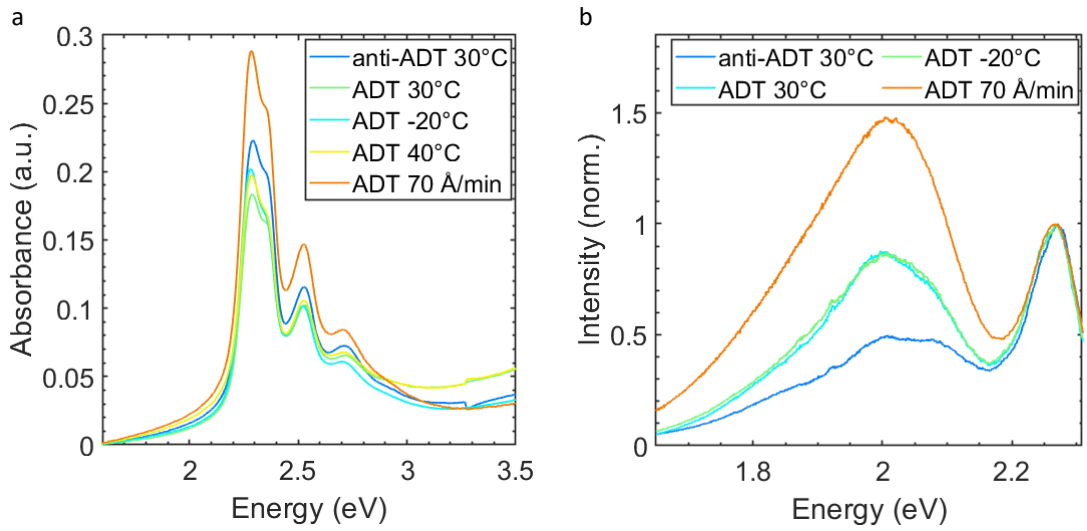

Figure E.6.: Absorbance (a) and PL (b) spectra of the samples specified in Table E.2. For PL, a laser with a photon energy of 2.33 eV has been used for excitation and the spectra have been normalized with respect to the free exciton emission.

lowest appears significant first, however, it is just a factor of three between the two extremes. Changes in relative intensity between the free exciton and the excimer can have various reasons, such as changes in the singlet fission rate, in the excimer formation rate, or in the excimer quenching rate. Already a small change in any of these parameters, for example induced by a higher density of trap states, has a significant influence on the ratio between the two spectral features. Lastly, the high-energy shoulder of the excimer peak has to be discussed. At 2.1 eV, it is lower in energy compared to the free exciton emission by the energetic spacing of the vibronic progression (0.17 eV), which is known from the absorbance spectra (Figure E.6a). For spectra with a higher relative intensity of the excimer emission, the vibronic progression of the free exciton emission is overshadowed by the excimer emission, which makes it harder to see the shoulder in these spectra.

Concluding this chapter, the structure and the optical properties of isomerically mixed ADT have been compared to that of isomerically pure anti-ADT and in all aspects only very minor differences between the two materials have been found. The differences found can be attributed more reasonably to a lower purity of the anti-ADT sample than to actual effects of the differences in isomer composition. Additionally, films of isomeric ADT have been produced under different growth conditions, which neither influenced the resulting structural nor the optical properties. The latter result also indicates that preparing ADT films by means of OMBD is a controlled and reproducible process, which

is critical for the preparation of binary films including ADT as a compound, which plays a crucial role in this work.

List of contributions

Excimeric emission in blends with spacer molecules (Chapter 7)

Publication

J. Hausch, A. J. Berges, C. Zeiser, T. Rammler, A. Morlok, J. Bredehöft, S. Hammer, J. Pflaum, C. J. Bardeen, K. Broch; Distinguishing between triplet-pair state and excimer emission in singlet fission chromophores using mixed thin films. *J. Phys. Chem. C* **2022**, 126, 15, 6686–6693.

Single crystals

Single crystal growth	–	S. Hammer (Prof. Dr. J. Pflaum)

ADT:6Ph blends

Sample preparation	–	C. Zeiser
Structural characterization	–	J. H., C. Zeiser
Optical characterization	–	J. H., C. Zeiser
TCSPC measurements	–	C. Zeiser, T. Rammler (Prof. Dr. A. Meixner)
TRPL measurements	–	A. J. Berges (Prof. Dr. C. J. Bardeen)
Data analysis	–	J. H.

ADT:TET blends

Sample preparation	–	A. Morlok
Structural characterization	–	J. H., A. Morlok
Optical characterization	–	J. H., A. Morlok
TCSPC measurements	–	A. Morlok, T. Rammler (Prof. Dr. A. Meixner)
TRPL measurements	–	A. J. Berges (Prof. Dr. C. J. Bardeen)
Data analysis	–	J. H.

Singlet fission in the presence of energetically low-lying lattice sites (Chapter 8)

Publication

N. Hofeditz, J. Hausch, K. Broch, W. Heimbrodt, F. Schreiber, M. Gerhard; Efficient Energy Transfer and Singlet Fission in Co-Deposited Thin Films of Pentacene and Anthradithiophene *Adv. Opt. Mater.* **2023**, under review.

ADT:PEN blends

Sample preparation	–	J. H.
Structural characterization	–	J. H.
Optical characterization	–	J. H.
TRPL measurements	–	N. Hofeditz (JProf. Dr. M. Gerhard)
Data analysis	–	J. H., N. Hofeditz (JProf. Dr. M. Gerhard)

Excited-state delocalization and singlet fission (Chapter 9)

Publication

J. Hausch, N. Hofeditz, J. Bredehöft, S. Hammer, J. Pflaum, K. Broch, F. Schreiber; Influence of excited-state delocalization in singlet fission: Tuning triplet-pair state emission in thin films. *J. Phys. Chem. C* **2023**, 127, 7, 3778–3786.

Single crystals

Single crystal growth	–	S. Hammer (Prof. Dr. J. Pflaum)

ADT:ZnPC films

Sample preparation	–	J. H., J. Bredehöft
Structural characterization	–	J. H., J. Bredehöft
Optical characterization	–	J. H., J. Bredehöft
TRPL measurements	–	J. H., N. Hofeditz (JProf. Dr. M. Gerhard)
Data analysis	–	J. H.

Impact of thermal energy on singlet fission (Chapter 10)

ADT:HPhB films

Sample preparation	–	J. H., J. Bredehöft
Structural characterization	–	J. H., J. Bredehöft
Optical characterization	–	J. H., J. Bredehöft
TRPL measurements	–	J. H., N. Hofeditz (JProf. Dr. M. Gerhard)
Data analysis	–	J. H.

List of abbreviations

Table E.3.: List of abbreviations.

Abbreviation	Corresponding term
ADT	anthradithiophene
CT	charge transfer
CuPC	copper phthalocyanine
DFT	density functional theory
FRET	Förster resonance energy transfer
FWHM	full width half maximum
GA	global analysis
GIWAXS	grazing incidence wide-angle X-ray scattering
GID	grazing incidence diffraction
HPhB	hexaphenylbenzene
HOMO	highest occupied molecular orbital
IC	internal conversion
ISC	intersystem crossing
LUMO	lowest unoccupied molecular orbital
OFET	organic field effect transistor
OLED	organic light emitting diode
OMBD	organic molecular beam deposition
OPV	organic photovoltaics
OSC	organic semiconductor
PEN	pentacene
PL	photoluminescence
QCM	quartz crystal microbalance
RSL	red-shifted luminescence
SEM	scanning electron microscopy
SSA	singlet-singlet annihilation
STA	singlet-triplet annihilation
TDM	transition dipole moment

Abbreviation	Corresponding term
TET	tetracene
TRPL	time-resolved photoluminescence spectroscopy
TTA	triplet-triplet annihilation
XRD	X-ray diffraction
XRR	X-ray reflectivity
ZnPC	zinc phthalocyanine
6Ph	[6]-phenacene

Own publications

1. J. Hausch, N. Hofeditz, J. Bredehöft, S. Hammer, J. Pflaum, K. Broch, F. Schreiber; Influence of excited-state delocalization in singlet fission: Tuning triplet-pair state emission in thin films. *J. Phys. Chem. C* **2023**, 127, 7, 3778–3786.

2. J. Hausch, A. J. Berges, C. Zeiser, T. Rammler, A. Morlok, J. Bredehöft, S. Hammer, J. Pflaum, C. J. Bardeen, K. Broch; Distinguishing between triplet-pair state and excimer emission in singlet fission chromophores using mixed thin films. *J. Phys. Chem. C* **2022**, 126, 15, 6686–6693.

3. N. Hofeditz, J. Hausch, K. Broch, W. Heimbrodt, F. Schreiber, M. Gerhard; Efficient Energy Transfer and Singlet Fission in Co-Deposited Thin Films of Pentacene and Anthradithiophene *Adv. Opt. Mater.* **2023**, under review.

4. F. Unger, L. Moretti, J. Hausch, J. Bredehöft, C. Zeiser, S. Haug, R. Tempelaar, N. J. Hestand, G. Cerullo, K. Broch; Modulating singlet fission by scanning through vibronic resonances in pentacene-based blends. *J. Am. Chem. Soc.* **2022**, 144, 45, 20610–20619.

5. S. Giannini, L. Di Virgilio, M. Bardini, J. Hausch, J. J. Geuchies, W. Zheng, M. Volpi, J. Elsner, K. Broch, Y. H. Geerts, F. Schreiber, G. Schweicher, H. I. Wang, J. Blumberger, M. Bonn, D. Beljonne; Transiently delocalized states enhance hole mobility in organic molecular semiconductors. *Nat. Mater.* **2023**.

6. C. P. Theurer, A. M. Valencia, J. Hausch, C. Zeiser, V. Sivanesan, C. Cocchi, P. Tegeder, K. Broch; Photophysics of charge transfer complexes formed by tetracene and strong acceptors. *J. Phys. Chem. C* **2021**, 125, 11, 6313–6323.

7. N. Hofeditz, M. Gerhard, C. P. Theurer, J. Hausch, K. Broch, W. Heimbrodt, M. Koch; Photoexcitation dynamics in strongly interacting donor/acceptor blends probed by time-resolved photoluminescence spectroscopy. *J. Phys. Chem. C* **2021**, 125, 31, 17194–17201.

8. Q. Wang, A. Franco-Cañellas, J. Yang, J. Hausch, S. Struzek, M. Chen, P. K. Thakur, A. Gerlach, S. Duhm, F. Schreiber; Heteromolecular bilayers on a weakly interacting substrate: Physisorptive bonding and molecular distortions of copper–hexadecafluorophthalocyanine. *ACS Appl. Mater. Interfaces* **2020**, 12, 12, 14542–14551.

Danksagung

Im Folgenden möchte ich mich für die Unterstützung bedanken, die ich im Laufe des Erstellens dieser Arbeit erhalten habe.

An erster Stelle möchte ich Dr. Katharina Broch und Prof. Dr. Dr. h.c. Frank Schreiber danken, dass sie es mir ermöglicht haben, diese Arbeit zu verfassen. Weiter möchte ich mich bei beiden für die zuverlässige und bestmögliche Betreuung bedanken, sowie das großzügige Zurverfügungstellen von Laboren und Instrumenten.

Weiter möchte ich Prof. Dr. Dr. h.c. Frank Schreiber und JProf. Dr. Jannika Lauth für das Verfassen der Gutachten zu dieser Arbeit danken.

Bei Prof. Dr. Alfred J. Meixner, Tim Rammler und Dr. Clemens Zeiser möchte ich mich für die Durchführung von TCSPC-Messungen, bei Prof. Dr. Christopher J. Bardeen und Dr. Adam J. Berges für die Durchführung von TRPL-Messungen und bei Prof. Dr. Jens Pflaum und Dr. Sebastian Hammer für die Herstellung von Einkristallen bedanken. An dieser Stelle möchte ich mich ebenfalls bei JProf. Dr. Marina Gerhard und Nico Hofeditz für die Möglichkeit, TRPL-Messungen in Marburg durchzuführen, bedanken, sowie für ihre ausgiebige Hilfe während der Messungen. Zusätzlich möchte ich mich bei Dr. Florian Bertram, Dr. Dmitry Lapkin, Frederik Unger und Ingrid Dax für ihren großen Einsatz bei Messungen am DESY in Hamburg bedanken. Für die Synthese von anti-ADT danke ich Dr. Chengyuan Wang.

Ich danke allen Mitgliedern der Arbeitsgruppe, die mich bei dieser Arbeit maßgeblich unterstützt haben, zum Beispiel durch ihre fachliche Beratung oder durch tatkräftige Hilfe im Labor. Besonders möchte ich in diesem Zusammenhang Jona Bredehöft, Arne Morlok, Dr. Clemens Zeiser, Christoph Theurer und Frederik Unger hervorheben. Für das Gegenlesen der Arbeit danke ich Adina Hausch, Michael Zimmermann, Christoph Theurer, Dr. Clemens Zeiser, Frederik Unger, Dr. Elena Chulanova und Ingrid Dax.

Der gesamten Arbeitsgruppe möchte ich für die außerordentlich herzliche und produktive Arbeitsatmosphäre danken, sowie für das uneingeschränkt gemeinschaftliche Miteinander innerhalb und außerhalb des Arbeitsalltags. Besonders möchte ich mich bei Frederik Unger, Christoph Theurer, Clemens Zeiser und Ingrid Dax in diesem Zusammenhang für viele spannende Gespräche und zahlreiche gemeinsame Freizeitaktivitäten bedanken.

Zuletzt möchte ich mich noch bei meiner Familie und meinen Freunden für ihre Unterstützung in jeglicher Hinsicht während dieser Zeit bedanken.